

中国科学技术大学

博士学位论文



基于 ATLAS 探测器上 ZZ 玻色子到全轻子 衰变道的事例对电弱对称性破缺过程的研 究

作者姓名： 祝鹤龄

学科专业： 粒子与原子核物理

导师姓名： 赵政国 马宏

完成时间： 二〇二〇年十月五日

University of Science and Technology of China
A dissertation for doctor's degree



**Studies of Electroweak Symmetry
Breaking in ZZ Production in Purely
Leptonic Decay with ATLAS Detector**

Author: Heling Zhu

Speciality: Particle and Nuclear Physics

Supervisors: Zhengguo Zhao (USTC), Hong Ma (BNL)

Finished time: October 5, 2020

摘要

论文介绍了本人在粒子物理领域基于大型强子对撞机 (LHC) 上 ATLAS 实验做的研究工作。LHC 是当今世界上最大的、能量最高的对撞机，在其上发生的质子-质子对撞实验质心系能量最高可达 14 TeV。LHC 凭借其空前的能量，在理论与实验之间架起了一座重要桥梁。ATLAS 实验是 LHC 上的一个通用粒子探测器实验，同时也是体积最大的粒子探测器。该实验旨在利用 LHC 提供的超高能量和亮度来观测涉及大质量粒子的物理现象，而这些粒子是使用早期的低能加速器所无法观察到的。同时，ATLAS 实验也是 2012 年 7 月 LHC 上参与发现希格斯粒子的两个重要实验之一。

本文基于 ATLAS 实验在 LHC 上收集到的亮度为 139 fb^{-1} 能量为 13 TeV 的质子-质子对撞数据，重点介绍了两个 Z 玻色子衰变到四轻子末态过程的一系列研究。包括，标准模型(SM)下 ZZ 到四轻子过程截面的测量、矢量玻色子散射(VBS)过程在 ZZ 到四轻子末态的观测。首先， ZZ 到四轻子过程截面的测量结果为 $\sigma_{ZZjj}^{tot} = 1.27 \pm 0.12(\text{stat}) \pm 0.02(\text{theo}) \pm 0.07(\text{exp}) \pm 0.01(\text{bkg}) \pm 0.03(\text{lumi}) [\text{fb}]$ ，总体相对误差为 11%。在误差范围内，该结果和标准模型预言值 $1.14 \pm 0.04(\text{stat}) \pm 0.20(\text{theo}) [\text{fb}]$ 相吻合。同时，在两个 Z 玻色子伴随着两个喷注(jets) 末态的电弱相互作用过程的寻找中，我们观测到偏离本底假说超过 5 倍标准差 (5.5σ) 的明显偏差。在此基础上，本文也介绍了使用 3000 fb^{-1} 模拟数据，质心能量为 14 TeV 的高亮度大型强子对撞机(HL-LHC) 产生 EW-ZZjj 过程的前景研究，预言将可以观测到大于 7 倍标准差 (7σ) 的明显偏差。

本文还介绍了在一对 Z 玻色子衰变至四轻子末态过程中寻找重共振态的实验。根据不同的信号模型，寻找的粒子质量区间设置在 200 GeV 到 2000 GeV 之间。基于该测量结果，没有证据可以证明重共振态的存在。因此，研究给出了基于不同信号模型的截面上限，包括在不同衰变宽度假说下自旋为 0 的共振态，以及基于 Randall-Sundrum 模型的自旋为 2 的引力子(graviton)。在该分析中，我们认为，信号主要可通过 gluon-gluon Fusion (ggF) 和 Vector Boson Fusion (VBF) 过程产生。在自旋为 0 的窄衰变宽度模型下，我们对 ggF 和 VBF 两个过程都进行了研究。而对于大宽度模型，由于在质量很高的区间分辨率很差以及 VBF 过程的统计量太小等客观原因，只对 ggF 过程进行了研究。对于自旋为 2 的模型，实验给出了 Randall-Sundrum 模型的引力子的理论质量下限，为 1500 GeV。

本文所介绍的 ZZ 玻色子衰变到四轻子末态过程的结果都与标准模型预测的一致。该结果完善了 Vector Boson Scattering 过程在各个衰变末态的观测，是对电弱对称性坏研究的新的里程碑。同时，没有发现明显的超标准模型新物理过程。我

摘 要

们期待，大大提高了亮度和能量的下一代高亮度大型强子对撞机（HL-LHC）实验能够为这些新物理过程的寻找带来更高的灵敏度，和对如四轻子末态这样的罕见物理过程更精确的测量。

ABSTRACT

This dissertation presents my research in the field of Particle Physics with the ATLAS experiment at the Large Hadron Collider (LHC). The LHC is the world's largest and most powerful collider, and it is the proton-proton collider with the centre-of-mass energy up to 14 TeV. With its unprecedented energy, the LHC was built as a bridge between the theories and the experiment. The ATLAS experiment is a general-purpose particle detector experiment with the largest volume at the LHC. The experiment was designed to take advantage of the extremely high energy and luminosity available at the LHC and observe phenomena that involve highly massive particles which were not observable using earlier lower-energy accelerators. And it was one of the two LHC experiments involved in the discovery of the Higgs boson in July 2012.

This dissertation focus on the studies with two Z bosons production decaying into $\ell\ell\ell'\ell'$ final state, where ℓ stands for electron or muon, using 139 fb^{-1} of 13 TeV proton-proton (pp) collision data collected by ATLAS experiment at the LHC. The ZZ production in $\ell\ell\ell'\ell'$ channel provides a most clean and sensitive tool to test the Standard Model (SM) at the energy frontier and to study the *Higgs* physics. First of all, studies including the measurement on SM $ZZjj$ production cross section and the observation of Vector Boson Scattering (VBS) process. The fiducial cross section for SM $ZZjj$ production is measured to be $\sigma_{ZZjj}^{tot} = 1.27 \pm 0.12(\text{stat}) \pm 0.02(\text{theo}) \pm 0.07(\text{exp}) \pm 0.01(\text{bkg}) \pm 0.03(\text{lumi}) [\text{fb}]$ with a total relative uncertainty of 11% for the $\ell\ell\ell'\ell'$ final state, and found to be compatible with the SM prediction of $1.14 \pm 0.04(\text{stat}) \pm 0.20(\text{theo}) [\text{fb}]$. The electroweak production of two jets in association with a Z -boson pair (EW- $ZZjj$) is observed with a significant deviation from the background-only hypothesis corresponding to a statistical significance of 5.5σ . Following with the observation, the prospect study for the EW- $ZZjj$ production at the High luminosity LHC (HL-LHC) using 3000 fb^{-1} simulated pp collision data at a centre-of-mass energy of 14 TeV is presented, with a expected significance of around 7σ .

Meanwhile, a search for heavy resonances decaying into a pair of Z bosons to $\ell\ell\ell'\ell'$ final state is also conducted in this dissertation. Different mass ranges for the hypothetical resonances are considered, depending on the signal models and spanning between 200 GeV and 2000 GeV. Data is found to agree with a background-only hypothesis, thus, the results are interpreted as upper limits on production cross section for sevaral different models, including heavy Higgs like (spin-0) narrow-width approximation (NWA) and

Abstract

large-width approximation (LWA), as well as the Randall–Sundrum model with a graviton excitation spin-2 resonance (RSG). The signal is assumed to generate dominantly via gluon-gluon Fusion (ggF) production mode and Vector Boson Fusion (VBF) production mode. Both ggF and VBF channels are studied in NWA, while for LWA, only ggF channel is studied due to worse resolution in higher mass region and the lack of statistic for VBF process. In addition, mass of RS Graviton is constrained, $m(G_{KK}) < 1500$ GeV is excluded at 95% CL by $ZZ \rightarrow \ell\ell\ell'\ell'$ analysis.

The ZZ to $\ell\ell\ell'\ell'$ production presented in this dissertation are consistent with the SM prediction. This result completes the observation of weak boson scattering that is a new milestone in the study of electroweak symmetry breaking. In the meantime, no indication of new physics is observed. We are looking forward to the HL-LHC, with greatly increased luminosity and higher centre-of-mass energy, which should enhance the sensitivity for new physics search and precise measurement for rare process.

Acknowledgments

First of all, I would like to express my great gratitude to my supervisors Prof. Zhao Zhengguo and Dr. Ma Hong, for their guidance and patience during my Ph.D years. It's Zhengguo, who inspire me with his deep physics insight when I was an undergraduate student and led me enter the field of Particle Physics. I will never forget how I was attracted by his broad knowledge and the amazing picture of particles he showed me, which became the reason I choose the Particle Physics as my major. It's always relaxed and benificial greatly when chating with him, which broads my version, makes me to be more confident and helps me step out of so many difficulties.

Thanks to Hong, for giving me the oppotunity to study in Brookhaven National Lab (BNL) that I can work with so many senior and brilliant physicists, and teaching me a lot in the details of physics. As the chair of physics department at BNL, can you imagine that he managed to take time sitting with me every week, teaching me the details and techniques of my analysis as well as helping me to parepre my talks at conference.

Thank you both for leading me to the field of physics, showing me how beautiful the science and the world are. And thank you for providing me so many oppotunities and tremendous supports to work at physics frontier and work with people all over the world. It's my greatest honor to be your student. Your strong personalitis will definitely influence my future life and career.

I would like to give my large gratitude to Prof. Zhou Bing. It's Bing who introduced me to ATLAS experiment when I was a junior. As a professor and group leader of ATLAS group in University of Michigan with busy schedule, Bing still took time to teach me in physics start from simple formulas and help me to prepare my first academic presentation patiently when I was a undergraduate student. Also it's my great fortune that I can have opportunities to work with you and learn from you in so many analyses during these years. Your kind and patience, your high standard influence me deeply in all these years.

Moreover, I really want to give my sincere gratitudo to Dr. Xu Lailin. Thank you, Lailin, for all your helps during the passing five years. Thanks for teaching me in all the analysis details, coding techniques, presentation skills hand by hand. You are really a very good and patient teacher and give me as many knowledges as you can. Your broad knowledge, your perseverance in science and your very hard working indeed affect me a lot.

In the meantime, I want to give my special thanks to Dr. Li Bing, who helped me

Acknowledgments

a lot in several different analyses (low-mass 4μ resonance search, VBSZZ analysis, Z' search), he never hesitated to give his hand to me when I faced difficulties.

I would like to express my gratitude to many colleagues in both USTC and BNL team. Thanks to Prof. Sun Yongjie, who is the supervisor of my undergraduate thesis, helped me start my first detector project on MRPC. Also thanks Dr. Liu Zhen who taught me in details in this project, and helped me a lot for my life at BNL too. Thanks to Prof. Peng Haiping, Prof. Zhu Yingchun and Dr. Hu Qipeng for helping me all the details and techniques in HWW analysis when I was a beginner. Thanks to Dr. Dai Tiesheng, I have learnt quite a lot in the project of Monitored Drift Tubes (MDT) when working with you at CERN and also thank you for all the help in regular life since that was my first time to Europe. Thanks to Dr. Chen Hucheng, who is the supervisor of my ATLAS qualification task on LAr Trigger Digitizer Boards (LTDB) and the person lead me into this interesting electronic project. And my appreciation to Dr. Xu Hao, Dr. Chen Kai and Dr. Liu Hongbin who taught me in patience for this project as I was really a freshman on electronics. Thanks to Prof. Yuji Enari and Dr. Georges Aad for the help in LAr software tasks when I moved from BNL to CERN. In the meantime, I would really like to give my gratitude to Dr. Michael Begal, Dr. Marc-Andre Pleier, Dr. Alessandro Tricoli, Dr. George Redlinger, Dr. Viviana Cavalieri, Dr. Gaetano Barone and many senior physicists in BNL omaga group. I have learnt a lot from every chat with you and every seminar you hosted. Also I want to thanks to Prof. Wu Yusheng, Prof. Qian Jianming, Prof. Liu Yanwen, Dr. Ju Xiangyang for teaching me in lots of details in different physics analyses.

Moreover, I want to give my thanks to friends I met at USTC, BNL and CERN during my Ph.D years. Thanks to Dr. Yang Qian, Dr. Chu Xiaoxuan, Dr. Tu Biao, Dr. Gao Shanshan, Dr. Liu Feng, Dr. Yuan Guangyuan, and many other friends I met at BNL. Thanks to Prof. Geng Cong, Dr. Li Peilian, Dr. Zhang Liqing, Dr. Guo Yicheng, Dr. Xu Tairan, Dr. Wang Rongkun, Chen Jing, He Fudong, Guo Qianying, Chen Ye, Xu Hao, Wang Tao, Xie Xiangyu, Liu Xiangtian and all friends I met at USTC and CERN. Thank you all my friends! I will always remember all the happiness with you, and best wishes to you in the future!

Last but not least, I would give my greatest gratitude to my families. Thanks my parents for giving me all your endless loves and supports in my whole life. My deep appreciation to my three aunts for loving and caring me so much since I was born and help me to accompany with my mother when I was thousands miles far away from home. And my husband, Lin, thank you for your understanding and walk through all difficulties with me in these years especially when we were in a foreign country.

Contents

Acknowledgments	V
Chapter 1 Introduction	1
Chapter 2 Theory	3
2.1 The Standard Model of Particle Physics	3
2.1.1 Elementary particles in the Standard Model	3
2.1.2 Electroweak theory	4
2.1.3 Higgs mechanism and Electroweak symmetry breaking	6
2.1.4 Beyond the SM Higgs sector	9
2.2 Phenomenology of Large Hadron Collider	10
2.2.1 Physics at hadronic collision	11
2.2.2 Higgs physics at the LHC	13
2.2.3 Diboson physics at the LHC	15
Chapter 3 The Large Hadron Collider and the ATLAS Detector	19
3.1 The Large Hadron Collider	19
3.1.1 Operation history and machine layout	19
3.1.2 Luminosity and pile-up	22
3.2 ATLAS detector	24
3.2.1 Detector overview	24
3.2.2 Physics requirement	26
3.2.3 Magnet system	26
3.2.4 Inner detector	27
3.2.5 Calorimeters	30
3.2.6 Muon spectrometer	31
3.2.7 Trigger system	33
Chapter 4 Simulation and Event Reconstruction for the ATLAS Experiment	37
4.1 Event simulation	37
4.2 Event reconstruction	40
4.2.1 Track	40
4.2.2 Primary vertex	42
4.2.3 Electron	43

4.2.4	Muon	48
4.2.5	Jets	52
4.2.6	Missing transverse energy	56
Chapter 5	Statistical treatment of searching for new particles or processes	59
5.1	The likelihood function	59
5.2	Test statistic	60
5.3	The CLs upper limit	62
5.4	Nuisance parameters	63
Chapter 6	Studies of SM ZZ production in $\ell\ell\ell'\ell'$ final state using pp collision data collected by ATLAS detector from 2015 to 2018	64
6.1	Introduction	64
6.2	Data and MC samples	65
6.2.1	Data samples	65
6.2.2	MC simulations	66
6.3	Objects and Event selection	67
6.3.1	Objects selection	67
6.3.2	Event selection	68
6.4	Background estimation	69
6.4.1	QCD backgrounds	69
6.4.2	Reducible backgrounds	70
6.5	Systematics	74
6.5.1	Theoretical systematics	74
6.5.2	Experimental systematics	76
6.6	Measurement of fiducial cross section	79
6.6.1	Calculation of C-factor	79
6.6.2	Result of fiducial cross section	80
6.7	Search for EW- $ZZjj$	80
6.7.1	MD discriminant	80
6.7.2	Fitting procedure	80
6.7.3	Result of fit	82
6.8	Prospect study of EW- $ZZjj$ production in HL-LHC	84
6.8.1	The ATLAS detector at HL-LHC	85

6.8.2	Simulation	85
6.8.3	Event selection	85
6.8.4	Systematics	86
6.8.5	Results	88
6.9	Conclusion	91
Chapter 7	Search for heavy resonances decaying into a pair of Z bosons in $\ell\ell\ell'\ell'$ final state using pp collision data collected by ATLAS detector from 2015 to 2018	92
7.1	Introduction	92
7.2	Data and MC samples	93
7.2.1	Data samples	93
7.2.2	Background MC simulations	93
7.2.3	Signal MC simulations	94
7.3	Analysis selections	95
7.3.1	Objects selection	95
7.3.2	Event selection	96
7.3.3	Event categorizations	98
7.3.4	Signal acceptance	104
7.4	Background estimation	105
7.4.1	Irreducible backgrounds	106
7.4.2	Reducible backgrounds	110
7.5	Signal modelling	111
7.5.1	Modelling of narrow-width signal	112
7.5.2	Modelling of large-width signal	112
7.5.3	Modelling of interference	116
7.5.4	Modelling of spin-2 RS Graviton signal	120
7.6	Systematic uncertainties	121
7.6.1	Theoretical uncertainties	122
7.6.2	Experimental systematics	124
7.7	Results in $\ell\ell\ell'\ell'$ channel	124
7.7.1	Statistical procedure	125
7.7.2	For the likelihood function under background-only hypothesis for MVA-based analysis	126
7.7.3	Interpretations	129
7.8	Conclusion	135

Contents

Chapter 8 Summary	136
Bibliography	139

List of Figures

2.1	The elementary particles of the Standard Model.	3
2.2	The Feynman diagrams of interactions that form the basis of the standard model.	5
2.3	The Higgs potential $V(\phi)$ with $\mu^2 > 0$ (left) and $\mu^2 < 0$ (right).	7
2.4	Schematic view of a hadron-hadron collision ^[8] .	11
2.5	The PDF4LHC15 NLO PDFs at a low scale $\mu^2 = Q^2 = 4\text{GeV}^2$ (left) and at $\mu^2 = Q^2 = 100\text{GeV}^2$ (right) as a function of x.	12
2.6	Feynman diagrams of the Higgs production modes: (a) ggF; (b) VBF; (c) VH; (d) ttH.	14
2.7	The SM Higgs boson production cross sections for various production modes as a function of the centre-of-mass energy for pp collision.	14
2.8	Higgs boson production cross section for various production modes as a function of the Higgs mass for $\sqrt{s} = 13 \text{ TeV}$ (left) and 14 TeV (right) for pp collision.	14
2.9	SM Higgs decay channels.	15
2.10	Branching ratio of Higgs decays in various channels as a function of Higgs mass ^[14] .	16
2.11	The tree-level Feynman diagrams of diboson production at the LHC.	16
2.12	Total production cross-section presented by ATLAS as a function of centre-of-mass energy \sqrt{s} from 7 to 13 TeV for some selected processes, the diboson measurements are scaled by a factor 0.1 to allow a presentation without overlaps.	17
2.13	Feynman diagrams of the vector boson scattering.	17
2.14	Feynman diagrams of vertexes involving QGC, TGC and Higgs.	18
3.1	Cumulative luminosity as a function of time in years from 2011 to 2018 for ATLAS detector.	20
3.2	CERN accelerator complex ^[20] .	21
3.3	Integrated luminosity in ATLAS.	23
3.4	Number of Interactions per Crossing from 2015-2018 in ATLAS.	23
3.5	Coordinate system used by the ATLAS experiment at the LHC ^[22] .	24
3.6	Cut-away view of the ATLAS detector ^[23] .	25

List of Figures

3.7	Schematic diagram of the ATLAS magnet system.	27
3.8	Schematic diagram of the ATLAS inner detector ^[25] .	28
3.9	Schematic diagram of the ATLAS 4-Layer Pixel Detector.	28
3.10	SCT (a) barrel module and (b) end-cap ^[29] .	29
3.11	Cut-away view of the ATLAS calorimeters. The LAr calorimeters are seen inside the scintillator-based tile hadronic calorimeters ^[31] .	30
3.12	Schematic diagram of a LAr EM calorimeter barrel module.	31
3.13	Schematic diagram of tile calorimeter module ^[33] .	32
3.14	Cut-away view of the ATLAS muon spectrometer ^[35] .	32
3.15	Schematic diagram of the ATLAS trigger and data acquisition system in run-2.	34
3.16	An examples of L1 calorimeter trigger tower for electron and photon triggers ^[37] .	35
3.17	The HLT trigger algorithm sequence ^[37] .	36
4.1	The flow of the ATLAS simulation software.	37
4.2	Sketch of a hardon-hardon collision simulated by MC event generator. The red blob in center denotes the hard collision, surrounded by tree-like structures representing Bremsstrahlung which is simulated by Parton Showers. The purple blob stands for a secondary hard scattering event. The light green blobs indicate the parton-to-hardon transitions and the dark green blobs represents hardon decays. The yellow lines are soft photon radiations.	39
4.3	The flowchart of the ATLAS data processing.	40
4.4	Schematic view of the ATLAS inner detector showing all the corresponding components.	41
4.5	Schematic of the impact parameters of a track in the transverse plane (left) and RZ-plane (right), as defined in the global ATLAS tracking frame ^[59] .	46
4.6	The efficiencies of three electron identification WPs from $Z \rightarrow ee$ (left) events and hadrons misidentified as electrons estimated using di-jet MC samples (right).	47
4.7	Distributions of $E_T^{cone0.2}$ (left) and $p_T^{varcone0.2}$ (right) for electrons from $ZZ \rightarrow ee$ events in data and MC simulation. The simulated events (full histograms) are normalized to data.	48
4.8	Muon reconstruction efficiency as a function of η for: Medium (and Loose), Tight and High- p_T working points.	51
4.9	Muon reconstruction efficiency for Low- p_T working point as a function of η .	52

4.10	Distributions of the calorimeter-based (right) and the track-based (left) relative isolation variables measured in $Z \rightarrow \mu\mu$ events	53
4.11	A overview schematic of ATLAS jet reconstruction ^[65]	53
4.12	A overview schematic of ATLAS jet calibration ^[66]	54
4.13	MV2c10 BDT output for b- (solid blue), c- (dashed green) and light-flavour (dotted red) jets in $t\bar{t}$ events ^[67]	56
4.14	Measured E_T^{miss} distribution for $Z \rightarrow \mu\mu$ events (left) and $W \rightarrow e\nu$ events (right)	57
5.1	(a) Illustration of the relationship between the observed t_μ and its p -value. (b) The relationship between p -value and the observed significance Z , where $\phi(x)$ is the standard normal distribution	61
6.1	Typical diagrams for the production of $ZZjj$, including the relevant EW VBS diagrams (first row) and QCD diagrams (second row)	65
6.2	Pre-fit m_{ZZ} and m_{jj} distribution in QCD-enriched CR	71
6.3	Fake factor for $Z+jets$ background, constructed with additional electron, as a function of p_T (left) and η (right)	72
6.4	Fake factor for $Z+jets$ background, constructed with additional muon, as a function of p_T (left) and η (right)	72
6.5	Fake factor for $t\bar{t}$ background, constructed with additional electron, as a function of p_T (left) and η (right)	73
6.6	Fake factor for $t\bar{t}$ background, constructed with additional muon, as a function of p_T (left) and η (right)	73
6.7	The theoretical uncertainties for $gg \rightarrow ZZ$ background in particle-level SR (left) and CR (right)	76
6.8	MD distribution for QCD- $ZZjj$ process in low and high pile-up events for SR (left) and CR (right)	78
6.9	MD shape difference for QCD $q\bar{q} \rightarrow ZZ$ background between different Sherpa theoretical uncertainties and sample from MadGraph5_aMC@NLO on SR (left) and CR (right)	78
6.10	Observed and post-fit expected multivariate discriminant distributions after the statistical fit in the $\ell\ell\ell'\ell'$ SR (left) and QCD CR (right). The error bands include the experimental and theoretical uncertainties, as well as the uncertainties in μ_{EW} and $\mu_{QCD}^{\ell\ell\ell'jj}$. The error bars on the data points show the statistical uncertainty on data	82

6.11	Observed and post-fit expected m_{jj} distributions in SR (left) and QCD CR (right). The error bands include the expected experimental and theoretical uncertainties. The error bars on the data points show the statistical uncertainty. The contributions from the QCD and EW production of $ZZjj$ events are scaled by 0.96 and 1.35, respectively, corresponding to the observed normalization factors in the statistical fit. The last bin includes the overflow events.	83
6.12	Observed and post-fit expected m_{ZZ} spectrum in SR. The error bands include the expected experimental and theoretical uncertainties. The error bars on the data points show the statistical uncertainty. The contributions from the QCD and EW production of $ZZjj$ events are scaled by 0.96 and 1.35, respectively, corresponding to the observed normalization factors in the statistical fit. The last bin includes the overflow events.	83
6.13	Display of an event candidate of EW- $ZZjj$ production in $2e2\mu$ channel in last MD bin ($0.875 < \text{MD} < 1.0$). The invariant mass of the di-jet (four-lepton) system is 2228 (605) GeV.	84
6.14	Detector-level distributions of EW- and QCD- $ZZjj$ processes with selected events in defined phase space at 14 TeV of (a) m_{jj} , (b) m_{ZZ} , (c) $ \Delta\phi(ZZ) $, (d) ZZ centrality, normalized to 3000 fb^{-1}	87
6.15	Jet variations on m_{jj} distribution for EW- $ZZjj$ (left) and QCD- $ZZjj$ (right) processes with luminosity of 3000 fb^{-1} at 14 TeV. <i>Upgrade Performance Function</i> is used to extract the uncertainties with <i>baseline</i> setting.	88
6.16	The expected significance of EW- $ZZjj$ processes as a function of different m_{jj} cut with 3000 fb^{-1} , under conditions of different sizes of theoretical uncertainties on the QCD- $ZZjj$ background modelling. The statistical uncertainty is estimated from expected data yield at 14 TeV with 3000 fb^{-1} . Different uncertainties are summed up quadratically.	89
6.17	The projected differential cross-sections at 14 TeV for the EW- $ZZjj$ processes as a function of m_{jj} (left) and m_{ZZ} (right). The top panel shows measurement with statistical only case, where statistical uncertainty is estimated from expected data yield at 14 TeV with 3000 fb^{-1} . The bottom panel shows impact of different sizes of systematic uncertainties.	89
7.1	(a) VBF DNN architecture diagram. (b) ggF DNN architecture.	100

7.2	(a) $m_{4\ell}$ distribution of raw (unweighted) training events for VBF signal (blue) and background (black); (b) $m_{4\ell}$ distribution of weighted VBF signal (blue) and background (black) used at training time.	101
7.3	(a) $m_{4\ell}$ distribution of raw (unweighted) training events for ggF signal (blue) and background (black); (b) $m_{4\ell}$ distribution of weighted ggF signal (blue) and background (black) used at training time.	101
7.4	The output score of “ggF-classifier” (a) and “VBF-classifier” (b) with the events passing the common event selections for the data, the SM backgrounds and an example of a NWA signal with a mass of 600 GeV. For the “VBF-classifier”, an additional requirement of at least two jets in the event is applied. The signals cross section are set to 100 times of the observed limit for the “ggF-classifier” and 30 times of the observed limit for the “VBF -classifier”. The $Z Z$ backgrounds are scaled by the normalisation factors shown in Table 7.10. The lower panels show the ratio of data to prediction. Statistical and experimental systematic uncertainties are included.	103
7.5	Significance improvements of the MVA-based over the cut-based categorization of the VBF (ggF) category for VBF (ggF) signal samples from 300 to 2000 GeV for seven different cuts on the VBF (ggF) output score. The optimal cut of 0.8 (0.5) for VBF (ggF) score is chosen as the solid line, while other alternative cuts are plotted with dashed lines. For VBF category, results at 2000 GeV for cuts of 0.8 and 0.9 are missing due to a lack of background events passing this tight selection.	103
7.6	Illustration of the MVA-based VBF and ggF event classification for events with (a) $N_{\text{jets}} < 2$ and (b) $N_{\text{jets}} \geq 2$	105
7.7	NWA acceptance as a function of m_H for the MVA-based categorization for the samples of (a) ggF production; (b) VBF production.	105
7.8	NWA acceptance as a function of m_H for the Cut-based categorization for the samples of (a) ggF production mode; (b) VBF production mode.	106
7.9	Distributions of the $m_{4\ell}$ invariant mass fit projections of the $q\bar{q} \rightarrow Z Z$ background samples for the 4μ , $4e$ and $2\mu 2e$ final states in the ggF-CBA-enriched category, and the 4ℓ inclusive VBF-CBA-enriched category. Cut-based categorization is used.	107

7.10 Distributions of the $m_{4\ell}$ invariant mass fit projections of the $gg \rightarrow ZZ$ background samples for the 4μ , $4e$ and $2\mu2e$ final states in the ggF-CBA-enriched category, and the 4ℓ inclusive VBF-CBA-enriched category. Cut-based categorization is used.	108
7.11 Distributions of the $m_{4\ell}$ invariant mass fit projections of the $q\bar{q} \rightarrow ZZ$ (EW) background samples for the 4μ , $4e$ and $2\mu2e$ final states in the ggF-CBA-enriched category, and the 4ℓ inclusive VBF-CBA-enriched category. Cut-based categorization is used.	108
7.12 Distributions of the $m_{4\ell}$ invariant mass fit projections of the $q\bar{q} \rightarrow ZZ$ background samples for the 4μ , $4e$ and $2\mu2e$ final states in the ggF-MVA-high category, the 4ℓ inclusive ggF-MVA-low category and VBF-MVA-enriched category. DNN-based categorization is used.	109
7.13 Distributions of the $m_{4\ell}$ invariant mass fit projections of the $gg \rightarrow ZZ$ background samples for the 4μ , $4e$ and $2\mu2e$ final states in the ggF-MVA-high category, the 4ℓ inclusive ggF-MVA-low category and VBF-MVA-enriched category. DNN-based categorization is used.	109
7.14 Distributions of the $m_{4\ell}$ invariant mass fit projections of the $q\bar{q} \rightarrow ZZ$ (EW) background samples for the 4μ , $4e$ and $2\mu2e$ final states in the ggF-MVA-high category, the 4ℓ inclusive ggF-MVA-low category and VBF-MVA-enriched category. DNN-based categorization is used.	110
7.15 Distributions of the $m_{2\mu2e}$ and fit projection for signal samples between 200 to 3000 GeV for ggF production mode. Three MC campaigns, mc16a, mc16d and mc16e, are combined. The lower panel in each plot shows the pull distribution.	113
7.16 Polynomial fits of the parameters μ , f_C , σ_G , σ_C , n_C and α_C for the signal $C + G$ model in the $2\mu2e$ channel as a function of m_H for the ggF production mode. The combination of the mc16a, mc16d and mc16e MC campaigns is used.	114
7.17 The difference between MC simulation and parameterization of 4μ (left), $4e$ (middle) and $2\mu2e$ (right) for the ggF production mode. The combination of the mc16a, mc16d and mc16e MC campaigns is used.	114
7.18 The final signal shapes for the ggF production mode, interpolated from the polynomial fit parameters.	114
7.19 Comparison of the analytical shape to a truth $m_{4\ell}$ distribution of gg2VV MC samples for $m_H = 450$ GeV (top), 700 GeV (bottom) and width equal to 5% (left), 10% (middle), 15% (right) of the mass.	116

7.20 Comparison between the analytical shape convoluted with detector effects and the reconstructed $m_{2\mu 2e}$ MC distribution for mass points ranging from 400 to 1800 GeV and width equal to 15% of the mass.	117
7.21 The interference (H-B) model fitted to the truth $m_{4\ell}$ MC distribution after signal region selection for $2\mu 2e$ channel.	119
7.22 The signal modelling for the large-width scenario at m_H of 400 GeV (top), 600 GeV (middle) and 800 GeV (bottom), as well as three different signal width: 5% (left), 10% (middle) and 15% (right). The contribution of the interference between heavy Higgs and SM Higgs (H-h) is shown together with the one between heavy Higgs and SM $gg \rightarrow ZZ$ background (H-b).	121
7.23 Fitted parameters of the graviton RBW, m_{RBW} and Γ_{RBW} , as a function of the graviton resonance mass, m_G	122
7.24 Reconstructed $m_{4\ell}$ distributions in the $2\mu 2e$ channel with the final signal model superimposed for each RS graviton signal sample at masses of 600 GeV, 1600 GeV and 2000 GeV. The lower panel in each plot shows the pull distribution. The dashed green lines show the truth-level graviton signal models for reference.	122
7.25 Distribution of the four-lepton invariant mass $m_{4\ell}$ for (a), (b), (c) the ggF-MVA-high categories, (d) the ggF-MVA-low category and (e) the VBF-MVA-enriched category. The backgrounds are determined from a combined likelihood fit to the data under the background-only hypothesis. The simulated signal at 600 GeV is normalized to a cross section corresponding to 50 (5) times the observed upper limit given in section 7.7.3 for the ggF (VBF) production. The error bars on the data points indicate the statistical uncertainty, and the systematic uncertainty in MC prediction is shown by the hatched band. The lower panels show the ratio of data to prediction. The red arrows indicate data points that are outside the displayed range.	127
7.26 Pulls and constraints of nuisance parameters after a background only fit to (a) Asimov data and (b) observed data in the $\ell\ell\ell'\ell'$ channel. The Asimov data is generated with background data only, and the observed data includes datasets from 2015 to 2018.	129
7.27 Correlation of nuisance parameters after a background only fit to Asimov data in the $\ell\ell\ell'\ell'$ channel. The Asimov data is generated with background data only.	130

7.28 The expected and observed upper limits at 95% CL on $\sigma \times B(H \rightarrow ZZ)$ using the MVA-based analysis for ggF (left) and VBF (right) production. The green and yellow bands represent the $\pm 1\sigma$ and $\pm 2\sigma$ uncertainties in the expected limits.	130
7.29 The expected and observed upper limits at 95% CL on $\sigma \times B(H \rightarrow ZZ)$ using the cut-based analysis for ggF (left) and VBF (right) production. The green and yellow bands represent the $\pm 1\sigma$ and $\pm 2\sigma$ uncertainties in the expected limits.	131
7.30 The local p0 scan as functions of m_H on $\sigma \times B(H \rightarrow ZZ)$ using the MVA-based analysis for ggF (left) and VBF (right) production.	131
7.31 The upper limits at 95% confidence level on $\sigma_{ggF} \times B(H \rightarrow ZZ)$ as a function of the heavy resonance mass m_H for the ggF production mode with an intrinsic width of 1% (top left), 5% (top right), 10% (bottom left) and 15% (bottom right) for both the case where interference with Standard Model processes is considered. The green and yellow bands represent the $\pm 1\sigma$ and $\pm 2\sigma$ uncertainties in the expected limits.	132
7.32 The upper limits at 95% confidence level on $\sigma_{ggF} \times B(G_{KK} \rightarrow ZZ)$ as a function of the heavy resonance mass $m(G_{KK})$ for the ggF production mode in RS Graviton model. The green and yellow bands represent the $\pm 1\sigma$ and $\pm 2\sigma$ uncertainties in the expected limits.	133
7.33 The expected (left) and observed (right) upper limits at 95% CL on $\sigma \times B(S \rightarrow ZZ)$ for ggF production mode at different hypothetical models including the MVA- and cut- based NWA, LWA with width assumptions of 1, 5, 10, 15%, and the RSG.	133
7.34 Comparisons of the expected upper limits at 95% CL on the cross section times branching ratio as a function of the heavy resonance mass m_H for the ggF production mode (left) and for the VBF production mode (right) in the case of the NWA. The expected limits from the previous publication are shown in the green dashed line and are projected to the 139 fb^{-1} as shown in the blue dashed line. In addition, the current results based on either cut-based categorisation or the multivariate-based categorisation are shown in red and black lines.	134
7.35 Display of one candidate event in 4μ final state with the mass of 1.35 TeV.	134

List of Tables

3.1	Summary of design parameters of the LHC for pp collisions.	20
4.1	Overview of the contributions to E_T^{miss} .	58
6.1	Overlap removal criteria between pre-selection objects for the $\ell\ell\ell'\ell'$ channel. The overlap removal follows the order shown in this table. Once an object has been marked as removed, it does not participate in the subsequent stages of the overlap removal procedure.	68
6.2	Summary of selection of physics objects and candidate events at detector level in the $\ell\ell\ell'\ell'jj$ signal region.	69
6.3	Observed data and expected signal and background yields in 139 fb^{-1} of luminosity. Minor backgrounds are summed together as ‘Others’. Uncertainties on the predictions include both statistical and systematic components.	69
6.4	Observed data and expected signal and background yields in 139 fb^{-1} of luminosity. Diboson background in table includes all the other diboson processes discussed in section 6.2.2, except those with four-lepton final state. Uncertainties include only MC statistic. No events from $Z+jets$ and $t\bar{t}$ MC samples pass the selection, and are indicated as 0 in the table.	70
6.5	Fake background estimations in the SR. For nominal value, the 2D fake factor together with the $Z+jets$ and $t\bar{t}$ combination applied. The other lines show the estimations with different uncertainty variations.	74
6.6	Summary of different variations for EW- and QCD- $ZZjj$ theoretical uncertainties measurement.	75
6.7	Summary of theoretical uncertainties for the fiducial volume (SR) for both EW and QCD qq -initial processes.	75
6.8	Summary of theoretical uncertainties for the control region for EW and qqQCD processes.	75
6.9	Experimental systematic uncertainties in $\ell\ell\ell'\ell'$ channel with the luminosity of 139 fb^{-1} . The “Electron Exp.”, “Muon Exp.” and “Jet Exp.” represent the quadrature of the respective sources from electron, muon, and jets.	77
6.10	C Factor of different $ZZjj$ processes.	79
6.11	Measured and predicted fiducial cross-sections in $\ell\ell\ell'\ell'jj$ final-state. Uncertainties due to different sources are presented.	80

6.12	Input features for the training of MD.	81
6.13	Observed μ_{EW} and $\mu_{\text{QCD}}^{\ell\ell\ell'jj}$, as well as the observed and expected significance from the individual $\ell\ell\ell'\ell'$ channel. The full set of systematic uncertainties are included.	82
6.14	Comparison of event yields for signal ($N_{\text{EW-ZZjj}}$) and background ($N_{\text{QCD-ZZjj}}$) processes, and expected significance of EW-ZZjj processes, normalized to 3000 fb^{-1} data at 14 TeV, with baseline and alternative selections. Uncertainties in the table refer to expected data statistical uncertainty at 14 TeV with 3000 fb^{-1}	86
6.15	Summary of expected cross-section measured with different theoretical uncertainties. The statistical uncertainty is computed from expected data yield with 3000 fb^{-1} at 14 TeV. Different uncertainties are treated as uncorrelated and summed quadratically.	90
7.1	Summary of the recorded integrated luminosity (lumi), average and peak pile-up (PU) of data from 2015 to 2018.	93
7.2	Summary of the p_T (E_T) trigger thresholds (in GeV) employed for the muon (electron) trigger selection in the year of 2015, 2016, 2017, and 2018.	96
7.3	Summary of the object and event selection requirements.	99
7.4	Input features used in the “VBF-classifier” for the $\ell\ell\ell'\ell'$ analysis. The RNN stands for the recurrent neural network and MLP for the multilayer perceptron.	102
7.5	Input features used in the “ggF-classifier” for the $\ell\ell\ell'\ell'$ analysis. The RNN stands for the recurrent neural network and MLP for the multilayer perceptron.	104
7.6	Summary of acceptance uncertainties of PDF, QCD scale and parton shower variations for ggF production. The MVA-based categorization is used.	123
7.7	Summary of acceptance uncertainties of PDF, QCD scale and parton shower variations for VBF production. The MVA-based categorization is used.	123
7.8	Summary of acceptance uncertainties of PDF, scale, and parton showering variations for QCD $q\bar{q} \rightarrow ZZ$ background. The MVA-based categorization is used.	124

7.9	Expected and observed numbers of events for $m_{4\ell} > 200$ GeV, together with their systematic uncertainties, for three MVA-based categories. The expected number of events, as well as their uncertainties, are obtained from a likelihood fit to the data under the background-only hypothesis. The uncertainties of the ZZ normalisation factors, presented in table 7.10, are also taken into account.	126
7.10	ZZ normalization factor in each category, obtained from a likelihood fit to the data under the background-only hypothesis.	128
7.11	Impact of the leading systematic uncertainties, the data statistic uncertainties, as well as the total uncertainties on the predicted signal event yield with the cross section times branching ratio being set to the expected upper limit, expressed as a percentage of the signal yield for the ggF (left) and VBF (right) production modes at $m_H = 400$ and 1000 GeV.	128

Dedicated to my mother!

献给我的母亲！

Chapter 1 Introduction

The goal of particle physics is to understand how our universe works at its most fundamental level. It can be accomplished by pursuing the mysteries of the basic construction of matter and energy, probing the interactions between elementary particles, and exploring the basic nature of space and time itself.

Elementary particles

From around the 6th century BC, ancient Greek philosophers Leucippus, Democritus, and Epicurus brought up a philosophical idea that everything is composed of “uncuttable” elementary particles. In the 19th century, John Dalton, through his work on stoichiometry, concluded that each element of nature was composed of a single, unique type of particle. The particle was named as “atom” after the Greek word atomos, with the meaning of “in-divisible”. However this Dalton’s atom theory was strongly challenged later. Near the end of 19th century, physicists discovered that Dalton’s atoms are not, in fact, the fundamental particles of nature, but conglomerates of even smaller particles. Electron was discovered by J. J. Thomson in 1897, and then its charge was carefully measured by Robert Andrews Millikan and Harvey Fletcher in their “oil drop experiment” of 1909. In early 20th-century, Rutherford’s “gold foil experiment” showed that the atom is mainly empty space, with almost all its mass concentrated in a tiny positively charge atomic nucleus. Then the discoveries of anti-particles (the positron in 1932) and other particles (e.g. the muon in 1936) show that more discoveries could be expected in future experiments.

Starting from 1950s, more accelerator facilities were put into service. Throughout the 1950s and 1960s, a bewildering variety of particles were found in collisions of particles from increasingly high-energy beams. It was referred to informally as the “particle zoo”. In 1964, the quark model was independently proposed by physicists Murray Gell-Mann and George Zweig, and experimentally confirmed of their existence in mid-1970s. In 1970s, the establishment of quantum chromodynamics (QCD) postulated the fundamental strong interaction, experienced by quarks and mediated by gluons.

The well-known Standard model (SM) was developed in stages throughout the latter half of the 20th century. Since then, confirmation of the top quark (1995), the tau neutrino (2000), and the Higgs boson (2012) have added further credence to the Standard Model. Now, the quarks, leptons and gauge bosons are the elementary constituents in a framework of Standard Model of particle physics, which theoretically describes three of the four known fundamental forces (the electromagnetic, weak, and strong interactions,

and not including the gravitational force) in the universe, as well as classifies all known elementary particles.

Higgs mechanics and electroweak symmetry breaking

In 1961, Sheldon Glashow, Steven Weinberg and Abdus Salam together brought forward a unified electroweak theory to combine the electromagnetic and weak interactions. In the standard model, if under the condition that the energy is high enough but electroweak symmetry is unbroken, all elementary particles are massless. But measurements show the fact that the W and Z bosons actually have masses. Later on, the Higgs mechanics resolves this conundrum. The simplest description of the mechanism adds a Higgs field that permeates all space to the Standard Model. Below some extremely high energy, the field causes spontaneous symmetry breaking during interactions. All massive particles in the Standard Model, including the W and Z bosons, interact with Higgs boson to acquire their mass.

Over the past few decades, with the combination of electroweak theory, Higgs mechanics and strong interactions has been widely accepted. But the Higgs boson, which is essential to explain the mechanics of the property “mass” for gauge bosons and fermions, had been the final missing piece in the Standard Model of particle physics at that time. The mass of Higgs boson was not specifically predicted, and it has been searched in several large experiments (eg. LEP at CERN, Tevatron at Fermilab, and LHC at CERN) with different energy. In 2012, the discovery of Higgs boson was finally announced by the ATLAS and CMS collaborations at the Large Hadron Collider (LHC) with its mass round 125 GeV. Peter Higgs and Francois Englert were award the 2013’s Nobel Prize in Physics for their theoretical discovery of a mechanism that contributes to our understanding of the origin of mass of subatomic particles.

Contents of this thesis

This dissertation is organized as follows. Section 2 briefly introduces the Standard Model of particle physics, the Higgs mechanism related to the dissertation and the LHC phenomenology. Section 3 gives an overview of the LHC and the ATLAS detector. The detector simulation and the reconstruction of physics objects are described in section 4. And then section 5 focuses on the Standard model ZZ production cross section measurement in $ZZ \rightarrow \ell\ell\ell'\ell'$ channel, where ℓ stands for electron or muon, and the observation of its electroweak component as well as its further prospects in High luminosity LHC (HL-LHC). Section 6 present the search of possible heavy resonances in $ZZ \rightarrow \ell\ell\ell'\ell'$ channel. In the end, section 7 gives the summary and outlook for future physics in LHC.

Chapter 2 Theory

2.1 The Standard Model of Particle Physics

The standard model (SM) reflects our current understanding of elementary particles and several basic interactions. It is a gauge quantum field theory containing the internal symmetries of the unitary product group $SU(3) \times SU(2) \times U(1)$, in which the color group $SU(3)$ presents the strong interaction, and $SU(2) \times U(1)$ describes the electroweak interactions. Over the past decades, the SM has been widely tested through various experiments with extremely high precision.

2.1.1 Elementary particles in the Standard Model

The elementary particles in SM can be classified into 3 class: *fermions*, *gauge bosons* and the *Higgs boson* as shown in Figure 2.1.

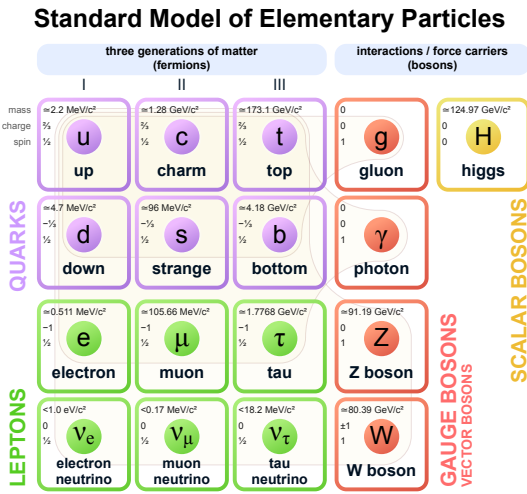


Fig. 2.1 The elementary particles of the Standard Model.

Fermions The Standard Model includes 12 elementary particles of spin- $\frac{1}{2}$ obeying the Fermi-Dirac statistics, known as fermions. They are classified into two types: *leptons* and *quarks* according to their interactions. The *leptons* include three generations: electron (e) and electron neutrino (ν_e); muon (μ) and muon neutrino (ν_μ); tau (τ) and tau neutrino (ν_τ). The e , μ and τ carry electric charge of -1 and three neutrinos are electrically neutral. All the leptons can participate in electroweak interactions. Also there are three generations of *quarks*: up (u) and down (d); charm (c) and strange (s); top (t) and bottom (b). The defining property of the quarks is that they carry color charge (while leptons don't), and hence interact via the strong interaction, letting them to be strongly bound from one to

another, forming color-neutral composite particles (known as hadrons) containing either a quark and an antiquark (mesons) or three quarks (baryons). In the meantime, u , c and t -quark carry electric charge of $2/3$, and d , s and b -quark carry electric charge of $-1/3$. Hence they interact via all three interactions described in SM. Each fermion also has a corresponding antiparticles.

Gauge bosons act as force carriers that mediate the strong, weak, and electromagnetic interactions in SM. They are spin-1 particles obeying the Bose-Einstein statistics. There are three types of gauge bosons:

- The eight massless *gluons* mediate the strong interactions between color charged particles (quarks).
- The massless *photons* mediate the electromagnetic force between electrically charged particles.
- The W^+ , W^- and Z bosons mediate the weak interactions between particles of different flavors (all quarks and leptons). All these three bosons are massive, the W^\pm carries an electric charge of $+1$ and -1 and couples to the electromagnetic interaction while Z boson is electrically neutral.

Figure 2.2 shows the Feynman diagrams of corresponding interactions in SM.

Higgs boson is a massive scalar elementary particle with spin-0. It plays a unique role in the SM by explaining the origin of masses of massive gauge bosons (W^\pm and Z) and fermions. And it is the last discovered particle in SM.

2.1.2 Electroweak theory

The electroweak interaction is the unified description of two of the four known fundamental interactions of nature: electromagnetism and the weak interaction. It is based on the gauge group of $SU(2)_L \times SU(1)_Y$, in which L is the left-handed fields and Y is the weak hypercharge^[1]. It follows the Lagrangian of

$$L_{EW} = L_{gauge} + L_{Higgs} + L_{fermion} + L_{Yukawa} \quad (2.1)$$

L_{gauge} is the **gauge term** part

$$L_{gauge} = -\frac{1}{4} W_{\mu\nu}^i W^{\mu\nu i} - \frac{1}{4} B_{\mu\nu} B^{\mu\nu} \quad (2.2)$$

where W_μ^i and B_μ present the $SU(2)_L$ and $SU(1)_Y$ gauge fields respectively, with the

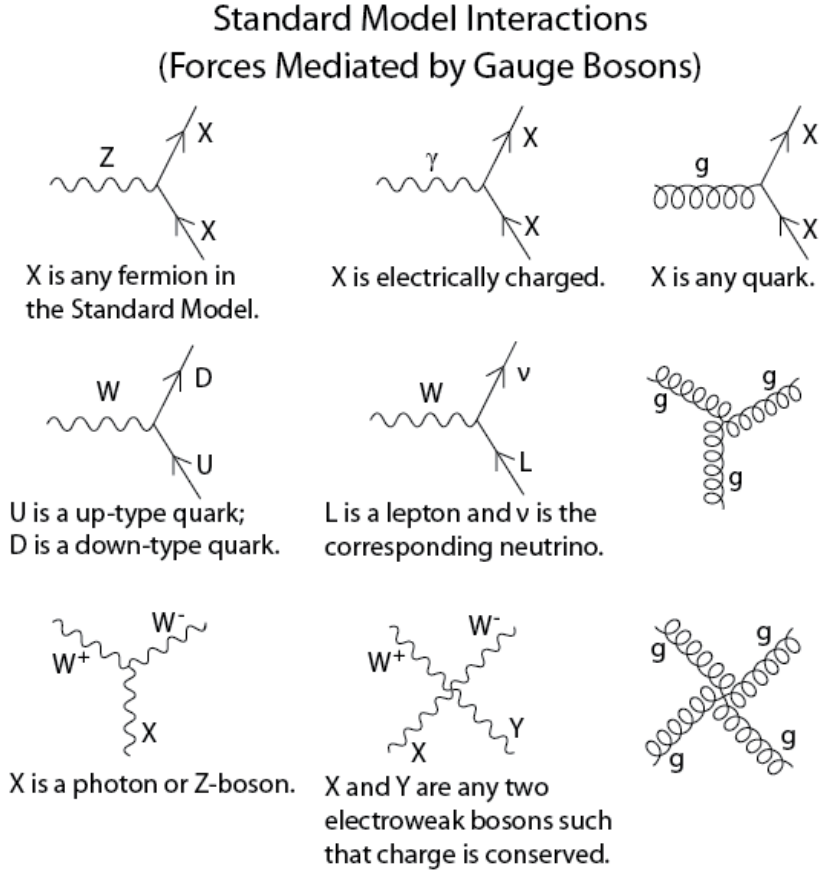


Fig. 2.2 The Feynman diagrams of interactions that form the basis of the standard model.

corresponding field strength tensors of

$$\begin{aligned} B_{\mu\nu} &= \partial_\mu B_\nu - \partial_\nu B_\mu \\ W_{\mu\nu}^i &= \partial_\mu W_\nu^i - \partial_\nu W_\mu^i - g \epsilon_{ijk} W_\mu^j W_\nu^k \end{aligned} \quad (2.3)$$

In the equations above, g is the $SU(2)_L$ gauge coupling and ϵ_{ijk} is the totally antisymmetric tensor. The gauge Lagrangian has three and four-point self interactions of W^i , which result in triple and quartic gauge boson couplings.

The second term of the Lagrangian is the **scalar part**:

$$L_{Higgs} = (D^\mu \phi)^\dagger D_\mu \phi - V(\phi) \quad (2.4)$$

where $\phi = \begin{pmatrix} \phi^+ \\ \phi^0 \end{pmatrix}$ is a complex Higgs scalar, and $V(\phi)$ is the Higgs potential which is restricted into the form of

$$V(\phi) = +\mu^2 \phi^\dagger \phi + \lambda (\phi^\dagger \phi)^2 \quad (2.5)$$

due to the combination of $SU(2)_L \times SU(1)_Y$ invariance and renormalizability. In Eq. 2.5,

μ is a mass-dependent parameter and λ is the quartic Higgs scalar coupling, which represents a quartic self-interaction between the scalar fields. When $\mu^2 < 0$, there will be spontaneous symmetry breaking (more details in section 2.1.3). To maintain vacuum stability, $\lambda > 0$ is required. And in Eq. 2.4, the gauge covariant derivative is defined as

$$D_\mu \phi = \left(\partial_\mu + ig \frac{\tau^i}{2} W_\mu^i + \frac{ig'}{2} B_\mu \right) \phi \quad (2.6)$$

in which τ^i represents the Pauli matrices, and g' is the $U(1)_Y$ gauge coupling. The square of the covariant derivative results in three and four -point interactions between the gauge and scalar fields.

The third term of the Lagrangian is the **fermion part**

$$\begin{aligned} L_{fermion} = & \sum_{m=1}^F (\bar{q}_{mL}^0 \gamma_\mu D_\mu q_{mL}^0 + \bar{l}_{mL}^0 \gamma_\mu D_\mu l_{mL}^0 + \bar{u}_{mR}^0 \gamma_\mu D_\mu u_{mR}^0 \\ & + \bar{d}_{mR}^0 \gamma_\mu D_\mu d_{mR}^0 + \bar{e}_{mR}^0 \gamma_\mu D_\mu e_{mR}^0 + \bar{\nu}_{mR}^0 \gamma_\mu D_\mu \nu_{mR}^0) \end{aligned} \quad (2.7)$$

In Eq. 2.7, m is the family index of fermions, F is the number of families. The subscripts L(R) stand for the left (right) chiral projection $\psi_{L(R)} \equiv (1 \mp \gamma_5) \psi / 2$.

$$q_{mL}^0 = \begin{pmatrix} u_m^0 \\ d_m^0 \end{pmatrix}_L \quad l_{mL}^0 = \begin{pmatrix} v_m^0 \\ e_m^{-0} \end{pmatrix}_L \quad (2.8)$$

are the $SU(2)$ doublets of left-hand quarks and leptons, while u_{mR}^0 , d_{mR}^0 , e_{mR}^{-0} and ν_{mR}^0 are the right-hand singlets.

The last term in Eq. 2.1 is **Yukawa term**

$$\begin{aligned} L_{Yukawa} = & - \sum_{m,n=1}^F [\Gamma_{mn}^u \bar{q}_{mL}^0 \tilde{\phi} u_{nR}^0 + \Gamma_{mn}^d \bar{q}_{mL}^0 \phi d_{nR}^0 \\ & + \Gamma_{mn}^e \bar{l}_{mL}^0 \phi e_{nR}^0 + \Gamma_{mn}^\nu \bar{l}_{mL}^0 \tilde{\phi} \nu_{nR}^0] + h.c. \end{aligned} \quad (2.9)$$

the matrices Γ_{mn} refer to the Yukawa couplings between single Higgs doublet (ϕ) and the various flavors of quarks (m) and leptons (n).

2.1.3 Higgs mechanism and Electroweak symmetry breaking

As shown in previous subsection, the Lagrangian L_{gauge} does not involve any mass term due to the requirement of gauge invariance. So all the W and B bosons should be massless. But experimental observations show that the gauge bosons are massive. Therefore, the gauge invariance must be broken spontaneously. The Higgs field is introduced to break the $SU(2)_L \times U(1)_Y$ symmetry and gauge bosons and fermions can interact with

Higgs filed to acquire their masses. And this specific process is named *Higgs mechanism* in SM.

The Higgs field ϕ is a doublet and can be written in a Hermitian basis as

$$\phi = \begin{pmatrix} \phi^+ \\ \phi^0 \end{pmatrix} = \frac{1}{\sqrt{2}} \begin{pmatrix} \phi_1 - i\phi_2 \\ \phi_3 - i\phi_4 \end{pmatrix} \quad (2.10)$$

where $\phi_i = \phi_i^+$ stand for four Hermitian field. In this new basis, the Higgs potential in Eq. 2.5 can be expressed as:

$$V(\phi) = \frac{1}{2}\mu^2 \left(\sum_{i=1}^4 \phi_i^2 \right) + \frac{1}{4}\lambda \left(\sum_{i=1}^4 \phi_i^2 \right)^2 \quad (2.11)$$

To simplify the situation, the axis in this four-dimensional space can be chosen to satisfied $\langle 0 | \phi_i | 0 \rangle = 0$ for $i = 1, 2, 4$, and $\langle 0 | \phi_3 | 0 \rangle = v$. Thus,

$$V(\phi) \rightarrow V(v) = \frac{1}{2}\mu^2 v^2 + \frac{1}{4}\lambda v^4 \quad (2.12)$$

The minimization of this potential depends on the sign of μ^2 as shown in figure 2.3. When $\mu^2 > 0$ the minimum occurs at $v = 0$, namely the vacuum is empty space and $SU(2)_L \times U(1)_Y$ symmetry is unbroken. In the case of $\mu^2 < 0$, the $v = 0$ symmetric point is no longer stable and the minimum occurs at nonzero value of $v = (-\mu^2/\lambda)^{1/2}$ which breaks the $SU(2)_L \times U(1)_Y$ symmetry. Thus, the classical vacuum ϕ_0 of Higgs doublet can be

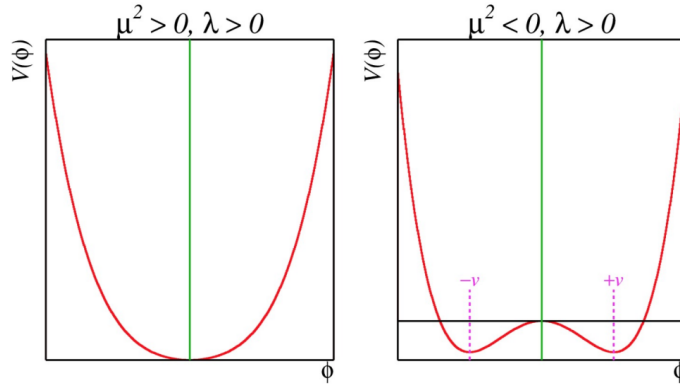


Fig. 2.3 The Higgs potential $V(\phi)$ with $\mu^2 > 0$ (left) and $\mu^2 < 0$ (right).

expressed by

$$\phi_0 = \frac{1}{\sqrt{2}} \begin{pmatrix} 0 \\ v \end{pmatrix} \quad (2.13)$$

And to quantize around the classical vacuum in a general form:

$$\phi = \frac{1}{\sqrt{2}} \begin{pmatrix} 0 \\ v + H \end{pmatrix} \quad (2.14)$$

Where H is a Hermitian field for physical Higgs scalar. In this gauge, the Lagrangian L_{Higgs} in Eq. 2.4 takes a simple form

$$\begin{aligned} L_{Higgs} &= (D^\mu \phi)^\dagger D_\mu \phi - V(\phi) \\ &= M_W^2 W^{\mu+} W_\mu^- \left(1 + \frac{H}{v}\right)^2 + \frac{1}{2} M_Z^2 Z^\mu Z_\mu \left(1 + \frac{H}{v}\right)^2 \\ &\quad + \frac{1}{2} (\partial_\mu H)^2 - V(\phi) \end{aligned} \quad (2.15)$$

where the W and Z fields are

$$\begin{aligned} W^\pm &= \frac{1}{\sqrt{2}} (W^1 \mp iW^2) \\ Z &= -\sin\theta_W B + \cos\theta_W W^3 \end{aligned} \quad (2.16)$$

Therefore, in Eq. 2.15 spontaneous symmetry breaking brings out masses for the W and Z gauge bosons

$$\begin{aligned} M_W &= \frac{gv}{2} \\ M_Z &= \sqrt{g^2 + g'^2} \frac{v}{2} = \frac{M_W}{\cos\theta_W} \end{aligned} \quad (2.17)$$

where θ_W is the weak angle defined as

$$\sin\theta_W = \frac{g'}{\sqrt{g^2 + g'^2}} \quad \cos\theta_W = \frac{g}{\sqrt{g^2 + g'^2}} \quad \tan\theta_W = \frac{g'}{g} \quad (2.18)$$

Then another gauge boson photon remains massless with the field of

$$A = \cos\theta_W B + \sin\theta_W W^3 \quad (2.19)$$

After the symmetry breaking, the Higgs potential in unitary gauge can be written into

$$V(\phi) = -\frac{\mu^4}{4\lambda} - \mu^4 H^2 + \lambda v H^3 + \frac{\lambda}{4} H^4 \quad (2.20)$$

The first term in V is a constant, while the second term denotes a (tree-level) mass of Higgs boson

$$M_H = \sqrt{-2\mu^2} = \sqrt{2\lambda} v \quad (2.21)$$

Due to the unknown of quartic Higgs coupling λ , the Higgs mass is not predicted. The

third and fourth terms in the Higgs potential V denote the induced cubic and quartic interactions of the Higgs scalar.

Through the Higgs mechanism, fermions can also acquire their masses. In the unitary gauge, Yukawa Lagrangian (L_{Yukawa}) can be written as a simple form of^[2]

$$L_{Yukawa} = - \left(1 + \frac{H}{v} \right) (m_d \bar{d}d + m_u \bar{u}u + m_l \bar{l}l) \quad (2.22)$$

in which $m_f = \frac{y_f v}{\sqrt{2}}$ for $f = d, u, l$.

2.1.4 Beyond the SM Higgs sector

After the discovery of the Higgs boson by the ATLAS and CMS Collaborations at the LHC^[3-4] in 2012, one question comes out: if this Higgs boson at around 125 GeV is fully responsible for the unitarization of the scattering amplitudes? The possibility that this discovered particle is just a part of the extended Higgs sector by various extensions cannot be ruled out. Many models, motivated by hierarchy and naturalness arguments, predicted the extended Higgs sector, such as the electroweak-singlet model and the two-Higgs-doublet models (2HDM).

Singlet scalar extension of the SM

The electroweak singlet model can be considered as the minimal extension of the SM Higgs sector^[5], encompassing a single gauge singlet real scalar field S . In this model, a heavy, real singlet is introduced in addition to the SM one. The associated zero temperature, tree-level scalar potential can be written as:

$$V = V_{SM} + V_{HS} + V_S \quad (2.23)$$

where

$$\begin{aligned} V_{SM} &= \mu^2 (H^\dagger H) + \bar{\lambda}_0 (H^\dagger H) \\ V_{HS} &= \frac{a_1}{2} (H^\dagger H) S + \frac{a_2}{2} (H^\dagger H) S^2 \\ V_S &= \frac{b_2}{2} S^2 + \frac{b_3}{3} S^3 + \frac{b_4}{4} S^4 \end{aligned} \quad (2.24)$$

where H stands for the SM scalar field of the original Higgs mechanism. After electroweak symmetry breaking, this model gives rise to two CP -even Higgs bosons, in which the lighter one is the Higgs boson that has been discovered at around 125 GeV. And the new heavy scalar (S) is allowed to have both SM and non-SM decays. One would expect to see suppressions of the branching ratio to SM Higgs decay modes, as the branching ratio to the pair of singlet-like scalars would be considerable.

Two Higgs Doublet Model

The two-Higgs-doublet model (2HDM)^[6] is another extension of SM Higgs sector carried by an additional scalar doublet. In this model, through electroweak symmetry breaking, there are five physical Higgs bosons: two CP-even, one CP-odd, and two charged ones.

The most general CP-conserving 2HDM has seven free parameters:

- The Higgs boson masses: m_h , m_H , m_A and $m_{H^{\pm}}$.
- $\tan\beta$: the ratio of the vacuum expectation values of the two doublets.
- α : the missing angle between the CP-even Higgs bosons.
- m_{12}^2 : the potential parameter that mixes the two Higgs doublets.

where the m_h can be identified as the mass of observed Higgs boson at around 125 GeV, and m_H is another heavy scalar with similar properties as h boson. The coupling of the neutral Higgs bosons to the W and Z are the same:

1. The coupling of the light Higgs, h , to either WW or ZZ is the same as the Standard Model coupling times $\sin(\beta - \alpha)$
2. The coupling of the heavier Higgs, H , is the same as the Standard Model coupling times $\cos(\alpha - \beta)$.
3. The coupling of the pseudoscalar, A , to vector bosons vanishes.

The two Higgs doublets, Φ_1 and Φ_2 , can couple to fermions (leptons and up- and down-type quarks) in several ways, which leads to several types of 2HDM models:

- Type-I model: all quarks and leptons couple only to Φ_2 .
- Type-II model: down-type quarks and leptons couple to Φ_1 , and up-type quarks couple to Φ_2 .
- The “lepton-specific” model: leptons couple to Φ_1 , while all quarks couple to Φ_2 .
- The “flipped” model: down-type quarks couple to Φ_1 , while up-type quarks and leptons couple to Φ_2 .

2.2 Phenomenology of Large Hadron Collider

The Large Hadron Collider (LHC) was built as a bridge between the theories and the experiment. Physicists hope that the LHC can help to answer some of the fundamental open questions in physics, concerning the basic laws of interactions and forces among the elementary particles, the deep structure of space and time, and in particular the interrelation between quantum mechanics and general relativity. This section will talk about firstly the general introduction of Physics inside hadronic collision, then followed by two important LHC phenomenologies of the Higgs physics and Diboson physics that are related

closely to this dissertation.

2.2.1 Physics at hadronic collision

Protons are not the elementary particle, which actually are composed of quarks and gluons. So in proton-proton (pp) collision at the LHC, it is not protons themselves interact but quarks and gluons. Scattering processes can then be further classified into either *hard* or *soft* processes according to the momentum transfer during the interaction^[7]. QCD, as an underlying theory for both processes, its approach and level of understandings in two cases are quite different. For hard process, eg. Higgs, vector bosons and jets production, the rates and event properties can be precisely predicted based on perturbation theory. However, for soft processes like total cross-section, the underlying events, the rates and properties are dominated by non-perturbative QCD effects that are less understood. For many hard processes, the hard interactions are accompanied by soft ones. An example of the hadronic collision is illustrated in figure 2.4. and the typical features are summarized

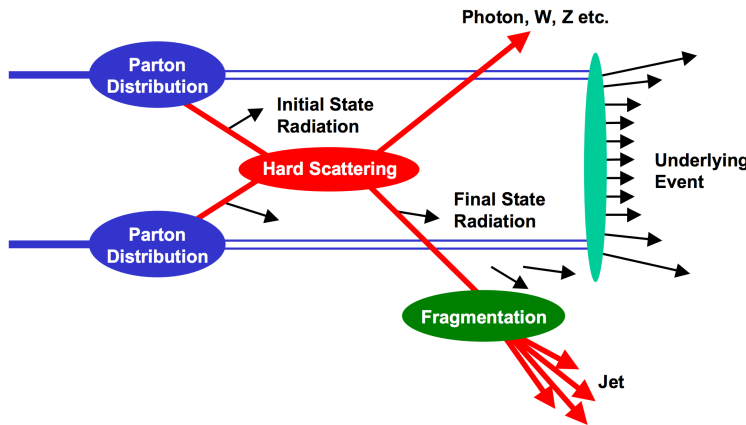


Fig. 2.4 Schematic view of a hadron-hadron collision^[8].

as below:

- **Parton Distribution Function (PDF):** $f_i(x, Q^2)$ gives the probability of finding a parton with flavor i (quark or gluon), carrying a momentum fraction of x and with the scale of momentum transfer Q in a proton. Parton distribution function cannot be fully calculated by perturbative QCD because of the inherent non-perturbative nature of partons. There are many different sets of PDFs that are determined by fits to data from experimental observables in various processes. As an example, figure 2.5 shows the *PDF4LHC15 NLO PDFs*, which are based on the combination of the *CT14*, *MMHT14* and *NNPDF3.1 NNLO* PDF sets^[9].
- **Fragmentation and hadronization:** The processes to produce final state particles

(or jets) from the partons produced in hard scattering.

- **Initial/Final state radiation:** The incoming and outgoing partons that carry color charge can emit QCD radiation, which gives rise to additional jets. Also the charged incoming and outgoing particles can emit Quantum Electrodynamics (QED) radiations with photons.
- **Underlying events:** Products from soft processes (not come from the primary hard scattering) as the remnants of scattering interactions.

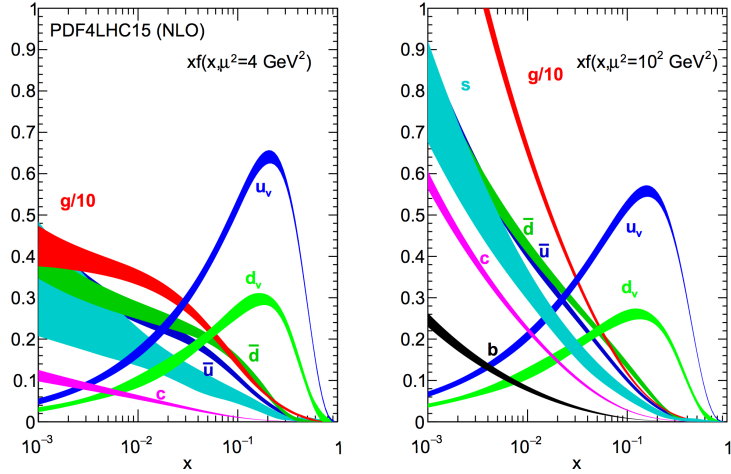


Fig. 2.5 The PDF4LHC15 NLO PDFs at a low scale $\mu^2 = Q^2 = 4\text{GeV}^2$ (left) and at $\mu^2 = Q^2 = 100\text{GeV}^2$ (right) as a function of x .

Cross section of hard scattering

According to *QCD factorization theorems*^[10], the perturbative calculations can be applied to many important hard processes involving hadrons. The basic problem addressed by factorization theorems is how to calculate high energy cross sections. Consider the process of scattering between two hardons A and B to produce a final state X, the cross section σ can be obtained by summing over all the subprocess cross section $\hat{\sigma}$ ^[11]

$$\sigma_{AB} = \int dx_a dx_b f_{q/A}(x_a) f_{q/B}(x_b) \hat{\sigma}_{ab \rightarrow X} \quad (2.25)$$

where $f_{q/A}(x_q)$ is the parton distribution functions of parton q . Taking into account the leading order correction:

$$\sigma_{AB} = \int dx_a dx_b f_{q/A}(x_a Q^2) f_{q/B}(x_b Q^2) \hat{\sigma}_{ab \rightarrow X} \quad (2.26)$$

where Q^2 represents large momentum scale that characterizes the hard scattering. Later on, since the finite corrections were not universal and had to be calculated separately for each process, the perturbative $O(\alpha_S^n)$ corrections to the leading logarithm cross section

in Eq. 2.26 need to be applied, one can get:

$$\sigma_{AB} = \int dx_a dx_b f_{a/A}(x_a \mu_F^2) f_{b/B}(x_b \mu_F^2) \hat{\sigma}_{ab \rightarrow X}(\alpha_S, \mu_R, \mu_F) \quad (2.27)$$

in which μ_F is *factorization scale* which can represent the scale that separates the long- and short-distance physics, and μ_R is the *renormalization scale* for QCD running coupling. $\hat{\sigma}_{ab \rightarrow X}$ is the parton-level hard scattering cross section that can be calculated perturbatively in QCD with the form of

$$\hat{\sigma}_{ab \rightarrow X}(\alpha_S, \mu_R, \mu_F) = (\alpha_S)^n \left[\hat{\sigma}^{(0)} + (\alpha_S/2\pi) \hat{\sigma}^{(1)}(\mu_R, \mu_F) + (\alpha_S/2\pi)^2 \hat{\sigma}^{(2)}(\mu_R, \mu_F) + \dots \right] \quad (2.28)$$

where $\hat{\sigma}^{(0)}$ stands for the leading-order (LO) partonic cross section, while $\hat{\sigma}^{(1)}$ and $\hat{\sigma}^{(2)}$ are the next-to-leading-order (NLO) and next-to-next-to-leading-order (NNLO) cross section.

μ_R and μ_F depend on the order of truncation in Eq. 2.28. In principle, if cross section is calculated to all orders, it is invariant under changes in these parameters. The choices of μ_R and μ_F are arbitrary. To avoid unnaturally large logarithms reappearing in the perturbation series, it is sensible to choose μ_R and μ_F values of the order of the typical momentum scales of the hard scattering process and $\mu_R = \mu_F$ is also often assumed. Take Drell–Yan process as an example, the standard choice is $\mu_R = \mu_F = m_{ll}$, where m_{ll} is the invariant mass of di-lepton pair.

2.2.2 Higgs physics at the LHC

One important physics purpose of the LHC is searching for the Higgs boson, which was the last missing part in the SM. This section will discuss both the production and decay modes of the SM Higgs boson in proton-proton collision.

Higgs productions

The Higgs boson can be produced through several processes. There are 4 main production modes at the LHC: gluon-gluon Fusion (ggF), vector boson Fusion (VBF), associated production with vector-bosons (VH) (also called the Higgs Strahlung) and associated production with a pair of top/anti-top quarks ($t\bar{t}H$)^[12]. Figure 2.6 shows the corresponding Feynman diagrams of each process (at LO). For pp collisions, the cross section of production of Higgs boson is a function of centre-of-mass energy \sqrt{s} . Figure 2.7 depicts the cross section of SM Higgs, whose mass is 125 GeV, for several different production modes when centre-of-mass energy varying from 6 to 15 TeV. Figure 2.8 shows the prospect of production cross section as a function of Higgs mass from 10 to 2000 GeV for pp collision at the centre-of-mass energy of 13 TeV and 14 TeV^[13].

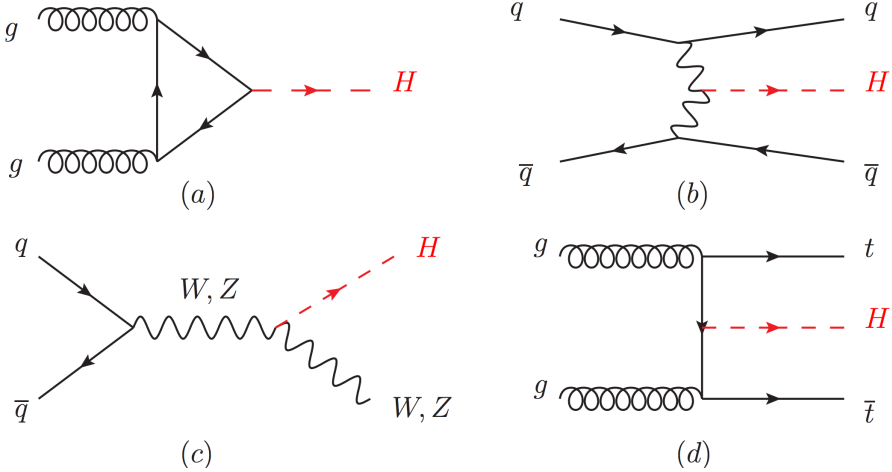


Fig. 2.6 Feynman diagrams of the Higgs production modes: (a) ggF; (b) VBF; (c) VH; (d) ttH.

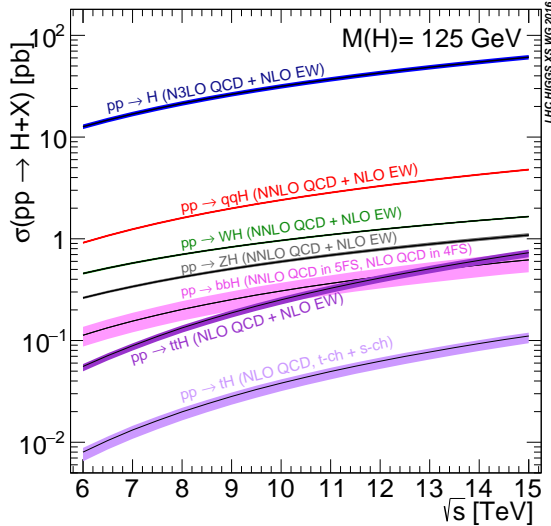


Fig. 2.7 The SM Higgs boson production cross sections for various production modes as a function of the centre-of-mass energy for pp collision.

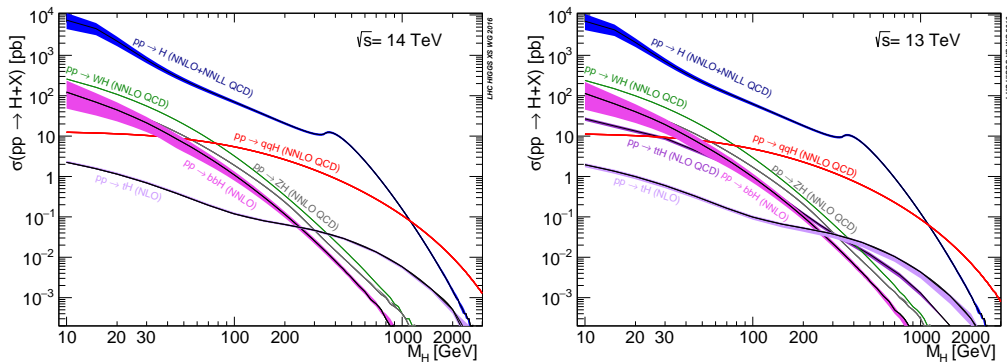


Fig. 2.8 Higgs boson production cross section for various production modes as a function of the Higgs mass for $\sqrt{s} = 13$ TeV (left) and 14 TeV (right) for pp collision.

Higgs decays

The Higgs boson can interact with gauge bosons and fermions through gauge coupling

and the Yukawa coupling as introduced in section 2.1.3. Figure 2.9 depicts the Feynman diagrams of various possible Higgs decay channels. The branching ratio of Higgs boson

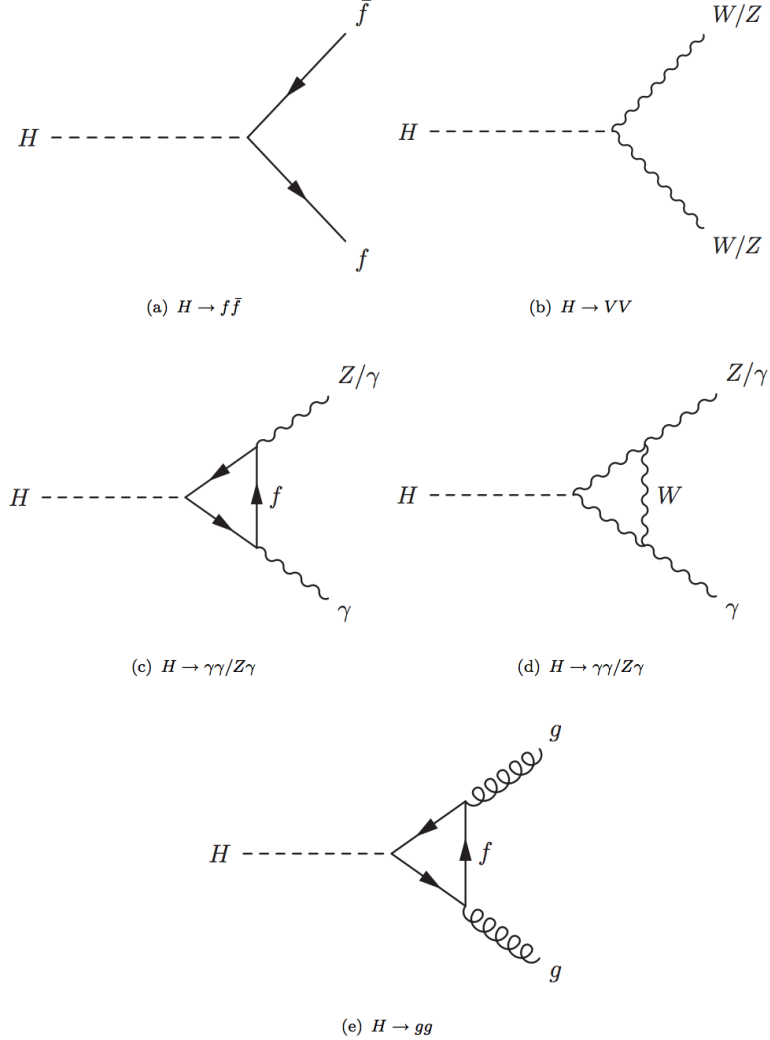


Fig. 2.9 SM Higgs decay channels.

decaying into different final states as a function of Higgs mass is shown in figure 2.10.

2.2.3 Diboson physics at the LHC

The study of diboson physics is another important test for SM of particle physics in electroweak sector, while the Vector Boson Scattering (VBS) is a key process for probing the mechanism of the electroweak symmetry breaking (EWSB). In the meantime, the non-resonant diboson productions are crucial backgrounds for Higgs studies at the LHC, which make the precise measurement of their cross section becomes very important.

Diboson productions

About 90% of diboson productions at hadron collider is from quark-antiquark annihilation, while others are from gluon initiated process. Figure 2.11 shows the tree-level

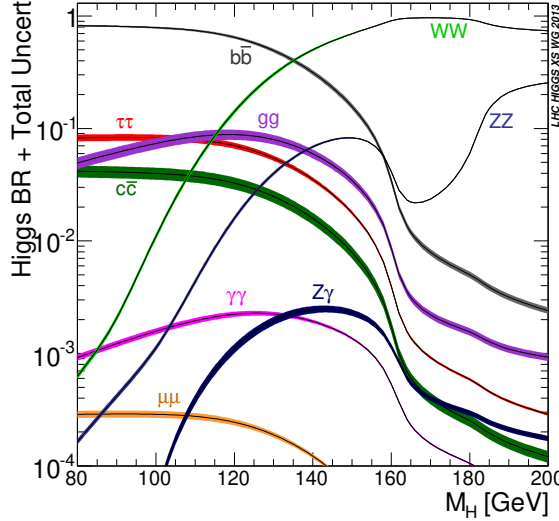


Fig. 2.10 Branching ratio of Higgs decays in various channels as a function of Higgs mass^[14].

Feynman diagrams of diboson production. Then figure 2.12 illuminates the total produc-

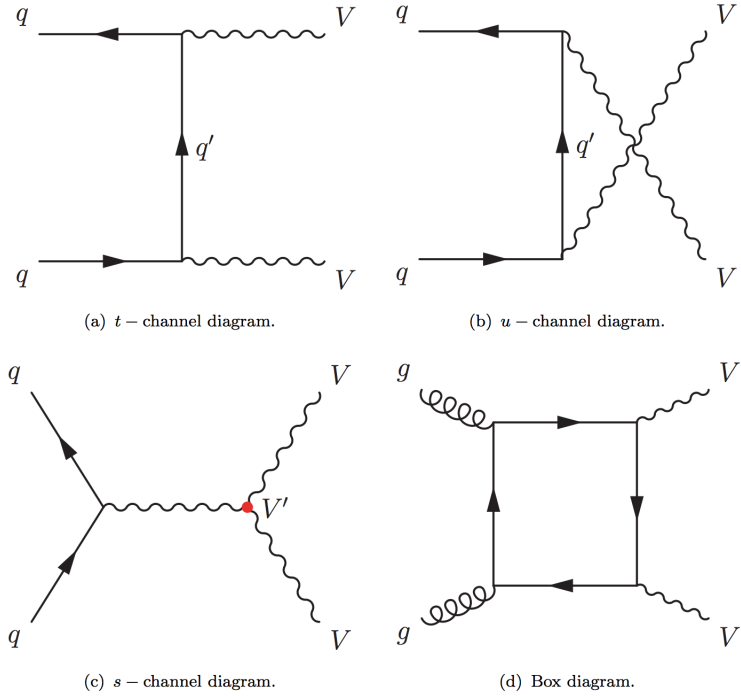


Fig. 2.11 The tree-level Feynman diagrams of diboson production at the LHC.

tion cross-section presented by ATLAS as a function of centre-of-mass energy \sqrt{s} from 7 to 13 TeV for several diboson processes compared to some other major processes in hadron collision. The cross section for diboson processes are calculated at next-to-next leading order (NNLO).

Vector boson scattering

The $SU(2)_L \times U(1)_Y$ structure in SM predicts self-interactions between electroweak gauge bosons. Those self-couplings can involve either three or four gauge bosons at a

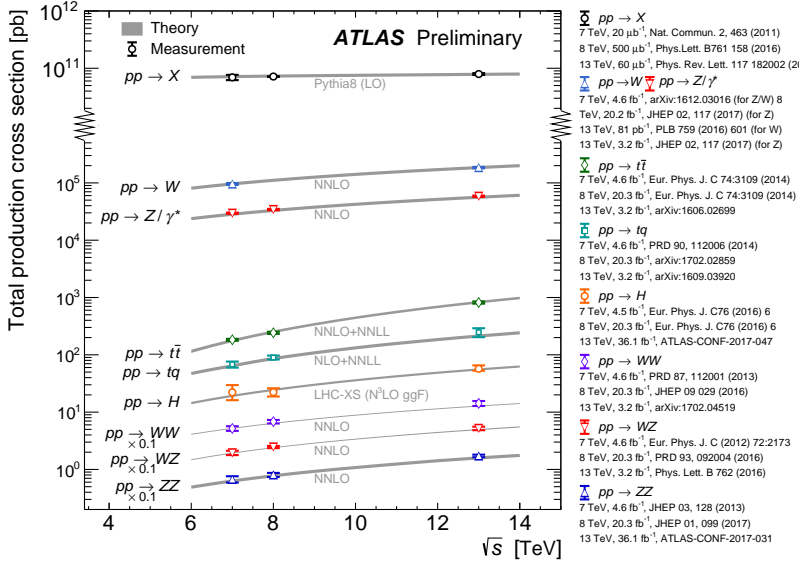


Fig. 2.12 Total production cross-section presented by ATLAS as a function of centre-of-mass energy \sqrt{s} from 7 to 13 TeV for some selected processes, the diboson measurements are scaled by a factor 0.1 to allow a presentation without overlaps.

single vertex, known as triple gauge coupling (*TGC*) or quartic gauge couplings (*QGC*), respectively. Vector boson scattering (*VBS*) is carried out by four electroweak vector bosons, namely Z , W^\pm and photon (γ) as the Feynman diagrams shown in figure 2.13. And the vertexes include either those self-interactions or the interactions with the Higgs boson are described in figure 2.14.

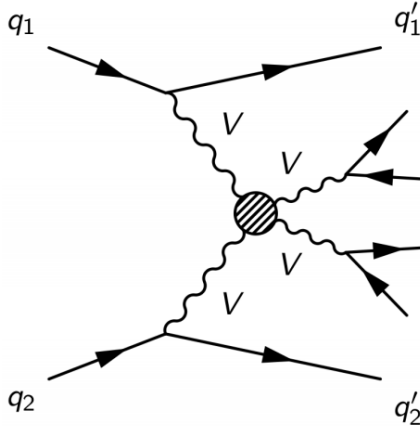


Fig. 2.13 Feynman diagrams of the vector boson scattering.

The amplitudes of leading-order (LO) VBS can be expressed as^[15]:

$$\begin{aligned} iM_{TGC}^{s-channel} &= -i \frac{g_1^2}{4m_W^4} [s(t-u) - 3m_W^2(t-u)] \\ iM_{TGC}^{t-channel} &= -i \frac{g_1^2}{4m_W^4} \left[(s-u)t - 3m_W^2(s-u) + \frac{8m_W^2}{s}u^2 \right] \end{aligned} \quad (2.29)$$

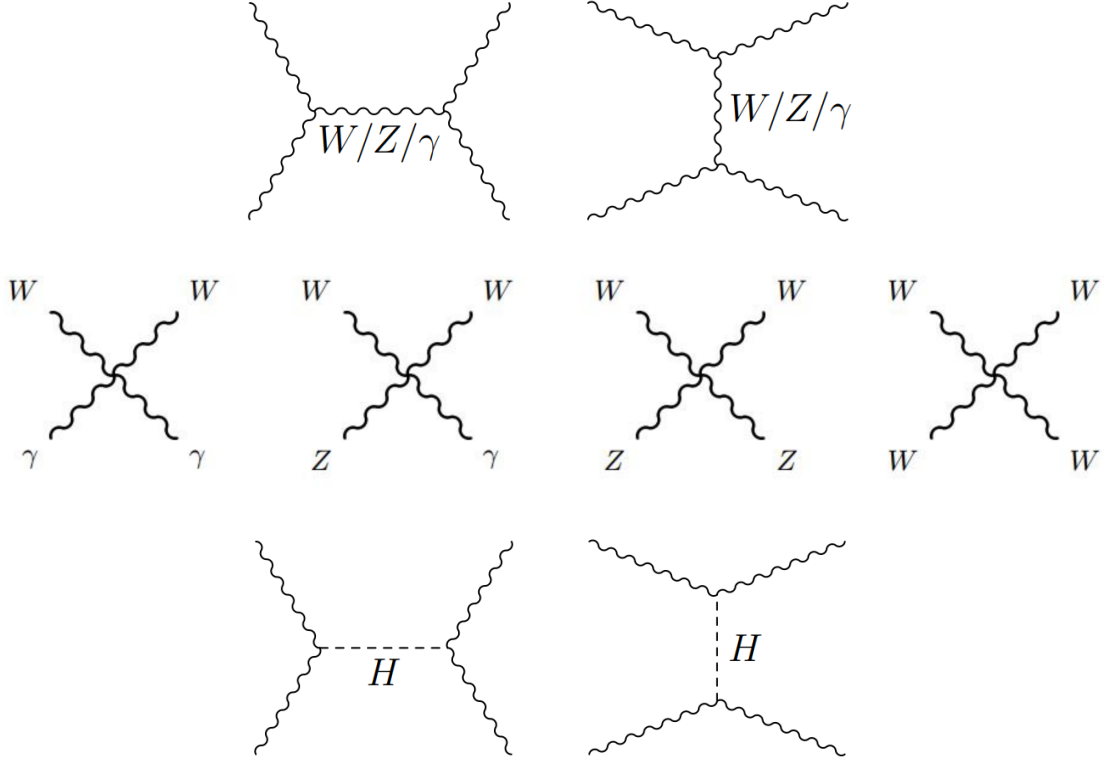


Fig. 2.14 Feynman diagrams of vertexes involving QGC, TGC and Higgs.

$$iM_{QGC} = i \frac{g_1^2}{4m_W^4} \left[s^2 + 4st + t^2 - 4m_W^2(s+t) - \frac{8m_W^2 ut}{s} \right] \quad (2.30)$$

$$\begin{aligned} iM_{Higgs} &= -i \frac{C_v g_1^2}{4m_W^2} \left[\frac{(s-2m_W^2)^2}{s-m_H^2} + \frac{(t-2m_W^2)^2}{t-m_H^2} \right] \\ &\simeq -i \frac{C_v g_1^2}{4m_W^2} (s+t) \end{aligned} \quad (2.31)$$

Combining s- and t-channel of TGC in Eq. 2.29 and the QGC term in Eq. 2.30:

$$iM_{TGC} + iM_{QGC} = i \frac{g_1^2}{4m_W^2} (s+t) + O((s/m_W^2)^0) \quad (2.32)$$

In Eq. 2.32, the amplitude grows as a function of centre-of-mass energy (\sqrt{s}), which violates the unitarity in the TeV region. Considering the Higgs term in Eq. 2.31 can perfectly cancel out this growing, and the remaining term $O((s/m_W^2)^0)$ only depends on the total amplitude in SM.

In conclusion, the Higgs boson acts as "moderator" to unitarize high-energy longitudinal vector boson scattering as introducing the Higgs restores the unitarity of total amplitude in high energy region.

Chapter 3 The Large Hadron Collider and the ATLAS Detector

3.1 The Large Hadron Collider

Located near the French-Swiss border at the European Organization for Nuclear Research (CERN), the Large Hadron Collider (LHC) is the world's largest and most powerful particle collider. It's the proton-proton collider with the centre-of-mass energy up to 14 TeV. The beams inside the LHC are made to collide at four locations around its 27-kilometer accelerator ring, corresponding to the positions of four particle detectors - ATLAS, CMS, ALICE and LHCb. With its unprecedented energy, the LHC is designed to observe physics that involve highly massive particles, which have never been observed in previous accelerators with lower energies.

3.1.1 Operation history and machine layout

Operation history

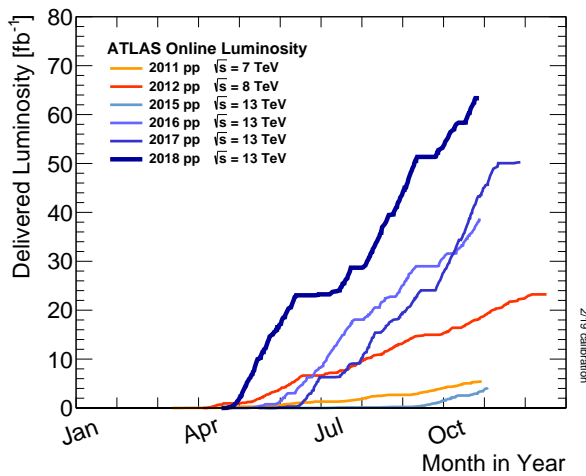
The LHC^[16-19] is a two-ring-superconducting-hadron accelerator and collider lies in a tunnel 27 kilometres in circumference and as deep as 175 metres underground. It's designed to provide proton-proton (pp) collisions at the centre-of-mass energy (\sqrt{s}) up to 14 TeV with a unprecedented luminosity of $10^{34} \text{ cm}^{-2} \text{ s}^{-1}$. In the meantime, it can also collide heavy (Pb) ions with an energy of 2.8 TeV per nucleon and a peak luminosity of $10^{27} \text{ cm}^{-2} \text{ s}^{-1}$. Table 3.1 shows the main design parameters of the LHC for proton-proton collisions.

The LHC was built from 1998 to 2008. It started its first beam in September 2008, but then was interrupted by a quench incident only after a few days running. Then it resumed the operation in November 2009 with a low energy beams. From March 2010, physics runs took place at the centre-of-mass energy of 7 TeV. Later on, this energy was increased in 2012 to $\sqrt{s} = 8 \text{ TeV}$, with an integrated luminosity of 20.3 fb^{-1} , and this period is called “run-1”. After run-1, the LHC was shut down for two years for hardware maintenance and upgrade, starting from February 2013.

The second operation period with higher centre-of-mass energy at 13 TeV started from 2015 called “run-2”. And it continued to the end of 2018 with total integrated luminosity reaching about 147 fb^{-1} for ATLAS experiment. Figure 3.1 shows the cumulative luminosity as a function of time in month delivered to ATLAS experiment during stable beams in years from 2011 to 2018.

Table 3.1 Summary of design parameters of the LHC for pp collisions.

Circumference	26.7 km
Beam energy at collision	7 TeV
Beam energy at injection	0.45 TeV
Dipole field at 7 TeV	8.33 T
Luminosity	$10^{34} \text{ cm}^{-2} \text{ s}^{-1}$
Beam current	0.56 A
Protons per bunch	1.1×10^{11}
Number of bunches	2808
Nominal bunch spacing	24.95 ns
Normalized emittance	$3.75 \mu\text{m}$
Total crossing angle	$300 \mu\text{rad}$
Energy loss per turn	6.7 keV
Critical synchrotron energy	44.1 eV
Radiated power per beam	3.8 kW
Stored energy per beam	350 MJ
Stored energy in magnets	11 GJ
Operating temperature	1.9 K

**Fig. 3.1 Cumulative luminosity as a function of time in years from 2011 to 2018 for ATLAS detector.**

Machine layout

The layout of CERN accelerator complex is shown in figure 3.2. The protons are accelerated by a series of machines before being injected into the main ring. At beginning, the 50 MeV protons are produced in the linear particle accelerator LINAC2, and further accelerated to 1.4 GeV in Proton Synchrotron Booster (PSB). The protons are

then injected into the Proton Synchrotron (PS) to gain the energy of 26 GeV and further accelerated to 450 GeV in Super Proton Synchrotron (SPS). At the end, they are injected into the main ring, and can reach a maximum energy of 7 TeV.

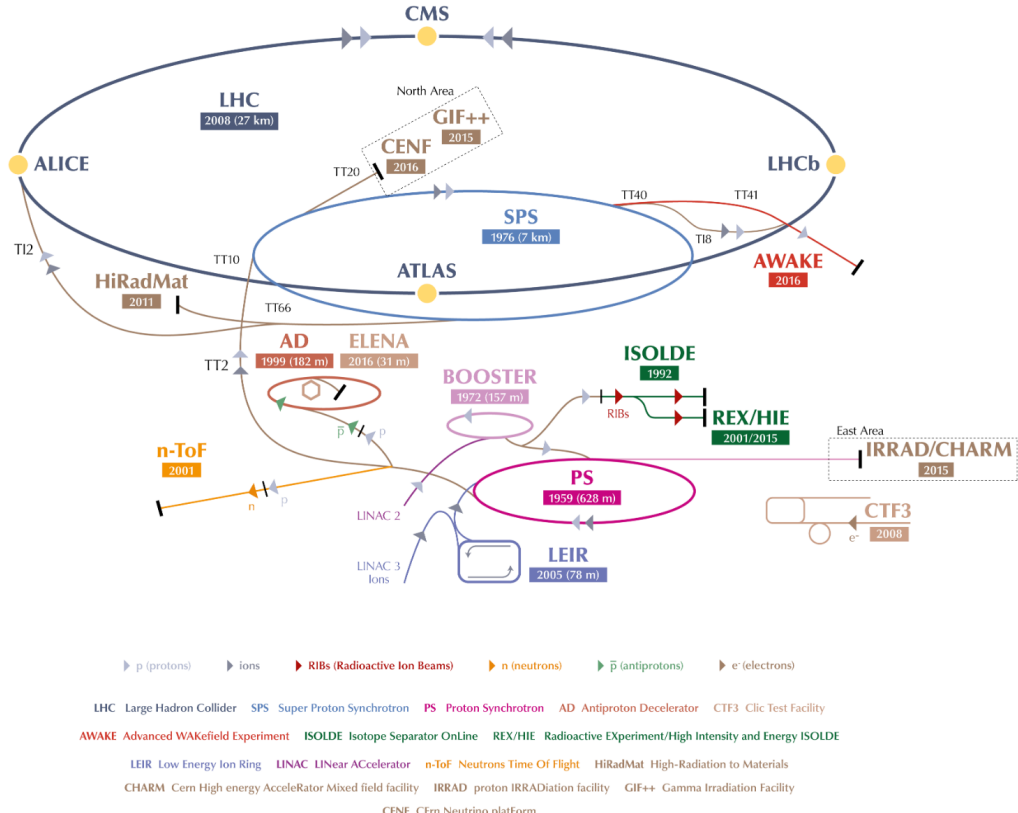


Fig. 3.2 CERN accelerator complex^[20].

The collisions can occur in 4 points, with corresponding 4 major detector experiments that are briefly described as follows:

- **ATLAS:** A Toroidal LHC ApparatuS, one of the two general-purpose particle detector experiments and detector with largest volume at the LHC. It is designed to search for the Higgs boson, test the stardand model of particle physics and search for possible beyond SM physics.
- **CMS:** Compact Muon Solenoid, another large general-purpose particle physics detector, with the same physics goal (also cross check) as ATLAS.
- **ALICE:** A Large Ion Collider Experiment, it is optimized to study heavy-ion (Pb-Pb nuclei) collisions at a centre-of-mass energy of 2.76 TeV per nucleon pair.
- **LHCb:** Large Hadron Collider beauty, it is a specialized b-physics experiment, designed primarily to measure the parameters of CP violation in the interactions of b-hadrons.

3.1.2 Luminosity and pile-up

Luminosity

In beam-beam collisions, the event rate for a process is given by^[19]:

$$N = \mathcal{L}\sigma \quad (3.1)$$

where σ is the cross section of the process, and \mathcal{L} is the luminosity. For the studies of rare events, \mathcal{L} must be as high as possible. The luminosity only depends on the beam parameters, and can be written as:

$$\mathcal{L} = \frac{N_b^2 n f_r \gamma}{4\pi \epsilon_n \beta^*} \quad (3.2)$$

where N_b denotes the number of particles per bunch, n is the number of bunches per beam, f_r is the revolution frequency, γ represents relativistic γ factor, ϵ_n is the normalized transverse emittance and β^* denotes the β function at the collision point. To reduce the beam-beam interaction effects, the bunches must have a crossing angle, which produces a geometrical luminosity reduction factor F :

$$F = 1/\sqrt{1 + \left(\frac{\theta_c \sigma_Z}{2\sigma^*}\right)} \quad (3.3)$$

where θ_c denotes the crossing angle at the interaction point, σ_Z is the root mean square (RMS) bunch length and σ^* is the transverse RMS beam size at crossing point.

The luminosity expressed in Eq. 3.2 is normally the instantaneous luminosity. In fact the running conditions usually vary with time, so the luminosity can change as well. To take into account the time dependence, integrated luminosity is invited, by integrating the instantaneous luminosity over time:

$$L = \int \mathcal{L}(t) dt \quad (3.4)$$

The unit of integrated luminosity we commonly use is b^{-1} that satisfying $1b^{-1} = 10^{24} cm^{-2}$. Figure 3.3 shows integrated luminosity as a function of time delivered to ATLAS (green), recorded by ATLAS (yellow), and certified to be good quality data (blue) during run-2 pp collisions. For most physics analysis, the data with good quality (require to satisfy *Good Run List*) is used.

Pile-up

In collisions, multiple interactions can happen in one single bunch crossing, which is called “*pile-up*”. The variable $\langle \mu \rangle$, representing the average number of interactions per

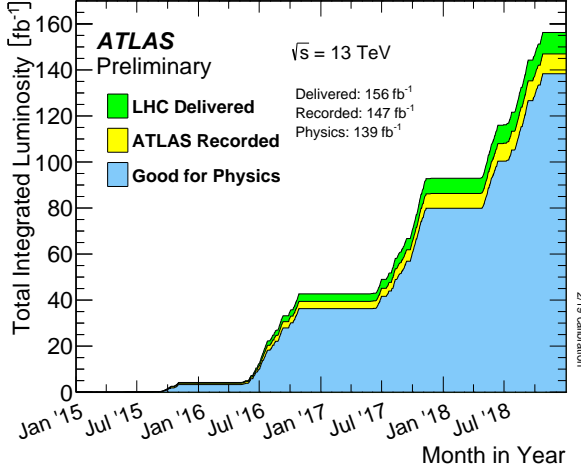


Fig. 3.3 Integrated luminosity in ATLAS.

bunch crossing, is defined to describe pile-up effect:

$$\langle \mu \rangle = \frac{L_{tot}\sigma}{f_r n_{bunch}} \quad (3.5)$$

where L_{tot} is the instantaneous luminosity, σ is the inelastic cross section, f_r is the LHC revolution frequency and n_{bunch} is the number of colliding bunches. Normally, with increasing luminosity, the pile-up becomes more significant. Figure 3.4 shows the luminosity-weighted distribution of the mean number of interactions per crossing for pp collision data from 2015 to 2018 (full run-2), the challenge of pile-up increased in each year.

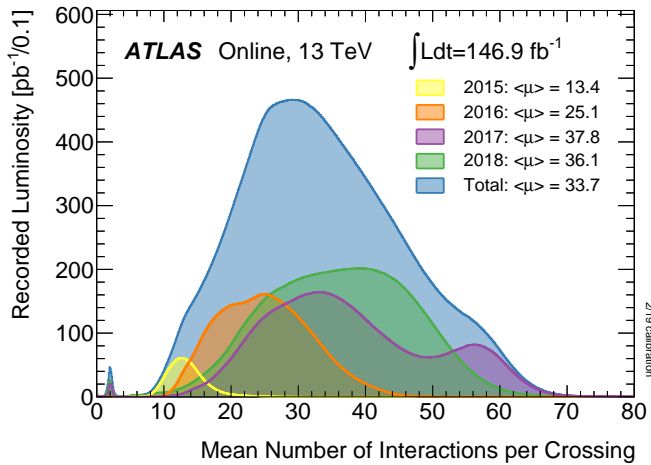


Fig. 3.4 Number of Interactions per Crossing from 2015-2018 in ATLAS.

3.2 ATLAS detector

3.2.1 Detector overview

ATLAS (A Toroidal LHC ApparatuS) is the largest volume detector ever constructed for a particle collider. It is a cylinder with 46 meters long, 25 meters in diameter, and sits in a cavern 100 meters below ground. The detector contains about 3000 km of cables and it weights 7000 tonnes.

This paragraph briefly summarizes the coordinate system and nomenclature used to describe the ATLAS detector^[21]. As depicted in figure 3.5, we define the nominal interaction point as the origin of the coordinate system, the beam direction as the z -axis and the x - y plane is transverse to the beam direction. The positive x -axis is defined to be the direction pointing to the center of the LHC ring, while the positive y -axis is pointing upwards. There are two sides of detector A and C, in which A (C) -side is in the positive

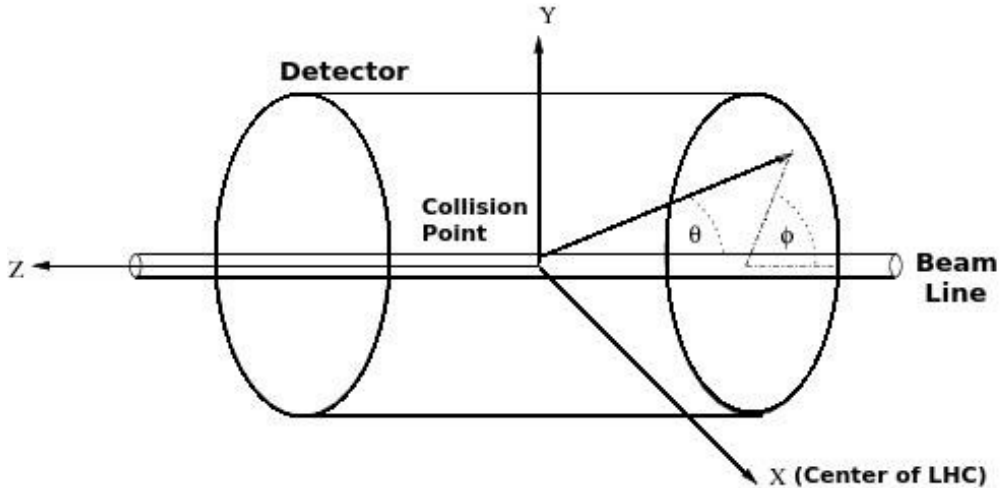


Fig. 3.5 Coordinate system used by the ATLAS experiment at the LHC^[21].

(negative) z direction. The azimuthal angle ϕ is measured as usual around the beam axis, while the polar angle θ is the angle from the beam axis. In physics analysis, we usually use the pseudorapidity instead of θ angle, which is designed as $\eta = -\ln \left[\tan \left(\frac{\theta}{2} \right) \right]$.

For massive objects (eg. jets), the rapidity $y = \frac{1}{2} \ln \left[\frac{E+p_z}{E-p_z} \right]$ is used. In addition, the transverse momentum p_T , transverse energy E_T and the missing transverse energy E_T^{miss} are defined in x - y plane. The ΔR , a commonly used distance measurement, is defined in the pseudorapidity-azimuthal angle space as $\Delta R = \sqrt{\Delta\eta^2 + \Delta\phi^2}$.

The overall ATLAS layout is shown in figure 3.6, which is forward-backward symmetric with respect to the interaction point. The magnet configuration comprises a thin superconducting solenoid surrounding the inner-detector cavity, and three large superconducting toroids (one barrel and two end-caps) arranged with an eight-fold azimuthal

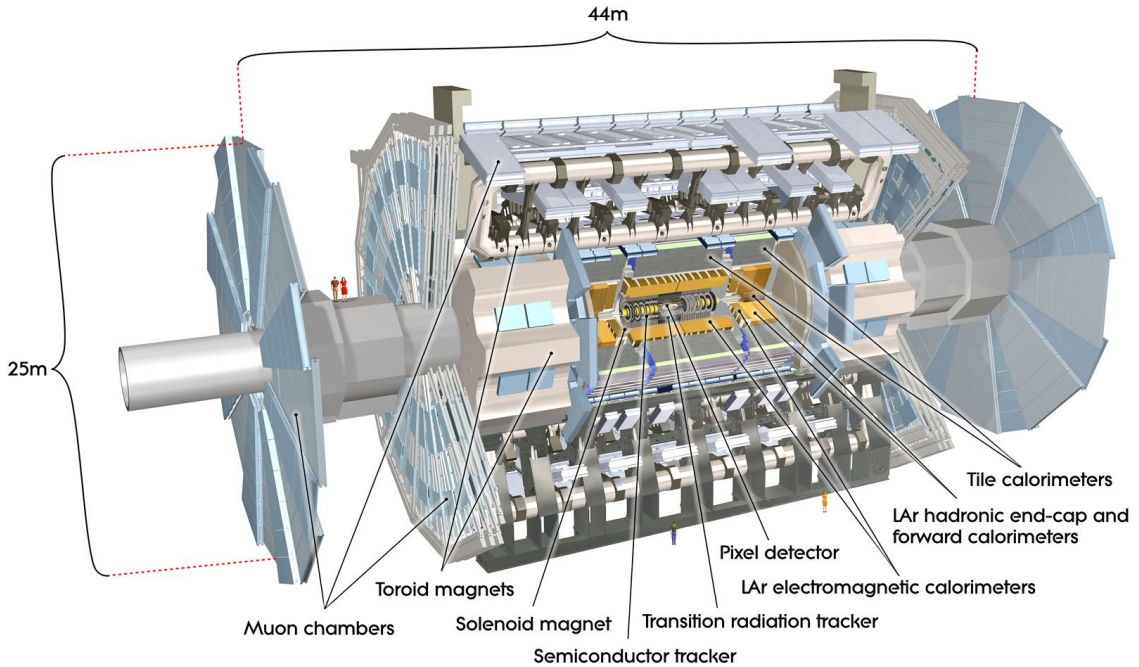


Fig. 3.6 Cut-away view of the ATLAS detector^[23].

symmetry around the calorimeters.

The inner detector, which is the innermost part of ATLAS, is immersed in a 2 T solenoidal magnetic field. It's used for pattern recognition, momentum and vertex measurements and electron identification, with the combination of tracking system.

The calorimeter is outside the solenoid, for electromagnetic and hadronic energy measurements. The high granularity liquid-argon (LAr) electromagnetic sampling calorimeters is used to measure energy and position with range up to $|\eta| < 3.2$ for electrons and photons. For hadron, a scintillator-tile calorimeter is used in the range of $|\eta| < 1.7$, and the liquid-argon hadronic endcap calorimeters (HEC) is used in end-cap region. And then the LAr forward calorimeters provide both electromagnetic and hadronic energy measurements with the coverage in forward region up to $|\eta| = 4.9$.

The muon spectrometer is the outermost layer. It's a air-core toroid system, with a long barrel and two inserted end-cap magnets that provides strong bending power in a large volume within a light and open structure. A set of chambers measuring the tracks of muons with high spatial precision and accurate time-resolution are used. Multiple-scattering effects are minor, and excellent muon momentum resolution can be achieved.

3.2.2 Physics requirement

As mentioned previously, ATLAS is one of two general-purpose particle detector experiment at the LHC. It's designed to take advantage of the unprecedented energy at the LHC, as the discovery of Higgs boson is one of its benchmark. Lots of precise tests and measurements of SM physics are ongoing with ATLAS experiment. While, in the meantime, ATLAS is also designed to observe the phenomena that involve highly massive particles, which can also explore the possibility of extra dimensions proposed by several models in TeV region. To fulfil many diverse physics goals, a set of general requirements are needed:

- The high-speed and radiation-hard electronics are required due to the experimental conditions at the LHC.
- High detector granularity is needed to reduce the overlapping events and handle the particle fluxes.
- Large acceptance in pseudorapidity and azimuthal angle coverage is needed.
- For inner detector, good charged-particle momentum resolution and reconstruction efficiency are crucial. And the vertex detectors close to the interaction region are required to be able to observe secondary vertices for offline tagging of τ -lepton and b -jets.
- Good electromagnetic (EM) calorimetry for electron and photon, as well as full-coverage hadronic calorimetry for accurate jet and missing transverse energy measurements, are essentially required, since these measurements form the basis of many studies.
- Good muon spectrometer is also required for muon identification and momentum measurement over a wide range of momenta.
- Highly efficient but with sufficient background rejection triggers are also needed and extremely important for objects with low transverse-momentum.

More detailed descriptions of each sub-system will be given in the following subsections.

3.2.3 Magnet system

A strong magnetic field is required for precise measurement of charged particle momenta. The ATLAS detector uses two large superconducting magnet systems, a hybrid system of a central superconducting solenoid and three outer superconducting toroids, to bend charged particles^[24]. The total magnet system is 22 m in diameter and 26 m in length as shown in figure 3.7.

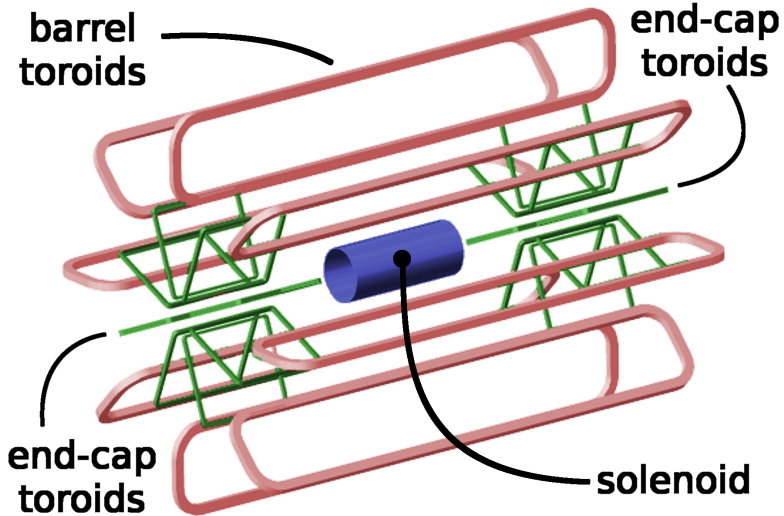


Fig. 3.7 Schematic diagram of the ATLAS magnet system.

The central solenoid produces two Tesla (T) magnetic field surrounding the inner Detector. When obtaining such high field strength, at the same time, the solenoid needs to be thin in order to reduce the material in front of the calorimeter.

The outer toroid system comprises one barrel superconducting toroid and two end-caps. The barrel one is composed of eight coils encased in individual racetrack-shaped, stainless-steel vacuum vessels and produces the magnetic field in the cylindrical volume surrounding the calorimeters. Each end-cap toroid consists of a single cold mass built up from eight flat, square coil units and eight keystone wedges and provides a magnetic field of approximately 1 T for the muon detectors in the end-cap regions.

3.2.4 Inner detector

The inner detector, as shown in figure 3.8, is the detector closest to beam pipe. It's used to measure the position of charged particle tracks in high precision together with good momentum resolution, among which the measurement of primary and secondary vertices and electron identification are especially important. Due to the extremely high luminosity produced by the LHC, the precise measurements of vertex and momentum becomes tough and fine-granularity detectors are crucial. The inner detector consists of three subdetectors described as below:

Pixel detector

The pixel detector^[26] is the innermost part of ATLAS tracking system. With finest granularity of materials, it has the best spatial resolution and 3-dimensional space-point measurement in inner detector. ATLAS Pixel Detector for the LHC run-2 is composed of 4 layers of barrel pixel detector and two end-caps with three pixel disks each, as shown in

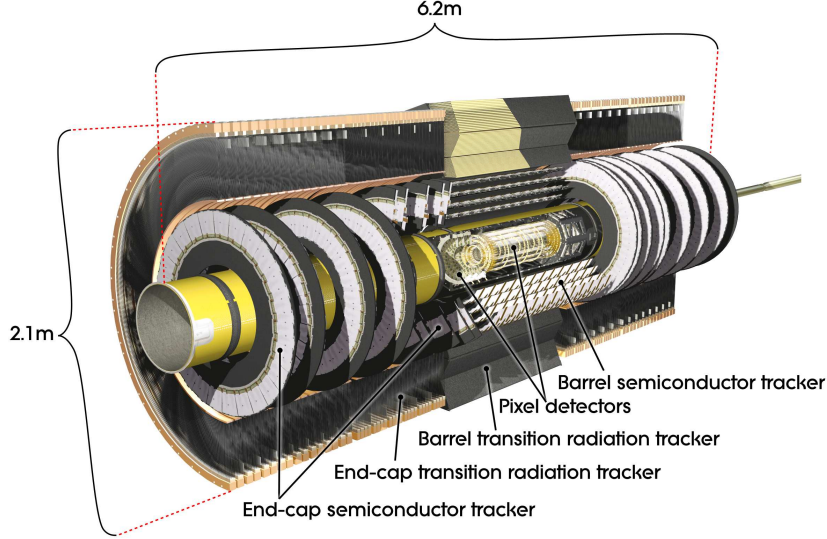


Fig. 3.8 Schematic diagram of the ATLAS inner detector^[25].

figure 3.9. There are three outer layers that originally installed for run-1 and one additional layer called Insertable B-Layer (IBL) that newly constructed in run-2^[27]. Now the 4-layer pixel detector has very good reconstruction of primary and secondary vertices, which is even crucial for long-lived particles like τ -lepton and b-quark.

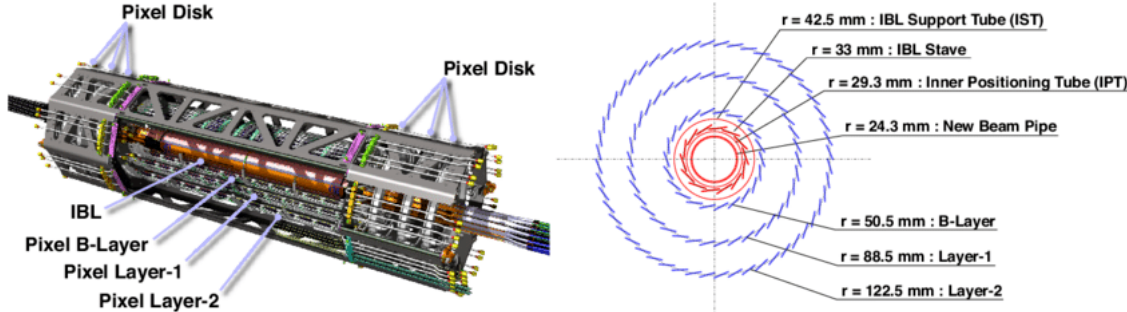


Fig. 3.9 Schematic diagram of the ATLAS 4-Layer Pixel Detector.

Semiconductor Tracker

The Semiconductor Tracker (SCT)^[28] installed outside the pixel detector is the middle component of the inner detector. It has similar function as pixel detector but with long and narrow strips instead of small pixels, which makes a much larger coverage than pixel detector. The SCT consists of 4088 modules, and contains four concentric layers in barrel (2112 modules) and nine disks in each of the two end-caps (1976 modules) as shown in figure 3.10. And it measures particles over a large area with 6.3 million readout channels and a total area of 61 square meters. The SCT is the most critical part of the inner detector for 2D track hit reconstruction. In barrel, the hit precision is $17 \mu\text{m}$ in the $r\text{-}\phi$ coordinate and $580 \mu\text{m}$ in z coordinate. In end-caps, the precision is $17 \mu\text{m}$ in the $z\text{-}\phi$ coordinate and $580 \mu\text{m}$ in r coordinate.

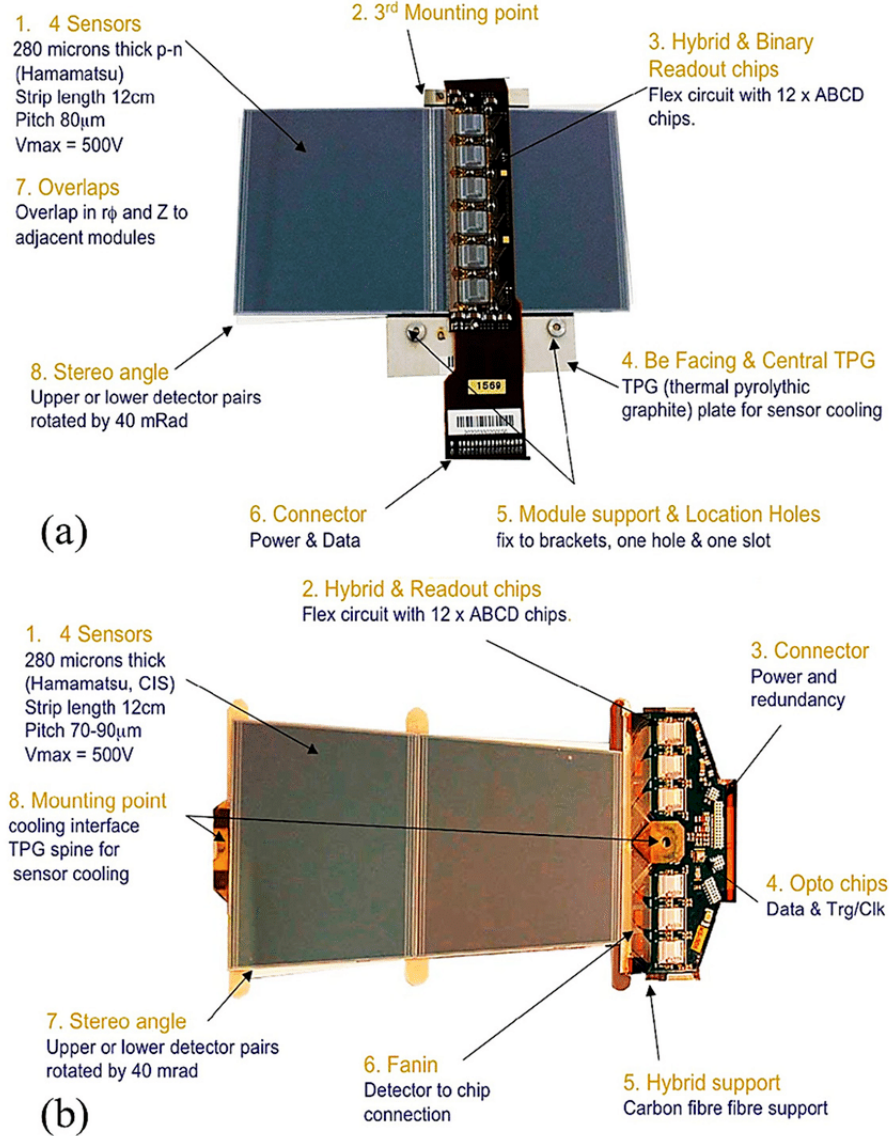


Fig. 3.10 SCT (a) barrel module and (b) end-cap^[29].

Transition radiation tracker

The transition radiation tracker (TRT)^[30] is the outermost part of inner detector, which has a very different design comparing to the two previously described sub-detectors. It can be separated into three parts: one barrel and two end-cap regions with the $|\eta|$ coverage up to 2.0. There are 73 barrel layers and 224 end-cap layers (112 in each) with 372000 straws in total, and about 351000 readout channels for TRT. The TRT provides better z resolution but much worse $r\phi$ resolution (about 130 μ m) comparing to the pixel detector and SCT per straw. But the straw hits still make significant contributions to momentum measurement, since its lower precision per point (compared to silicon) can be compensated by the large number of measurements and long track length.

3.2.5 Calorimeters

The calorimeters are designed to measure the energy from particles by absorbing them. They are located outside the solenoidal magnet that surrounds the inner detector. The ATLAS calorimeters are comprised of a number of sampling calorimeters with full ϕ -symmetry and the pseudorapidity range of $|\eta| < 4.9$. Figure 3.11 shows the layout of the ATLAS calorimeter system. There are two basic calorimeter systems: an inner electromagnetic (EM) calorimeter and an outer hadronic calorimeter. The EM calorimeter is designed for precise measurements of electrons and photons with fine granularity; while the hadronic one has relative coarser granularity but satisfies the physics requirements for jets reconstructions and E_T^{miss} measurements. Two different sampling techniques are used, the EM calorimeter is purely based on liquid-argon (LAr) technology, while the hadronic one use both LAr and scintillating tiles calorimeters. More details are described as below:

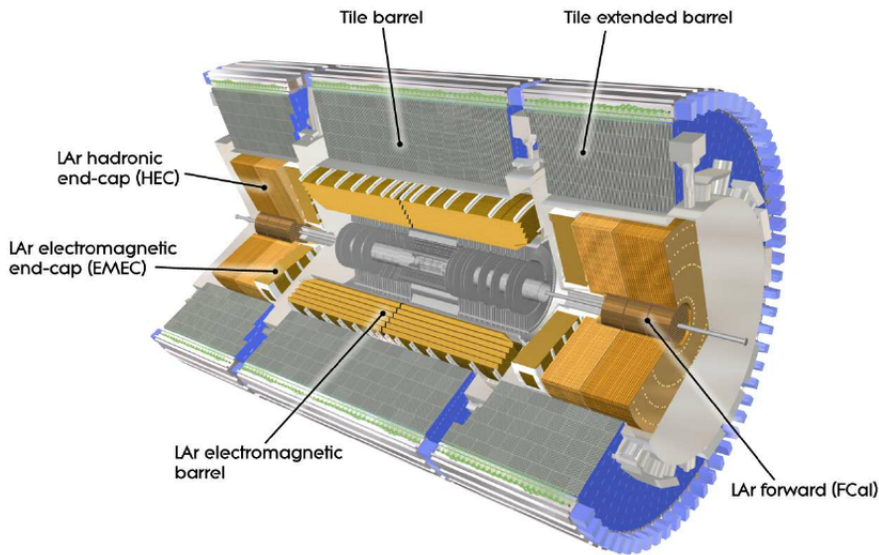


Fig. 3.11 Cut-away view of the ATLAS calorimeters. The LAr calorimeters are seen inside the scintillator-based tile hadronic calorimeters^[31].

Liquid Argon calorimeter

The LAr calorimeter uses liquid-argon as active medium. The LAr sampling calorimeter technique with “accordion-shaped” electrodes is used for all electromagnetic calorimetry covering the pseudorapidity range of $|\eta| < 3.2$; and for hadronic calorimetry with range from $|\eta| = 1.4$ to the acceptance limit $|\eta| = 4.9$ ^[32]. Figure 3.12 depicts a segment of the barrel calorimeter, which had “accordion-shaped” electrodes and absorber. For barrel EM calorimeter, the absorbing material is lead-liquid argon, while the hadronic end-cap calorimeter uses copper plates. In addition, the forward calorimeter is split into

three parts, an EM sector in which copper is used as absorbing material and two hadronic sectors using tungsten outside the EM sector.

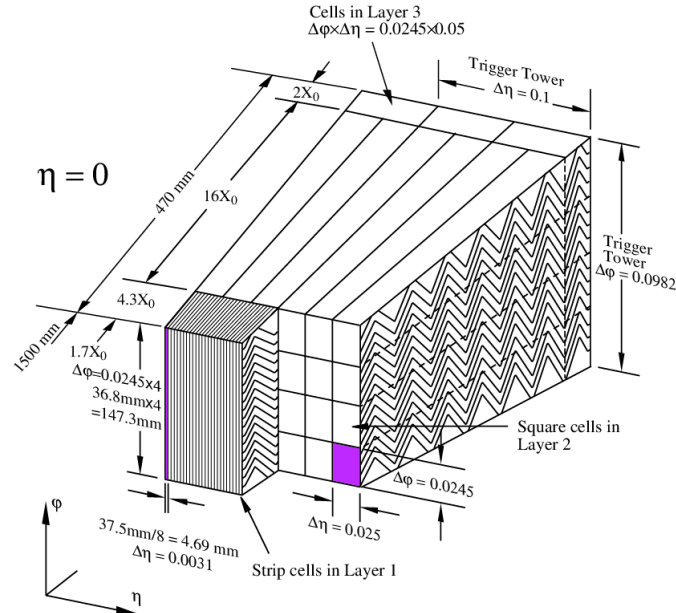


Fig. 3.12 Schematic diagram of a LAr EM calorimeter barrel module.

Tile calorimeter

Tile calorimeter is a sampling calorimeter using scintillating plates as active medium and steel as absorber. It consists of three sections: the central barrel with the pseudorapidity range of $|\eta| < 1.0$ and two extended barrels with $0.8 < |\eta| < 1.7$. Figure 3.13 shows the design of one tile calorimeter module. It's used for energy reconstruction of jets and E_T^{miss} measurement by combining the measurements with the end-cap and forward LAr hadronic calorimeter.

3.2.6 Muon spectrometer

Muon spectrometer^[34] is the outermost part of the ATLAS detector with an extremely large tracking system. It measures a large range of muon momentum, and the accuracy is about 3% at 100 GeV and 10% at 1 TeV. The muon spectrometer comprises three main parts: a magnetic field produced by three toroidal magnets; a set of chambers measuring the tracks of muons with high spatial precision; and triggering chambers with accurate time-resolution. Figure 3.14 shows the schematic of ATLAS muon spectrometer that consists of four types of muon chambers (*MDT*, *CSC*, *RPC*, *TGC*) as well as the magnet systems (barrel and end-cap toroid).

More details of four chambers are given as below:

- **Monitored Drift Tubes (MDT).** MDTs provide the precise momentum measure-

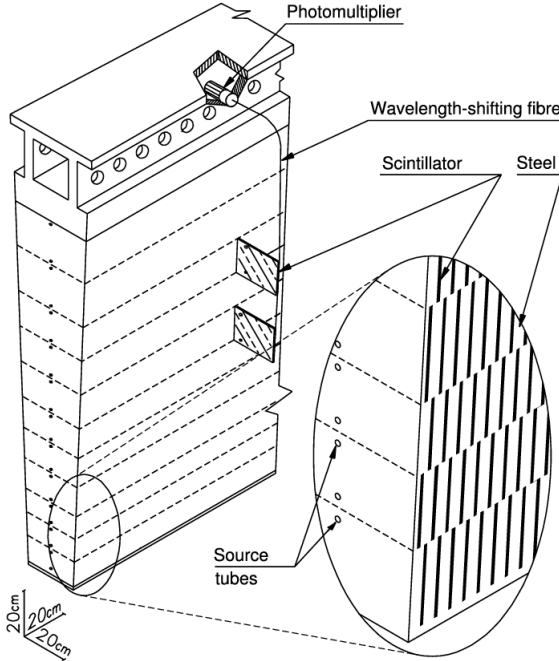


Fig. 3.13 Schematic diagram of tile calorimeter module^[33].

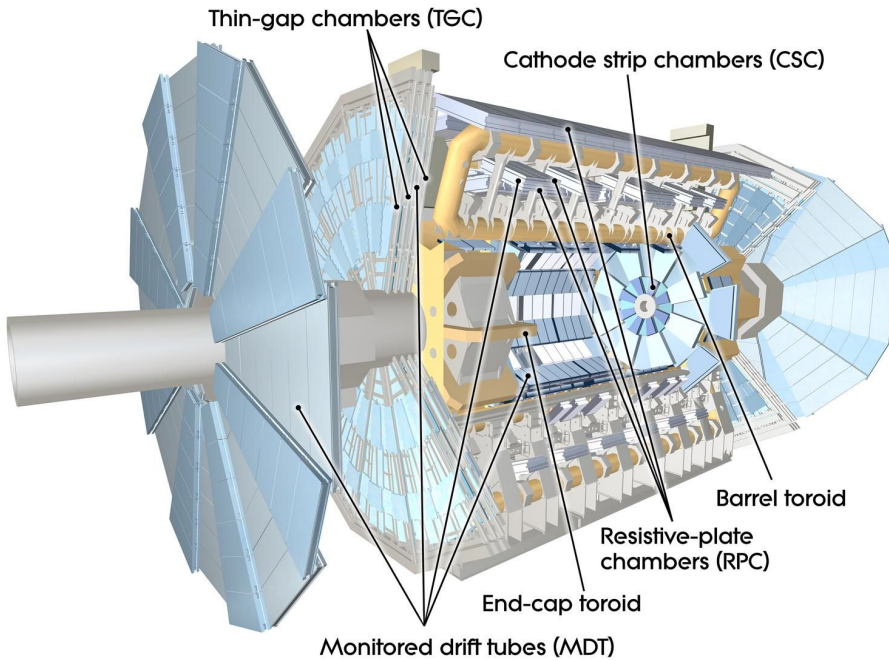


Fig. 3.14 Cut-away view of the ATLAS muon spectrometer^[35].

ment with the $|\eta|$ range up to 2.7, except in the innermost end-cap layer where the coverage is limited to $|\eta| < 2.0$. The chambers comprises three or four layers of drift tubes, with a diameter of 29.970 mm, operated with Ar/CO₂ gas (93/7) at 3 bar. The average resolution can reach 80 μm per tube and 30 μm per chamber.

- **Cathode strip chambers (CSC).** CSCs are used in the forward region of $2 < |\eta| < 2.7$ in the innermost tracking layers, due to their good time resolution and high

rate capability. The CSCs are multi-wire proportional chambers (MWPC) with the cathode planes segmented into strips in orthogonal directions, which allows both coordinates to be measured from the induced-charge distribution. The resolution of a chamber is about $40 \mu\text{m}$ for bending plane and 5 mm for the transverse plane.

- **Resistive plate chambers (RPC).** The RPCs serve as fast triggers in the barrel region of $|\eta| < 1.05$ due to the high rate capability and good spatial and time resolution. It is a gaseous parallel electrode-plate detector without any wires. There are three concentric cylindrical layers around the beam axis, as three trigger stations. Each station consists of two independent layers to measure the transverse coordinates of η and ϕ .
- **Thin gap chambers (TGC).** TGCs are used as trigger system for the end-cap region of $1.5 < |\eta| < 2.4$, and works based on the same principle as multi-wire proportional chambers. In addition, they can also provide the second azimuthal coordinate to complement the measurement of MDT in bending direction.

3.2.7 Trigger system

Trigger system in ATLAS is a very essential component, which is responsible for deciding whether to keep a given collision event for later study or not. In the LHC run-2, higher energy, luminosity and pile-up lead to a large increase of event rate by up to a factor of five, which causes to a even larger challenge and more strict requirement of trigger system.

The trigger system in run-2 consists of a hardware-based first level trigger (Level-1) and a software-based high level trigger (HLT)^[36]. As depicted in figure 3.15, in Level-1, the inputs from coarse granularity calorimeter and muon detector information together with some other subsystems are sent to the Central Trigger Processor to determine Regions-of-Interest (RoIs) in the detector. The event rate can be reduced by Level-1 triggers from 30 MHz to 100 kHz. After that, the RoI information from Level-1 is sent to HLT, in which more sophisticated selection algorithms are run for regional reconstruction. The HLT reduces the rate from Level-1 from 100 kHz to about 1 kHz on average. At the end, the events that accepted by HLT are transferred to local storage at experimental site for offline reconstruction. Details about Level-1 and HLT trigger systems are described as below:

Level-1 trigger

Substantial upgrades have been delivered in ATLAS Level-1 trigger system for run-2 data taking. The upgrades took place in both hardware and detector readout, allow the

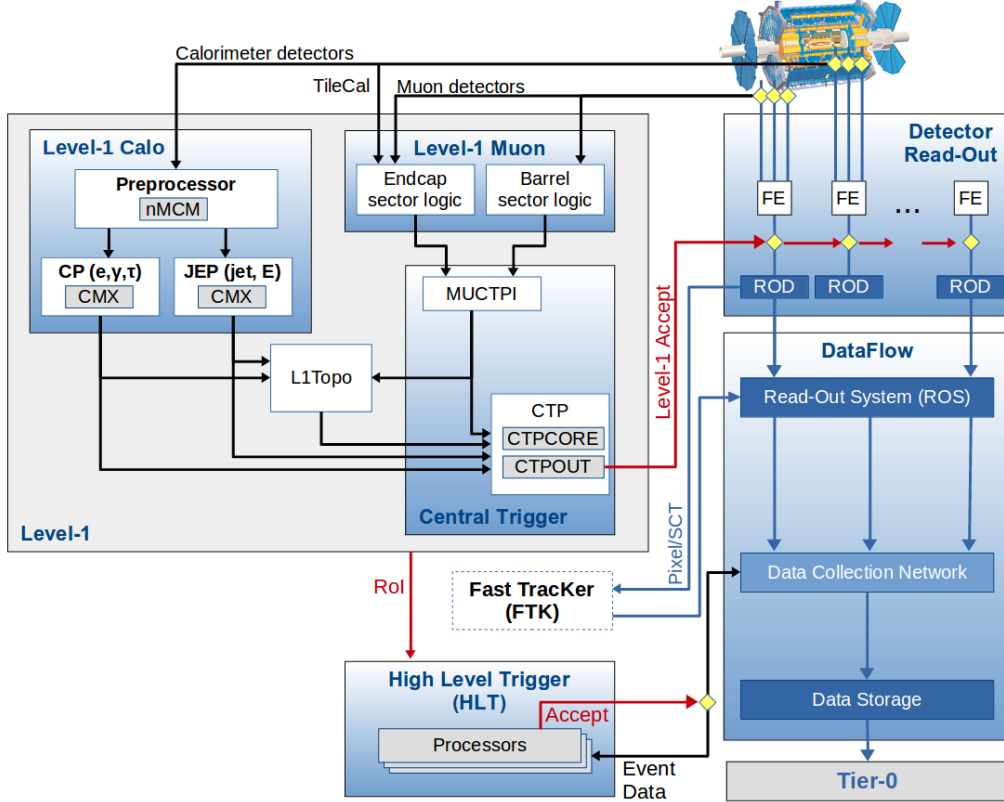


Fig. 3.15 Schematic diagram of the ATLAS trigger and data acquisition system in run-2.

trigger rate increasing from 70 kHz (in run-1) to 100 kHz (in run-2). There are two major parts of Level-1 triggers, including Level-1 calorimeter (L1calo) trigger and Level-1 muon (L1mu) trigger.

Level-1 Calorimeter trigger uses the reduced granularity information from the electromagnetic and hadronic calorimeters to search for electrons, photons, taus and jets and missing transverse energy (E_T^{miss}). It can identify an Region-of-Interest (RoI) as a 2×2 trigger tower cluster in the EM calorimeter as shown in figure 3.16, and 4×4 or 8×8 trigger tower for Jet RoIs. One important upgrade was that, the new FPGA-based (field-programmable gate array) Multi-Chip Modules are used to replace the ASICs (application-specific integrated circuits) included in the modules used in run-1, which allows the use of auto-correlation filters to suppress pile-up.

The Level-1 Muon trigger system includes one barrel section (RPC) and two end-cap section (TGC), which provides fast trigger signals from the muon detectors for the Level-1 trigger decision. By requiring a coincidence with hits from the innermost muon chambers, it can reduce the L1_MU15 rate by about 50% in the region of $1.3 < |\eta| < 1.9$ with only a loss of around 2% signal efficiency. In addition, the coverage was extended by around 4% due to installing new chambers in the feet region of the muon detector.

High Level Trigger

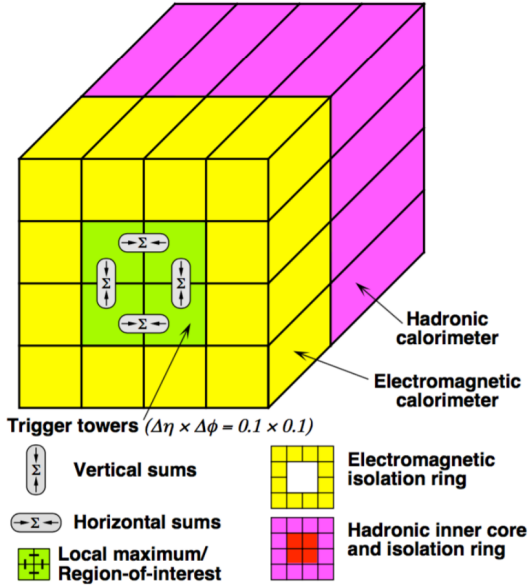


Fig. 3.16 An examples of L1 calorimeter trigger tower for electron and photon triggers^[37].

In run-1, the Event Filter computer clusters and Level-2 trigger system were separated, while now in run-2, they have been merged into a single HLT event processing. The new arrangement helps to reduce the complexity and duplication of algorithm, which leads to a more flexible high level trigger system. During the long-shutdown between the LHC run-1 and run-2, lots of reoptimizations have been done for trigger reconstruction algorithms as well as the offline analysis selections, which can improve the efficiency by more than a factor of two in some cases like hadronic tau triggers. For some triggers, the HLT processing performed within RoIs also allows to aggregate from RoIs to single objects. This improvement reduces the CPU processing for events with overlapping RoIs, and the average output rate has been increased from 400 Hz to 1 kHz.

The HLT reconstruction algorithm can be divided into fast and precision online reconstruction steps. As illuminated by figure 3.17, the initial fast reconstruction helps to reduce the event rate, and to seed into precision reconstruction. Then the final online precision reconstruction is improved and uses offline-like algorithms as much as possible. In particular, multivariate analysis techniques (based on machine learning) have been introduced online in many aspects.

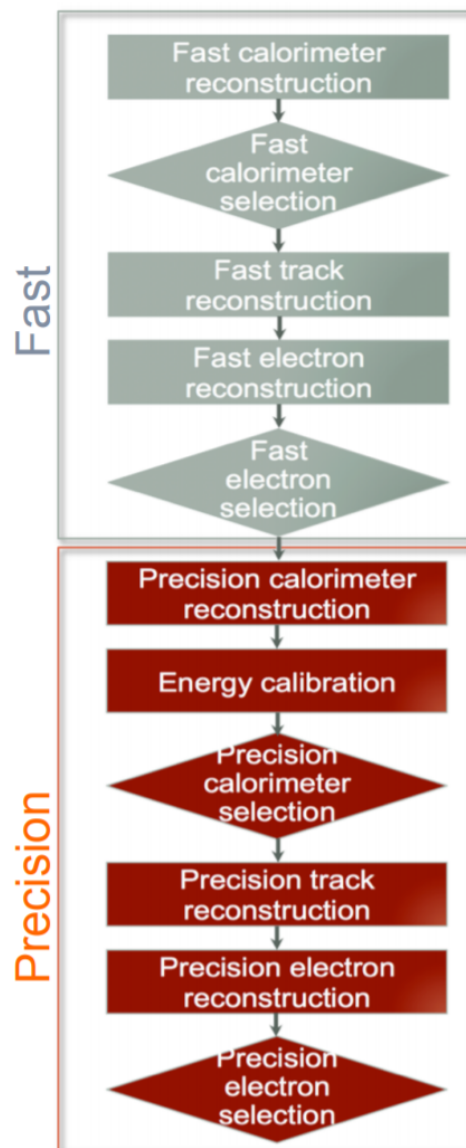


Fig. 3.17 The HLT trigger algorithm sequence^[37].

Chapter 4 Simulation and Event Reconstruction for the ATLAS Experiment

In current LHC pp collision, bunches of protons collide every 25 nanoseconds (ns), which gives a large challenge to event reconstruction and selections. To predict and model each process, Monte Carlo simulations of physics events are essential for high-energy physics experiments. This section will briefly discuss the event simulation and reconstruction programs based on the ATLAS software framework.

4.1 Event simulation

The ATLAS simulation program is integrated into the ATLAS software framework called *Athena*^[38], which uses Python as an object-oriented scripting and interpreter language to configure and load C++ algorithms and objects. Figure 4.1 shows the overview of ATLAS simulation data flow^[39]. In the diagrams, the square-cornered boxes represents algorithms and applications to be run and round-cornered boxes denote data objects.

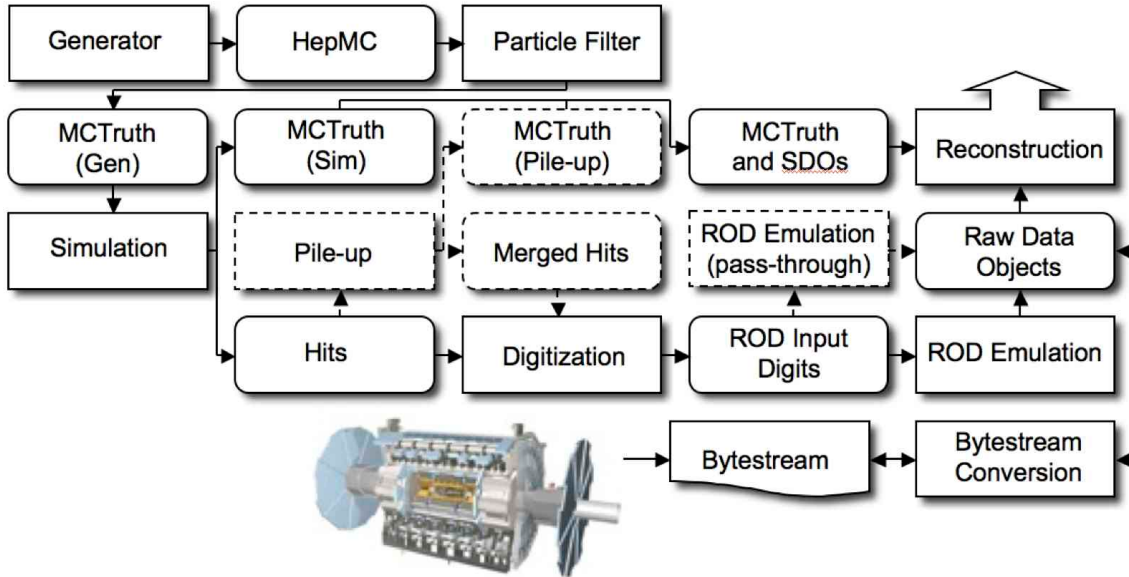


Fig. 4.1 The flow of the ATLAS simulation software.

First of all, events are produced by MC generators in standard HepMC format and then read into the simulation. During the simulation, particles are propagated through the full ATLAS detector whose configurations can be set by users via GEANT4 toolkit. The energies deposited in the sensitive regions of the detector are recorded as *hits* that contains the total energy deposition, position and time, and are written to a simulation hit file. In

the meantime, the events in “truth” format are also recorded to contain the history of the interactions from the generator, including incoming and outgoing particles. Simulated Data Objects (SDOs) are created from truth, which are maps between hits in sensitive portions of the detector and truth information of particles in simulation. The files are then sent to digitization, with constructs “digits” inputs and be written into Raw Data Object (RDO) file used for reconstruction.

In conclusion, there are three main parts of framework: *Generation*, *Simulation* and *Digitization*. More details are given as below:

Event generation

As shown in figure 4.2^[40], at hadron colliders, multiple scattering and rescattering effects arise, which needs to be simulated by Monte Carlo (MC) event generators to reflect the full complexity of those event structures. Several MC event generators can be used to generate events in HepMC format. The events can be filtered at generation time with some certain requirements (eg. decay channel or missing energy above a certain threshold). The generator is responsible for any prompt decays (e.g. W or Z bosons) and stores any “stable” particle expected to propagate through a part of the detector. During the generation steps, any interactions with detector are ignored and only immediate decays are considered.

There are several MC generators that have been widely used with general purpose, including Sherpa^[41], Herwig++^[42], PowhegBox^[43], MC@NLO^[44] and Pythia8^[45].

Simulation

GEANT4 is used as standard simulation toolkit for the ATLAS experiment, which transports physics particles through the detector’s geometry. During the generation level, the entire connected chain of the HepMC event is stored as the Monte Carlo truth. Only the stable particles are read into GEANT4 for further simulation and selection, and transformations can be applied to these events to select certain processes. During the simulation, many secondary tracks can be produced, therefore only information from the interactions of interest are stored, including the incoming particles, step sequence, vertex as well as outgoing particles. The output of GEANT4 is called *hit file*, which contains metadata describing the configuration of the simulation during the run, all requested truth information and a collection of hits for each subdetector.

Since the standard ATLAS detector simulation cost very large computing resources to accurately model the complex detector geometry and physics descriptions, some fast simulation programss are developed according to different user purpose. Some popular fast-sim toolkits include *Fast G4 Simulation*^[46], *ATLFAST-I*^[47] and *ATLFAST-II*^[48].

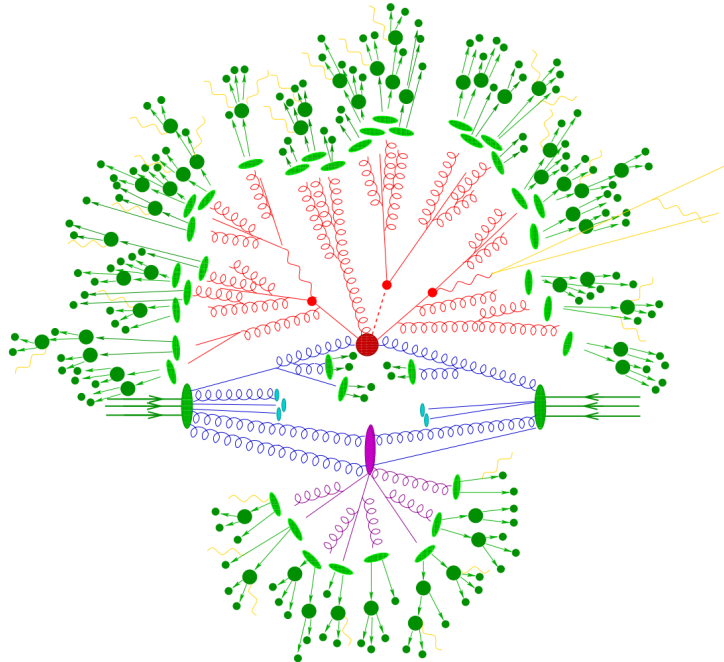


Fig. 4.2 Sketch of a hardon-hardon collision simulated by MC event generator. The red blob in center denotes the hard collision, surrounded by tree-like structures representing Bremsstrahlung which is simulated by Parton Showers. The purple blob stands for a secondary hard scattering event. The light green blobs indecate the parton-to-hardon transitions and the dark green blobs represents hadron decays. The yellow lines are soft photon radiations.

Digitization

The hit outputs from simulated events, including hard scattering signal, minimum bias, beam halo, beam gas and cavern background events, are then sent into digitization procedure, converted into detector response called “digits”. Before converted into detector signal as “digits” formart, each type of event can be overlaid at a user-specified rate. Those overlay, called “pile-up”, can be done during digitization to save the CPU time. At this stage, the detector noise and the first level trigger that implemented with hardware on the real detector are added into events. The digitization firstly constructs “digits” inputs to the readout drivers (RODs) in the detector electronics. Then the ROD functionality is emulated, and the output digits are written out as Raw Data Object (RDO) file. In addition, the digitization algorithms can also produce Simulated Data Objects (SDOs), which contain information about all the particles, noise and the amount of energy that contributed to the signal. Then all information are sent into reconstruction level described in next subsection.

4.2 Event reconstruction

The data flow of ATLAS data processing is sketched in figure 4.3^[49]. Data from detector is firstly filtered by online trigger system before sending to the *Tier-0* (*T0*) for initial processing by offline reconstruction software based on Athena. A small amount of data named “express stream” is processed in almost real time in *T0* for online data quality monitoring. In addition, some other dedicated data streams are sent out at trigger level for detector alignment and calibration. These calibration and alignment information are then used for bulk reconstruction in *T0*. At the end of the reconstruction chain, the data are delivered into *Tier-1* (*T1*) and *Tier-2* (*T2*) centers around the world for further analysis and production of simulated data. *T1* centers are also responsible for data reprocessing by re-running data reconstruction with improved calibration and alignment constants and with improved reconstruction algorithms.

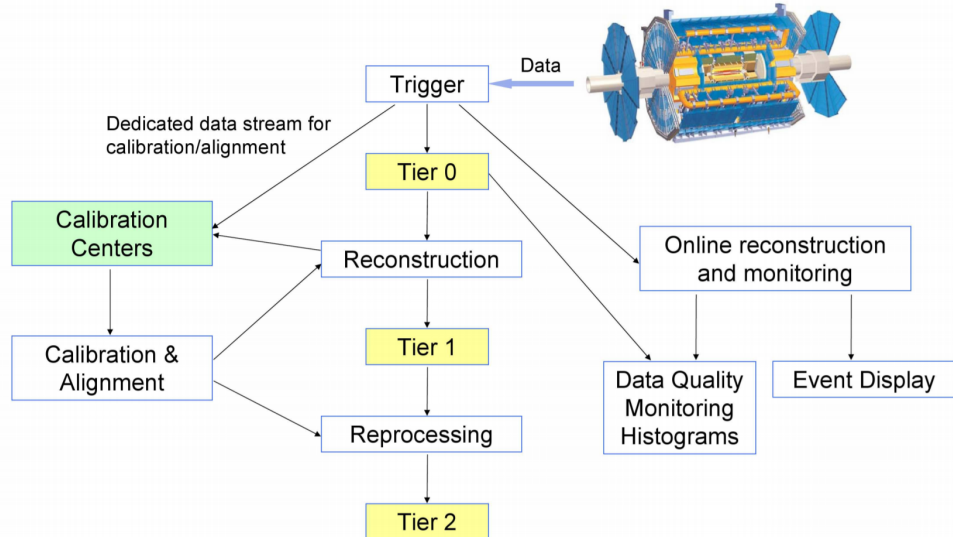


Fig. 4.3 The flowchart of the ATLAS data processing.

This section describes the reconstruction of some important physics objects in ATLAS experiment: tracks, vertices, electrons, muons, jets, and missing energies.

4.2.1 Track

The ATLAS detector is composed of two independent tracking systems: the Inner Detector (ID) close to the interaction point, and the Muon Spectrometer (MS) located in the outermost region. The reconstructed charged-particle trajectories in the ID and MS are referred to as ID tracks and MS tracks respectively. The challenge of ID reconstruction is that it needs to handle high track density that imposes a large number of combinatorial track candidates, while the MS reconstruction is however largely limited by the huge

amount of inert material, the large background and the highly inhomogeneous magnetic field^[50]. More details of these two types of track are given as below:

Inner detector track

Figure 4.4 sketches the ID system used for detecting charge-particle tracks. The ID track reconstructions contains two sequences: *inside-out* track reconstruction and *outside-in* one.

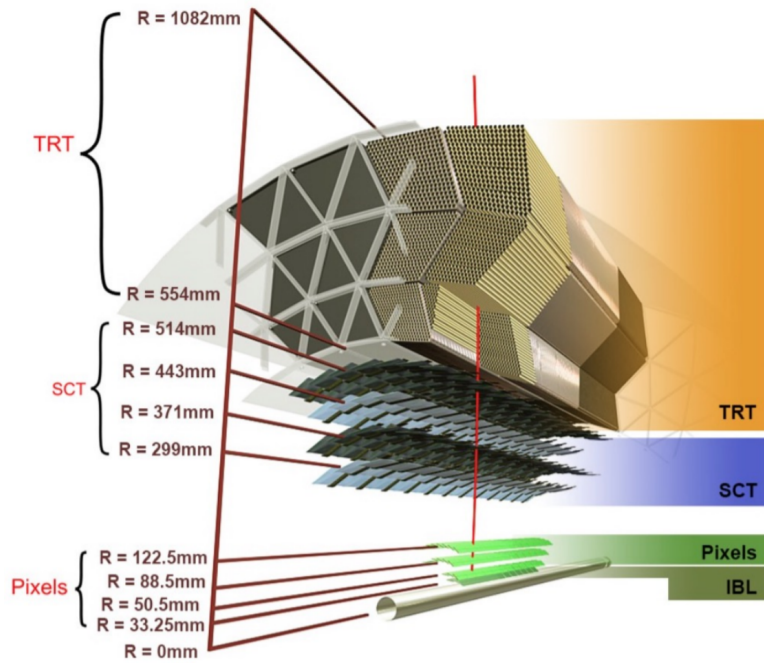


Fig. 4.4 Schematic view of the ATLAS inner detector showing all the corresponding components.

For inside-out tracking, it exploits the high granularity of the pixel and SCT detectors to discover prompt tracks originating from the interaction point. In first step, the track seeds are formed by combining the information of space-points in the three pixel layers and the first SCT layer. Then, these seeds are extended throughout the SCT to build track candidates. After that, these candidates are fitted with some quality cuts applied to remove the outlier clusters, reject the fake tracks and resolve ambiguities in the cluster-to-track association. The selected tracks are then further extended to TRT, and refitted with the full information from pixel, SCT and TRT detectors.

Another complementary approach, outside-in, searches for unused track segments start from TRT instead. These segments are then extended into the SCT and pixel detectors to improve the tracking efficiency for secondary tracks from conversions or decays of long-lived particles.

Muon spectrometer track

The MS track reconstruction^[51] starts from searching hit patterns inside each muon chamber to form segments. In each MDT chamber and nearby trigger chamber, a Hough transform^[52] is used to search the hits lie on a certain trajectory in the bending plane of the detector. The MDT segments are reconstructed by performing a linear fit to the hits found in each layer. The RPC or TGC hits can be built by measuring the coordinate orthogonal to the bending plane. And the segments of CSC can be built using a separate combinatorial search in the η and ϕ detector planes.

Then muon track candidates are built by fitting hits from segments in different layers together. This task makes use of the algorithm by performing a segment-seeded combinatorial search, which starts by using the segments generated in the middle layers of the detector where more trigger hits are available as seeds. The search is then extended to use the segments as seeds from the inner and outer layers. The segments are selected based on criteria of hit multiplicity and fit quality, and are matched using their relative positions and angles. To build a track, at least two matching segments are required, except in the barrel-endcap transition region where a single high-quality segment with η and ϕ information can be used to build a track. At beginning, the same segment can be used to build more than one track candidates. Later on, an overlap removal algorithm is performed to select the best assignment to a single track, or decide whether allows the certain segment to be shared between two tracks.

The hits associated with each track candidate are then fitted using a global χ^2 fit. The algorithm accepts the track candidate if its fitting χ^2 passes the selection criteria. Hits with large contribution to χ^2 are removed and the track fit is repeated. In addition, the algorithm performs a hit recovery procedure looking for additional hits consistent with the candidate trajectory, and the track candidate is refit if additional hits are found.

4.2.2 Primary vertex

The reconstruction of primary vertex (PV) uses the reconstructed tracks introduced in previous section as inputs. The tracks must satisfy the following criteria^[53]:

- $p_T > 400$ MeV
- $|\eta| < 2.5$
- Number of silicon hits $\geq \begin{cases} 9 & \text{if } |\eta| \leq 1.65 \\ 11 & \text{if } |\eta| > 1.65 \end{cases}$
- IBL hits + B-layer hits ≥ 1
- A maximum of 1 shared module (1 shared pixel hit or 2 shared SCT hits)
- Pixel holes = 0

- SCT holes ≤ 1

A candidate vertex is formed by requiring two tracks passing these selection criteria.

The reconstruction of PV can be divided into two steps^[54]: vertex finding and vertex fitting. The first step is the pattern recognition process, namely the association of reconstructed tracks to vertex candidates. The latter one works on the reconstruction of the actual vertex position and its covariance matrix. More details are described as below:

First of all, a set of tracks passing the selection criteria mentioned above is selected. Then a seed position for the first vertex is chosen. This seed position is determined by beam spot in the transverse plane. The starting point for x- and y- coordinates are directly from the centre of the beam spot, while the one for z-coordinate is calculated as the mode of z-coordinates of tracks at their respective points with closest approach to the reconstructed centre of the beam spot.

After determining the seed position, the iterative primary vertex finding procedure starts. An vertex fitting algorithm is adopted to find the optimal vertex position by performing an iterative χ^2 minimization, in which the seed position is used as the start point and the reconstructed tracks are used as input measurements. For this fitting procedure, the input tracks are assigned weights to reflect their compatibility with the vertex estimation, and the vertex position is re-calculated based on these weighted tracks. Then the iterative procedure is repeated by re-calculating the track weight according to the new vertex position. After the last iteration, the final weight of each track used in vertex fit is estimated. And those incompatible tracks ($> 7\sigma$) are then rejected from this vertex candidate and moved back to the unused pool for next vertex finding. Then iteration procedure describes above are repeated again by using the remaining tracks, until no un-associated tracks are left or no additional vertex can be found in remaining tracks.

At the end, the vertices with at least two associated tracks passing through are treated as possible PV candidates. And the output of this vertex reconstruction algorithm is the information of three dimensional vertex positions and their covariance matrices. In physics analysis, it's most often to choose the one with highest sum of transverse momentum ($\sum p_T^2$) as PV.

4.2.3 Electron

Many interesting physical processes are with the involvement of one or more electrons (or positrons) at the LHC. But these electrons can be subjected to large amount of backgrounds such as hadrons, non-prompt electrons from photon conversions and non-isolated electrons from heavy flavor hadon decays. It is therefore essential to efficiently

reconstruct and identify electrons as well as, in the meantime, to keep high background rejection.

In ATLAS, in central region, the electrons leave tracks in inner detector (ID) and deposit the energies in the electromagnetic (EM) calorimeter. Firstly the signals from calorimeter are used for L1 trigger system, and then combined with the information from ID tracks to reconstruct electron candidates that will be used for the high level trigger (HLT) decision algorithms^[55]. The backgrounds mentioned above can then be further suppressed by using several identification criteria. In addition, electrons are required to be isolated from other activities to be further distinguished from background.

More details of electron *reconstruction*, *identification* and *isolation* are described as below.

Electron reconstruction

Several steps are proceeded for electron reconstruction in the central region of ATLAS detector ($|\eta| < 2.47$):

1. **Seed-cluster reconstruction:** A sliding window with size of 3×5 in unit of $\Delta\eta^{tower} \times \Delta\phi^{tower} = 0.025 \times 0.025$ in $\eta \times \phi$ space is utilized to search for electron cluster seeds with total cluster transverse energy greater than 2.5 GeV. Then a clustering algorithm^[56] is applied to form the clusters around the seeds, which can take advantage of removing the duplications. The kinematics of clusters are then reconstructed by using an extended window depending on the cluster position. The efficiency of cluster search is from about 95% at $E_T = 7\text{GeV}$ to 99% for $E_T \geq 15\text{GeV}$.
2. **Track reconstruction:** The track reconstruction can be divided into two steps: pattern recognition and track fit. The standard pattern recognition in ATLAS uses pion hypothesis for energy loss caused by interactions with detector material. If a track seed with $p_T > 1$ GeV cannot be successfully extended to a full track required at least seven hits using this pion hypothesis, but still falls inside one of the EM cluster region of interest, as a second attempt, the pattern recognition using electron hypothesis is then used to allow larger energy loss. Depending on the pattern used in previous stage, the track candidates are then fitted with either the pion hypothesis or the electron hypothesis by using ATLAS Global χ^2 Track Fitter^[57]. If a track candidate fails the fit by using pion hypothesis, it can be refit with the electron hypothesis again. In this method, a specific electron-oriented algorithm is integrated into the ATLAS standard track reconstruction, which improves the performance for electron and as well as maintain minimal interference with the main track recon-

struction.

3. **Electron specific track fit:** Once the tracks are obtained, they are loosely matched to EM cluster using the distance in η and ϕ between the position of track (after extrapolation) in calorimeter's middle layer and the cluster barycentre. The matching conditions take into account the energy loss of bremsstrahlung and the number of precise hits in silicon detector.
4. **Electron candidate reconstruction:** The electron candidate is reconstructed by matching the track candidate to EM cluster seed to eventually completes the electron reconstruction procedure. If more than one track satisfy the matching condition, one track is chosen as primary track based on the information of the cluster-track distance R , the number of pixel hits and the presence of a hit in the first silicon layer^[58]. In addition, the electron candidates are removed from electron pool if it's without any associated precise hit tracks, and moved into photon candidates pool. Then we reformed the electron clusters by using 3×7 (5×5) longitudinal towers of cells in barrel (end-caps) in EM calorimeter. The measured energy is calibrated to original electron energy based on MC simulated samples by using multivariate techniques (MVA).

In addition, in physics analysis, to reduce the background from photon conversions and secondary particles, the track associated with electron is required to be compatible with the primary vertex of the hard collision. Practically, the impact parameters cuts such as $d_0/\sigma_{d_0} < 5$ and $z_0 \sin\theta < 0.5$ mm are usually applied, where d_0 is the closest distance of the track to the measured beam-line, z_0 is the distance along the beam-line between the point where d_0 is measured and the beam-spot position, and θ is polar angle of the track, σ_{d_0} denotes the estimated uncertainty of d_0 parameter. Figure 4.5 depicts the definition of each track impact parameter.

Electron identification

The electron identifications are applied to determine whether the reconstructed electron candidate is more signal-like or background-like object. The identification algorithms make use of quantities of related variables from electron cluster and track measurements including calorimeter shower shapes, track properties, as well as variables measuring bremsstrahlung effects for distinguishing signal from background. Taking the advantage of new IBL in run-2, the number of hits in this innermost pixel layer is utilized for discriminating between electrons and converted photons. In addition, a likelihood method based on the TRT high-threshold hits is adopted to compensate the lower transition radiation absorption probability of the argon.

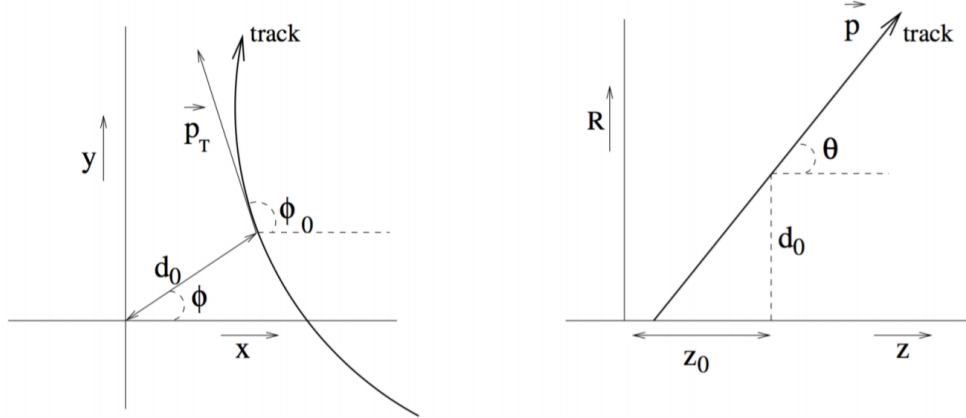


Fig. 4.5 Schematic of the impact parameters of a track in the transverse plane (left) and RZ-plane (right), as defined in the global ATLAS tracking frame^[59].

The baseline identification algorithm introduced for ATLAS run-2 data analysis is the likelihood-based (LH) method, which uses a MVA technique to simultaneously evaluate several properties of electron candidates when making a decision. The LH method utilizes the probability density functions (PDFs) of signal and background as the input discriminating variables. Based on these PDFs, it can calculate overall probabilities of the object to be signal or background. Then the probabilities of signal and background are combined together into a discriminant $d_{\mathcal{L}}$:

$$d_{\mathcal{L}} = \frac{\mathcal{L}_S}{\mathcal{L}_S + \mathcal{L}_B}, \quad \mathcal{L}_{S(B)}(\mathbf{x}) = \prod_{i=1}^n P_{s(b),i}(x_i) \quad (4.1)$$

where \mathbf{x} denotes the vector of discriminating variables and $P_{s(b),i}(x_i)$ represents the value of signal (background) PDF of the i^{th} variable as x_i .

Three levels of working points (WPs) for electron identification are provided: *Loose*, *Medium* and *Tight*, in order of increasing background rejection. Samples selected by a looser WP are subsets of a tighter one, for example, the electrons passing Medium can all be selected by Loose. The identification efficiency varies as function of transverse energy (E_T) as shown in figure 4.6. For evaluations, the electron candidates from MC simulation of $Z \rightarrow ee$ decays (di-jet) are used as signal (background). Depending on the working point, the signal (background) efficiencies for reconstructed electron candidates at $E_T = 25 GeV$ are in the range of 78 to 90% (0.3 to 0.8%), and increase (decrease) with E_T .

Electron isolation

In addition to the identification criteria, most analyses have electron isolation requirement to further distinguish signal from background. To quantify the energy of particles

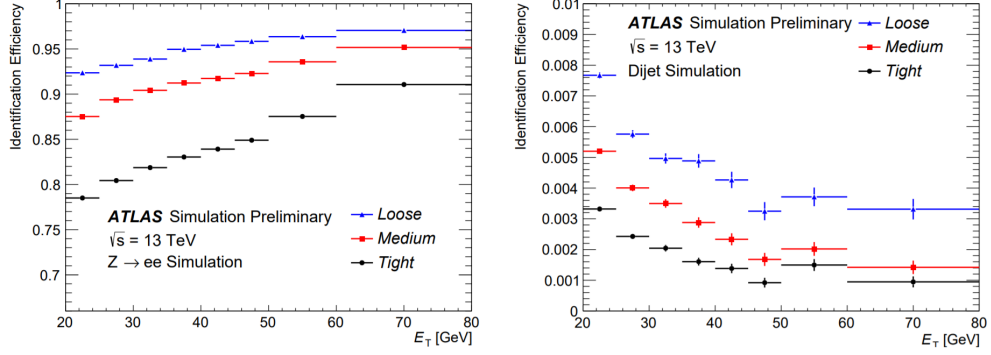


Fig. 4.6 The efficiencies of three electron identification WPs from $Z \rightarrow ee$ (left) events and hadrons misidentified as electrons estimated using di-jet MC samples (right).

around the electron candidate, the isolation variables can help to separate the prompt electron from other non-isolated electrons, like the electrons from converted photons or from heavy flavour hadron decays. There are two kinds of discriminating variables that have been designed:

- **Calorimeter-based variable:** $E_T^{topocone20}$. It's defined as the sum of transverse energies of topological clusters^[60], calibrated at EM scale within a cone of $\Delta R = 0.2$ around the candidate electron cluster. It only considers the clusters with positive reconstructed energy. In addition, a correction as a function of (E_T, η) values is applied to account for the electron energy leakage outside the cluster.
- **Track-based variable:** $p_T^{varcone20}$. It's calculated as the sum of transverse momentum of all satisfied tracks within a cone of $\Delta R = \min(0.2, 10\text{GeV}/E_T)$ around the candidate electron track. To calculate the sum, it requires the tracks are originating from the reconstruction PV of hard collision, and exclude the associated tracks of electron itself.

Based on the values of $E_T^{topocone20}/p_T$ and $p_T^{varcone20}/p_T$, a series of working points with different selection requirements are defined. The resulting WPs are divided into two kinds:

- Efficiency targeted working points: varying requirements to obtain a certain isolation efficiency, which can either be a constant or as a function of E_T .
- Fixed requirement working points: set the constant upper thresholds on isolation variables.

The distribution of two discriminating variables are shown in figure 4.7 for $ZZ \rightarrow ee$ events with $E_T > 27\text{GeV}$ and satisfying *Tight* requirement.

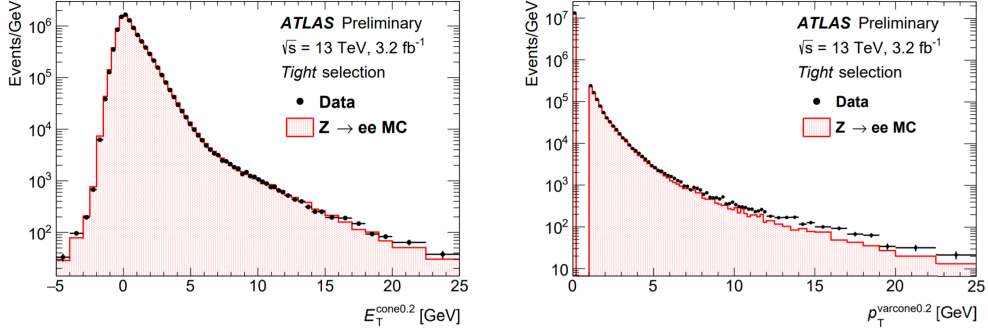


Fig. 4.7 Distributions of $E_T^{cone0.2}$ (left) and $p_T^{varcone0.2}$ (right) for electrons from $ZZ \rightarrow ee$ events in data and MC simulation. The simulated events (full histograms) are normalized to data.

4.2.4 Muon

Muons are distinctive signatures in final states of many physics analyses at the LHC including the Higgs analyses, SM measurements, BSM searches and so on. High performance of muon reconstruction and identifications are crucial. This section briefly describes some more details of the *reconstruction*, *identification* and *isolation* of muon.

Muon reconstruction

Muon reconstruction is firstly performed in inner detector (ID) and muon spectrometer (MS) independently as given in section 4.2.1. The information from each individual detector is then combined together to form the muon tracks for physics analyses. The combined ID-MS reconstruction is developed according to several algorithm based on the information from ID, MS and calorimeters. Four different muon types are defined^[51]:

- **Combined (CB) muons:** a combined track is formed by using the reconstructed tracks performed independently in ID and MS with a global refit. To improve the fit quality, the hits from MS may be added to or removed from the track. The outside-in pattern recognition is utilized for the reconstruction of most muons, in which the muons are first reconstructed in MS and then extrapolated inward to match the ID track. In the meantime, the inside-out pattern is also used as a complementary method.
- **Segment-tagged (ST) muons:** a reconstructed track in ID is defined as muon, if it can be associated with at least one track segment in MDT or CSC chambers. These ST muons are used when they can only pass across one layer of MS chambers due to their low p_T or falling into regions with less MS acceptance.
- **Calorimeter-tagged (CT) muons:** a reconstructed track in ID is categorized as muon if it's matched to the energy deposit in calorimeter which is recognized with

a minimum-ionizing particle. This CT muons have lowest purity amount all types of muons, but it covers the region where ATLAS muon spectrometer is only partially constructed. For the region of $|\eta| < 0.1$ and $15GeV < p_T < 100GeV$, the identification of CT muons are optimal.

- **Extrapolated (ME) muons:** the muon is reconstructed based only on the MS track and a loose requirement of originating from the interaction point. In general, this type of muon needs to pass at least two (three) layers of MS chambers to provide a track measurement in barrel (forward) region. ME muons are designed to extend the acceptance for muon reconstruction into the region $2.5 < |\eta| < 2.7$ where ID doesn't cover.

Before collecting those muons for physics analyses, overlap removals are performed between different muon types with the priority of CB > ST > CT, when two types of muons share the same ID track. Besides, the overlaps with ME muons are resolved by analyzing the track hit content, and selecting the track with better fit quality and larger number of hits.

Muon identification

After reconstruction, the muon identification is then performed to further discriminate between signal and background, especially to suppress backgrounds from pion and kaon decays by requiring prompt muons with high efficiency and guaranteeing a robust momentum measurement. The muon identification is defined by using the fit quality of combined track. The variables utilized in judgement for CB tracks include:

- *q/p significance*, the absolute difference between q/g (charge over momentum) of muons measured in ID and MS divided quadratic sum of their corresponding uncertainties;
- ρ' , the absolute value of difference between the p_T (transverse momentum) measured in ID and MS, divided by the p_T of combined track;
- *Nomalized χ^2* of the combined track fit;
- *Number of hits in ID and MS*

In addition, some new variables used for *LowPt* muon working point what will be described later^[61]:

- *Momentum balance significance (MBS)* is computed as momentum difference between the ID and MS standalone measurements with respect to the uncertainty σ on energy lost in the calorimeter system.
- *Scattering neighbor significance (SNS)* is defined to estimated the significance of a change in trajectory along the track, expected in the presence of a hadron decaying

to a muon.

- *Scattering curvature significance (SCS)* is defined as the normalized integral of the scattering angle significances, corrected for large kinks along the trajectory.

Five selection working points are developed to satisfy the different needs for different physics goals: *LowPt*, *Loose*, *Medium*, *Tight* and *HighPt*. The *Tight*, *Medium*, *Loose* are subsets from the tighter one to looser one. More detailed definition of each working point is given as follow:

- *Loose*: this working point is designed to maximize the reconstruction efficiency while keeping good-quality of muon tracks. And they are specifically developed for reconstructing the Higgs boson candidates from four-lepton final states. All four muon types are used for this selection level. The CB and ME muons passing Medium WP that will mentioned below are all included into Loose category. In addition, the CT and ST muons are restricted to $|\eta| < 0.1$ region. In the range of $|\eta| < 2.5$, around 97.5% Loose muons are CB muons, and about 1.5% are CT while remaining 1% are ST muons.
- *Medium*: this working point is the default criteria of muon identification in ATLAS. This selection minimizes the systematic uncertainties of muon reconstruction and calibration. In this category, we only use CB and ME muons. For CB muons, at least 3 hits in at least two layers of MDT are required, except $|\eta| < 0.1$ region, in which tracks with ≥ 1 MDT layer but ≤ 1 MDT hole layer are allowed. For ME muons, at least 3 MDT/CSC layers are required. Furthermore, a loose cut on the compatibility between measured momentum in ID and MS is applied to reduce the fake muons from hadrons misidentification. Besides, the q/p-significance is required to be less than 7.
- *Tight*: this working point is used to maximize the purity of muons but with sacrifice of some selection efficiency. Only CB muons with hits in ≥ 2 stations of MS and passing Medium criteria are selected. In addition, the normalized χ^2 of combined track fit should be smaller than 8. Then, a two-dimensional cut of q/p-significance and ρ' is adopted as a function of muon p_T to ensure tighter background rejection for momentum below 20 GeV, in which the fake rate is usually higher.
- *High- p_T* : this set of selections aims to maximize the momentum resolution for tracks with $p_T > 100\text{GeV}$ region. The selection is especially optimized for searching high-mass Z' and W' resonances. CB muons satisfying Medium selection and with ≥ 3 hits in 3 MS stations are chosen. The specific region in MS where alignment is suboptimal are removed as a precaution.

- *Low- p_T* : this type of muon is newly designed for physics analyses with ATLAS software release version 21. It's designed to obtain a optimal muon identification with very low transverse momentum of $3GeV < p_T < 5GeV$, which is crucial for B-physics measurement in ATLAS. In this muon requirement, only CB muons are used. In the range of $|\eta| < 1.3$, it requests muons hit at least one MS station; in $1.3 < |\eta| < 1.55$, a least two MS stations are required; while in region of $|\eta| > 1.55$, *Medium WP* is required. In addition, cuts are applied to suppress fakes as: $|\text{MBS}| < 3.0$, $|\text{SNS}| < 3.0$ and $|\text{SCS}| < 3.0$.

Figure 4.8 and 4.9 show the selection efficiency of different muon identification working points. For *Medium (Loose)*, *Tight* and *High- p_T* : $Z \rightarrow \mu\mu$ events with $p_T > 10GeV$ are used for measurement. In the top figure of figure 4.8, the efficiency of the Loose selection (squares) is shown comparing to Medium one, where significant difference can be observed in region of $|\eta| < 0.1$. For *LowPt*, $J/\Psi \rightarrow \mu\mu$ events with $3GeV < p_T < 10GeV$ are used for measurement.

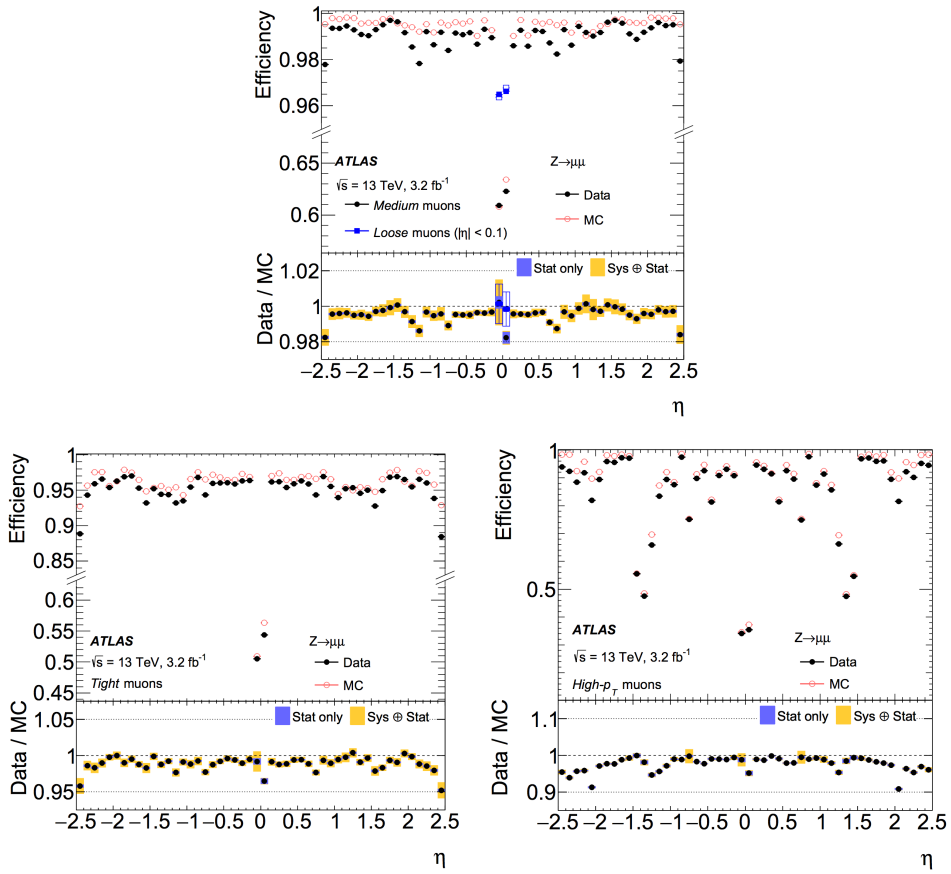


Fig. 4.8 Muon reconstruction efficiency as a function of η for: Medium (and Loose), Tight and High- p_T working points.

Muon isolation

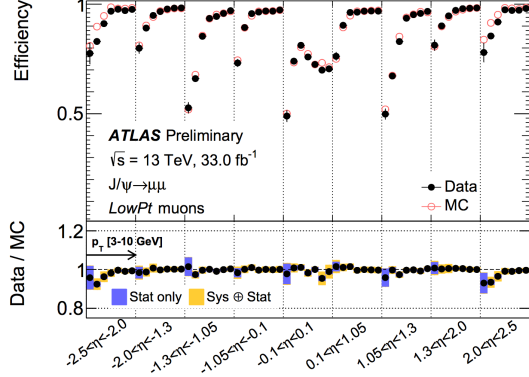


Fig. 4.9 Muon reconstruction efficiency for Low- p_T working point as a function of η .

Similar to electron, the muon isolation is used to further distinguish the prompt muon from non-prompt backgrounds. There are also two types of isolation variables for muon:

- **Calorimeter-based variable:** $E_T^{topocone20}$. It's defined as the sum of the transverse energy of topological clusters within a cone of size $\Delta R = 0.2$ around the candidate muon, after subtracting the contribution from the energy deposit of the muon itself and correcting for pile-up effects. The contributions from pile-up and underlying events are computed using the ambient energy-density technique^[62] and are corrected on an event-by-event basis.
- **Tracked-based variable:** $p_T^{varcone30}$. It's computed as the scalar sum of the transverse momenta of the tracks with $p_T > 1\text{GeV}$ in a cone size of $\Delta R = \min(10\text{GeV}/p_T^\mu, 0.3)$ around the candidate muon whose transverse momenta is p_T^μ after excluding the muon track itself. This p_T -dependent cone size can help to improve the performance for muons produced in the decay of particles with a large transverse momentum.

Then the isolation selections are applied based on *relative isolation variables*, which are computed as the ratio of the track- or calorimeter-based isolation variables to the transverse momentum of the muon. Figure 4.10 shows the distribution of those relative isolation variables by using $Z \rightarrow \mu\mu$ events for muons passing *Medium* identification criteria.

4.2.5 Jets

Jets are another important features for many physics analyses at the LHC, and especially the key signatures for vector boson fusion/scattering (VBF/VBS) processes. In ATLAS detector, jets are reconstructed as groups of topologically associated energy deposits in the calorimeters, tracks associated with charged particles measured in the inner

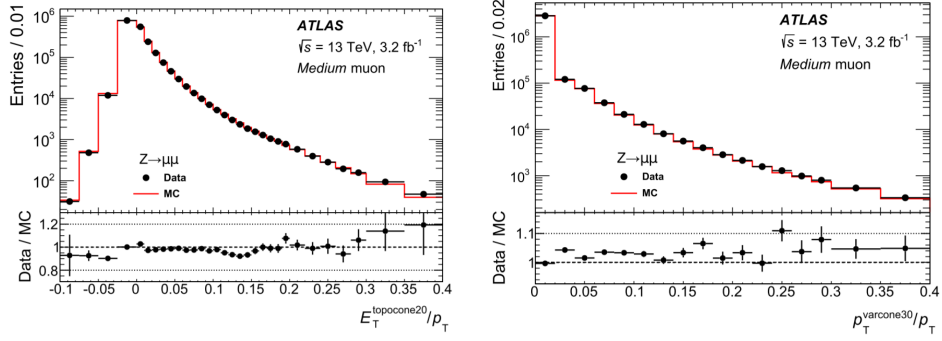


Fig. 4.10 Distributions of the calorimeter-based (right) and the track-based (left) relative isolation variables measured in $Z \rightarrow \mu\mu$ events.

tacking detector, or simulated particles. This section introduces the jet reconstruction, jet energy scale (JES) calibration and the b-jet tagging techniques.

Jet reconstruction

Jets are reconstructed using anti- k_t algorithm^[63] and with radius parameter of $R = 0.4$ in most cases. The FastJet software package^[64] is utilized for jet finding and reconstruction. A collection of four-vectors are used as inputs at each combination step in jet clustering, the total four-momentum is therefore computed as the sum of four-vector of all its constituents. There are three types of jets in ATLAS:

- *Truth jets*: the inputs to jet algorithm are simulated particles.
- *Track jets*: the inputs are charged tracks measured from inner detector.
- *Calorimeter jets*: the inputs are energy deposits in calorimeters.

Figure 4.11 shows the schematic of ATLAS jet reconstruction.

Jet reconstruction

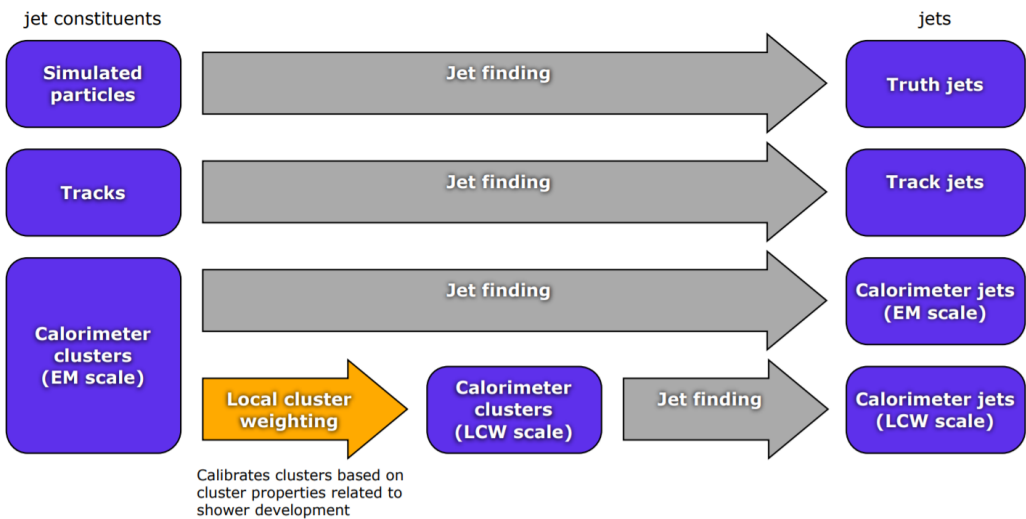


Fig. 4.11 A overview schematic of ATLAS jet reconstruction^[65].

The *truth jets* are reconstructed using anti- k_t algorithm with $R = 0.4$ by using final-

state, stable particles from MC simulation as inputs. It requires the candidate particles with lifetime $c_\tau > 10$ mm and excludes the particles from pile-up. Truth jets with $p_T > 7\text{GeV}$ and $|\eta| < 4.5$ are then used for jets calibration described later.

The *track jets* are reconstructed from charged particles within the full acceptance of inner detector ($|\eta| < 2.5$). The track reconstruction has been introduced in section 4.2.1. Reconstructed jets with $p_T > 500\text{MeV}$ and associated with primary vertex are then selected. Tracks are assigned to jets using ghost association^[62], a procedure that treats selected tracks as four-vectors of infinitesimal magnitude during the jet reconstruction and assigns them to the jet which they are clustered with. In addition, muon track segments are used as a compensation for those uncaptured jet energy carried by energetic particles passing through the calorimeters without being completely absorbed. Similar to the ID track, muon segments are assigned to jets using the method of ghost association mentioned above as well.

The *calorimeter jets* are reconstructed using a set of three-dimensional, positive-energy topological clusters (topo-clusters) made of calorimeter cell energies as input to the anti- k_t algorithm^[66]. Topo-clusters are built from near-by calorimeter cells that contains a significant energy above a noise threshold, which is estimated from measurements of calorimeter electronic noise and simulated pile-up noise. Those calorimeter cell energies are measured at electromagnetic energy scale (EM scale) corresponding to the energy deposited by electromagnetically interacting particles. And jets passing a p_T threshold of 7 GeV are reconstructed with the anti- k_t algorithm.

Jet energy scale calibration

Figure 4.12 depicts an overview of ATLAS jet calibration scheme for EM-scale calorimeter jets. In this procedure, the jet energies are scaled to truth jets, which is reconstructed at the particle-level. Each step of the calibration corrects the full four-momentum unless otherwise stated, scaling the jet p_T , energy, and mass.

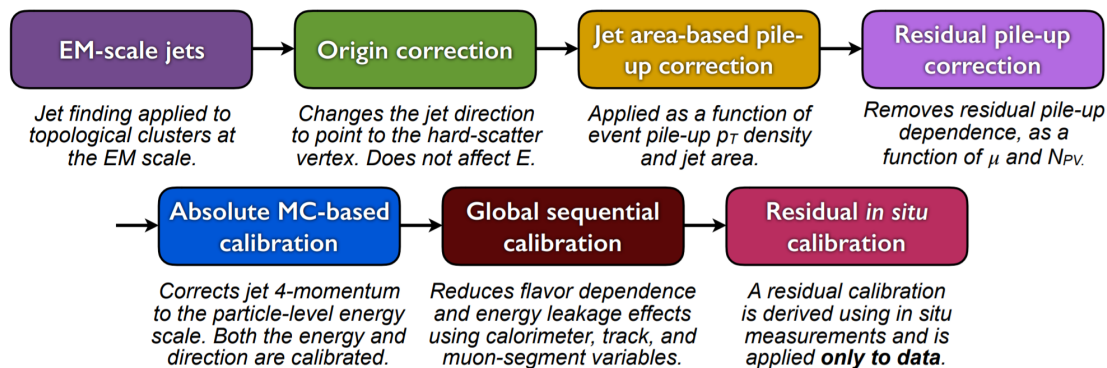


Fig. 4.12 A overview schematic of ATLAS jet calibration^[66].

First of all, the origin correction recompute the four-momentum of jets to point them to the hard-scatter primary vertex instead of the centre of detector, and in the meantime keep the jet energy unchanged. This correction improves the η resolution of jets by roughly 25% at a jet p_T of 20 GeV and > 5 times improvement for jet with p_T above 200 GeV, as measured from the difference between reconstructed jets and truth jets in MC simulation. Secondly, the pile-up correction is adopted to remove the excess energy due to in-time and out-of-time pile-up, which consists of two processes: an area-based p_T density subtraction applied on the top of each event; and a residual correction derived from the simulation. Thirdly, the absolute JES calibration corrects the jet four-momentum to the particle-level energy scale, using truth jets in di-jet MC events. Furthermore, the step of global sequential calibration uses calorimeter, track and MS-based variables to reduce the flavor dependence and energy leakage effects. Finally, the residual in situ calibration is adopted to correct jets in data by using well-measured objects eg. photons, Z bosons and calibrated jets.

B-jet tagging

Tagging of b-jets plays a important role in many physics analyses involving b- or t-quark. In the meantime, lots of analyses need to apply b-jet veto to suppress $t\bar{t}$ process. There are three major types of algorithms that have been developed to distinguish b-quark jets from light-quark (u,d,s) jets^[67]:

- **Impact parameter based algorithms (IP2D and IP3D):** b-hadrons usually have long lifetime (~ 1.5 ps, $c_\tau \sim 450$ μm), which leads to large impact parameter for tracks produced from b-hadron decay. The impact parameter taggers are developed based on these variables. The IP2D tagger makes use of the transverse impact parameter significance $d_0/\sigma(d_0)$ as discriminant, while IP3D tagger uses two-dimensional discriminant of both transverse and longitudinal impact parameter significances: $d_0/\sigma(d_0)$ and $z_0 \sin\theta/\sigma(z_0)$.
- **Secondary vertex finding algorithm (SV1)** makes use of the secondary vertex formed by decay products of b-hadron within the jet. All track pairs within a jet are tested for a two-track vertex hypothesis, and removed if they are likely to originate from a long-live particle decay (eg. K_s or Λ), hadronic interactions or photon conversions. After that, a new vertex is fitted with all tracks from remaining two-track vertices, and the outliers are removed from this set of tracks.
- **Decay chain multi-vertex algorithm (JetFitter)**^[68] exploits the topological structure of weak b- and c- hadron decays inside the jet and tries to reconstruct the full b-hadron decay chain. A Kalman filter is adopted to find a common line between

primary vertex and b-/c- vertices, as well as their position in this line, which gives a approximated flight path for the b-hadron. In this approach, the b- and c-hadron vertices, whenever resolution allows, can be resolved, even when there is only a single track associated to them.

The final discrimination commonly used in many physics analyses is called **Multivariate Algorithm (MV2)**, which is based on Boosted Decision Tree (BDT) implemented in the TMVA package^[69] by combining the outputs from underlying taggers mentioned above. The MV2 was trained using jets in $t\bar{t}$ sample, where the b-jets are treated as signal while the c- and light-flavor jets are treated as backgrounds. There are three kinds of MV2 depending on the fraction of c-jets in background for training: *MV2c00*, *MV2c10* and *MV2c20*. Figure 4.13 presents the output score of MV2c10 for different flavor jets.

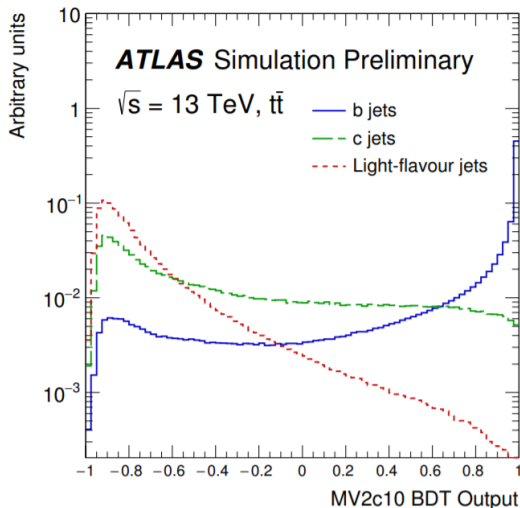


Fig. 4.13 MV2c10 BDT output for b- (solid blue), c- (dashed green) and light-flavour (dotted red) jets in $t\bar{t}$ events^[67].

4.2.6 Missing transverse energy

Many interesting physics processes are with the involvement of neutrinos. Since they do not interact with any materials in the detector, neutrinos cannot be detected directly; but instead, they can result in imbalance in the plane transverse to the beam axis, where momentum conservation is assumed. It is known as the missing transverse momentum denoted as E_T^{miss} , which is obtained from the negative vector sum of the momenta of all particles detected in a proton-proton collision event.

The E_T^{miss} is measured using selected, reconstructed and calibrated hard objects in an

event. Its x- and y- components can be calculated as follow^[70]:

$$E_{x(y)}^{miss} = E_{x(y)}^{miss,e} + E_{x(y)}^{miss,\gamma} + E_{x(y)}^{miss,\tau} + E_{x(y)}^{miss,jets} + E_{x(y)}^{miss,\mu} + E_{x(y)}^{miss,soft} \quad (4.2)$$

where each object term is given by the negative vectorial sum of the momenta of the respective calibrated objects. The calorimeter signals are associated with the reconstructed objects in the following order: electrons, photons, hadronically decaying taus, jets, muons. The soft term is reconstructed from detected objects not match any hard object passing the selections, but associated with the primary vertex. Details of applied selections for each term are summarized in table 4.1.

Based on $E_{x(y)}^{miss}$, the magnitude of E_T^{miss} and the azimuthal angle ϕ^{miss} are computed:

$$\begin{aligned} E_T^{miss} &= \sqrt{(E_x^{miss})^2 + (E_y^{miss})^2} \\ \phi^{miss} &= \arctan(E_y^{miss}/E_x^{miss}) \end{aligned} \quad (4.3)$$

In equation 4.2, each objects are required to pass certain reconstruction and calibrated criteria and selections mentioned above before taken as inputs.

In figure 4.14, left plot shows the observed E_T^{miss} distribution for data and MC of $Z \rightarrow \mu\mu$ events without genuine missing transverse momentum; and right plot shows the E_T^{miss} distribution for $W \rightarrow e\nu$ events that has genuine (true) missing transverse momentum due to real neutrino.

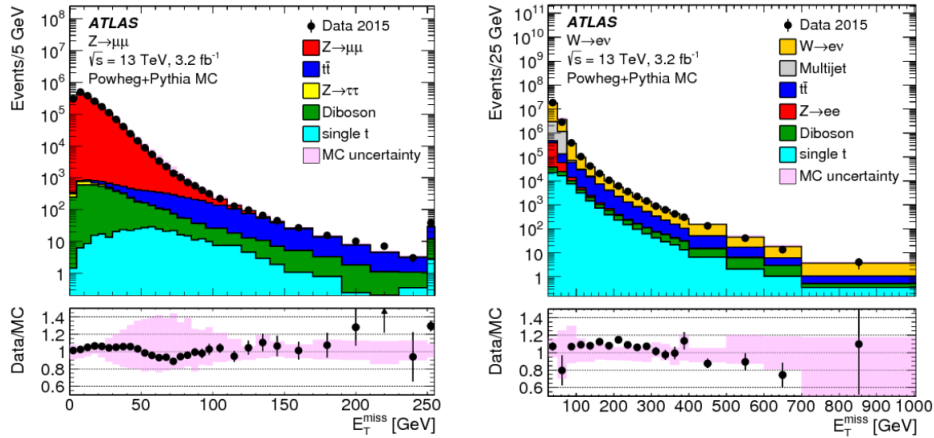


Fig. 4.14 Measured E_T^{miss} distribution for $Z \rightarrow \mu\mu$ events (left) and $W \rightarrow e\nu$ events (right).

Table 4.1 Overview of the contributions to E_T^{miss} .

Objects contributing to E_T^{miss}				
Priority	Type	Selections	Variables	Comments
(1)	e	$ \eta < 1.37 \text{ or } 1.52 < \eta < 2.47$ $p_T > 10GeV$	$E_T^{miss,e}$	all e^\pm passing kinematic selections and medium reconstruction quality
(2)	γ	$ \eta < 1.37 \text{ or } 1.52 < \eta < 2.47$ $p_T > 25GeV$	$E_T^{miss,\gamma}$	all γ passing kinematic selections and tight reconstruction quality, and without overlapping with (1)
(3)	τ_{had}	$ \eta < 1.37 \text{ or } 1.52 < \eta < 2.47$ $p_T > 20GeV$	$E_T^{miss,\tau}$	all τ_{had} passing kinematic selections and medium reconstruction quality, and without overlapping with (1) and (2)
(4)	μ	$ \eta < 2.7$ $p_T > 10GeV$	$E_T^{miss,\mu}$	all μ passing kinematic selections and medium reconstruction quality
(5)	jet	$ \eta < 4.5$ $p_T > 60GeV$ --- or --- $2.4 < \eta < 4.5$ $20GeV < p_T < 60GeV$ --- or --- $ \eta < 2.4$ $20GeV < p_T < 60GeV$ $JVT > 0.59$	$E_T^{miss,jet}$	all jets passing kinematic selections and reconstruction quality (jet cleaning), and without overlap with (1)–(4)
(6)	ID track	$p_T > 400MeV$ $ d_0 < 1.5mm$ $ z_0 \sin\theta < 1.5mm$ $\Delta R(track, e/\gamma cluster) > 0.05$ $\Delta R(track, \tau_{had}) > 0.2$	$E_T^{miss,soft}$	all ID tracks from the hard-scattering vertex passing kinematic selections and reconstruction quality, and not associated with any particle from (1), (3) or (4), or associated with a jet from (5)

Chapter 5 Statistical treatment of searching for new particles or processes

In the experiments of particle physics, one often searches for particles or processes that have been predicted but not yet observed, such as the two analysis presented in this dissertation: searching for the vector boson scattering process and searching for the heavy resonance(s). Usually two hypotheses are defined:

- H_0 : null hypothesis, in most cases are designated as background-only hypothesis.
- H_1 : signal plus background hypothesis, where signal is a new model one would like to search for.

For the purpose of discovering a new signal process, the H_0 hypothesis is tested against the alternative H_1 . When setting limits, the H_1 hypotheses with different signal strengths are tested against the H_0 .

The level of agreement between observed data and a given hypothesis can be quantified by computing the p -value, the probability under this hypothesis assumption, or its equivalent Gaussian significance. This section describes the statistical treatment for searches related to this dissertation.

5.1 The likelihood function

The likelihood function is defined as the product of a set of the probability density functions (pdfs) of variables x , that used to evaluate the probability of the observed dataset:

$$\mathcal{L}(x_1, \dots, x_N; \theta_1, \dots, \theta_M) = \prod_i^N f(x_i; \theta_1, \dots, \theta_M) \quad (5.1)$$

where $\theta_1, \dots, \theta_M$ are the nuisance parameters that can be written as $\boldsymbol{\theta}$, and x_1, \dots, x_N denote the observables of dataset. Usually one measures the variable x by constructing a histogram $\mathbf{n} = (n_1, \dots, n_N)$. The expectation value of the i th bin n_i is written as^[71]:

$$E[n_i] = \mu s_i + b_i \quad (5.2)$$

where μ is the signal strength, s_i and b_i are the number of signal and background events in that bin. In addition to the histogram \mathbf{n} , in some cases, one would like to use subsidiary measurements to further constrain the nuisance parameters. For instance, due to the lack of background simulation or the mismodelling issue of one MC sample, one can choose

a control region and construct another histogram $\mathbf{m} = (m_1, \dots, m_M)$ to constrain the contribution of one certain background in data. For this measurement, the expectation value of the i th bin m_i is written as:

$$E[m_i] = u_i(\boldsymbol{\theta}) \quad (5.3)$$

In most particle experiments, the number of these events observed in one bin follows the Poisson distribution, by combining the equation 5.2 and 5.3, one can get the likelihood function for all bins as:

$$\mathcal{L}(\mu, \boldsymbol{\theta}) = \prod_{i=1}^N \frac{(\mu s_i + b_i)^{n_i}}{n_i!} e^{-(\mu s_i + b_i)} \prod_{k=1}^M \frac{u_k^{m_k}}{m_k!} e^{-u_k} \quad (5.4)$$

Then the profile likelihood ratio is defined to test the hypothesized value of μ :

$$\lambda(\mu) = \frac{\mathcal{L}(\mu, \hat{\boldsymbol{\theta}})}{\mathcal{L}(\hat{\mu}, \hat{\boldsymbol{\theta}})} \quad (5.5)$$

where numerator denotes the local maximum-likelihood for a specific μ , $\hat{\boldsymbol{\theta}}$ is the value of $\boldsymbol{\theta}$ that maximizes the numerator. And the denominator is the global maximum-likelihood with the $\hat{\mu}$ and $\hat{\boldsymbol{\theta}}$ as their best fit value.

5.2 Test statistic

To test the level of agreement between the data and the hypothesized value μ , a test statistic t_μ can be defined as^[71]:

$$t_\mu = -2 \ln \lambda(\mu) \quad (5.6)$$

From the definition of $\lambda(\mu)$ in equation 5.5, one can see that $0 \leq \lambda \leq 1$, while a λ with value close to 1 implies good agreement between data and μ . Thus, smaller value of t_μ means the increase of compatibility between data and μ . To quantify the level of disagreement, one can calculate the p -value as:

$$p_\mu = \int_{t_{\mu,obs}}^{\infty} f(t_\mu | \mu) dt_\mu \quad (5.7)$$

in which $t_{\mu,obs}$ is the value of test statistic from observed data, and $f(t_\mu | \mu)$ is the pdf of t_μ under the assumption of hypothesized value μ . This is a one-side p -value with its

corresponding observed significance, Z , is defined as:

$$Z = \Phi^{-1}(1 - 2p_\mu) \quad (5.8)$$

The relationship between the t_μ , p -value and significance Z are depicted in figure 5.1. When searching for a signal process, such as Higgs boson, the particle physics community tends to claim a discovery when the rejection of background-only hypothesis has a significance of at least $Z = 5$.

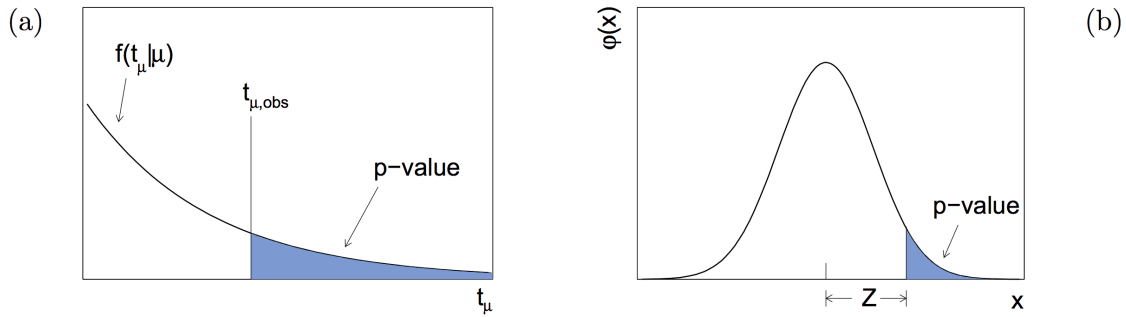


Fig. 5.1 (a) Illustration of the relationship between the observed t_μ and its p -value. (b) The relationship between p -value and the observed significance Z , where $\phi(x)$ is the standard normal distribution.

In most cases, one assumes that the presence of a new signal can only increase the event rate comparing to the background only model, which means the signal strength cannot be a negative value ($\mu \geq 0$). And for the case of discovery, the hypothesis of a positive signal strength should be tested against to the background-only (null) hypothesis by using the test statistic called q_0 :

$$q_0 = \begin{cases} -2 \ln(\lambda(0)) & \hat{\mu} \geq 0 \\ 0 & \hat{\mu} < 0 \end{cases} \quad (5.9)$$

which corresponds to the p -value called p_0 :

$$p_0 = \int_{q_{0, \text{obs}}}^{\infty} f(q_0 | 0) dq_0 \quad (5.10)$$

to quantify the level of disagreement between the data and the null hypothesis ($\mu = 0$).

5.3 The CLs upper limit

For a signal hypothesized value μ , one can compute the probability that this hypothesis (called S+B hypothesis) gives a **greater** test statistic value than the observed one q_{obs} as:

$$p_{s+b} = \int_{q_{obs}}^{\infty} f(q_{\mu}|\mu) dq_{\mu} \quad (5.11)$$

In the meantime, the probability that the background-only hypothesis gives a **smaller** test statistic than observed data can also be calculated as:

$$1 - p_b = \int_{-\infty}^{q_{obs}} f(q_{\mu}|0) dq_{\mu} \quad (5.12)$$

Then we define the CLs^[72] of a hypothesized value μ as:

$$CLs = \frac{p_{s+b}}{1 - p_b} \quad (5.13)$$

For purpose of excluding a signal hypothesis, a threshold CLs of 0.05 is often used. For this reason, usually under the circumstance that no significant derivation between data and background-only hypothesis is found, one would like to find the value of hypothesized signal strength μ by requiring its $CLs = 0.05$ (called 95% CLs upper limit) for exclusion.

The sensitivity of an experiment to exclude a new signal process is quantified by *median upper limit*^[73], which is obtained using “Asimov dataset”. The Asimov dataset is defined such that when one uses it to evaluate the estimators for all parameters, one obtains the true parameter values. Moreover, it is useful to use Asimov dataset to compute how much the sensitivity is expected to vary, given the expected fluctuations in the data. The $\hat{\mu}$ is assumed to follow a Gaussian distribution with a mean value of μ' and the standard deviation of σ . First of all, the test statistic from profile likelihood ratio can be approximated as^[71]:

$$-2\ln\lambda(\mu) = \frac{(\mu - \hat{\mu})^2}{\sigma^2} + \mathcal{O}(1/\sqrt{N}) \quad (5.14)$$

Given that the Asimov dataset corresponding to a signal strength μ' , one finds:

$$-2\ln\lambda_A(\mu) \approx \frac{(\mu - \mu')^2}{\sigma^2} = q_{\mu,A} \quad (5.15)$$

where $q_{\mu,A} = -2\ln\lambda_A(\mu)$ is the observed test statistic of Asimov dataset. Then the stan-

dard derivation can be computed as:

$$\sigma_A^2 = \frac{(\mu - \hat{\mu})^2}{q_{\mu,A}} \quad (5.16)$$

In a special situation where one wants to find the median exclusion significance for the hypothesis μ assuming that there is no signal ($\mu' = 0$), one gets:

$$\sigma_A^2 = \frac{\hat{\mu}^2}{q_{0,A}} \quad (5.17)$$

5.4 Nuisance parameters

The expected numbers and pdf shapes of signal and background events also depend on a series of systematic uncertainties, which are described as a set of nuisance parameters (NPs). As showed in equation 5.1, θ is a set of NPs that plays as an additional “penalty” term to likelihood function, which will increase the negative log likelihood when any nuisance parameter is shifted from its nominal value. Usually those NPs are constrained by using Gaussian function with their estimated uncertainties provided by the experiment condition.

Chapter 6 Studies of SM ZZ production in $\ell\ell\ell'\ell'$ final state using pp collision data collected by ATLAS detector from 2015 to 2018

6.1 Introduction

After the discovery of Higgs boson^[3,4], the examination of electroweak symmetry breaking (EWSB) becomes a main focus at the LHC. In addition to measuring the properties of Higgs boson directly, the vector boson scattering (VBS) process is another key avenue to probe EWSB^[74-76]. As introduced in section 2.1.3, in Standard Model (SM), the Higgs boson acts as “moderator” to unitarize high-energy longitudinal VBS amplitudes at the TeV scale. Therefore, studying high-energy behaviours of VBS is crucial to understand the mechanism of EWSB.

Since no VBS process was observed prior to the LHC era, LHC provides an exceptional opportunity to study them due to its unprecedented high energy and luminosity. At the LHC, the VBS process is typically studied through the measurements of electroweak (EW) production of two vector bosons radiated from quark-quark initial state, plus a pair of hadronic jets with high energy in the back and forward regions (denoted as EW- $VVjj$). The quantum chromodynamics (QCD) production of $VVjj$ containing two QCD vertices at the lowest order (denoted as QCD- $VVjj$) is an irreducible background to the search of EW- $VVjj$ production. The features of EW- $VVjj$ production including a large invariant mass of jet pair (m_{jj}) and a significant separation of rapidity between two jets (Δy_{jj}). Figure 6.1 presents some typical Feynman diagrams of EW- and QCD- $ZZjj$ processes.

The first evidence of the EW- $VVjj$ process was seen in same-sign WW channel (EW- $W^\pm W^\pm jj$) by ATLAS collaboration with 20.3 fb^{-1} 8 TeV data^[77], in which a 3.6σ excess was observed in data over the background-only prediction. In the LHC run-2, the observation (with $> 5 \sigma$ statistical significance) of EW- $W^\pm W^\pm jj$ process has been reported in both ATLAS and CMS collaboration with 36 fb^{-1} 13 TeV data^[78-79]. In WZ channel (EW- $WZjj$), an observation with 5.3σ excess was also reported by the ATLAS collaboration recently^[80]. As for the EW- $ZZjj$ production, it was searched by CMS using 35.9 fb^{-1} 13 TeV data but no evidence was found^[81]. The EW production in ZZ final state (EW- $ZZjj$) is typically rare, whose fiducial cross section has an order of $O(0.1) \text{ fb}^{-1}$ in the final state where both Z bosons decay leptonically. But in the mean-

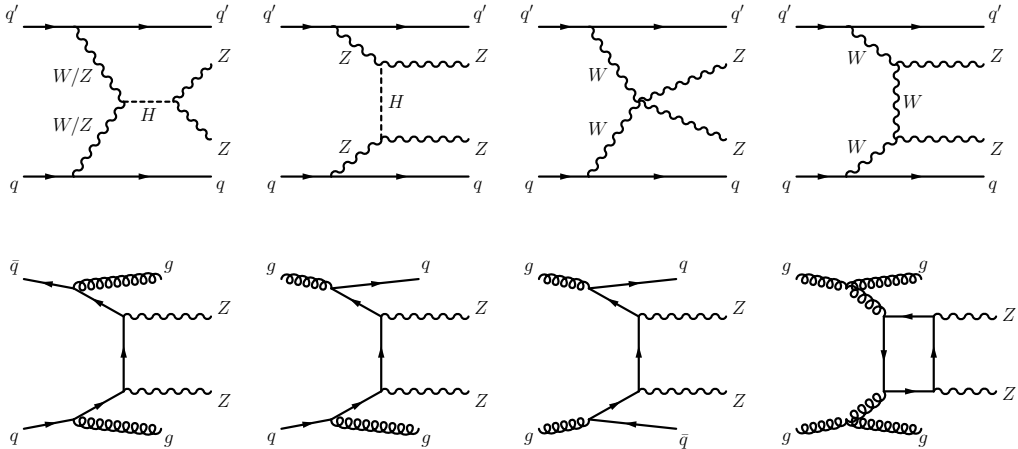


Fig. 6.1 Typical diagrams for the production of $ZZjj$, including the relevant EW VBS diagrams (first row) and QCD diagrams (second row).

time, $ZZ \rightarrow \ell\ell\ell'\ell'$ process offers an extremely clean channel than all the others. So with more data collected in the LHC, the observation of EW- $ZZjj$ becomes possible.

This section presents the first observation of EW- $ZZjj$ production decaying to four charged leptons with two jets ($\ell\ell\ell'\ell' jj$) by ATLAS collaboration using the complete set of the LHC run-2 data with 139 fb^{-1} luminosity^[82-83]. It is a new milestone in the study of EWSB at the LHC, and completes the last missing part of observation of weak boson scattering for massive bosons. In the meantime, the measurement of fiducial cross-sections for SM ZZ production including both EW and QCD processes is also reported. The $ZZjj$ production involving intermediate τ -leptons from Z decays is considered as signal but has a negligible contribution to the selected events. Reducible backgrounds give minor contributions in the $\ell\ell\ell'\ell' jj$ channel are also studied. To further separate the EW signal and the QCD background, multivariate discriminant (MD) is trained using event kinematic information from simulated samples. The MD distribution is then used as discriminant in statistical fit to evaluate the signal strength of EW process.

6.2 Data and MC samples

6.2.1 Data samples

The datasets for this analysis include the full run-2 pp collision data collected by the ATLAS experiment during the years from 2015 to 2018. Data event is only used if it passed the latest Good Run List (GRL) released by the Data Quality group from ATLAS experiment, corresponding to an integrated luminosity of $139.0 \pm 2.4 \text{ fb}^{-1}$.

6.2.2 MC simulations

The EW- $Z Z jj$ production is modelled using MadGraph5_aMC@NLO 2.6.1^[84] with the matrix elements (ME) calculated in the leading-order (LO) approximation in perturbative QCD (pQCD) and with the NNPDF2.3LO^[85] parton distribution functions (PDF). The VBF Higgs process is also included.

The QCD- $Z Z jj$ production is modelled using Sherpa 2.2.2^[86] with the NNPDF3.0NNLO^[87] PDF, where events with up to one (three) outgoing partons are generated at NLO (LO) in pQCD. The production of $Z Z jj$ from the gluon-gluon initial state with a four-fermion loop or with an exchange of the Higgs boson has an order of α_S^4 in QCD, and is not included in the Sherpa simulation. A separate gg induced $Z Z + 2\text{jets}$ sample is modelled using Sherpa 2.2.2 with the NNPDF3.0NNLO PDF and with an additional 1.7 k-factor^[88] being applied. Then the interference between EW- and QCD- $Z Z jj$ is modelled with MadGraph5_aMC@NLO 2.6.1 calculated at LO.

The diboson productions from QCD $WW \rightarrow \ell\nu qq$ as well as QCD and EW $WZ \rightarrow \ell\ell qq$ are modelled using Sherpa 2.2.2 with the NNPDF3.0NNLO PDF. The productions of semileptonic decays ($WW \rightarrow \ell\nu qq$ and $WZ \rightarrow qq\ell\ell$) are modelled using Powheg-Box v2^[89] with the CT10 PDF^[90]. The triboson production is modelled using Sherpa 2.2.2 with the NNPDF3.0NNLO PDF.

For top-quark pair ($t\bar{t}$) production, the Powheg-Box v2 is used with the CT10 PDF. The single top-quark production in t -channel, s -channel and Wt -channel are simulated using the Powheg-Box v1 event generator^[91-93]. The productions of $t\bar{t}$ in association with vector boson(s) ($t\bar{t}V$) are modelled with MadGraph5_aMC@NLO 2.3.3 for $t\bar{t}W$ and $t\bar{t}Z$ with $Z \rightarrow \nu\nu/qq$ decays, with Sherpa 2.2.1 for $t\bar{t}Z$ where the Z decays to dilepton, and with MadGraph5_aMC@NLO 2.2.2 for $t\bar{t}WW$ respectively.

The $Z+jets$ processes are modelled using Sherpa 2.2.1 with the NNPDF3.0NNLO PDF, in which the ME is calculated for up to two partons with next-to-leading-order (NLO) accuracy in pQCD and up to four partons with LO accuracy.

For all the samples except those from Sherpa, the parton showering is modelled with Pythia8^[45] using the NNPDF2.3^[85] PDF set, and the A14 set of tuned parameters^[94]. While for Sherpa samples, the parton showering is simulated within the programme.

All simulated events are processed with detector response simulation based on Geant4 described in section 4.1. In addition, simulated inelastic pp collisions are overlaid to model additional pp collision in the same and neighbouring bunch crossings (pile-up), and reweighted to match the pile-up conditions in data. Moreover, all simulated events are processed using the same reconstruction algorithms as data. And the leptons and

jets reconstruction, energy scale and resolution, and the leptons identification, isolation, trigger efficiencies for simulated events, as described in section 4.2, are all corrected to match the data measurements.

6.3 Objects and Event selection

6.3.1 Objects selection

The selection of analysis relies on the definition of multiple objects: *electrons*, *Muons*, and *jets*. Details of definition for each object are described as below:

Muon: To increase the acceptance range in reconstruction (reco) -level for $\ell\ell\ell'\ell'$ channel, all four types of muons (CB, ST, CT, ME muons, described in section 4.2.4) are used. The identified muons are then required to pass $p_T > 7$ GeV and $|\eta| < 2.7$, and satisfy the *Loose* identification criterion (see definition in sec 4.2.4). The impact parameter cuts are further applied to suppress the contribution from cosmic muons and non-prompt muons, with the value of: $|d_0/\sigma(d_0)| < 3.0$ and $|z_0 \sin\theta| < 0.5$ mm, where d_0 is the transverse impact parameter relative to the beam line, $\sigma(d_0)$ is its uncertainty, and z_0 is the longitudinal impact parameter relative to the primary vertex. In order to avoid muons associated with jets, all muons are required to be isolated and pass *FixedCutLoose* isolation criteria of $E_T^{\text{topocone}20}/p_T < 0.3$ and $p_T^{\text{varcone}30}/p_T < 0.15$.

Electron: As described in section 4.2.3, electrons are reconstructed from energy deposits in the EM calorimeter matched to a track in the inner detector. The electron candidates must satisfy the *Loose* criterion defined by the likelihood-based (LH) method. And electrons are required to have $p_T > 7$ GeV and $|\eta| < 2.47$. Moreover, the impact parameter requirements of $|d_0/\sigma(d_0)| < 5.0$ and $|z_0 \sin\theta| < 0.5$ mm are applied. Same as muon, all electrons are required to satisfy *FixedCutLoose* isolation criteria, which, for electrons, is $E_T^{\text{topocone}20}/p_T < 0.2$ and $p_T^{\text{varcone}20}/p_T < 0.15$.

Jets: Jet are key signatures for VBS processes. This analysis use the jets clustered using the anti- k_t algorithm with radius parameter $R = 0.4$, more details of jets' reconstruction can be found in section 4.2.5. The jets are required to satisfy $p_T > 30$ (40) GeV in the $|\eta| < 2.4$ ($2.4 < |\eta| < 4.5$) region. To further reduce the effects of pile-up jets, a jet vertex tagger (JVT) is applied to jets with $p_T < 60$ GeV and $|\eta| < 2.4$ to select jets from hard-scattering vertex^[95].

Overlap removal: An overlap-removal procedure is applied to selected leptons and jets. To enhance the selection efficiency, leptons are given higher priority to be kept when overlapping with jets. More details of the strategy is summarized in table 6.1.

	Reference objects	Criteria
Remove electrons	electrons	Share a track or have overlapping calorimeter cluster. Keep higher p_T electron
Remove muons	electrons	Share track and muon is calo-tagged
Remove electrons	muons	Share track
Remove jets	electrons	$\Delta R_{e-jet} < 0.2$
	muons	$\Delta R_{\mu-jet} < 0.2$ OR muon track is ghost-associated to jet AND ($N_{Trk}(jet) < 3$ OR ($p_T^{jet}/p_T^\mu < 2$ and $p_T^\mu/\Sigma_{TrkP_t} > 0.7$))

Table 6.1 Overlap removal criteria between pre-selection objects for the $\ell\ell\ell'\ell'$ channel. The overlap removal follows the order shown in this table. Once an object has been marked as removed, it does not participate in the subsequent stages of the overlap removal procedure.

6.3.2 Event selection

The events are required to additionally be recorded by single or multi-lepton triggers, with transverse momentum (p_T) thresholds varying from 8 to 26 GeV. The overall trigger efficiency for selected inclusive $\ell\ell\ell'\ell' jj$ signal events in the analysis region are from 95 to 99%.

The $\ell\ell\ell'\ell'$ quadruplets are formed by two opposite-sign, same-flavour (OSSF) lepton pairs ($\ell^+\ell^-$), in which leptons are required to be separated by $\Delta R > 0.2$ in table 6.1. At most one muon is allowed to be ME or CT muon. The p_T threshold of first three leading leptons are 20, 20 and 10 GeV. If more than one quadruplets are found, the one with minimum sum of difference between two dilepton pair masses and Z boson mass ($|m_{l_1^+ l_1^-} - m_Z| + |m_{l_2^+ l_2^-} - m_Z|$) is selected. Both two dilepton pair masses are required to be between 66 to 116 GeV. In addition, the invariant masses of all possible OSSF pairs are required to be greater than 10 GeV to reject events from J/ϕ or Y decay.

For VBS topology, the two most energetic jets in different detector side ($y_{j1} \times y_{j2} < 0$) are selected. Furthermore, the invariant mass of two jets (m_{jj}) is required to be greater than 300 GeV, while Δy_{jj} is required to be larger than 2. Table 6.2 summarizes the above selection requirements, which is defined as signal region (SR).

Electrons	$p_T > 7 \text{ GeV}, \eta < 2.47$ $ d_0/\sigma_{d_0} < 5 \text{ and } z_0 \times \sin \theta < 0.5 \text{ mm}$
Muons	$p_T > 7 \text{ GeV}, \eta < 2.7$ $ d_0/\sigma_{d_0} < 3 \text{ and } z_0 \times \sin \theta < 0.5 \text{ mm}$
Jets	$p_T > 30 (40) \text{ GeV for } \eta < 2.4 (2.4 < \eta < 4.5)$
ZZ selection	$p_T > 20, 20, 10 \text{ GeV for the leading, sub-leading and third leptons}$ Two OSSF lepton pairs with smallest $ m_{\ell^+\ell^-} - m_Z + m_{\ell'^+\ell'^-} - m_Z $ $m_{\ell^+\ell^-} > 10 \text{ GeV for all OSSF lepton pairs}$ $\Delta R(\ell, \ell') > 0.2$ $66 < m_{\ell^+\ell^-} < 116 \text{ GeV}$
Dijet selection	Two most energetic jets with $y_{j_1} \times y_{j_2} < 0$ $m_{jj} > 300 \text{ GeV and } \Delta y_{jj} > 2$

Table 6.2 Summary of selection of physics objects and candidate events at detector level in the $\ell\ell\ell'\ell'jj$ signal region.

6.4 Background estimation

Table 6.3 summarizes the background yields for $ZZjj \rightarrow \ell\ell\ell'\ell'jj$ process in 139 fb^{-1} . Uncertainties on the predictions include both statistical and systematic components. ‘‘Others’’ includes minor contributions from non- ZZ processes including $Z+jets$, top-quark, triboson and $t\bar{t}V$ processes. Details of estimation for each source are described as below.

Process	$\ell\ell\ell'\ell'jj$
EW- $ZZjj$	20.6 ± 2.5
QCD- $q\bar{q} \rightarrow ZZ$	77 ± 25
QCD- $gg \rightarrow ZZ$	13.1 ± 4.4
Others	3.2 ± 2.1
Total	114 ± 26
Data	127

Table 6.3 Observed data and expected signal and background yields in 139 fb^{-1} of luminosity. Minor backgrounds are summed together as ‘‘Others’’. Uncertainties on the predictions include both statistical and systematic components.

6.4.1 QCD backgrounds

The QCD- $ZZjj$ production, which include both qq and gg initial processes, is the irreducible background in the search of EW- $ZZjj$ production. A QCD-enriched control region, named as QCD CR, is defined to constrain the normalization of ZZ background

by reverting either the m_{jj} or Δy_{jj} requirements as:

$$m_{jj} < 300 \text{ GeV} \text{ OR } \Delta y_{jj} < 2 \quad (6.1)$$

Then this normalization factor is included into statistical fit as a free parameter to properly treat the uncertainty correlations between SR and CR, while the shapes are taken from MC simulation. Table 6.4 shows the event yields of each background components in this CR. Uncertainties are statistical one only. The distributions of invariant mass of $\ell\ell\ell'\ell'$ and

Process	$\ell\ell\ell'\ell' jj$
EW- $ZZ jj$	3.9 ± 0
QCD- $ZZ jj$	136.9 ± 0.6
QCD- $ggZZ jj$	16.8 ± 0.1
Diboson	0.3 ± 0.1
Triboson	1.6 ± 0.1
$Z+jets$	0
$t\bar{t}$	0
Total	159.5 ± 0.62
Data	152

Table 6.4 Observed data and expected signal and background yields in 139 fb^{-1} of luminosity. Diboson background in table includes all the other diboson processes discussed in section 6.2.2, except those with four-lepton final state. Uncertainties include only MC statistic. No events from $Z+jets$ and $t\bar{t}$ MC samples pass the selection, and are indicated as 0 in the table.

dijet in QCD CR are shown in figure 6.2.

6.4.2 Reducible backgrounds

Backgrounds from $Z+jets$, top-quark and WZ processes called reducible backgrounds can be estimated by data-driven method. These events usually contain two or three leptons from Z/W decays, together with heavy-flavor jets or misidentified components of jets reconstructed as leptons called “fake leptons”. A *fake factor* method is used to estimate these backgrounds, where the lepton misidentification is measured in data with the region enhances contributions from $Z+jets$ and top-quark processes. The method is described as below:

1. Define a dedicated background dominant region to derive the fake factor for this

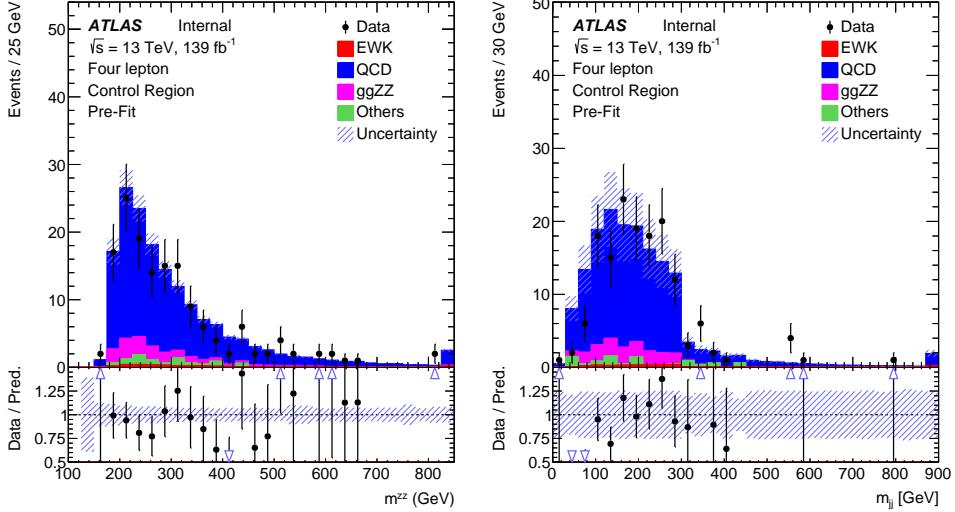


Fig. 6.2 Pre-fit m_{ZZ} and m_{jj} distribution in QCD-enriched CR.

background. The *fake factor* is defined as:

$$\mathcal{F} = \mathcal{N}_{good}/\mathcal{N}_{pool} \quad (6.2)$$

where \mathcal{N}_{good} refers to the number of good leptons passing all SR selection, while \mathcal{N}_{pool} denotes the number of poor leptons passing most SR selection but fail one certain requirement.

2. Define a fake control region, where one or two lepton(s) pass *poor* requirement while all the other leptons are required to pass SR selection.
3. The number of fake events are calculated as:

$$\mathcal{N}_{fake} = (N_{gggp} - N_{ggp}) \times \mathcal{F} - (N_{gppg} - N_{gpp}) \times \mathcal{F}^2 \quad (6.3)$$

with the subtraction of ZZ contribution, and the double counting between N_{gggp} and N_{gppg} .

For the definition of *poor* leptons: The poor electrons are defined as failing “Fixed-CutLoose” isolation requirement, or failing “LooseLH” electron ID requirement but satisfying “VeryLooseLH” WP. The poor muons are required to fail the “FixedCutLoose” isolation requirement or invert the impact parameter cut to be $3 < d_0/\sigma(d_0) < 10$. The dedicated $Z+jets$ and $t\bar{t}$ dominant regions are defined to calculate the fake factor respectively in the following subsections.

1. Fake factor for $Z+jets$

Fake factor for $Z+jets$ background is calculated in $Z+jets$ enriched region, where events with one OSSF lepton pair around Z mass associated with two jets are selected. The value of fake factor is driven from data, and is a function of p_T and η as shown in

figure 6.3 for electrons and figure 6.4 for muons. During calculation, the contributions from non- $Z+jets$ backgrounds ($t\bar{t}$, ZZ , WZ) have been subtracted from data. The values calculated directly from $Z+jets$ MC are also shown in plots for comparison.

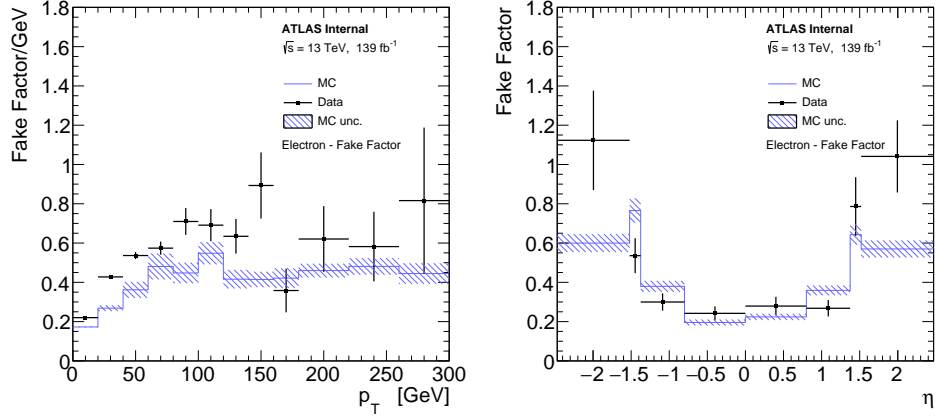


Fig. 6.3 Fake factor for $Z+jets$ background, constructed with additional electron, as a function of p_T (left) and η (right).

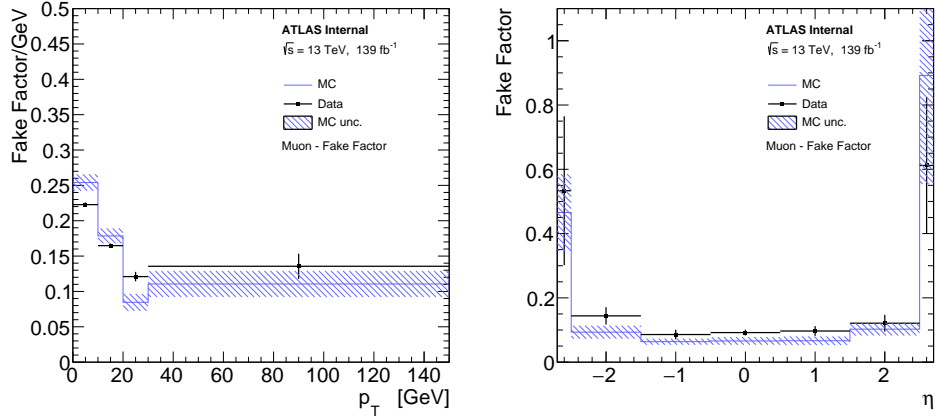


Fig. 6.4 Fake factor for $Z+jets$ background, constructed with additional muon, as a function of p_T (left) and η (right).

2. Fake factor for $t\bar{t}$

The fake factor for $t\bar{t}$ are calculated in $t\bar{t}$ dominant region by selecting the events that have one $e\mu$ -pair with additional two jets. For events with three leptons, $m_T^W < 60 \text{ GeV}$ cut is applied to reject the contribution from $t\bar{t} + W$ events. The m_T^W is defined as below:

$$m_T^W = \sqrt{2p_T^{l_3}E_T^{\text{miss}} \left[1 - \cos(\Delta\phi(p_T^{l_3}, E_T^{\text{miss}})) \right]} \quad (6.4)$$

In addition, at least one b-jet is required to enhance the top component. The fake factors of $t\bar{t}$ calculated from data as the function of p_T and η are shown in figure 6.5 for electrons and 6.6 for muons. The non- $t\bar{t}$ contributions including $Z+jets$, ZZ and WZ , are subtracted

from data.

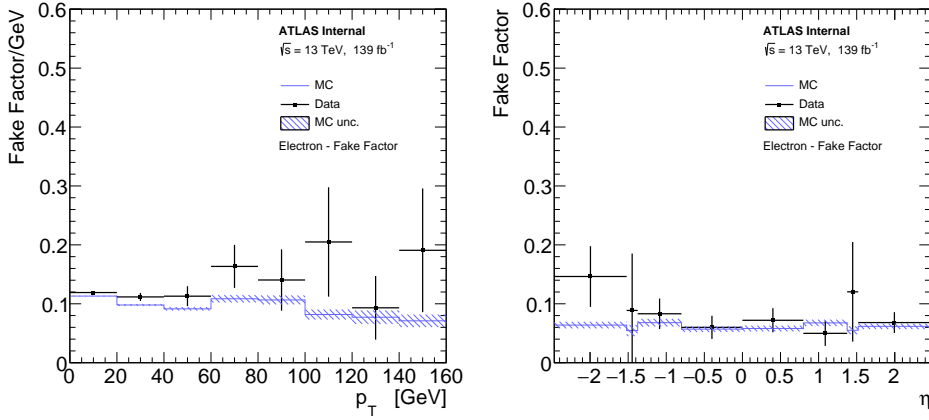


Fig. 6.5 Fake factor for $t\bar{t}$ background, constructed with additional electron, as a function of p_T (left) and η (right).

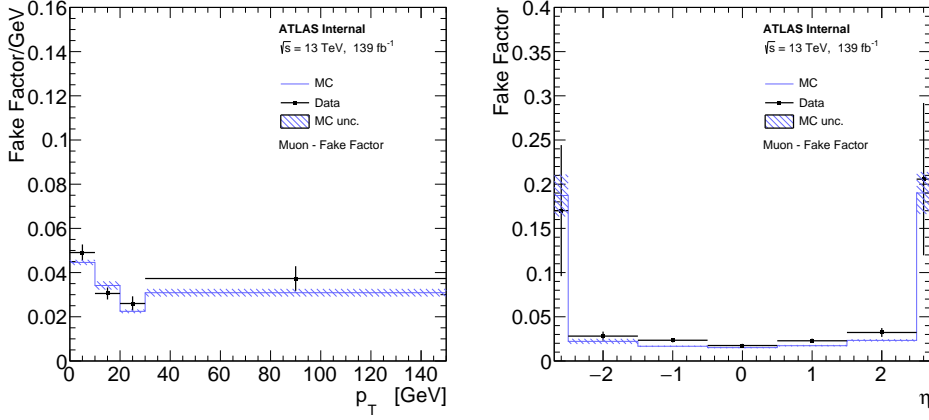


Fig. 6.6 Fake factor for $t\bar{t}$ background, constructed with additional muon, as a function of p_T (left) and η (right).

3. Systematics of fake estimation and results

The systematics of fake factor method can be measured by varying the parameters and selection requirements in fake factor calculation. In addition, due to the very limited data statistic in $\ell\ell\ell'\ell'$ channel, to be more conservative, the difference between data measurement and MC simulation are also considered as additional systematics component. The sources of systematics that have been included are listed as below:

- Variations of isolation cut for the poor lepton definition up and down scaled by a factor of two.
- Variations of the yields of those subtracted MC in fake control region scaled by 30% up and down.
- The difference of fake factors between driven from data and from MC simulation.

- The difference of fake factors when changing to one bin measurement (instead of p_T or η dependent).
- The statistical uncertainties on fake factor in fake control region.

Table 6.5 summarizes the contribution of fake backgrounds in signal region under different systematic conditions mentioned above as well as the nominal one, together with their statistical uncertainties.

channel	4e	2e2 μ	4 μ	inclusive
Nominal estimate	0.678 ± 0.652	1.023 ± 0.740	0.566 ± 0.240	2.268 ± 1.015
F stat. uncertainty varied down	0.698 ± 0.622	0.872 ± 0.652	0.509 ± 0.214	2.079 ± 0.926
F stat. uncertainty varied up	0.657 ± 0.685	1.173 ± 0.840	0.622 ± 0.267	2.452 ± 1.116
One bin F	0.653 ± 0.590	0.594 ± 0.558	0.646 ± 0.313	1.892 ± 0.870
MC F	0.534 ± 0.471	1.415 ± 0.993	0.439 ± 0.184	2.389 ± 1.114
Isolation varied down	0.938 ± 0.686	0.552 ± 0.466	0.215 ± 0.107	1.704 ± 0.837
Isolation varied up	0.723 ± 0.646	1.104 ± 0.739	0.559 ± 0.237	2.386 ± 1.010
MC corr. varied down	0.697 ± 0.695	1.048 ± 0.811	0.832 ± 0.385	2.577 ± 1.136
MC corr. varied up	0.660 ± 0.614	0.984 ± 0.687	0.316 ± 0.159	1.961 ± 0.935

Table 6.5 Fake background estimations in the SR. For nominal value, the 2D fake factor together with the $Z+jets$ and $t\bar{t}$ combination applied. The other lines show the estimations with different uncertainty variations.

6.5 Systematics

The analysis includes both the statistical fit to MD distribution to search the EW- $Z Z jj$ process, as well as the cross section measurement of inclusive EW and QCD $Z Z jj$ process in fiducial volume. Therefore, theoretical and experimental uncertainties may affect the predicted background yields and shapes, the correction factors from detector-level to particle-level measurement, as well as the $Z Z jj$ MD shapes and so on. Moreover, the statistical uncertainties of simulated samples are also taken into account. Due to the extremely low cross section of $\ell\ell\ell'\ell'$ channel, the analysis is still data statistic dominant. This section describes the measurement of both theoretical and experimental systematics for $Z Z jj$ productions. The systematics for fake backgrounds have been elaborated in section 3.

6.5.1 Theoretical systematics

The theoretical systematics on EW- and QCD- $Z Z jj$ processes including the uncertainties from PDF, QCD scale, α_S and parton showering variations are summarized in ta-

ble 6.6. The PDF uncertainty is estimated from the envelop of NNPDF internal variations and the difference between nominal and alternative PDF sets, following the PDF4LHC as introduced in section 2.2.1. The QCD scale uncertainty is estimated by varying the nominal renormalization scale (μ_R) and factorisation scale (μ_F) by a factor of 0.5 or 2.0. There are seven different configurations being considered, where the maximum of variations is chosen as final uncertainty. The parton showering uncertainty is estimated by comparing events with different parton showering setting between the nominal Pythia8 and the alternative Herwig7^[96-97] algorithm. The α_S uncertainty is estimated by varying the value of α_S within ± 0.001 . Due to the lack of simulation sample for alternative parton showering on QCD- $Z Z jj$ process, the value of parton showering component is taken from the measurement of EW process.

Process	EW- $Z Z jj$	QCD- $Z Z jj$
PDFs	NNPDF30lo (nominal), CT14lo	NNPDF30nnlo (nominal), MMHT2014nnlo68cl, CT14nnlo
α_S	0.118	0.117, 0.118 (nominal), 0.119
QCD scale ($[\mu_R, \mu_F]$)	[0.5,0.5], [0.5,1], [1,0.5], [1,1], [1,2], [2,1], [2,2]	[0.5,0.5], [0.5,1], [1,0.5], [1,1], [1,2], [2,1], [2,2]
Parton showering algorithm	Pythia8, Herwig7	-

Table 6.6 Summary of different variations for EW- and QCD- $Z Z jj$ theoretical uncertainties measurement.

Table 6.7 summarizes the uncertainties of each theoretical components in fiducial volume of SR, while table 6.8 shows the numbers in QCD-enriched CR region. For QCD process, the uncertainty is QCD scale dominant. Both of them are taken as inputs for statistical fit.

Process	PDF (%)	α_S (%)	QCD scale (%)	Parton shower (%)
EW	+5.9 -5.9		+6.1 -5.6	+3.3 -3.3
qqQCD	+2.0 -1.0	+2.6 -2.6	+34.2 -22.8	

Table 6.7 Summary of theoretical uncertainties for the fiducial volume (SR) for both EW and QCD $q q$ -initial processes.

Process	PDF (%)	α_S (%)	QCD scale (%)	Parton shower (%)
EW $\ell\ell\ell'\ell'$	+6.1 -6.1		+0.8 -1.1	+10.1 -10.1
qqQCD $\ell\ell\ell'\ell'$	+2.0 -1.0	+2.6 -2.6	+31.5 -22.0	

Table 6.8 Summary of theoretical uncertainties for the control region for EW and qqQCD processes.

The uncertainties of QCD gg -induced process ($gg \rightarrow ZZ$) as the function of MD discriminant is shown in figure 6.7 for both fiducial volume (SR) and QCD CR.

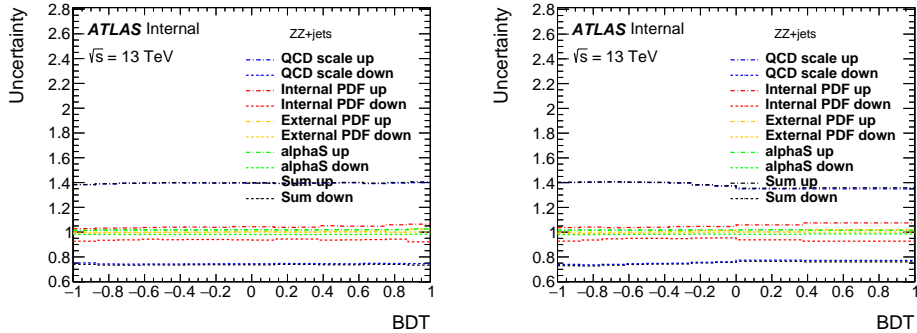


Fig. 6.7 The theoretical uncertainties for $gg \rightarrow ZZ$ background in particle-level SR (left) and CR (right).

6.5.2 Experimental systematics

The dominant experimental uncertainties are from the luminosity uncertainty, the momentum scale and resolution of leptons and jets, as well as the lepton reconstruction and selection efficiency. Some smaller uncertainties, such as trigger efficiency and pile-up correction, are also considered. Table 6.9 lists the major systematic components from leptons and jets for signal and major background processes in $\ell\ell\ell'\ell'$ channel. The total uncertainties for sources from electron, muon and jet respectively, as well as the sum (quadratic sum) of them are also summarized in this table.

name	EW- $Z Z jj$	QCD qq -initial	QCD gg
nominal yield	20.61	76.69	13.10
EG_RESOLUTION_ALL	$\pm^{0.00\%}_{0.03\%}$	$\pm^{0.02\%}_{0.04\%}$	$\pm^{0.01\%}_{1.41\%}$
EG_SCALE_ALL	$\pm^{0.03\%}_{0.05\%}$	-0.04%	$\pm^{0.01\%}_{0.06\%}$
EL_EFF_ID_TOTAL_1NPCOR_PLUS_UNCOR	$\pm^{2.66\%}_{2.58\%}$	$\pm^{2.60\%}_{2.53\%}$	$\pm^{2.65\%}_{2.57\%}$
EL_EFF_Iso_TOTAL_1NPCOR_PLUS_UNCOR	$\pm 0.70\%$	$\pm 0.47\%$	$\pm 0.42\%$
EL_EFF_Reco_TOTAL_1NPCOR_PLUS_UNCOR	$\pm 0.55\%$	$\pm 0.55\%$	$\pm 0.63\%$
JET_EtaIntercalibration_NonClosure	-0.01%	-0.03%	0%
JET_GroupedNP_1	$\pm 1.97\%$	$\pm^{11.82\%}_{10.14\%}$	$\pm^{16.21\%}_{12.92\%}$
JET_GroupedNP_2	$\pm 0.23\%$	$\pm 1.26\%$	+5.3%
JET_GroupedNP_3	$\pm 0.55\%$	$\pm 2.94\%$	$\pm^{3.14\%}_{0.12\%}$
JET_JER_SINGLE_NP	0.11%	+5.47%	+6.31%
JET_JvtEfficiency	$\pm 0.04\%$	$\pm 0.12\%$	$\pm 0.15\%$
MUON_EFF_ISO_STAT	$\pm 0.09\%$	$\pm 0.08\%$	$\pm 0.07\%$
MUON_EFF_ISO_SYS	$\pm 0.54\%$	$\pm 0.55\%$	$\pm 0.56\%$
MUON_EFF_RECO_STAT	$\pm 0.15\%$	$\pm 0.19\%$	$\pm 0.15\%$
MUON_EFF_RECO_STAT_LOWPT	$\pm 0.06\%$	$\pm 0.02\%$	$\pm 0.03\%$
MUON_EFF_TTVA_STAT	$\pm 0.06\%$	$\pm 0.07\%$	$\pm 0.06\%$
MUON_EFF_TTVA_SYS	$\pm 0.03\%$	$\pm 0.4\%$	$\pm 0.03\%$
MUON_ID	$\pm 0.03\%$	$\pm 0.02\%$	<0.001%
MUON_MS	-0.05%	$\pm^{0.04\%}_{0.01\%}$	<0.001%
MUON_SAGITTA_RESBIAS	$\pm 0.01\%$	$\pm 0.02\%$	<0.001%
MUON_SAGITTA_RHO	+1.13%	-0.73%	$\pm 1.00\%$
MUON_SCALE	$\pm 0.02\%$	$\pm^{0.03\%}_{0.02\%}$	<0.001%
PRW_DATASF	$\pm 0.5\%$	$\pm^{0.42\%}_{1.02\%}$	$\pm^{2.17\%}_{1.46\%}$
Electron Exp.	$\pm^{2.8\%}_{2.7\%}$	$\pm^{2.70\%}_{2.62\%}$	$\pm^{2.75\%}_{2.64\%}$
Muon Exp.	$\pm 1.3\%$	$\pm 1.3\%$	$\pm 1.04\%$
Jet Exp.	$\pm 2.0\%$	$\pm^{13.39\%}_{10.64\%}$	$\pm^{18.54\%}_{13.57\%}$
Total experimental uncertainties	$\pm^{3.7\%}_{4.0\%}$	$\pm^{13.72\%}_{11.11\%}$	$\pm^{18.90\%}_{13.57\%}$

Table 6.9 Experimental systematic uncertainties in $\ell\ell\ell'\ell'$ channel with the luminosity of 139 fb^{-1} . The “Electron Exp.”, “Muon Exp.” and “Jet Exp.” represent the quadrature of the respective sources from electron, muon, and jets.

In addition, the uncertainty of the combined 2015 to 2018 integrated luminosity is 1.7%^[98] in ATLAS experiment, obtained using the LUCID-2 detector^[99] for the primary luminosity measurements.

On top of them, a systematic uncertainty for MD distribution with different pile-up ($\langle\mu\rangle$) is also considered for QCD- $Z Z jj$ background by comparing the distributions be-

tween events with low and high pile-up conditions. A boundary of $\langle\mu\rangle = 33$ is used to defined low/high pile-up according to the average $\langle\mu\rangle$ for signal (about 34.5) and QCD background (about 33). Figure 6.8 shows the MD distribution in SR (left) and QCD CR (right) in two different PU conditions, the difference as function of MD is then taken into account as additional shape uncertainty for statistical fit.

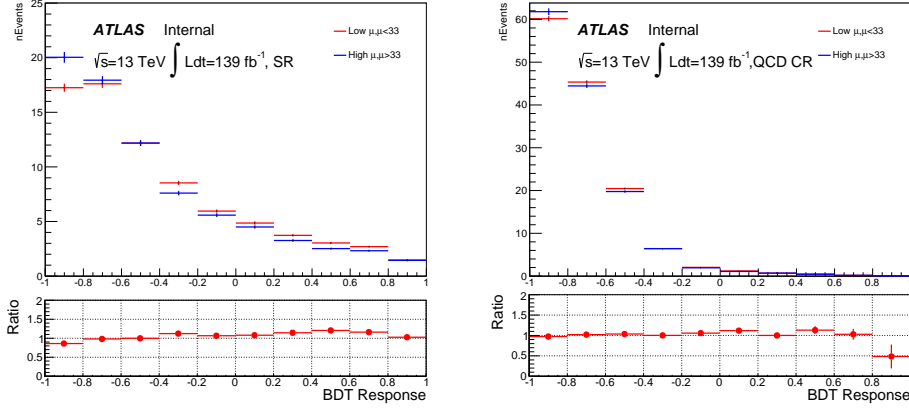


Fig. 6.8 MD distribution for QCD- $Z Z jj$ process in low and high pile-up events for SR (left) and CR (right).

Moreover, a conservative uncertainty is assigned to QCD- $Z Z jj$ process by comparing the sample modelled by Sherpa generator (nominal) with MadGraph5_aMC@NLO. The MD shape difference for both SR (left) and QCD CR (right) are shown in figure 6.9. The modelling uncertainty is then calculated from the envelop between nominal and alternative samples as function of MD as one additional shape uncertainty.

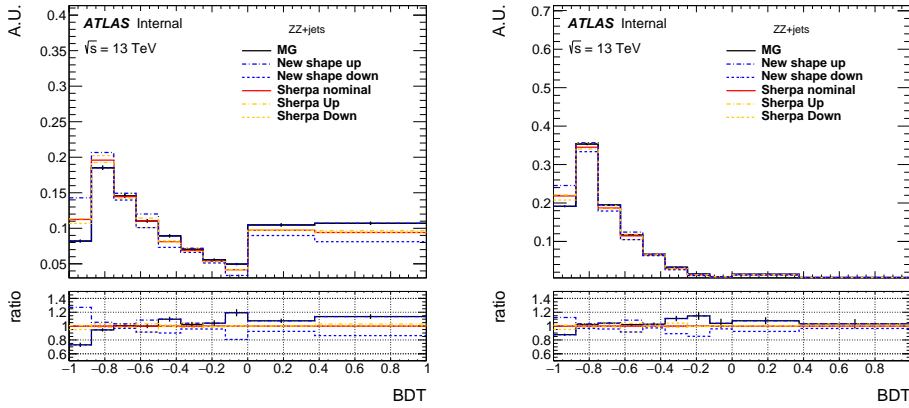


Fig. 6.9 MD shape difference for QCD $q\bar{q} \rightarrow ZZ$ background between different Sherpa theoretical uncertainties and sample from MadGraph5_aMC@NLO on SR (left) and CR (right).

6.6 Measurement of fiducial cross section

The fiducial cross section for inclusive $ZZjj$ production, including both EW and QCD components, is then measured. The definition of fiducial volume, which is used for cross section measurement, follows closely to the detector-level selection but use physics objects at particle-level, which are reconstructed in simulation from stable final-state particles, prior to their interactions with the detector.

For electrons and muons, QED final-state radiation is for the most part recovered by adding the four-momenta of surrounding photons that are not originating from hadrons and within an angular distance $\Delta R < 0.1$ to the lepton four-momentum, called lepton “dressing” at truth level. Particle-level jets are built with anti- k_T algorithm with radius parameter $R = 0.4$ using all final-state particles except leptons and neutrinos as inputs. Comparing to the events selection at detector-level in section 6.3, at particle-level, the selected dilepton pair mass required is relaxed to be within 60 to 120 GeV for the reasons of reducing the migration effect, as well as being more compatibility with CMS publication^[81]. All other kinematic selections are the same as the definition at detector-level.

6.6.1 Calculation of C-factor

C-factor is defined as the ratio between the number of selected events at detector-level and the number of particle-level events in fiducial volume (FV):

$$C = \frac{N_{\text{detector-level}}}{N_{\text{FV}}} \quad (6.5)$$

The value of C-factor for each $ZZjj$ process are calculated from each individual simulation samples as listed in table 6.10 together with their systematics.

Process	C	ΔC (stats.)	ΔC (sys.)	ΔC (theo.)
EWK $ZZjj$	0.663	± 0.002	$\pm^{0.032}_{0.031}$	NA
QCD $q\bar{q} \rightarrow ZZ$	0.702	± 0.003	$\pm^{0.061}_{0.051}$	$\pm^{0.015}_{0.018}$
QCD $gg \rightarrow ZZ$	0.741	± 0.021	$\pm^{0.143}_{0.072}$	± 0.002

Table 6.10 C Factor of different $ZZjj$ processes.

Then the C from different processes are combined together to be used as inputs for cross section calculation:

$$C = \sum_i \frac{N_{\text{FV}}^i}{\sum_j N_{\text{FV}}^j} \times C_i = 0.699 \pm 0.003(\text{stats.}) \pm^{0.011}_{0.013} (\text{theo.}) \pm 0.028(\text{exp.}) \quad (6.6)$$

The stats. refers to the statistical uncertainty from MC simulation statistics. The theo.

and exp. denote the theoretical and experimental uncertainties described in section 6.5.

6.6.2 Result of fiducial cross section

The cross section in fiducial volume is computed as:

$$\sigma^{FV} = \frac{N_{data} - N_{bkg}}{C \times Lumi} \quad (6.7)$$

where N_{data} and N_{bkg} denote the number of events selected from detector-level selection from data and sum of backgrounds, and C is the C-factor calculated above, Lumi represents the integrated luminosity of data from 2015 to 2018 of 139 fb^{-1} . Table 6.11 shows the fiducial cross section for $\ell\ell\ell'\ell'$ final state measured from equation 6.7, as well as the predicted cross section measured from MC simulation directly.

Measured fiducial σ [fb]	Predicted fiducial σ [fb]
$1.27 \pm 0.12(\text{stat}) \pm 0.02(\text{theo}) \pm 0.07(\text{exp}) \pm 0.01(\text{bkg}) \pm 0.03(\text{lumi})$	$1.14 \pm 0.04(\text{stat}) \pm 0.20(\text{theo})$

Table 6.11 Measured and predicted fiducial cross-sections in $\ell\ell\ell'\ell' jj$ final-state. Uncertainties due to different sources are presented.

The measured cross section has a total uncertainty of 11%, and is found to be compatible with SM prediction. This measurement is still dominant by data statistic.

6.7 Search for EW- $ZZjj$

6.7.1 MD discriminant

To further separate the EW- $ZZjj$ component from QCD- $ZZjj$, a MD based on Gradient Boosted Decision Tree (BDT) algorithm^[100] is trained with simulated events via TMVA framework^[69]. Training is performed between EW (signal) and QCD (background) processes. Twelve event kinematic variables sensitive to the characteristics of the EW signal are used as input features in training. Table 6.12 lists those input variables with the order of their importance in BDT response provided by TMVA tool. One can see the jet-related information provides larger sensitivity. Then the MD distributions in both SR and QCD CR region are used for statistical fit.

6.7.2 Fitting procedure

A profile likelihood fit, as described in chapter 5, is performed on MD discriminant to extract the EW- $ZZjj$ signal from backgrounds. The binning of MD distributions in SR

Rank	Variables	Description
1	m_{jj}	Dijet invariant mass
2	p_T^{j1}	p_T of the leading jet
3	p_T^{j2}	p_T of the sub-leading jet
4	$\frac{p_T(ZZjj)}{H_T(ZZjj)}$	p_T of the $Z Z jj$ system divided by the scalar p_T sum of Z bosons and two jets
5	$y_{j1} \times y_{j2}$	Product of jet rapidities
6	Δy_{jj}	Rapidity difference between two jets
7	Y_{Z2}^*	Rapidity of the second Z boson
8	Y_{Z1}^*	Rapidity of the Z boson reconstructed from the lepton pair with the mass closer to the Z boson mass
9	p_T^{ZZ}	p_T of 4l system
10	m_{ZZ}	Invariant mass of 4l system
11	p_T^{Z1}	p_T of the Z boson reconstructed from the lepton pair with the mass closer to the Z boson mass
12	$p_T^{\ell3}$	p_T of the third lepton

Table 6.12 Input features for the training of MD.

is optimized to maximize the sensitivity for detecting EW signal. The normalization of QCD- $Z Z jj$ production (μ_{QCD}^{III}) in $\ell\ell\ell'\ell'$ channel is determined by data from simultaneously fit in SR and QCD CR as described in section 6.4. The signal strength of EW- $Z Z jj$ production (μ_{EW}) is taken as parameter of interest and floated in the fit. The effects of the uncertainties related to normalizations and shapes described previously in section 6.5 of background processes in the MD distribution are all taken into account.

In most case, a common nuisance parameter is used for each source of systematic in all bins and all categories. The statistical uncertainties for simulated samples are uncorrelated among all bins, and the background uncertainties only applied to their corresponding backgrounds. Furthermore, to be more conservative, the generator modelling uncertainty for QCD- $Z Z jj$ production mentioned in section 6.5 is separated to be two nuisance pa-

rameters in low and high MD region.

6.7.3 Result of fit

The results of fitting to $\ell\ell\ell'\ell'$ final state are presented in table 6.13. To drive expected results, the observed data is used for QCD CR to extract normalization factor of QCD component (μ_{QCD}^{III}), while in SR, asimov data built from background prediction and signal model with SM assumed cross section is used.

	μ_{EW}	$\mu_{QCD}^{\ell\ell\ell'\ell' jj}$	Significance Obs. (Exp.)
$\ell\ell\ell'\ell' jj$	1.54 ± 0.42	0.95 ± 0.22	$5.48 (3.90) \sigma$

Table 6.13 Observed μ_{EW} and $\mu_{QCD}^{\ell\ell\ell' jj}$, as well as the observed and expected significance from the individual $\ell\ell\ell'\ell'$ channel. The full set of systematic uncertainties are included.

As a conclusion, the background-only hypothesis is rejected at 5.5σ (3.9σ) for observed (expected) data, which leads to the observation of EW- $ZZjj$ production.

Figure 6.10 shows the post-fit MD distributions for $\ell\ell\ell'\ell'$ channel in SR (left) and QCD CR (right). The EW- $ZZjj$ cross section measured in $\ell\ell\ell'\ell'$ channel is extracted to be 0.94 ± 0.26 fb.

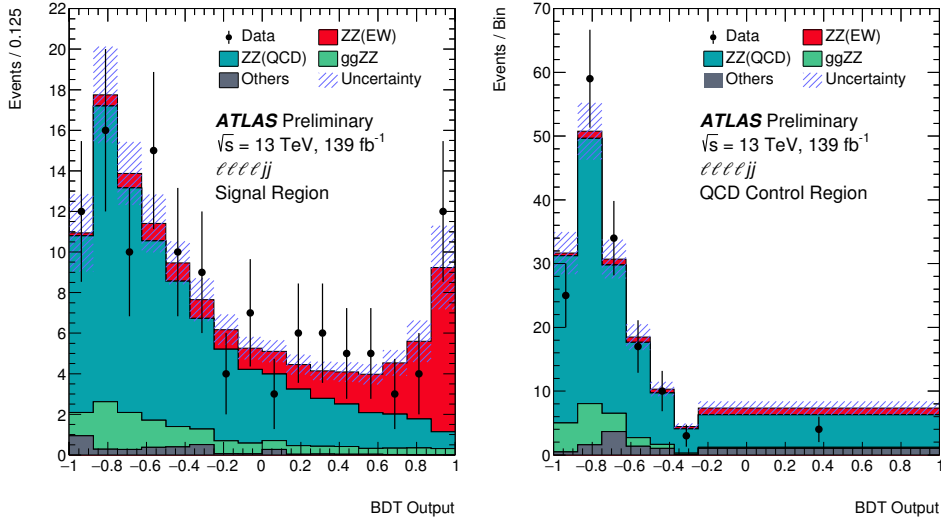


Fig. 6.10 Observed and post-fit expected multivariate discriminant distributions after the statistical fit in the $\ell\ell\ell'\ell'$ SR (left) and QCD CR (right). The error bands include the experimental and theoretical uncertainties, as well as the uncertainties in μ_{EW} and $\mu_{QCD}^{\ell\ell\ell' jj}$. The error bars on the data points show the statistical uncertainty on data.

Figure 6.11 shows the m_{jj} distribution in SR (left) and QCD CR (right), where the normalization of EW and QCD processes are scaled according to their observed value in table 6.13. High m_{jj} region is more sensitive for EW- $ZZjj$ events detection from this

figure. Figure 6.12 shows the spectrum of invariant mass of $\ell\ell\ell'\ell'$ system (m_{ZZ}) in SR also with the normalization of EW and QCD processes scaled.

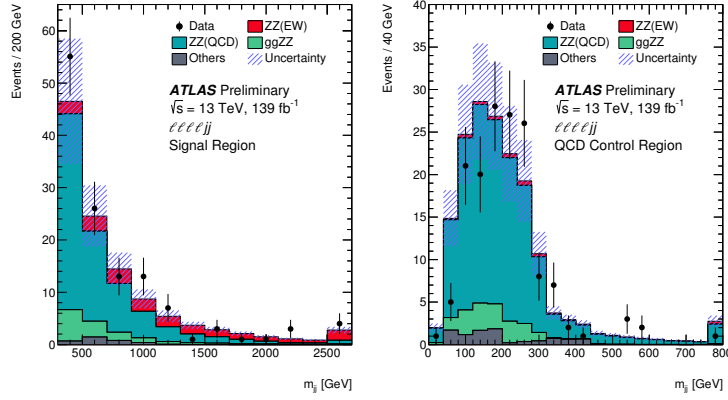


Fig. 6.11 Observed and post-fit expected m_{jj} distributions in SR (left) and QCD CR (right). The error bands include the expected experimental and theoretical uncertainties. The error bars on the data points show the statistical uncertainty. The contributions from the QCD and EW production of $Z Z j j$ events are scaled by 0.96 and 1.35, respectively, corresponding to the observed normalization factors in the statistical fit. The last bin includes the overflow events.

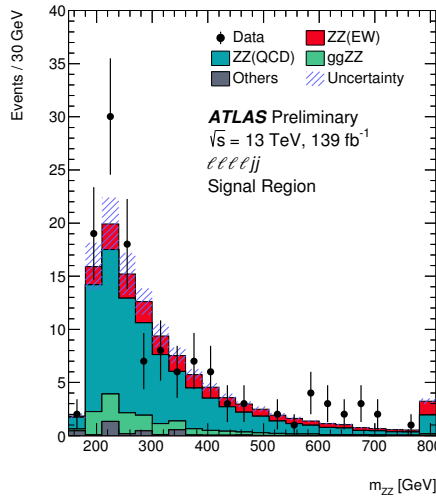


Fig. 6.12 Observed and post-fit expected m_{ZZ} spectrum in SR. The error bands include the expected experimental and theoretical uncertainties. The error bars on the data points show the statistical uncertainty. The contributions from the QCD and EW production of $Z Z j j$ events are scaled by 0.96 and 1.35, respectively, corresponding to the observed normalization factors in the statistical fit. The last bin includes the overflow events.

Figure 6.13 is the display of one event candidate of EW- $Z Z j j$ production in $2e2\mu$ final state with two jets in forward and backward region.

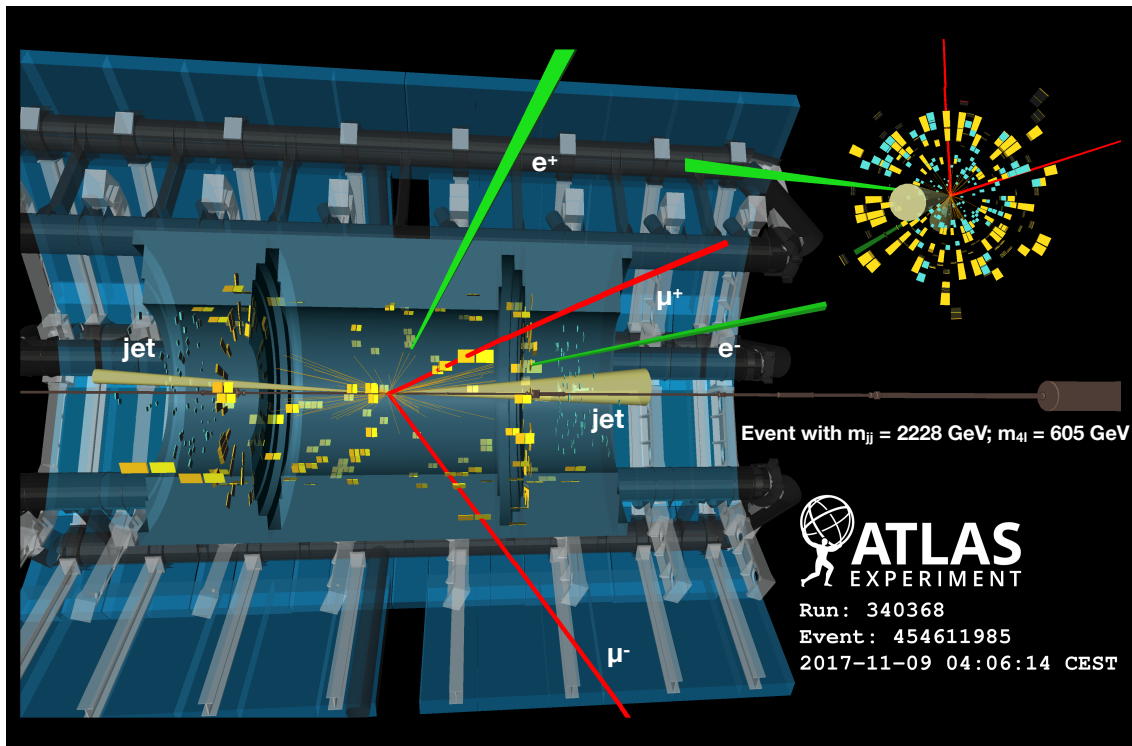


Fig. 6.13 Display of an event candidate of EW- $Z Z jj$ production in $2e2\mu$ channel in last MD bin ($0.875 < \text{MD} < 1.0$). The invariant mass of the di-jet (four-lepton) system is 2228 (605) GeV.

6.8 Prospect study of EW- $Z Z jj$ production in HL-LHC

The High-Luminosity Large Hadron Collider (HL-LHC) project aims to increase the luminosity by a factor of 10 beyond the LHC's design value to increase the potential for discoveries after 2025. The expected luminosity will reach 3000 fb^{-1} with the centre-of-mass energy of 14 TeV.

As introduced in previous sections, with full run-2 data of 139 fb^{-1} collected by ATLAS detector at the LHC, the EW- $Z Z jj$ production is the last channel of observation for VBS processes with massive bosons due to its very low cross section in $Z Z$ channel. So we expect that this channel will benefit significantly from the increased luminosity at the HL-LHC, and can be studied in great details for this known mechanism.

In this section, a prospective study is performed for EW- $Z Z jj$ production at the HL-LHC in the $\ell\ell\ell'\ell'$ channel. The study uses 3000 fb^{-1} of simulated pp collision data at a centre-of-mass energy of 14 TeV as expected to be recorded by the ATLAS detector at the HL-LHC. All simulated events are produced at particle-level, and the detector effects of leptons and jets reconstruction and identification are estimated by corrections assuming the mean number of interactions per bunch crossing ($\langle\mu\rangle$) of 200.

6.8.1 The ATLAS detector at HL-LHC

As the expectation of HL-LHC, the new Inner Tracker (ITk)^[101] will extend the tracking acceptance capability of ATLAS detector to pseudorapidity ($|\eta|$) up to 4.0. By including a forward muon trigger, the upgraded Muon Spectrometer^[102] is also expected to provide muon identification capabilities to $|\eta|$ up to 4.0. In addition, the new high granularity timing detector (HGTD)^[103] designed to mitigate the pile-up (PU) effects is also expected to be installed in the forward region of $2.4 < |\eta| < 4.0$. More details of expected performance of the upgraded ATLAS detector at the HL-LHC has been reported in Ref.^[104]

6.8.2 Simulation

The analysis is performed using particle-level events. The samples are generated at $\sqrt{s} = 14$ TeV. The signal in this analysis is EW- $ZZjj$ process, while only the dominant irreducible background of QCD- $ZZjj$ is considered. Both signal and background are generated using Sherpa with the NNPDF3.0NNLO PDF set. The signal sample is modelled with two jets at Matrix Element (ME) level. The background is generated with up to one (three) outgoing partons at NLO (LO) in pQCD. As a quick study, other minor backgrounds such as fake backgrounds from $Z+jets$ and top-quark processes, as well as Diboson without 4l final-state and Triboson processes are not considered in this analysis. Furthermore, for hard scattering events, the pile-up collisions are set with a mean value of 200 interactions per bunch crossing. Signal and background yields are then scaled to an integrated luminosity of 3000 fb^{-1} as expected at the HL-LHC.

6.8.3 Event selection

The analysis selection follows closely to the one in ATLAS run-2 analysis as described in section 6.3. Here are some changes according to the expectation of the HL-LHC scenario for ATLAS detector:

- Extend the lepton (both electron and muon) identification to $|\eta| < 4.0$
- Pile-up (PU) jet suppression is applied with a PU rejection factor of 50 for all PU jets in the region of $|\eta| < 3.8$, based on the expected ATLAS detector performance at the HL-LHC.
- The jets are required to have $p_T > 30$ (70) GeV in the $|\eta| < 3.8$ ($3.8 < |\eta| < 4.5$) region.
- For two selected jets, tighten the m_{jj} requirement to be $m_{jj} > 600$ GeV, and require $\Delta\eta_{jj} > 2$.

In addition, a fiducial volume, used to study the expected precision of the cross-section measurements, is defined at particle-level with the same kinematic requirements listed above.

Table 6.14 summarized the number of selected signal and background events normalized to 3000 fb^{-1} . In addition to the *baseline* selection listed above, to compare the different detector scenarios at the HL-LHC, two alternative selections are also studied:

1. Reduce the lepton η region to 2.7, to understand the effect due to forward lepton reconstruction and identification with the upgraded ATLAS detector.
2. Only apply the PU jet suppression with region $|\eta| < 2.4$, to measure the improvement of *baseline* by extending the rejection range of PU jets at the HL-LHC with the installation of HGTD.

Selection	$N_{\text{EW-ZZjj}}$	$N_{\text{QCD-ZZjj}}$	$N_{\text{EW-ZZjj}} / \sqrt{N_{\text{QCD-ZZjj}}}$
Baseline	432 ± 21	1402 ± 37	11.54 ± 0.58
Leptons with $ \eta < 2.7$	373 ± 19	1058 ± 33	11.46 ± 0.62
PU jet suppression only in $ \eta < 2.4$	536 ± 23	15470 ± 120	4.31 ± 0.19

Table 6.14 Comparison of event yields for signal ($N_{\text{EW-ZZjj}}$) and background ($N_{\text{QCD-ZZjj}}$) processes, and expected significance of EW- $ZZjj$ processes, normalized to 3000 fb^{-1} data at 14 TeV, with baseline and alternative selections. Uncertainties in the table refer to expected data statistical uncertainty at 14 TeV with 3000 fb^{-1} .

From this table, one can see the extended track coverage increases the $\ell\ell\ell'\ell'jj$ events by 15 to 30%, via improving the lepton efficiency. But the significance of searching for EW- $ZZjj$ process does not improve so much due to the large increment of background events.

Figure 6.14 shows the kinematic distributions of di-jet invariant mass (m_{jj}), the ZZ invariant mass (m_{ZZ}) and the ϕ separation of two Z bosons ($|\Delta\phi(ZZ)|$) as well as the centrality of the ZZ system. The ZZ centrality is defined as:

$$ZZ \text{ centrality} = \frac{|y_{ZZ} - (y_{j1} + y_{j2})/2|}{|y_{j1} - y_{j2}|} \quad (6.8)$$

To measure the event yield, the top panel shows the stack distribution for EW- and QCD- $ZZjj$ processes, while bottom panel is the ratio between two processes.

6.8.4 Systematics

According to studies in section 6.5, the dominant systematic in $\ell\ell\ell'\ell'$ channel is from theoretical systematic for QCD- $ZZjj$ background process. Different sizes of systematics

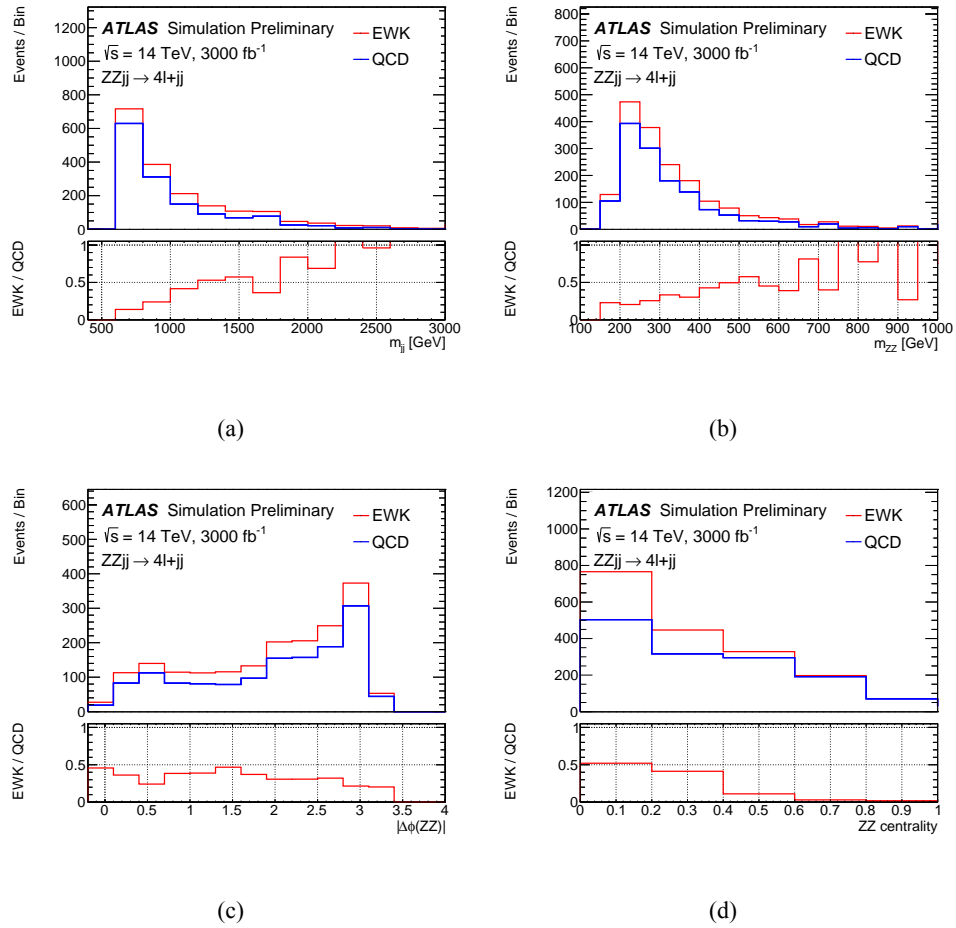


Fig. 6.14 Detector-level distributions of EW- and QCD- $Z Z j j$ processes with selected events in defined phase space at 14 TeV of (a) m_{jj} , (b) m_{ZZ} , (c) $|\Delta\phi(ZZ)|$, (d) ZZ centrality, normalized to 3000 fb^{-1} .

have been studied, at a factor of 5, 10 and 30% on background modelling. The 5% uncertainty is an optimal estimation when there is enough data events from QCD-enriched control region at the HL-LHC that can be used to constrain the theoretical normalization on QCD- $Z Z j j$ process. The 30% one is a conservative estimation, in which the uncertainties are directly calculated from different PDF sets and QCD renormalization and factorization scales, following recommendation from the PDF4LHC mentioned in section 6.5.

For experimental sources, the jet systematics have been checked following the setting provided by the HL-LHC in Ref.^[104], and the uncertainties are within 5% level, which is smaller than run-2 measurement at 10%. Figure 6.15 depicts the up and down variations for jet uncertainty provided by the HL-LHC performance tool as function of dijet invariant mass (m_{jj}). Therefore, a conservative 5% uncertainty is used as experimental uncertainty.

Since the final result relies greatly on the uncertainties, especially the theoretical un-

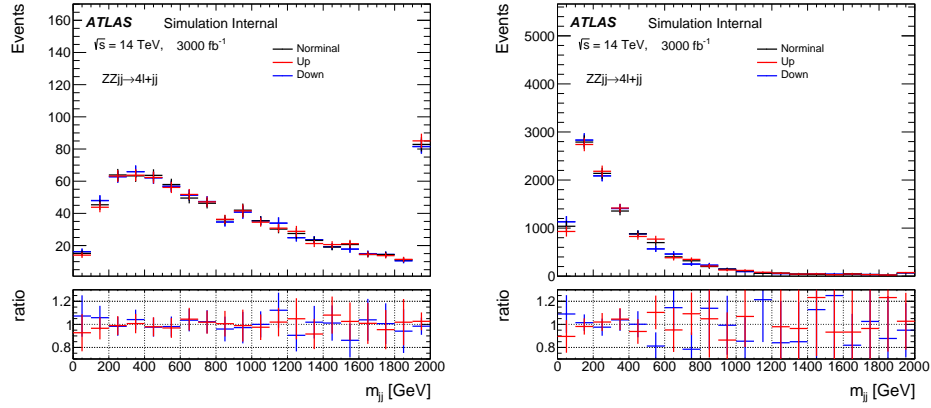


Fig. 6.15 Jet variations on m_{jj} distribution for EW- $Z Z jj$ (left) and QCD- $Z Z jj$ (right) processes with luminosity of 3000 fb^{-1} at 14 TeV. Upgrade Performance Function is used to extract the uncertainties with *baseline* setting.

certainties on QCD- $Z Z jj$ production. So results with different uncertainty conditions are shown as below:

- The case with statistical uncertainty of simulated samples only.
- The case with statistical and experimental uncertainties (5%)
- The case with statistical, experimental and additional theoretical uncertainties at 5%, 10% and 30% levels respectively.

Three different sources of uncertainties are treated as uncorrelated and summed up quadratically.

6.8.5 Results

In this analysis, instead of a statistical fit, the expected significance of EW- $Z Z jj$ production is calculated as:

$$\text{Significance} = \frac{S}{\sqrt{\sigma(B)_{\text{stat.}}^2 + \sigma(B)_{\text{syst.}}^2}}, \quad (6.9)$$

where S presents the number of selected signal events, and $\sigma(B)_{\text{stat.}}$ and $\sigma(B)_{\text{syst.}}$ denote the statistical and systematic (exp. + theo.) uncertainties from background processes. The statistical uncertainty is computed from expected data yield with an integrated luminosity of 3000 fb^{-1} .

Based on baseline selection of $m_{jj} > 600 \text{ GeV}$, an additional scan over different m_{jj} cuts is also performed with a step of 50 GeV under different systematic conditions, as shown in figure 6.16.

In addition, the expected differential cross section of EW- $Z Z jj$ process is measured in the defined phase space at 14 TeV, as a function of m_{ZZ} and m_{jj} , shown in figure 6.17.

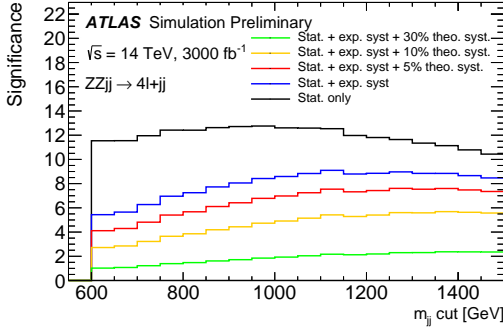


Fig. 6.16 The expected significance of EW-ZZjj processes as a function of different m_{jj} cut with 3000 fb^{-1} , under conditions of different sizes of theoretical uncertainties on the QCD-ZZjj background modelling. The statistical uncertainty is estimated from expected data yield at 14 TeV with 3000 fb^{-1} . Different uncertainties are summed up quadratically.

The expected differential cross sections are calculated as:

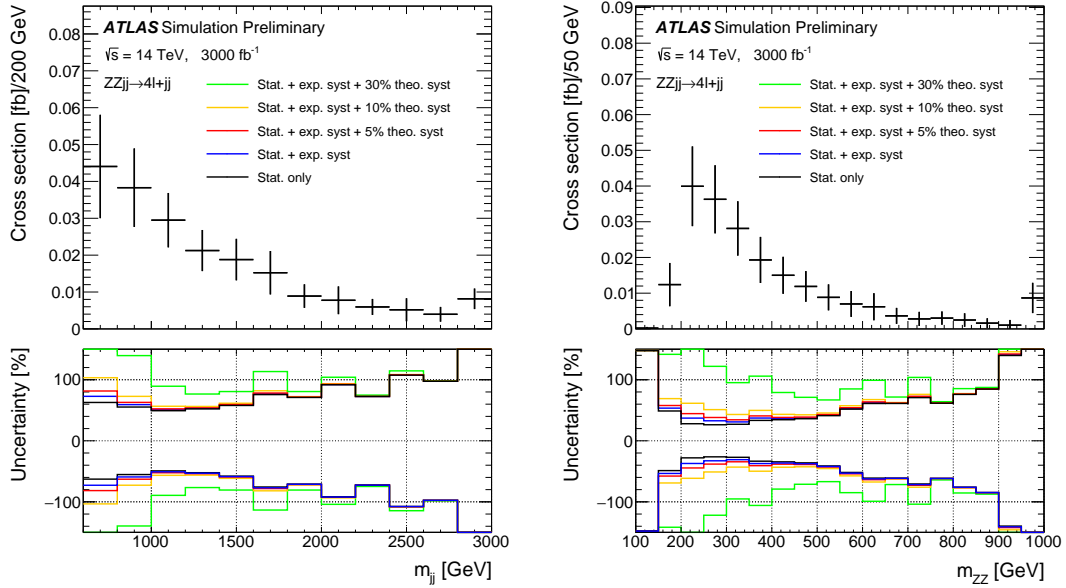


Fig. 6.17 The projected differential cross-sections at 14 TeV for the EW-ZZjj processes as a function of m_{jj} (left) and m_{ZZ} (right). The top panel shows measurement with statistical only case, where statistical uncertainty is estimated from expected data yield at 14 TeV with 3000 fb^{-1} . The bottom panel shows impact of different sizes of systematic uncertainties.

$$\sigma = \frac{N_{\text{pseudo-data}} - N_{\text{QCD-ZZjj}}}{L * C_{\text{EW-ZZjj}}} \quad (6.10)$$

$$C_{\text{EW-ZZjj}} = \frac{N_{\text{EW-ZZjj}}^{\text{det.}}}{N_{\text{EW-ZZjj}}^{\text{part.}}}$$

where $N_{\text{pseudo-data}}$ denotes the expected number of data events with 3000 fb^{-1} luminosity

at 14 TeV, and $N_{QCD-ZZjj}$ and $N_{EW-ZZjj}$ are the number of predicted events of QCD- $ZZjj$ and EW- $ZZjj$ processes in particle-level. The $C_{EW-ZZjj}$ factor represents the detector efficiency for EW- $ZZjj$ processes introduced in section 6.6.1. The interference between EW- and QCD- $ZZjj$ processes is ignored due to its minor contribution.

The value of expected integrated cross section as well as its uncertainty under different systematic conditions are shown in table 6.15 with 3000 fb^{-1} luminosity at 14 TeV. The statistical uncertainty is at 10% level when with such large luminosity. The result is dominated by systematics and can reach 100% level when theoretical modelling uncertainty is 30% for QCD- $ZZjj$ processes.

	Cross section [fb]	Stat. only	Plus exp.	Plus 5% theo.	Plus 10% theo.	Plus 30% theo.
EW- $ZZjj$	0.21	± 0.02	± 0.04	± 0.05	± 0.08	± 0.21

Table 6.15 Summary of expected cross-section measured with different theoretical uncertainties. The statistical uncertainty is computed from expected data yield with 3000 fb^{-1} at 14 TeV. Different uncertainties are treated as uncorrelated and summed quadratically.

6.9 Conclusion

The fiducial cross section for inclusive $Z Z jj$ production is measured in this section, with a total relative uncertainty of 11% for the $\ell\ell\ell'\ell'$ final state, and found to be compatible with the SM prediction. The observation of electroweak production of two jets in association with a Z -boson pair decay to $\ell\ell\ell'\ell'$ final state using 139 fb^{-1} of 13 TeV pp collision data collected by ATLAS experiment at the LHC is presented in this section. The search for electroweak production of two jets in association with a Z -boson pair is based on multivariate discriminants (MD) to enhance the separation between the signal and backgrounds. In $\ell\ell\ell'\ell'$ final state, the background-only hypothesis is rejected with an observed (expected) significance of 5.5 (3.9) σ , which gives the first observation of electroweak production in $Z Z jj$ channel.

In addition, the prospective study for the EW- $Z Z jj$ production at the HL-LHC in the $\ell\ell\ell'\ell'$ channel, using 3000 fb^{-1} simulated pp collision data at a centre-of-mass energy of 14 TeV has been presented. The precision of the expected measurements of the integrated and differential cross sections as a function of dijet or $\ell\ell\ell'\ell'$ invariant mass are shown. Under the assumption of theoretical uncertainty for the QCD- $Z Z jj$ processes and experimental uncertainty for jets being constraint at 5% level respectively, with statistical uncertainty in 3000 fb^{-1} being considered, the observation of the EW- $Z Z jj$ process can reach a significance of 7σ .

Chapter 7 Search for heavy resonances decaying into a pair of Z bosons in $\ell\ell\ell'\ell'$ final state using pp collision data collected by ATLAS detector from 2015 to 2018

7.1 Introduction

A new particle was discovered by the ATLAS and CMS Collaborations at the LHC^[3-4] in 2012. Both experiments have confirmed that the properties including spin, couplings and parity of this new particle are consistent with Higgs boson predicted in the Standard Model (SM), which is an important milestone in understanding of the mechanism of EWSB. Nevertheless, the possibility that this newly discovered particle is just a part of the extended Higgs sector as predicted by various extensions in the SM cannot be ruled out. Many models predicted the existence of new heavy resonances decaying into dibosons, such as a heavy spin-0 neutral Higgs boson^[105] and the two-Higgs-doublet models (2HDM)^[6], as well as the spin-2 Kaluza–Klein (KK) excitations of the graviton (G_{KK})^[106].

Though with smaller branching ratio compared to semileptonic or fully hadronic decay channels, the $\ell\ell\ell'\ell'$ final state has its unique sensitivity in mass range smaller than 1 TeV region due to its good mass resolution and relative smaller experimental and theoretical systematics. This section presents the search for heavy resonance decaying into a pair of Z bosons to the $\ell\ell\ell'\ell'$ final state, in which ℓ denotes to either an electron or a muon^[107]. Several signal hypotheses are considered. The first hypothesis is a heavy Higgs boson (spin-0 resonance) under the narrow-width approximation (NWA). Then as several theoretical models prefer non-negligible natural widths, the models under large-width approximation (LWA), assuming widths of 1%, 5%, 10% and 15% of the resonance mass, are also studied. In addition, the graviton excitations (spin-2 resonance) under the Randall–Sundrum model are also searched. It is assumed that the heavy resonance is produced predominantly via the gluon-gluon Fusion (ggF) and the Vector Boson Fusion (VBF) productions, but with the unknown ratio of two production rates. So the results are separated for ggF and VBF production modes. To gain more sensitivity, the $\ell\ell\ell'\ell'$ events are classified into ggF- and VBF-enriched categories. Moreover, for the NWA model, the categorizations are studied under both cut-based and multivariate (MVA) -based methods, the details of categorization are shown in following sections.

The search uses the four-lepton invariant mass in the range of 200 GeV to 2000 GeV for signal hypothesis of spin-0 resonance under the NWA model, and from 400 GeV to 2000 GeV for the one under the LWA models. And the spin-2 graviton signals are searched in the mass range from 600 GeV to 2000 GeV. The data collected by ATLAS detector at the LHC from 2015 to 2018 at the centre-of-mass energy of 13 TeV is used. In case of no excess, upper limits on the production rate of different signal hypotheses are computed from statistical fits to m_{4l} distribution.

7.2 Data and MC samples

7.2.1 Data samples

The data used in this analysis are collected by ATLAS detector at the centre-of-mass energy of 13 TeV during the years of 2015 to 2018. Only events passing the latest Good Run List (GRL) released by the Data Quality group from ATLAS experiment corresponding to an integrated luminosity of $139.0 \pm 2.4 \text{ fb}^{-1}$ are used. Table 7.1 listed the recorded integrated luminosity, average and peak pile-up of each year's data.

Table 7.1 Summary of the recorded integrated luminosity (lumi), average and peak pile-up (PU) of data from 2015 to 2018.

Year	recorded integrated lumi	lumi after GRL	average PU	peak PU
2015	3.86 fb^{-1}	36.2 fb^{-1}	13.4	28.1
2016	35.6 fb^{-1}		25.1	52.2
2017	46.9 fb^{-1}	44.3 fb^{-1}	37.8	79.8
2018	60.6 fb^{-1}	58.5 fb^{-1}	36.1	88.6

7.2.2 Background MC simulations

Background processes considered in this analysis include ZZ ($q\bar{q} \rightarrow ZZ$, $gg \rightarrow ZZ$), triboson (WWZ , WZZ , ZZZ), $Z+jets$ and top-quark ($t\bar{t}$, ttV) processes.

The QCD $q\bar{q} \rightarrow ZZ$ process is modelled using Sherpa 2.2.2^[86] with the NNPDF3.0NNLO^[87] PDF, where events with up to one (three) outgoing partons are generated at NLO (LO) in pQCD. The production of ZZ from the gluon-gluon initial state with a four-fermion loop or with an exchange of the Higgs boson, which has an order of α_S^4 in QCD, is not included in this Sherpa simulation. So a separate gg induced ZZ sample including the continuum background, the SM Higgs boson, and the interference contribution is modelled using Sherpa 2.2.2 with the NNPDF3.0NNLO PDF set, and with an additional k-factor^[88] of 1.7 applied. The EW- $ZZjj$ production is simulated using

Sherpa 2.2.2 with the NNPDF3.0NNLO PDF, and the $ZZZ \rightarrow \ell\ell\ell'\ell'qq$ process is also taken into account in this sample.

The $Z+jets$ events are generated using Sherpa 2.2.2 with the NNPDF3.0NNLO PDF, in which the ME is calculated for up to two partons with NLO accuracy in pQCD and up to four partons with LO accuracy. The $Z+jets$ events are normalized using the next-to-next-to-leading-order (NNLO) cross section. The triboson processes with full leptonic decays and at least four prompt charged leptons are generated using Sherpa 2.1.1. For top-quark pair ($t\bar{t}$) production and the single top-quark productions in t -channel, s -channel and Wt -channel, Powheg-Box v2 is used with the CT10 PDF. The productions of $t\bar{t}$ in association with Z boson(s) ($t\bar{t}Z$) is modelled with MadGraph5_aMC@NLO.

7.2.3 Signal MC simulations

One model considered in this analysis is heavy spin-0 resonance under the Narrow Width Approximation (NWA) simulated using Powheg-Box v2 MC event generator with the CT10 PDF. The gluon-gluon fusion (ggF) production mode and vector-boson fusion (VBF) production mode are calculated separately with matrix elements up to NLO in QCD. The Powheg-Box is interfaced to Pythia8 for parton showering, and for decaying the Higgs boson into the $H \rightarrow ZZ \rightarrow \ell\ell\ell'\ell'$ final states. Events of NWA signal are generated at mass points between 200 GeV to 2000 GeV using the step of 100 (200) GeV up to (above) 1 TeV in both ggF and VBF production modes.

In addition, heavy Higgs boson events under the Large Width Approximation (LWA) with widths of 1%, 5%, 10% and 15% of the boson mass are generated using MadGraph5_aMC@NLO 2.3.2 interfaced to Pythia8. Only ggF production is considered. Mass points between 400 GeV to 2000 GeV are simulated with the step of 100 (200) GeV up to (above) 1 TeV. To describe jet multiplicity, MadGraph5_aMC@NLO is used to simulate process of $pp \rightarrow H + \geq 2\text{jets}$ at NLO in QCD with the FxFx merging scheme^[108].

Spin-2 Kaluza–Klein (KK) gravitons (G_{KK}) from the Bulk Randall–Sundrum model^[109] are also studied in this analysis. Events are generated by MadGraph5_aMC@NLO at LO in QCD, which is then interfaced to Pythia8 for parton showering. The G_{KK} -gluon coupling $k/\overline{M}_{\text{Planck}}$, where k is the curvature scale of the extra dimension and $\overline{M}_{\text{Planck}}$ is the reduced Planck mass, is set to 1. The width of the resonance is correlated with the coupling $k/\overline{M}_{\text{Planck}}$ and in this configuration is around $\square 6\%$ of its mass. The mass of the G_{KK} is the only free parameter in this simplified model. Mass points between 600 GeV to 2 TeV with 200 GeV spacing were generated.

7.3 Analysis selections

7.3.1 Objects selection

Similar to VBSZZ analysis in section 6.3, the selection of this analysis relies on the definition of multiple objects: *electrons*, *Muons*, and *jets*. Details of definitions for each object are described as below:

Electron: As described in section 4.2.3, electrons are reconstructed from energy deposits in the EM calorimeter matched to a track in the inner detector. The electron candidates satisfying the *Loose* criterion from the likelihood-based (LH) method are selected, with a selection efficiency ranging from 90% for transverse momentum $p_T = 20$ GeV to 96% for $p_T > 60$ GeV. In addition, the electrons are required to have $p_T > 7$ GeV, $|\eta| < 2.47$ and $|z_0 \sin\theta| < 0.5$ mm.

Muon: To increase the acceptance range in reco-level for $\ell\ell\ell'\ell'$ channel, all four types of muons (CB, ST, CT, ME muons, described in section 4.2.4) are used. The CT muons are required to pass $p_T > 15$ GeV and $|\eta| < 0.1$, while the ST muons are also limited in $|\eta| < 0.1$ region. The ME muons are only used in the region of $2.5 < |\eta| < 2.7$. And at most one CT, ST or ME muon is allowed in one $\ell\ell\ell'\ell'$ quadruplet. The Muon candidates are required to pass $p_T > 5$ GeV and $|\eta| < 2.7$, and satisfy the *Loose* identification criterion with an efficiency of at least 98.5%. The impact parameter requirements of $|d_0| < 1$ mm and $|z_0 \sin\theta| < 0.5$ mm are further applied.

Jets: Jets are clustered using the anti- k_t algorithm with radius parameter $R = 0.4$ implemented in the FastJet package as described in section 4.2.5. The ‘particle flow’ (PFlow) objects^[110], which combines measurements from both the tracker and the calorimeter, are used as inputs to the FastJet package. The energy deposited in the calorimeter by all charged particles is removed, and the jet reconstruction is performed on an ensemble of PFlow objects consisting of the remaining calorimeter energy and tracks which are matched to the hard interaction. This improves the accuracy of the charged-hadron measurement, while retaining the calorimeter measurements of neutral-particle energies. Compared to only using topological clusters, jets reconstructed with the particle flow algorithm with $p_T > 30$ GeV have approximately 10% better transverse momentum resolution. The jets used in this analysis are then required to have $p_T > 30$ GeV and $|\eta| < 4.5$. To further reduce the effects of pile-up jets, a jet vertex tagger (JVT) is applied to jets with $p_T < 60$ GeV and $|\eta| < 2.4$.

Overlap removal: As the selected jet and lepton candidates can be reconstructed from same detector information, an overlap-removal procedure is applied. For electron

and muon sharing the same ID track, the electron is selected in the case that the muon is calorimeter-tagged and does not have a MS track, or is a segment-tagged muon, otherwise the muon is selected. The jet overlapping with electron (muon) within a cone of size of $\Delta R \equiv \sqrt{(\Delta\eta)^2 + (\Delta\phi)^2} = 0.2(0.1)$ are removed.

7.3.2 Event selection

First of all, the four-lepton events are required to pass single or multi-lepton triggers. Due to the increasing of peak luminosity and pile-up, the p_T and E_T thresholds of triggers increase slightly during the data-taking periods from 2015 to 2018. Table 7.2 summarizes the triggers used for $\ell\ell\ell'\ell'$ channel. The overall trigger efficiency for selected signal events passing final selection is around 98%.

Table 7.2 Summary of the p_T (E_T) trigger thresholds (in GeV) employed for the muon (electron) trigger selection in the year of 2015, 2016, 2017, and 2018.

Trigger item	Trigger threshold			
	2015	2016	2017	2018
single muon	$\mu20; \mu50; \mu60$	$\mu24; \mu26; \mu40; \mu50$	$\mu26; \mu50; \mu60$	$\mu26; \mu50; \mu60$
single electron	$e24; e60; e120$	$e26; e60; e140; e300$	$e26; e60; e140; e300$	$e26; e60; e140; e300$
dimuon	$2\mu10; \mu18_{-\mu8}$	$2\mu10; 2\mu14; \mu22_{-\mu8}$	$2\mu14; \mu22_{-\mu8}$	$2\mu14; \mu22_{-\mu8}$
dielectron	$2e12$	$2e15; 2e17$	$2e17; 2e24$	$2e17; 2e24$
electron-muon	$e24_{-\mu8}$	$e24_{-\mu8}; e26_{-\mu8}$ $e17_{-\mu14}; e7_{-\mu24}; 2e12_{-\mu10}; e12_{-\mu10}$	$e26_{-\mu8}$	$e26_{-\mu8}$
trimuon	$\mu18_{-2\mu4}$	$\mu11_{-2\mu4}; \mu6_{-2\mu4}; \mu20_{-2\mu4}; 3\mu4$ $3\mu6$	$4\mu4; \mu20_{-2\mu4}; 3\mu4$	$\mu20_{-2\mu4}$
trilepton	$e17_{-2e9}$	$e17_{-2e9}; e17_{-2e10}$	$e24_{-2e12}$	$e24_{-2e12}$

The $\ell\ell\ell'\ell'$ quadruplets are formed by two opposite-sign, same-flavour (OSSF) lepton pairs ($\ell^+\ell^-$). The p_T threshold of first three leading leptons are required to be 20, 15 and 10 GeV. If there are more than one combination of lepton pairing in quadruplet, the pairing is selected by keeping it with the mass of lepton pairs closest (leading pair, refers as m_{12}) and second closest (sub-leading pair, refers as m_{34}) to Z boson mass. The mass of leading pair is required to satisfy $50 < m_{12} < 106$ GeV, while the sub-leading pair is required to be less than 115 GeV and larger than 50 GeV.

The two lepton pairs in quadruplet are required to have angular separation with $\Delta R > 0.1$. To suppress the contribution from $J/\psi \rightarrow \ell\ell$ decays, for 4μ and $4e$ quadruplets, the events are rejected if any OSSF lepton pair is found with mass below 5 GeV. If there are more than one quadruplets from different channels in event at this point, the one with highest expected signal rate is selected in the order of $4\mu, 2e2\mu, 4e$. The transverse impact-parameter significance ($|d_0|/\sigma_{d_0}$) for muons (electrons) is then required to be smaller than

3 (5) to suppress the backgrounds from heavy-flavour hadrons.

In addition, the track- and calorimeter- based isolation criteria is required for all electrons and muons to further suppress the reducible backgrounds of $Z+jets$ and $t\bar{t}$. For lepton isolation selection, the two track- and calorimeter- based variables, $E_T^{topocone}$ and $p_T^{varcone}$ as described in section 4.2.4 (section 4.2.3) for muons (electrons), are vulnerable to pileup. For track-based variable, this is because of additional tracks in the event. The definition of $p_T^{varcone}$ attempts to limit the tracks used in the calculation to those from the vertex via a loose cut of $|z_0 \sin(\theta)| < 3$, which proved to be too loose in new pile-up regime in 2017 and 2018 datasets. So new track-based variable is used, by adding a requirement that the track be used in determining the vertex, or that, if not, it both passes the cut on $|z_0 \sin(\theta)|$ and is not used in determining any other vertex, which makes the track-based variable to be more isolation-robust in the high pile-up regime. The new variable is named as $ptvarcone[\text{cone}]_{_}\text{TightTTVA}_{_}pt[p_T \text{ cut}]$, where [cone] is the cone size and [p_T cut] is the cutoff for including tracks in the calculation.

For calorimeter-based variable, the calculation of $E_T^{topocone}$ corrects the pile-up effects by subtracting an average pileup contribution computed over the whole detector. But with the increasing of energy density of pile-up events, the root mean square (RMS) of $E_T^{topocone}$ variable increases, which leads to the increment of possibility that the pile-up fluctuations are not be accounted for correctly. One possible solution is using particle-flow (PFlow) method to calculate the calorimeter isolation. As part of PFlow reconstruction process, it assigns the clusters to tracks which improves the track-cluster association for better determination of the raw value of the E_T in the cone. And using PFlow jets to calculate the pileup correction provides a further improvement. So a resulting variable named $neflow-isol[\text{cone}]$ is used. Finally, a requirement of isolation, called *FixedCutPFlowLoose*, which gives better performance in high pile-up condition is applied to electrons and muons as:

$$(\max(ptcone20_{_}\text{TightTTVA}_{_}pt500, ptvarcone30_{_}\text{TightTTVA}_{_}pt500) + 0.4 \times neflow-isol20) / p_T < 0.16$$

On the top of impact parameter cut and lepton isolation cut, the four-lepton candidates are also required to originate from a common vertex to reduce $Z+jets$ and $t\bar{t}$ backgrounds. This is ensured by applying a vertex fit χ^2 cut of 4 ID tracks of lepton candidates satisfying $\chi^2/N_{dof} < 6$ (9) for events in 4μ ($4e$ and $2e2\mu$) channel(s).

To improve the mass resolution, the QED process of final state radiation (FSR) photons in Z boson decays are taken into account in the reconstruction of Z bosons. The four-momentum of any reconstructed photon that is consistent with having been radiated from lepton(s) in leading pair are added into final state. Moreover, the four-momenta of

leptons in both (leading and sub-leading) pairs are recomputed by performing a Z -mass-constrained kinematic fit, which uses a Breit Wigner Z boson line-shape and Gaussian function with width set to the expected lepton resolution per lepton to model the momentum response function. The Z -mass-constrained mass improves the $m_{4\ell}$ resolution by up to 15% depending on m_H .

In summary, table 7.3 lists a comprehensive object and event level selection as described above.

7.3.3 Event categorizations

To improve the sensitivity of search in both VBF and ggF production mode in NWA model, events are classified into the VBF- and ggF- enriched categories. With the statistic increasing in full run-2 data, a multivariate (MVA) based classifier has been studied for NWA signal, while in the meantime the traditional cut-based classifier is also used as a model-independent result for all three (NWA, LWA, graviton) models.

1. Cut-based categorization

There are four categories in total: one VBF-enriched category and three ggF-enriched categories. The categorization is defined based on kinematic cuts:

- VBF-CBA-enriched category: Events have at least two selected jets as defined in section 7.3.1, with the two leading jets being separated by $|\Delta\eta_{jj}| > 3.3$ and invariant mass satisfying $m_{jj} > 400$ GeV;
- ggF-CBA-enriched categories: The remaining events that are not classified into VBF-enriched category. Then events are categorized into three channels based on lepton-flavor, namely ggF_2e2μ, ggF_4e and ggF_4μ.

where ‘CBA’ stands for the cut-based categorization.

2. MVA-based categorization

In order to target different production modes, two types of classifiers, one dedicate to VBF production while the other one for ggF, have been trained using deep neural network technique. Details of two classifiers are described as below:

DNN models

Figure 7.1 shows the architecture of VBF (left) and ggF (right) network. The network structure was chosen based on its AUC^[11] value from evaluation samples. The VBF network includes three parts: two recurrent neural networks (RNNs) and one multilayer perceptron (MLP). The ggF network consists of one RNN and one MLP.

For training, the VBF and ggF signal samples at the masses of 200, 300, 400, 500, 600, 700, 800, 900, 1000, 1200, 1400 GeV are used with positive label. The VBF (ggF) signals

Table 7.3 Summary of the object and event selection requirements.

Physics Objects	
Electrons	
Loose Likelihood quality electrons with hit in innermost layer, $E_T > 7$ GeV and $ \eta < 2.47$	
Interaction point constraint: $ z_0 \cdot \sin \theta < 0.5$ mm	
Muons	
Loose identification with $p_T > 5$ GeV and $ \eta < 2.7$	
Calo-tagged muons with $p_T > 15$ GeV and $ \eta < 0.1$, segment-tagged muons with $ \eta < 0.1$	
Stand-alone and silicon-associated forward restricted to the $2.5 < \eta < 2.7$ region	
Combined, stand-alone (with ID hits if available) and segment-tagged muons with $p_T > 5$ GeV	
Interaction point constraint: $ d_0 < 1$ mm and $ z_0 \cdot \sin \theta < 0.5$ mm (if ID track is available)	
Jets	
anti- k_T jets with <i>bad-loose</i> identification, $p_T > 30$ GeV and $ \eta < 4.5$	
Overlap removal	
Jets within $\Delta R < 0.2$ of an electron or $\Delta R < 0.1$ of a muon are removed	
Vertex	
At least one collision vertex with at least two associated track	
Primary vertex	
Vertex with the largest p_T^2 sum	
Event Selection	
Quadruplet Selection	<ul style="list-style-type: none"> - Require at least one quadruplet of leptons consisting of two pairs of same-flavour opposite-charge leptons fulfilling the following requirements: - p_T thresholds for three leading leptons in the quadruplet: 20, 15 and 10 GeV - Maximum one calo-tagged or stand-alone muon or silicon-associated forward per quadruplet - Leading di-lepton mass requirement: $50 < m_{12} < 106$ GeV - Sub-leading di-lepton mass requirement: $50 < m_{34} < 115$ GeV - $\Delta R(\ell, \ell') > 0.10$ for all leptons in the quadruplet - Remove quadruplet if alternative same-flavour opposite-charge di-lepton gives $m_{\ell\ell} < 5$ GeV - Keep all quadruplets passing the above selection
Isolation	<ul style="list-style-type: none"> - Contribution from the other leptons of the quadruplet is subtracted - FixedCutPFlowLoose WP for all leptons
Impact Parameter	<ul style="list-style-type: none"> - Apply impact parameter significance cut to all leptons of the quadruplet
Significance	<ul style="list-style-type: none"> - For electrons: $d_0/\sigma_{d_0} < 5$ - For muons: $d_0/\sigma_{d_0} < 3$
Best Quadruplet	<ul style="list-style-type: none"> - If more than one quadruplet has been selected, choose the quadruplet with highest Higgs decay ME according to channel: 4μ, $2e2\mu$, $2\mu2e$ and $4e$
Vertex Selection	<ul style="list-style-type: none"> - Require a common vertex for the leptons: - $\chi^2/\text{ndof} < 5$ for 4μ and < 9 for others decay channels

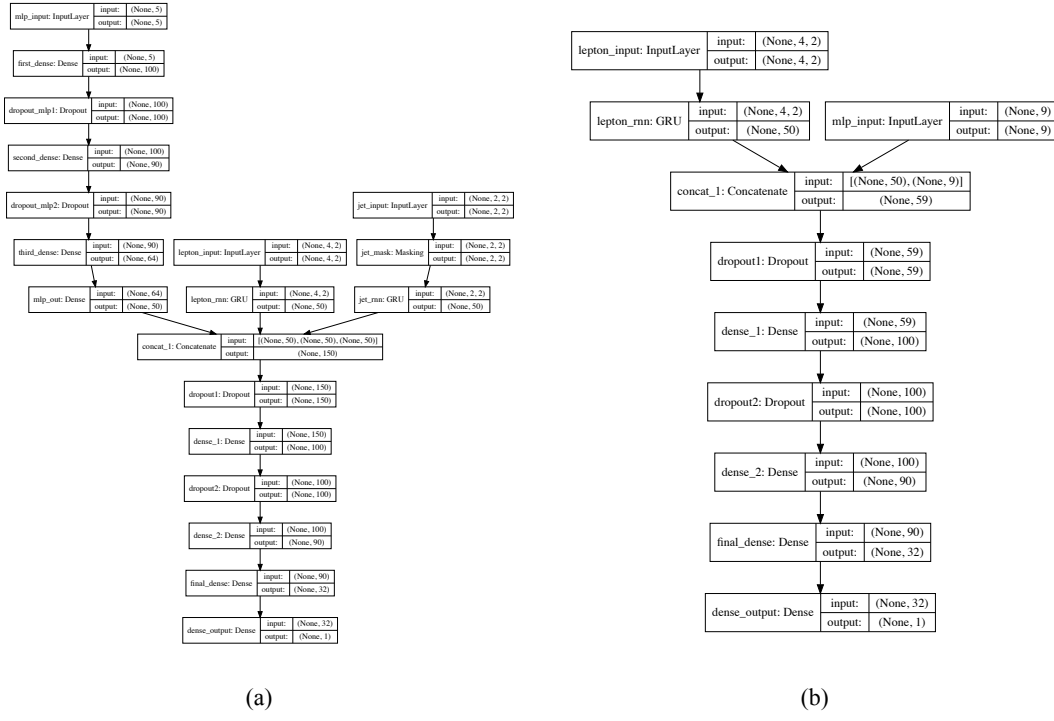


Fig. 7.1 (a) VBF DNN architecture diagram. (b) ggF DNN architecture.

are only used for VBF (ggF) classifier. The background including simulated samples of QCD and EW $q\bar{q} \rightarrow ZZ$ processes as well as $gg \rightarrow ZZ$ process summed according to their cross section are assigned with negative labels. In addition to the selections described in section 7.3.2, the events used for VBF network are required to have $N_{\text{jets}} \geq 2$, while $N_{\text{jets}} < 2$ is required for events in ggF network, so the training events for two network are independent.

In order to assign equivalent importance to signals with different mass assumptions, during the training, signal events are reweighted to follow the $m_{4\ell}$ distribution from background (idea from Ref.^[112] with a modified reweighting procedure), as shown in figure 7.2 (figure 7.3) before and after reweighting for VBF (ggF) samples.

Input features

Table 7.4 (table 7.5) lists the input features used for VBF (ggF) network during the training. For VBF network, one RNN (the other one) takes the p_T and η of p_T -ordered four leptons (two leading jets) as input features, which intends to study the time relationship from particle decay between leptons (jets). For ggF network, the only one RNN model takes the p_T and η of p_T -ordered four leptons as inputs.

Evaluation of models

Figure 7.4 shows the output of “ggF-classifier” and “VBF-classifier” for data, SM backgrounds and an example signal at 600 GeV. The ggF and VBF signals cross section

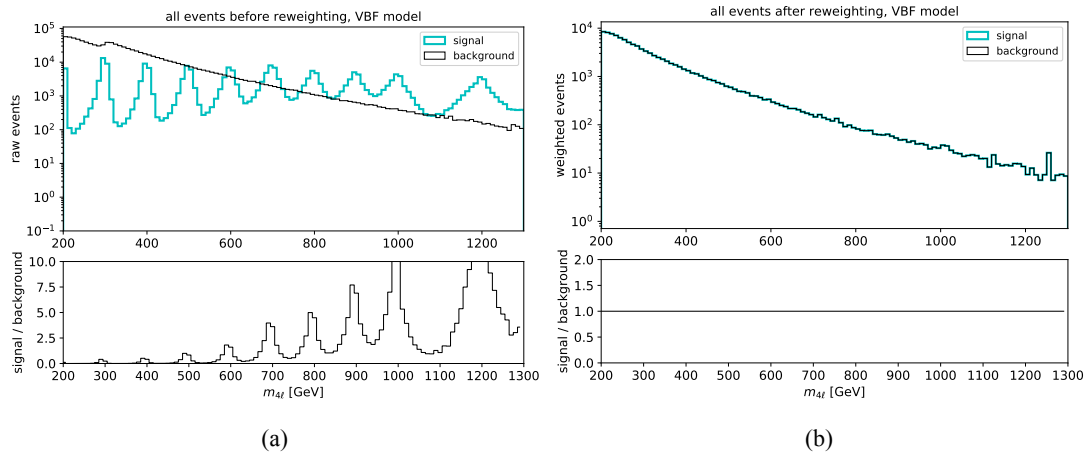


Fig. 7.2 (a) $m_{4\ell}$ distribution of raw (unweighted) training events for VBF signal (blue) and background (black); (b) $m_{4\ell}$ distribution of weighted VBF signal (blue) and background (black) used at training time.

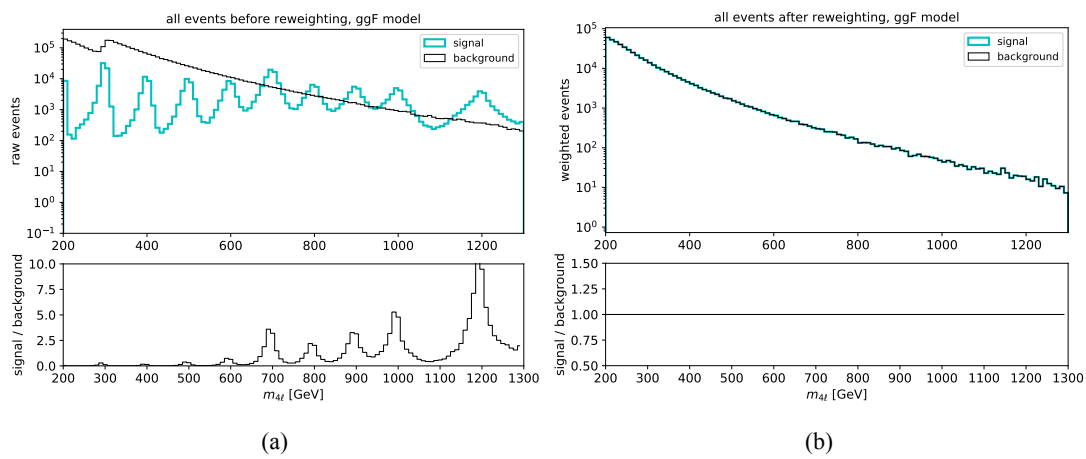


Fig. 7.3 (a) $m_{4\ell}$ distribution of raw (unweighted) training events for ggF signal (blue) and background (black); (b) $m_{4\ell}$ distribution of weighted ggF signal (blue) and background (black) used at training time.

Table 7.4 Input features used in the “VBF-classifier” for the $\ell\ell\ell'\ell'$ analysis. The RNN stands for the recurrent neural network and MLP for the multilayer perceptron.

Model	Inputs	Description
RNN	$p_T^{j0,j1}$	transverse momenta of the two leading jets
	$\eta^{j0,j1}$	pseudorapidity of the two leading jets
	$p_T^{\ell0,\ell1,\ell2,\ell3}$	transverse momenta of the four leptons
	$\eta^{\ell0,\ell1,\ell2,\ell3}$	pseudorapidity of the four leptons
MLP	$m_{4\ell}$	invariant mass of the four lepton system
	m_{jj}	invariant mass of the two leading jet system
	p_T^{jj}	transverse momentum of the two leading jet system
	$\Delta\eta_{H,j}$	difference in pseudorapidity between the four lepton system and the leading jet
	$\min\Delta R_{jZ}$	minimum distance between one of the two lepton pairs and a jet

are set to be 100 times of their observed upper limit described in section 7.7.3 for ggF output and 30 times of the observed upper limit for VBF output for best visibility.

Then the optimal cut at output score from each classifier is chosen based on an overall good performance of classifier to have a large significance improvement while retaining a high signal efficiency. Figure 7.5 shows the significance improvements of MVA-based cuts when comparing with cut-based one at different VBF (left) and ggF (right) mass samples, where the significance is calculated from an asymptotic approximation^[113]:

$$Z = \sqrt{2 \left(n \ln \left[\frac{nb + \sigma_b^2}{b^2 + n\sigma_b^2} \right] - \frac{b^2}{\sigma_b^2} \ln \left[1 + \frac{\sigma_b^2(n-b)}{b(b+\sigma_b^2)} \right] \right)} \quad (7.1)$$

where n denotes to the sum of expected signal and background, b is the background, and σ_b is the uncertainty of background. Cut at 0.5 (0.8) for VBF (ggF) classifier is chosen as shown in solid lines.

Then the events passing VBF classifier are categorized into VBF-MVA-enriched category. Otherwise, the events failing VBF classifier but passing ggF classifier are categorized into ggF-MVA-high category, which is further split into 3 channels based on their lepton flavor. All remaining events are sorted into one additional ggF-MVA-low category. Thus there are five categories defined in MVA-based categorization. In summary, cuts applied in categorization are defined as follow, and these different phase spaces are also illustrated in figure 7.6.

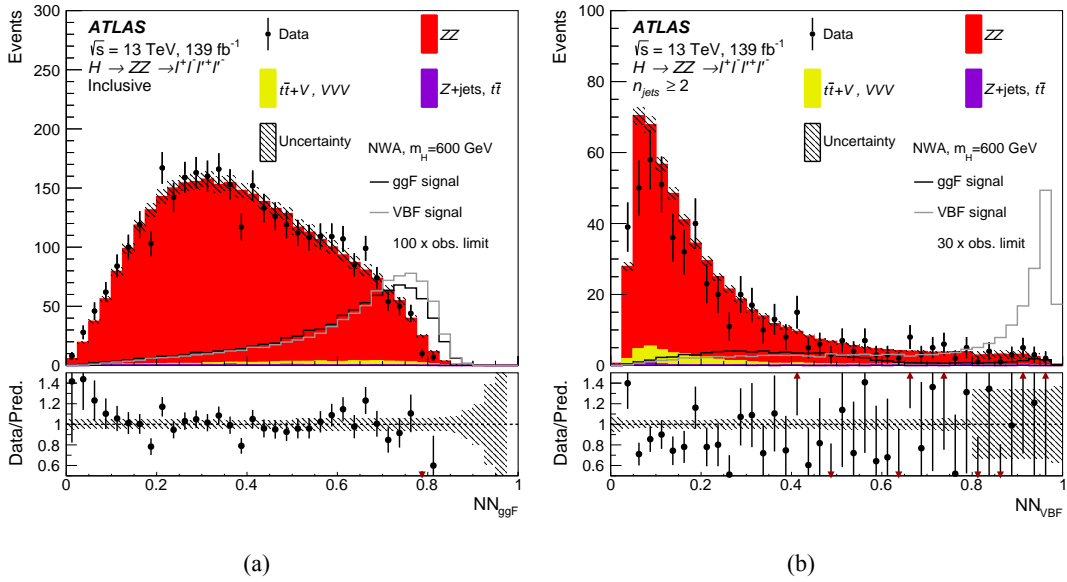


Fig. 7.4 The output score of “ggF-classifier” (a) and “VBF-classifier” (b) with the events passing the common event selections for the data, the SM backgrounds and an example of a NWA signal with a mass of 600 GeV. For the “VBF-classifier”, an additional requirement of at least two jets in the event is applied. The signals cross section are set to 100 times of the observed limit for the “ggF-classifier” and 30 times of the observed limit for the “VBF -classifier”. The ZZ backgrounds are scaled by the normalisation factors shown in Table 7.10. The lower panels show the ratio of data to prediction. Statistical and experimental systematic uncertainties are included.

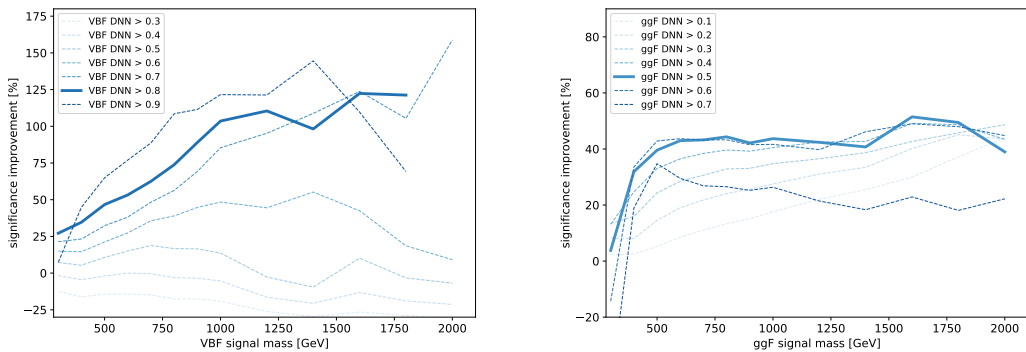


Fig. 7.5 Significance improvements of the MVA-based over the cut-based categorization of the VBF (ggF) category for VBF (ggF) signal samples from 300 to 2000 GeV for seven different cuts on the VBF (ggF) output score. The optimal cut of 0.8 (0.5) for VBF (ggF) score is chosen as the solid line, while other alternative cuts are plotted with dashed lines. For VBF category, results at 2000 GeV for cuts of 0.8 and 0.9 are missing due to a lack of background events passing this tight selection.

Table 7.5 Input features used in the “ggF-classifier” for the $\ell\ell\ell'\ell'$ analysis. The RNN stands for the recurrent neural network and MLP for the multilayer perceptron.

Model	Inputs	Description
RNN	$p_T^{\ell 0,\ell 1,\ell 2,\ell 3}$	transverse momenta of the four leptons
	$\eta^{\ell 0,\ell 1,\ell 2,\ell 3}$	pseudorapidity of the four leptons
MLP	$m_{4\ell}$	invariant mass of the four lepton system
	$p_T^{4\ell}$	transverse momentum of the four lepton system
	$\eta^{4\ell}$	pseudorapidity of the four lepton system
	$\cos \theta^*$	production angle of the leading Z defined in the four lepton rest frame
	$\cos \theta_1$	angle between the negative final state lepton and the direction of flight of leading Z in the Z rest frame
	$\cos \theta_2$	angle between the negative final state lepton and the direction of flight of sub-leading Z in the Z rest frame
	Φ	angle between the decay planes of the four final state leptons expressed in the four lepton rest frame
	p_T^{j0}	transverse momentum of the leading jet
	η^{j0}	pseudorapidity of the leading jet

- VBF-MVA-enriched category: Events have at least two selected jets ($N_{\text{jets}} \geq 2$), and with $\text{DNN}_{\text{VBF}} > 0.8$;
- ggF-MVA-high categories: $(N_{\text{jets}} \geq 2 \text{ \&& } \text{DNN}_{\text{VBF}} \leq 0.8 \text{ \&& } \text{DNN}_{\text{ggF}} > 0.5) \parallel (N_{\text{jets}} < 2 \text{ \&& } \text{DNN}_{\text{ggF}} > 0.5)$;
- ggF-MVA-low category: All remaining events that fail VBF and ggF cuts mentioned above.

7.3.4 Signal acceptance

The signal acceptance is defined as the ratio of events passing all analysis selection in each category to the total number of simulated events in whole phase space. In denominator, the events with τ final states are not taken into account. And the contribution of τ -lepton decay to electrons and muons final states is found to be negligible.

Figure 7.7 and 7.8 show the acceptance of NWA signals in DNN- and Cut- based categorization, estimated by merging the three signal MC campaigns, mc16a, mc16d and mc16e. A 3-rd order polynomial fit is applied for each category.

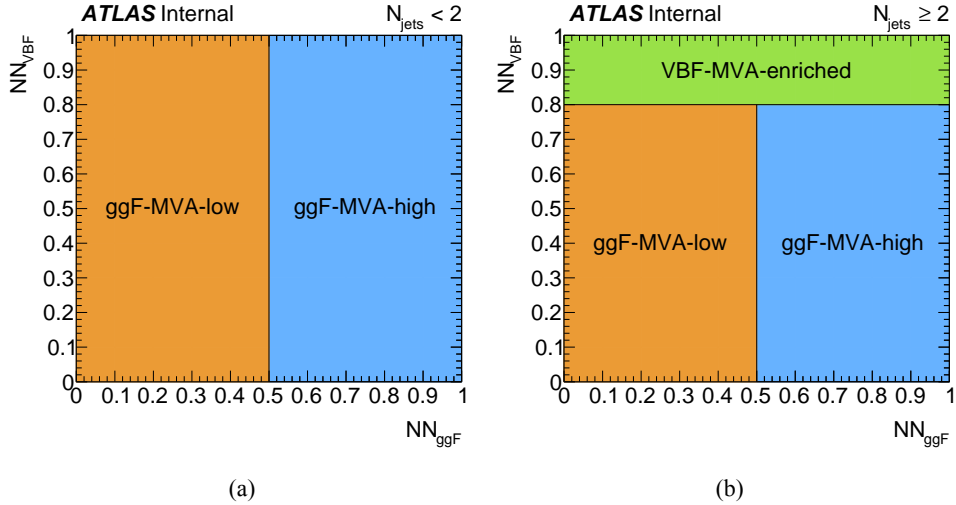


Fig. 7.6 Illustration of the MVA-based VBF and ggF event classification for events with (a) $N_{\text{jets}} < 2$ and (b) $N_{\text{jets}} \geq 2$.

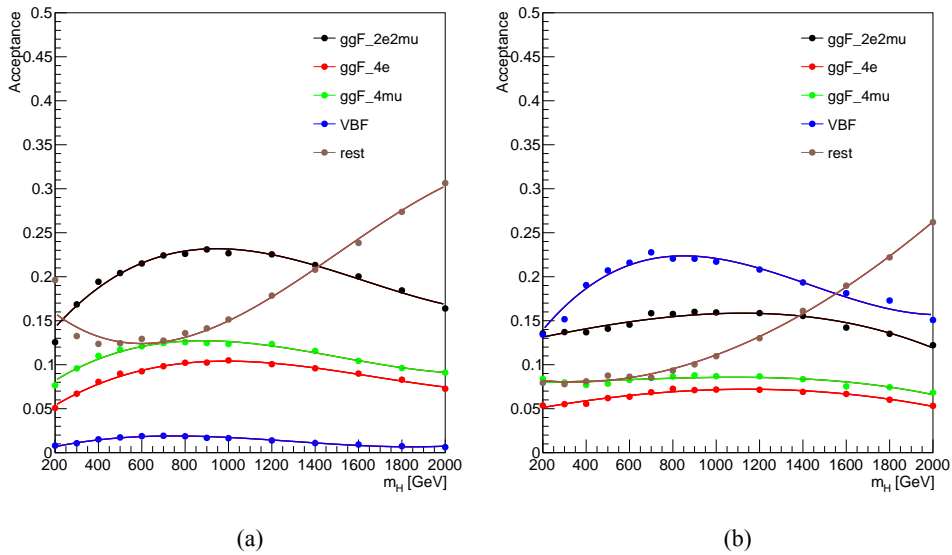


Fig. 7.7 NWA acceptance as a function of m_H for the MVA-based categorization for the samples of (a) ggF production; (b) VBF production.

7.4 Background estimation

In this analysis, 97% of total expected background events are from irreducible ZZ backgrounds, which includes about 86% quark-antiquark annihilation ($q\bar{q} \rightarrow ZZ$), 10% of gluon-induced production ($gg \rightarrow ZZ$) and around 1% of EW vector boson scattering ($q\bar{q} \rightarrow ZZ$ EW) contribution. For $q\bar{q} \rightarrow ZZ$ EW, although it has small contribution in total background events after analysis selection, it's important for VBF category with about 16% contribution.

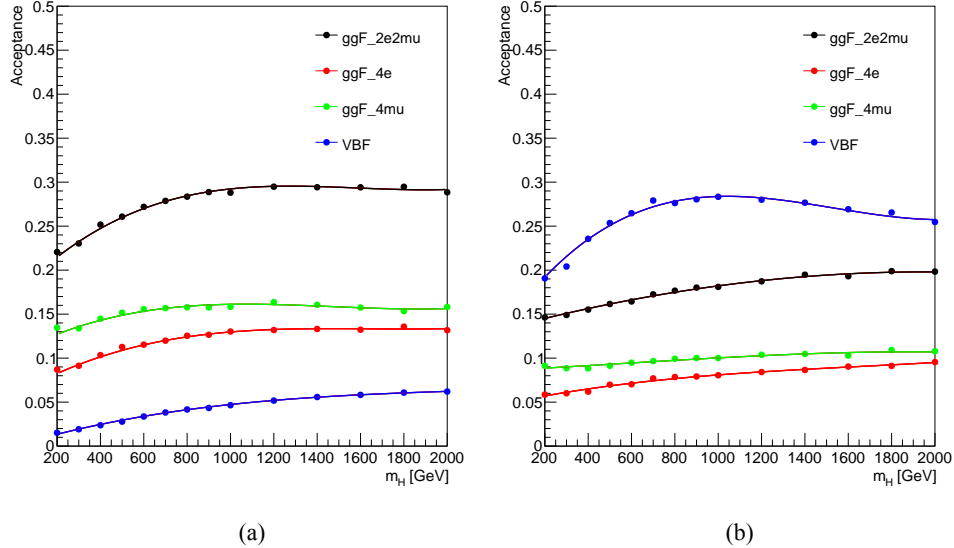


Fig. 7.8 NWA acceptance as a function of m_H for the Cut-based categorization for the samples of (a) ggF production mode; (b) VBF production mode.

In addition to irreducible backgrounds, events from $Z+jets$ and $t\bar{t}$ processes, represent as reducible backgrounds, contribute at a few percent level and can be measured using data driven method that will later be described briefly. Additional background called ‘Others’, including ttV and triple-V (VVV) processes, has tiny contribution and is estimated from MC simulation directly.

7.4.1 Irreducible backgrounds

The Irreducible backgrounds have events with four prompt leptons. The normalization of two dominant backgrounds $q\bar{q} \rightarrow ZZ$ and $gg \rightarrow ZZ$ are taken from data by statistical fit, and the normalization of small $q\bar{q} \rightarrow ZZ$ EW background is taken directly from MC simulation.

The $m_{4\ell}$ shapes of all three background components are taken from MC samples and then parameterized by an empirical function for each of them in each category respectively. Details of background modellings are illustrated as below:

The empirical function used for background parameterization is:

$$f(m_{4\ell}) = C_0 H(m_0 - m_{4\ell}) f_1(m_{4\ell}) + H(m_{4\ell} - m_0) f_2(m_{4\ell}), \quad (7.2)$$

where,

$$f_1(x) = \left(\frac{x - a_4}{a_3} \right)^{a_1-1} \left(1 + \frac{x - a_4}{a_3} \right)^{-a_1-a_2},$$

$$f_2(x) = \exp \left[b_0 \left(\frac{x - b_4}{b_3} \right)^{b_1-1} \left(1 + \frac{x - b_4}{b_3} \right)^{-b_1-b_2} \right],$$

$$C_0 = \frac{f_2(m_0)}{f_1(m_0)}.$$

The function consists of two parts, the first part f_1 describes the $m_{4\ell}$ spectrum in low mass region where both Z bosons decay on-shell, while the second one f_2 covers distribution at high mass tail. The transition between the low- and high- mass parts is presented in function 7.2 by the Heaviside step function $H(x)$ at the transition point m_0 . The m_0 is chosen to optimize the smoothness of the function, and practically $m_0 = 260$ (350) GeV is used for $q\bar{q} \rightarrow ZZ$ ($gg \rightarrow ZZ$ and $q\bar{q} \rightarrow ZZ$ EW). Besides, the continuity of two functions at m_0 is ensured by the factor C_0 applied to f_1 . The coefficients a_i in f_1 and b_i in f_2 are shape parameters obtained by fitting to $m_{4\ell}$ distribution from each MC simulated sample.

Figure 7.9 to 7.11 shows the fitting results of $q\bar{q} \rightarrow ZZ$, $gg \rightarrow ZZ$, $q\bar{q} \rightarrow ZZ$ EW backgrounds in four cut-based categories (ggF-CBA-enriched- $2e2\mu$, ggF-CBA-enriched- $4e$, ggF-CBA-enriched- 4μ and VBF-CBA-enriched). Figure 7.12 to 7.14 shows the fitting results of those backgrounds in five MVA-based categories (ggF-MVA-high- $2e2\mu$, ggF-MVA-high- $4e$, ggF-MVA-high- 4μ , ggF-MVA-low and VBF-MVA-enriched).

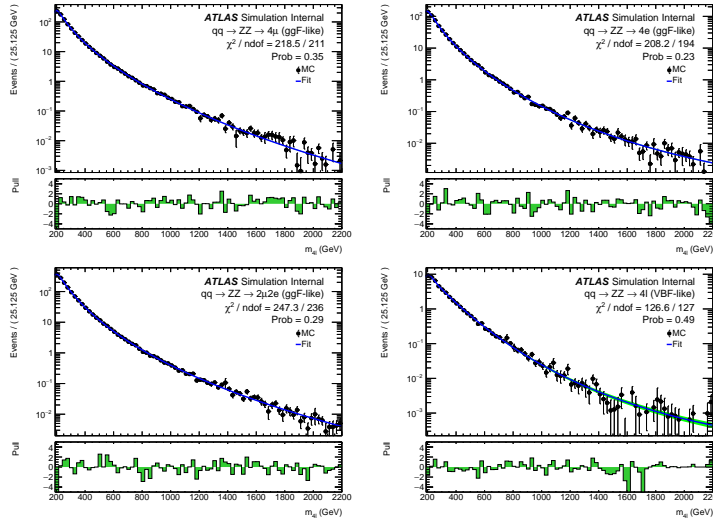


Fig. 7.9 Distributions of the $m_{4\ell}$ invariant mass fit projections of the $q\bar{q} \rightarrow ZZ$ background samples for the 4μ , $4e$ and $2\mu2e$ final states in the ggF-CBA-enriched category, and the 4ℓ inclusive VBF-CBA-enriched category. Cut-based categorization is used.

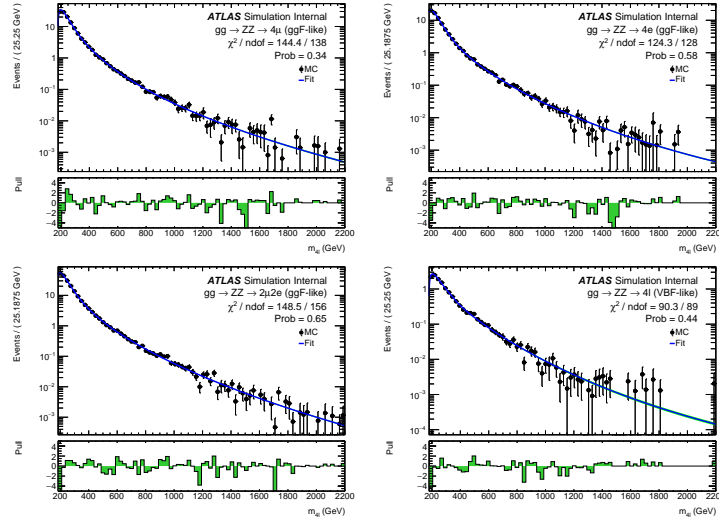


Fig. 7.10 Distributions of the $m_{4\ell}$ invariant mass fit projections of the $gg \rightarrow ZZ$ background samples for the 4μ , $4e$ and $2\mu2e$ final states in the ggF-CBA-enriched category, and the 4ℓ inclusive VBF-CBA-enriched category. Cut-based categorization is used.

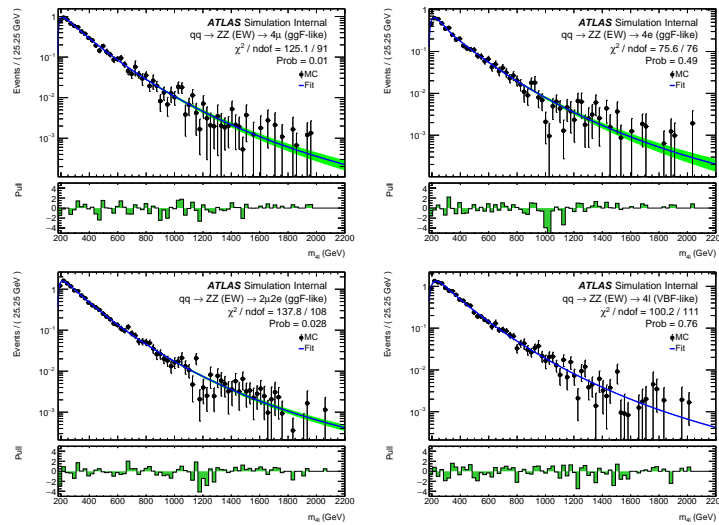


Fig. 7.11 Distributions of the $m_{4\ell}$ invariant mass fit projections of the $q\bar{q} \rightarrow ZZ$ (EW) background samples for the 4μ , $4e$ and $2\mu2e$ final states in the ggF-CBA-enriched category, and the 4ℓ inclusive VBF-CBA-enriched category. Cut-based categorization is used.

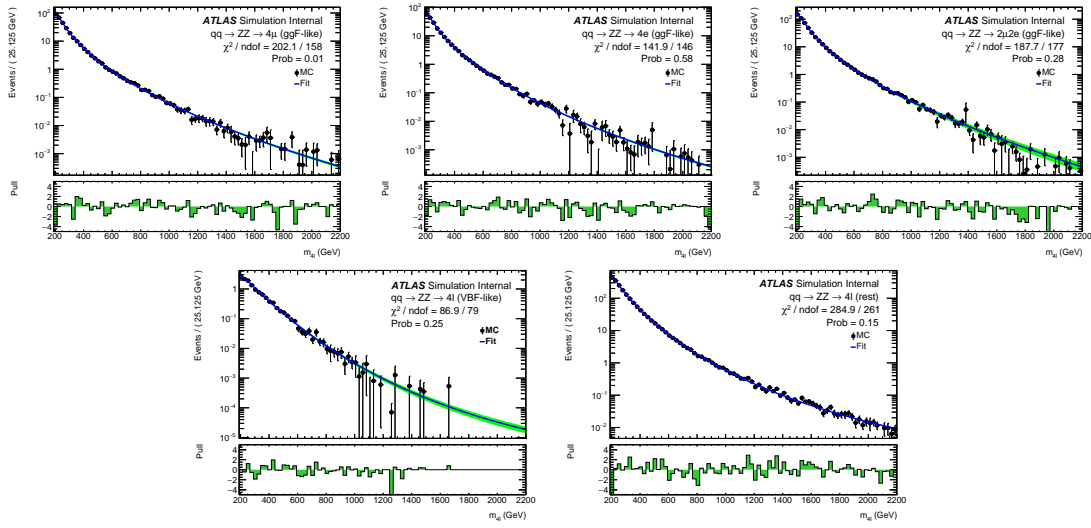


Fig. 7.12 Distributions of the $m_{4\ell}$ invariant mass fit projections of the $q\bar{q} \rightarrow ZZ$ background samples for the 4μ , $4e$ and $2\mu2e$ final states in the ggF-MVA-high category, the 4ℓ inclusive ggF-MVA-low category and VBF-MVA-enriched category. DNN-based categorization is used.

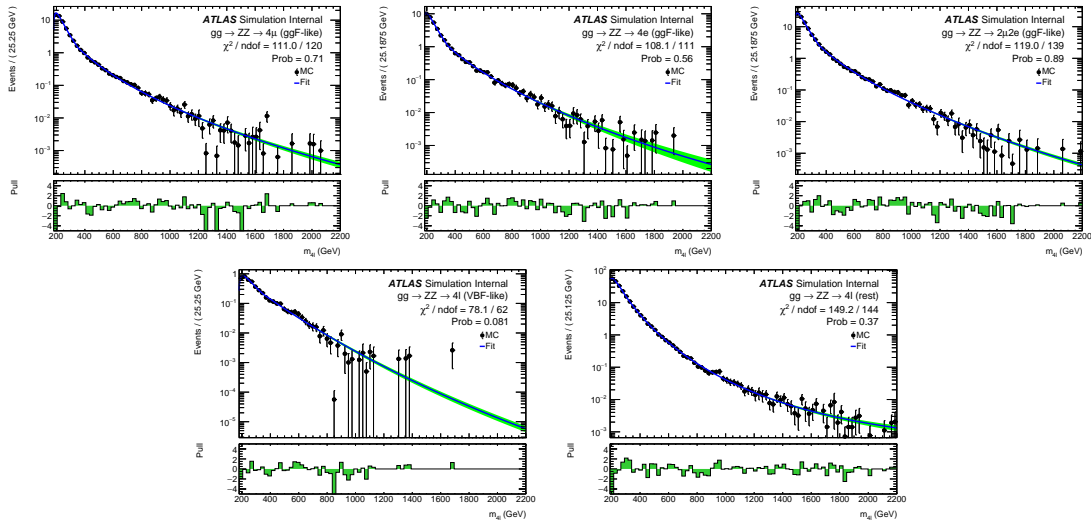


Fig. 7.13 Distributions of the $m_{4\ell}$ invariant mass fit projections of the $gg \rightarrow ZZ$ background samples for the 4μ , $4e$ and $2\mu2e$ final states in the ggF-MVA-high category, the 4ℓ inclusive ggF-MVA-low category and VBF-MVA-enriched category. DNN-based categorization is used.

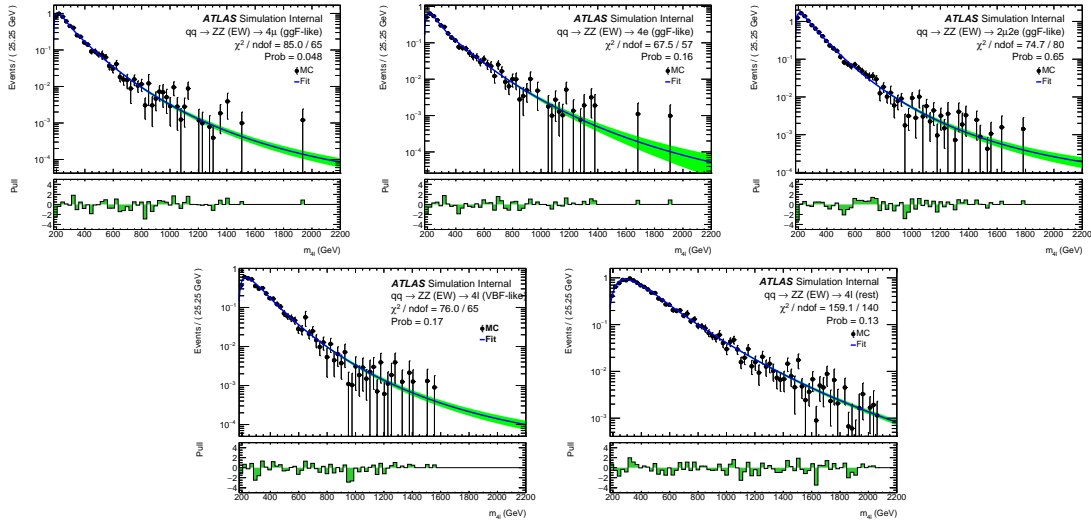


Fig. 7.14 Distributions of the $m_{4\ell}$ invariant mass fit projections of the $q\bar{q} \rightarrow ZZ$ (EW) background samples for the 4μ , $4e$ and $2\mu2e$ final states in the ggF-MVA-high category, the 4ℓ inclusive ggF-MVA-low category and VBF-MVA-enriched category. DNN-based categorization is used.

7.4.2 Reducible backgrounds

Similar to section 6.4, the reducible backgrounds include $Z+jets$ (consisting of both heavy- and light-flavour jets), top quark pair, and WZ production, which contain fake and non-isolated leptons. The simulations are not very robust in terms of the selection efficiencies. Thus, the data-driven method is applied to estimate the normalization of those processes in different control regions (CRs). The estimations in this analysis are performed separately for $\ell\ell + \mu\mu$ and $\ell\ell + ee$ final states, with slightly different approaches for “muon” and “electron” backgrounds.

The “electron” backgrounds mostly come from process of a Z boson with light-flavour jets ($Z+LF$) misidentified as electrons. The large contribution of “muon” backgrounds come from heavy-flavour jets produced in association with a Z boson ($Z+HF$) or in the decays of top quark. The estimations are done following the common H4l studies without a specific $m_{4\ell}$ range requirement^[114], and then the corresponding fraction of event yield in $m_{4\ell} > 200$ GeV is calculated from MC simulation.

$\ell\ell + \mu\mu$ final states

The normalizations of “muon” backgrounds are extracted from simultaneous fits of the leading lepton pair’s invariant mass (m_{12}) in four orthogonal CRs:

- **Inverted d_0 CR:** this CR is formed by inverting the d_0 selection for at least one lepton in subleading lepton pair while the leptons in leading pair are required to pass all standard selection. This CR enhances $Z+HF$ and $t\bar{t}$ as leptons from heavy-

flavour hadronic decays are characterised by large d_0 .

- **$e\mu + \mu\mu$ CR:** this CR is formed using an opposite-sign different-flavour dilepton in leading pair. It aims to enhance $t\bar{t}$ background as the leading lepton pair cannot come from Z boson decay.
- **Inverted isolation CR:** in this CR, leptons in leading pair are required to satisfy all standard analysis selection, but for leptons in subleading pair, they are required to pass d_0 selection but have at least one of them failing isolation selection. This CR enhances the events from $Z+LF$ processes while suppress $Z+HF$ by d_0 cut.
- **Same-sign CR:** in this CR, the leptons in subleading pair are required to have same-charge, while the leading pair still passes standard selection. This CR is not dominant by any specific background since all reducible backgrounds could have sizable contribution to it.

The fit results of normalizations are then propagated to signal region (SR) by applying transfer factors to account for the difference of selection efficiencies between SR and CRs. The transfer factors are computed using $Z + \mu$ MC samples.

$\ell\ell + ee$ final states

The “electron” backgrounds are estimated in $3\ell + X$ CR, where X denotes the lower p_T electron in the subleading pair. The selection and identification criterias for X are relaxed , while other three leptons must satisfy the standard selection. In this case, X could be a light-flavour jet, a photon conversion or an electron from heavy-flavour hadron decay. Moreover, the subleading pair is required to have same charge dilepton to ensure the orthogonality to the signal region. The normalization of backgrounds are obtained based on a fit to the number of hits in the innermost ID layer in CR, and the transfer factors are computed from $Z + e$ simulated sample.

The $m_{4\ell}$ shapes of reducible backgrounds are obtained from MC simulation in signal region, and then smoothed by an one-dimensional kernel estimation, which models the input data as a superposition of Gaussian kernels, one for each data point with contributing $1/N$ to total integral N ^[115]. The difference from using different smoothing strength (ρ) in kernel estimation is taken into account as additional shape uncertainties for these reducible backgrounds.

7.5 Signal modelling

The parameterization of $m_{4\ell}$ distributions based on simulated samples for signals are described in this section. Several signal models are studied, including heavy Higgs like

narrow-width signal (NWA) and large-width signal (LWA), as well as the modelling of Randall-Sundrum graviton (RSG) signal.

7.5.1 Modelling of narrow-width signal

For narrow-width (NWA) signal, the $m_{4\ell}$ width is totally determined by detector resolution, which is modelled by the sum of a Crystal Ball (C) function^[116-117] and a Gaussian (G) function:

$$P_s(m_{4\ell}) = f_C \cdot C(m_{4\ell}; \mu, \sigma_C, \alpha_C, n_C) + (1 - f_C) \cdot G(m_{4\ell}; \mu, \sigma_G) \quad (7.3)$$

The two functions share the same central value μ , while the resolution parameters, σ_C and σ_G , are different. In the Crystal Ball function, the parameters α_C and n_C model the shape of non-Gaussian tail, and the fraction parameter f_C is used to ensure the relative normalization between two functions.

The parameters are obtained by fitting to signal MC simulations combining the mc16a, mc16d and mc16e campaigns for each category at each mass points from 200 GeV to 2000 GeV respectively, and the shape of ggF and VBF signals are found to be similar. Figure 7.15 shows the $m_{4\ell}$ distribution and fitted curves for ggF production at mass from 200 GeV to 2000 GeV in $2e2\mu$ channel as examples.

Then the $C + G$ parameters are fitted with a polynomial function as the function of generated mass points (m_H), as an example shown in figure 7.16 for ggF production in $2e2\mu$ channel. The fitting quality can be measured by the Pearson's χ^2 , which is within 3 (2) for $2e2\mu$ ($4e$ and 4μ) channel.

In addition, possible difference on the signal yield extracted from parameterization and MC simulation is studied. Figure 7.17 shows this difference by computing $\frac{N_{\text{reco}} - N_{\text{fit}}}{N_{\text{fit}}}$, where N_{reco} denotes the total number of reconstructed events observed from MC simulation at that mass point and N_{fit} depicts the number of events obtained from the fitted pdf. The differences are treated as an additional systematic uncertainty with the value of 2% (1%) for $2e2\mu$ ($4e$ and 4μ) channel in statistical fit.

In summary, the final interpolated signal shapes for the ggF production mode are shown together in figure 7.18 for mass points with step of 100 GeV from 200 GeV to 3000 GeV.

7.5.2 Modelling of large-width signal

The $m_{4\ell}$ shape of heavy Higgs model in large-width (LWA) hypothesis can be described by a convolution of a truth distribution and a resolution from detector effect. The

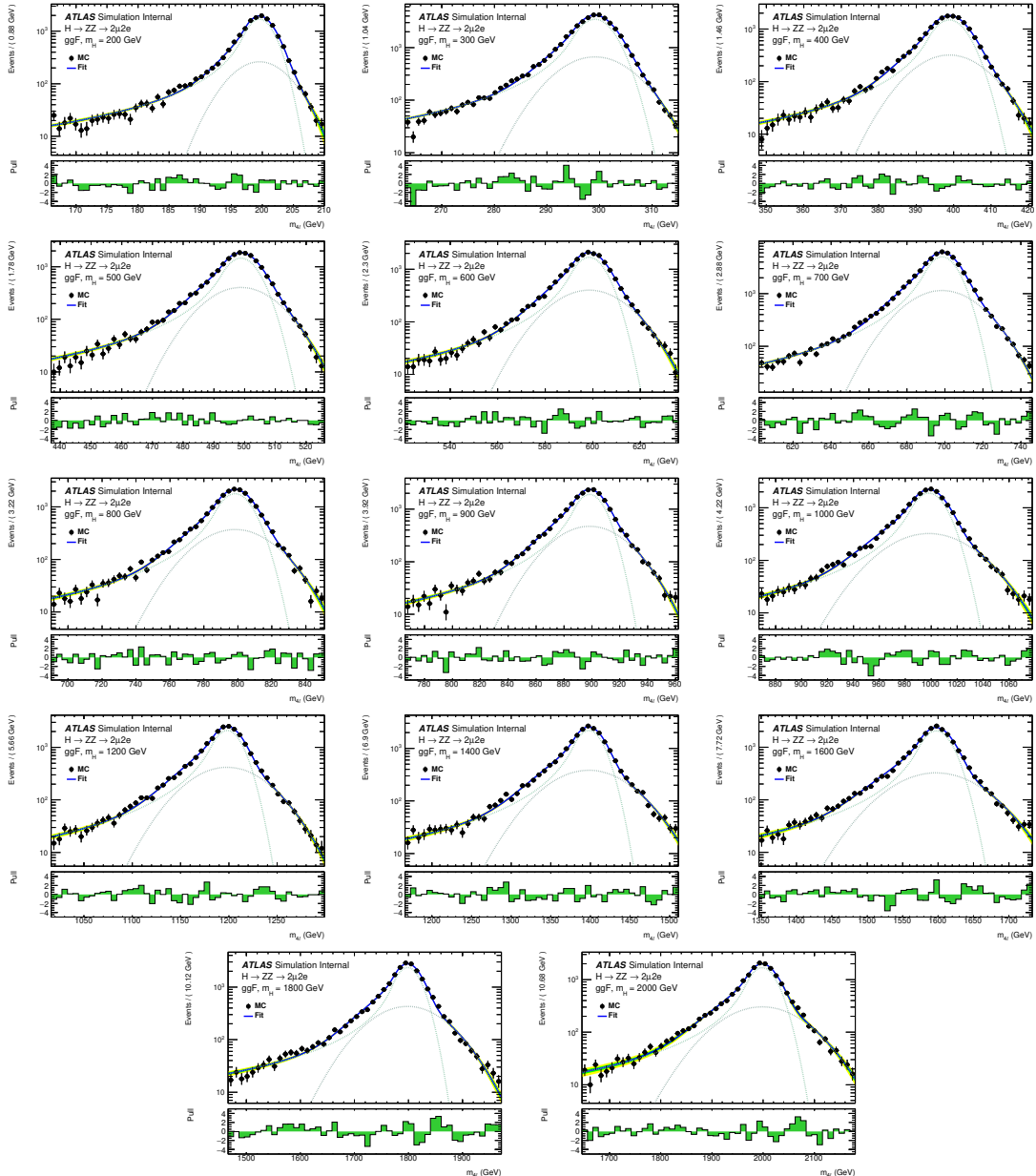


Fig. 7.15 Distributions of the $m_{2\mu 2e}$ and fit projection for signal samples between 200 to 3000 GeV for ggF production mode. Three MC campaigns, mc16a, mc16d and mc16e, are combined. The lower panel in each plot shows the pull distribution.

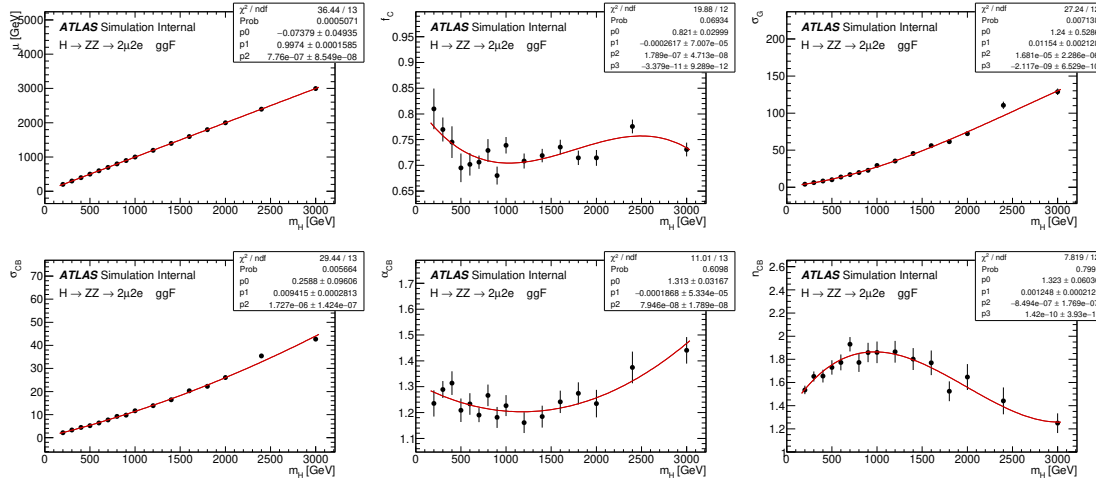


Fig. 7.16 Polynomial fits of the parameters μ , f_C , σ_G , σ_C , n_c and α_C for the signal $\mathcal{C} + \mathcal{G}$ model in the $2\mu 2e$ channel as a function of m_H for the ggF production mode. The combination of the mc16a, mc16d and mc16e MC campaigns is used.

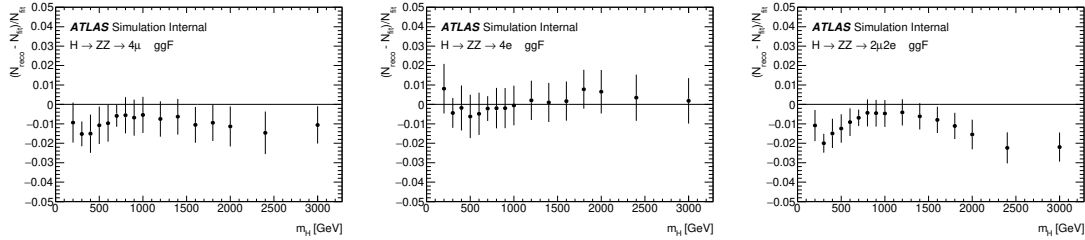


Fig. 7.17 The difference between MC simulation and parameterization of 4μ (left), $4e$ (middle) and $2\mu 2e$ (right) for the ggF production mode. The combination of the mc16a, mc16d and mc16e MC campaigns is used.

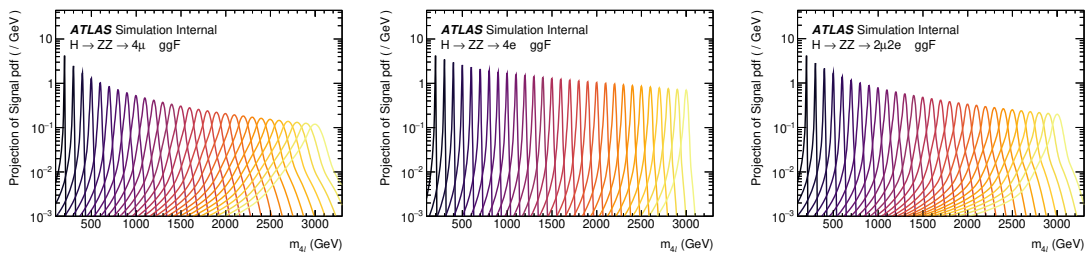


Fig. 7.18 The final signal shapes for the ggF production mode, interpolated from the polynomial fit parameters.

detector resolution effect is the one modelled by the function described in NWA parameterization, as in NWA model the truth level width is negligible.

The differential parton cross section for the heavy Higgs model can be written as^[118]:

$$\sigma_{gg \rightarrow H \rightarrow ZZ}(s) = \frac{1}{2s} \int d\Omega |A_{gg \rightarrow H}(s, \Omega)|^2 \frac{1}{|s - s_H|^2} |A_{H \rightarrow ZZ}(s, \Omega)|^2 \quad (7.4)$$

where $A_{gg \rightarrow H}(s, \Omega)$ and $A_{H \rightarrow ZZ}(s, \Omega)$ are corresponding Higgs production and decay amplitudes, and $\frac{1}{|s - s_H|}$ denotes the Higgs propagator and Ω represents the phase space of the process.

Using the definition of a partial width,

$$\Gamma_{H \rightarrow F}(s) = \frac{1}{2\sqrt{s}} \int d\Omega |A_{H \rightarrow F}(s, \Omega)|^2 \quad (7.5)$$

the parton cross section can be rewritten as,

$$\sigma_{gg \rightarrow H \rightarrow ZZ}(s) = 2 \frac{1}{|s - s_H|^2} \times \Gamma_{H \rightarrow gg}(s) \times \Gamma_{H \rightarrow ZZ}(s) \quad (7.6)$$

with the components computed in Ref^[118-119]:

$$\begin{aligned} \frac{1}{s - s_H} &= \frac{1 + i \cdot \bar{\Gamma}_H / \bar{m}_H}{s - \bar{m}_H^2 + i \cdot s \cdot \bar{\Gamma}_H / \bar{m}_H} \\ \bar{m}_H &= \sqrt{\bar{\Gamma}_H^2 + m_H^2} \\ \bar{\Gamma}_H &= \bar{m}_H \cdot \frac{\Gamma_H}{m_H} \end{aligned} \quad (7.7)$$

$$\Gamma_{H \rightarrow ZZ}(s) = C \cdot s^{\frac{3}{2}} \cdot \left[1 - \frac{4m_Z^2}{s} + \frac{3}{4} \left(\frac{4m_Z^2}{s} \right)^2 \right] \cdot \left[1 - \frac{4m_Z^2}{s} \right]^{\frac{1}{2}} \quad (7.8)$$

$$\begin{aligned} \Gamma_{H \rightarrow gg}(s) &= C \cdot s^{\frac{3}{2}} \cdot |A_t(\tau_t)|^2 \\ A_t(\tau) &= 2 \frac{\tau + (\tau - 1)f(\tau)}{\tau^2} \\ \tau_t &= \frac{s}{4m_t^2} \end{aligned} \quad (7.9)$$

$$f(\tau) = \begin{cases} \arcsin^2(\sqrt{\tau}), & \tau \leq 1 \\ -\frac{1}{4} \left[\log \frac{1+\sqrt{1-\tau^{-1}}}{1-\sqrt{1-\tau^{-1}}} - i\pi \right]^2, & \tau > 1 \end{cases}$$

where m_f stands for the mass of a fermion f , and Γ_H denotes an assumed total width of the heavy Higgs boson.

At the LHC, the $m_{4\ell}$ line shape can be defined by a hadron cross section that is derived from equation 7.6 by multiplication with gluon-gluon luminosity \mathcal{L}_{gg} described in^[120]. Meanwhile, the cross section is rewritten as a function of $m_{4\ell}$ instead of s , which will give an extra power of mass dependence in the formula:

$$\sigma_{pp \rightarrow H \rightarrow ZZ}(m_{4\ell}) = 2 \cdot m_{4\ell} \cdot \mathcal{L}_{gg} \cdot \frac{1}{|s - s_H|^2} \cdot \Gamma_{H \rightarrow gg}(m_{4\ell}^2) \cdot \Gamma_{H \rightarrow ZZ}(m_{4\ell}^2) \quad (7.10)$$

The analytical shapes of truth level $m_{4\ell}$ distribution of gg2VV MC samples is shown on figure 7.19.

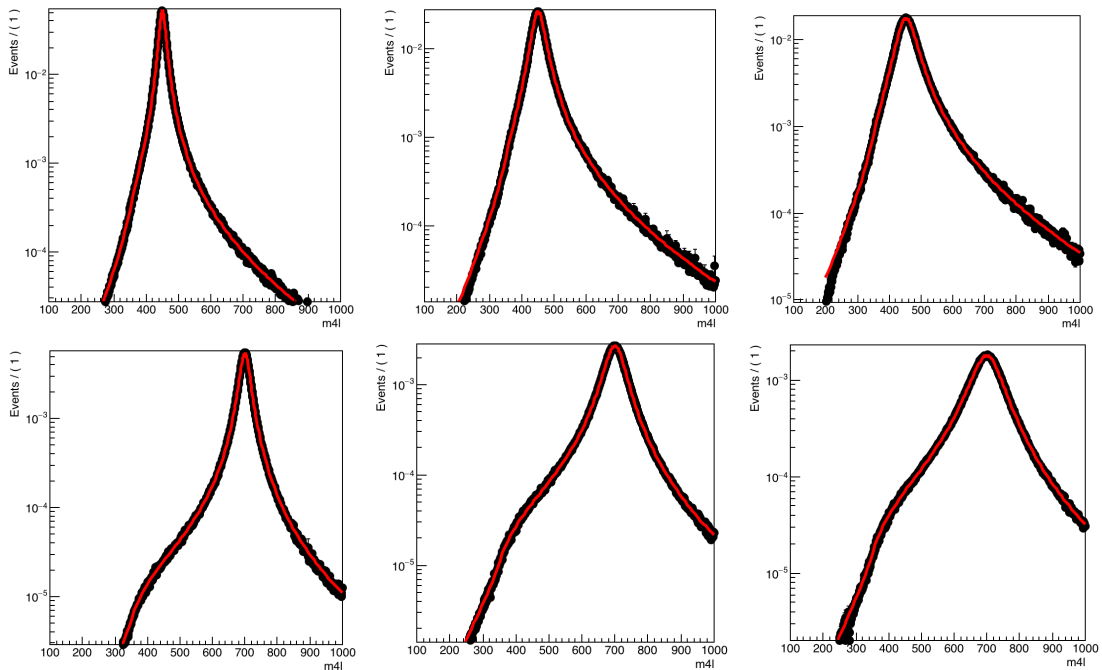


Fig. 7.19 Comparison of the analytical shape to a truth $m_{4\ell}$ distribution of gg2VV MC samples for $m_H = 450$ GeV (top), 700 GeV (bottom) and width equal to 5% (left), 10% (middle), 15% (right) of the mass.

The reconstruction level signal shape can then be modelled by the analytical truth shape convoluted with detector effects modelled in section 7.5.1. A comparison between the modelled shape and reconstruction level MC simulation for signal mass above 400 GeV (for ggF production in $2e2\mu$ channel as an example) are shown in figure 7.20, the shapes are well compatible between each other. This modelling is not valid for lower masses due to the rapid change of detector resolution.

7.5.3 Modelling of interference

There are three processes sharing the same gg initial state and ZZ final state:

- The SM $gg \rightarrow ZZ$ process with an amplitude A_B

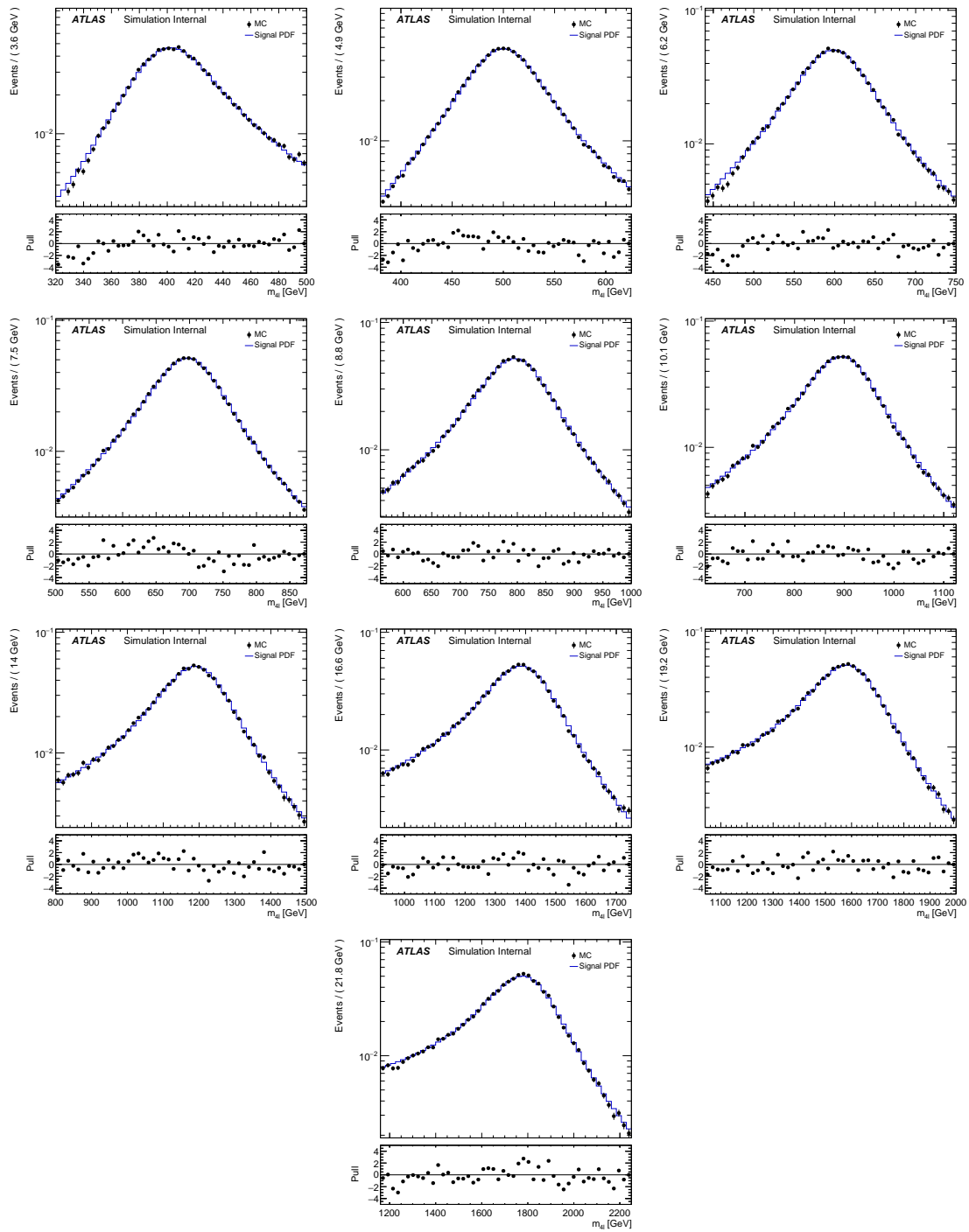


Fig. 7.20 Comparison between the analytical shape convoluted with detector effects and the reconstructed $m_{2\mu 2e}$ MC distribution for mass points ranging from 400 to 1800 GeV and width equal to 15% of the mass.

- The SM (light) Higgs at mass of around 125 GeV with an amplitude A_h
- The BSM heavy Higgs we are searching in this analysis with an amplitude A_H

The three processes can interfere with each other due to the same initial and final states.

The parton cross section for these processes can be written as:

$$\begin{aligned}\sigma_{gg \rightarrow (X) \rightarrow ZZ}(s) &= \frac{1}{2s} \int d\Omega |A_h(s, \Omega) + A_H(s, \Omega) + A_B(s, \Omega)|^2 \\ &= \frac{1}{2s} \int d\Omega (|A_h(s, \Omega)|^2 + |A_H(s, \Omega)|^2 + |A_B(s, \Omega)|^2) + \\ &\quad + \frac{1}{s} \int d\Omega (Re [A_h(s, \Omega) \cdot A_B^*(s, \Omega)] \\ &\quad + Re [A_H(s, \Omega) \cdot A_B^*(s, \Omega)] + Re [A_B(s, \Omega) \cdot A_h^*(s, \Omega)])\end{aligned}\quad (7.11)$$

The first term in equation 7.11 denotes the on-shell SM Higgs contribution, which is negligible in this analysis. The second term corresponds to the heavy Higgs contribution, whose line shape has been described in previous section. The third term is the $gg \rightarrow ZZ$ continuum process, while the forth term is the interference between SM Higgs and $gg \rightarrow ZZ$ continuum. The fifth and sixth terms are the interferences between heavy Higgs and $gg \rightarrow ZZ$ continuum (H-B), and between heavy Higgs and SM Higgs (H-h) that we are interested in. More details about the parameterization of these two interferences are described as below.

1. Interference between heavy Higgs and $gg \rightarrow ZZ$ continuum

The parton cross section of this interference term can be expressed as:

$$\sigma_{gg}(s) = \frac{1}{s} \text{Re} \left[\frac{1}{s - s_H} \int d\Omega \cdot A_H^P(s, \Omega) \cdot A_H^D(s, \Omega) \cdot A_B^*(s, \Omega) \right] \quad (7.12)$$

By assuming that this function has a smooth behaviour, it can be replaced with complex polynomial:

$$\int d\Omega \cdot A_H^P(s, \Omega) \cdot A_H^D(s, \Omega) \cdot A_B^*(s, \Omega) \approx (a_0 + a_1 \cdot \sqrt{s} + \dots) + i \cdot (b_0 + b_1 \cdot \sqrt{s} + \dots) \quad (7.13)$$

The parameters a_i and b_i can be extracted by fitting to the $m_{4\ell}$ distribution from truth level MC simulation after analysis selection. Since the signal mass and width does not enter into this function, the parameters should be independent for every tested signal hypothesis.

Same as description for equation 7.10, the parton cross section can be transformed into a hadron cross section as a function of $m_{4\ell}$:

$$\sigma_{pp}(m_{4\ell}) = \mathcal{L}_{gg} \cdot \frac{1}{m_{4\ell}} \cdot \text{Re} \left[\frac{1}{s - s_H} \cdot ((a_0 + a_1 \cdot m_{4\ell} + \dots) + i \cdot (b_0 + b_1 \cdot m_{4\ell} + \dots)) \right] \quad (7.14)$$

where the propagators are shown in equation 7.7.

Figure 7.21 shows the distributions of interference function obtained by simultaneous fitting to $m_{4\ell}$ shape from truth level H-B interference simulation at different mass in $2e2\mu$ channel as an example.

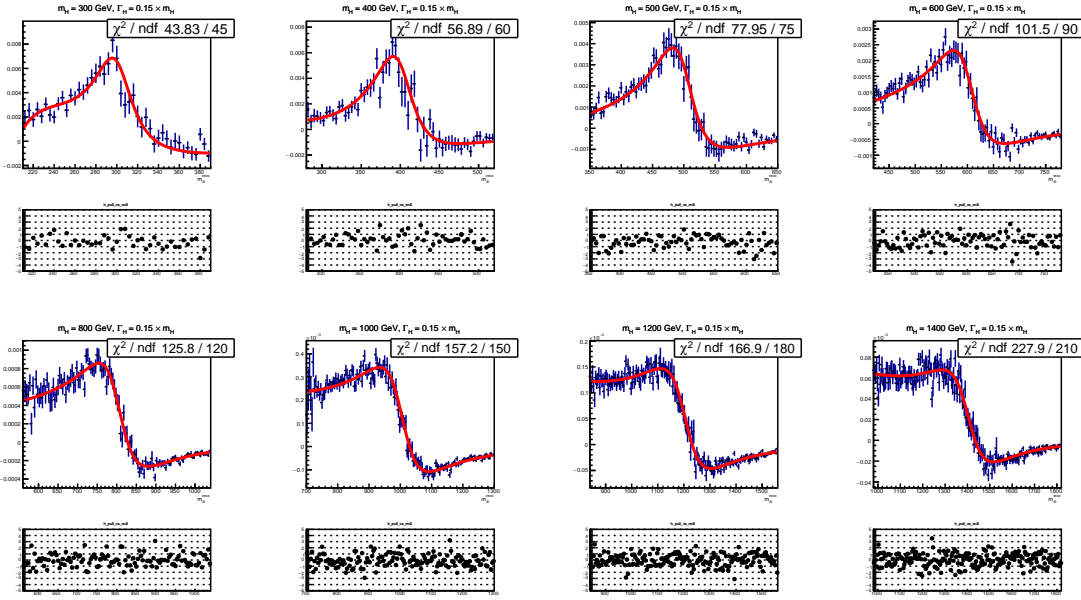


Fig. 7.21 The interference (H-B) model fitted to the truth $m_{4\ell}$ MC distribution after signal region selection for $2\mu 2e$ channel.

2. Interference between heavy Higgs and SM Higgs

The parton cross section of this interference term can be written as:

$$\sigma_{gg}(s) = \frac{1}{s} \int d\Omega \cdot \text{Re} \left[A_H^P(s, \Omega) \cdot \frac{1}{s - s_H} \cdot A_H^D(s, \Omega) \cdot A_h^{P*}(s, \Omega) \cdot \frac{1}{(s - s_h)^*} \cdot A_h^{D*}(s, \Omega) \right] \quad (7.15)$$

By assuming the production and decay amplitudes are the same for heavy Higgs boson and SM Higgs boson, the cross section function can be simplified to:

$$\sigma_{gg}(s) = \frac{1}{s} \int d\Omega \cdot \text{Re} \left[\frac{1}{s - s_H} \cdot \frac{1}{(s - s_h)^*} \right] \cdot |A_{gg \rightarrow H}(s, \Omega)|^2 |A_{H \rightarrow ZZ}(s, \Omega)|^2 \quad (7.16)$$

Taking into account Equation 7.5:

$$\sigma_{gg}(s) = 4 \cdot \text{Re} \left[\frac{1}{s - s_H} \cdot \frac{1}{(s - s_h)^*} \right] \cdot \Gamma_{H \rightarrow gg}(s) \cdot \Gamma_{H \rightarrow ZZ}(s) \quad (7.17)$$

where the propagators are described in equation 7.7, and the partial widths are described in equations 7.8 and 7.9.

Same as previous procedure, the parton cross section can be transformed to a hadron cross section as a function of $m_{4\ell}$:

$$\sigma_{pp}(m_{4\ell}) = 4 \cdot m_{4\ell} \cdot \mathcal{L}_{gg} \cdot \text{Re} \left[\frac{1}{s - s_H} \cdot \frac{1}{(s - s_h)^*} \right] \cdot \Gamma_{H \rightarrow gg}(m_{4\ell}) \cdot \Gamma_{H \rightarrow ZZ}(m_{4\ell}) \quad (7.18)$$

The modelling procedure of interference is the same as the way for large-width signal described in section 7.5.2. The truth line shape is measured as analytical function from equation 7.18, and then convolute with detector effect from NWA parameterization to get the reconstruction level shape.

For LWA signal model, these two interferences are carefully taken into account, and the integration of the pure LWA signal with the interferences is used for further studies. Figure 7.22 shows the signal model for large-width scenario at mass points of 400 GeV, 600 GeV, 800 GeV, for three different signal widths: 5%, 10%, 15%, with and without interference. Additionally, the contribution of the interference between heavy Higgs and SM Higgs (H-h) is shown together with the one between heavy Higgs and SM $gg \rightarrow ZZ$ background (H-b). One can see the interference effect on signal shape becomes less important when going to higher mass.

7.5.4 Modelling of spin-2 RS Graviton signal

The search for Randall-Sundrum (RS) graviton is performed in mass region between 600 to 2000 GeV. The width of resonance is determined by the $k/\overline{M}_{\text{Planck}}$, which, as mentioned in section 7.2.3, is set to be 1. In this configuration, the width of signal is expected to be about 6% of its mass.

The reconstructed $m_{4\ell}$ lineshape of graviton is also built by convolving the truth-level lineshape with a detector resolution function, where the detector resolution effect is modelled by a Gaussian + Crystal Ball function, whose parameters are taken from the NWA signal parameterization in section 7.5.1. And the truth-level shape is modelled as the product of a relativistic Breit-Wigner (RBW) term, a term corresponding to the squared matrix element of the production process and a parton luminosity term \mathcal{L} as given in [121]. So the truth lineshape of $m_{4\ell}$ is taken from:

$$m_{4\ell}^{\text{Truth}} \sim \mathcal{L}_{gg} \cdot s^2 \cdot \frac{s(1+s)(1+2s+2s^2)}{(s^2 - m_G^2)^2 + m_G^2 \Gamma^2}$$

The truth-level signal model is extracted by fitting to MC simulation at truth-level with the mass m_G and width Γ parameters floating at each mass points respectively. And then

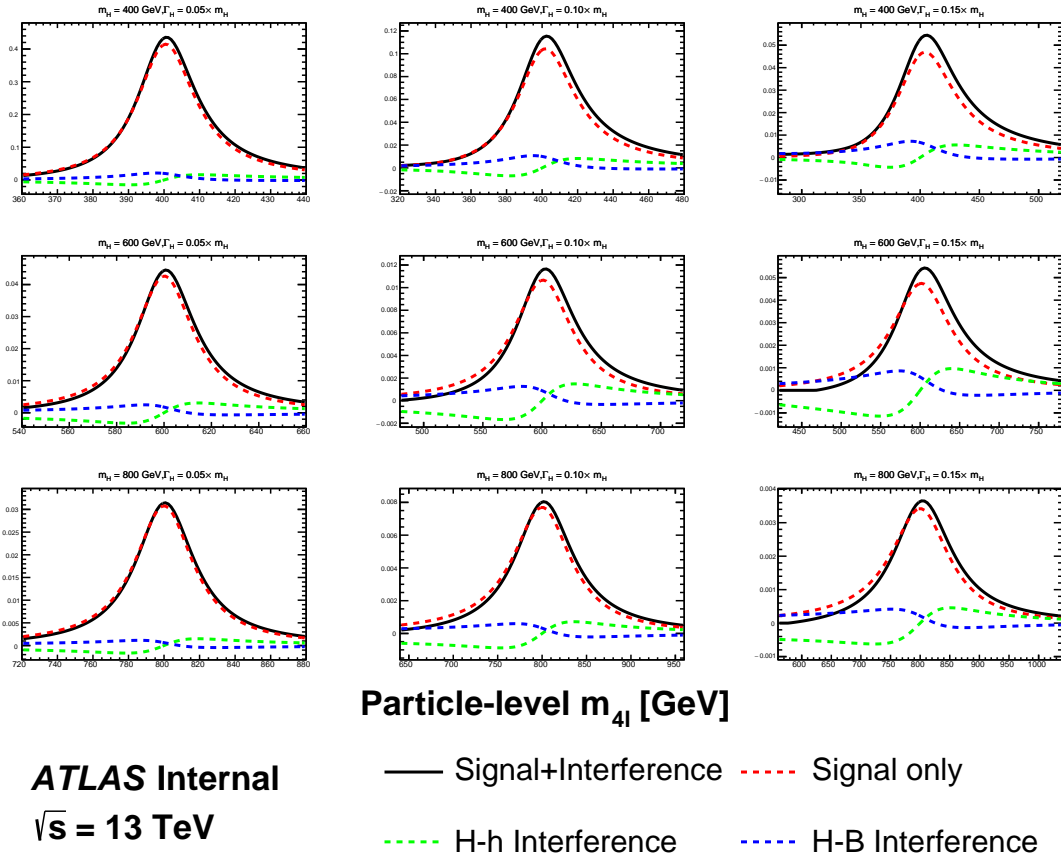


Fig. 7.22 The signal modelling for the large-width scenario at m_H of 400 GeV (top), 600 GeV (middle) and 800 GeV (bottom), as well as three different signal width: 5% (left), 10% (middle) and 15% (right). The contribution of the interference between heavy Higgs and SM Higgs (H-h) is shown together with the one between heavy Higgs and SM $gg \rightarrow ZZ$ background (H-b).

the two parameters are parameterized as the function of m_H by a linear fit as shown in figure 7.23.

The final signal model is obtained by convolving the truth-level lineshape with the detector resolution function. To verify the result, figure 7.24 compares the $m_{4\ell}$ lineshape from parameterization with the one observed from reconstructed-level MC simulation in $2e2\mu$ channel at masses of 600 GeV, 1600 GeV and 2000 GeV as examples.

7.6 Systematic uncertainties

This section describes the sources and values of theoretical and experimental systematic uncertainties considered in this analysis.

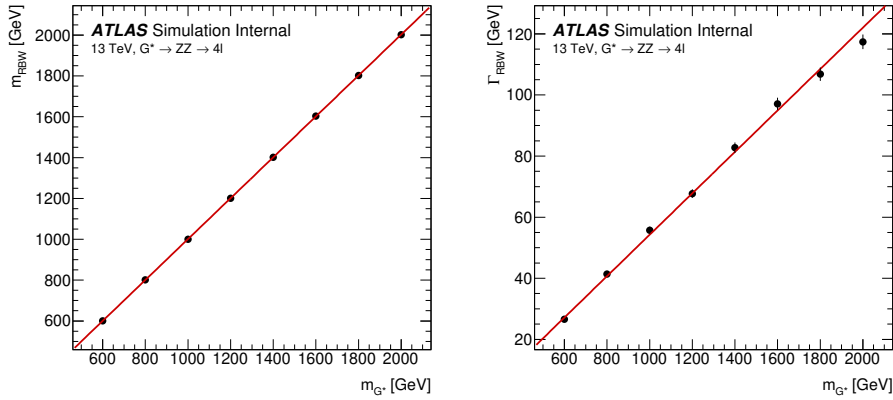


Fig. 7.23 Fitted parameters of the graviton RBW, m_{RBW} and Γ_{RBW} , as a function of the graviton resonance mass, m_G .

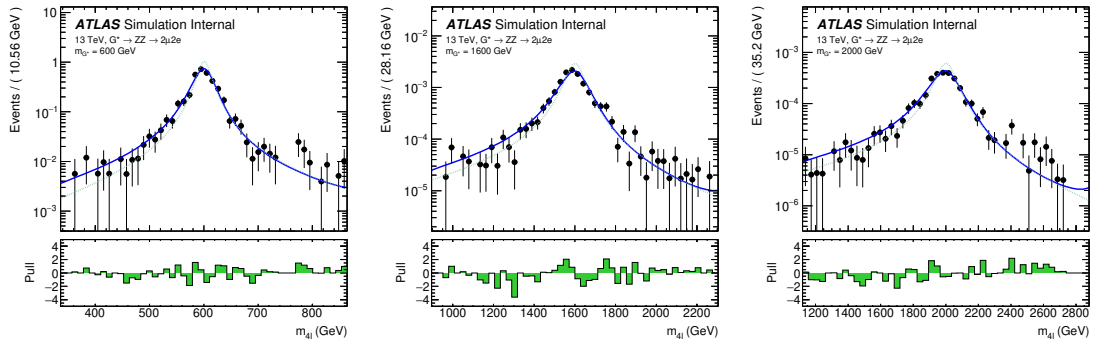


Fig. 7.24 Reconstructed $m_{4\ell}$ distributions in the $2\mu 2e$ channel with the final signal model superimposed for each RS graviton signal sample at masses of 600 GeV, 1600 GeV and 2000 GeV. The lower panel in each plot shows the pull distribution. The dashed green lines show the truth-level graviton signal models for reference.

7.6.1 Theoretical uncertainties

The theoretical modelling uncertainties include the PDF variations, missing QCD higher-order corrections via the variations of factorisation and renormalization scales, and the parton showering uncertainties.

1. Theoretical uncertainties for signal

The PDF, QCD scale and parton showering uncertainties affecting the acceptance difference originating from analysis selection for signal are taken into account in different categories. The acceptance uncertainties are calculated on the acceptance factor which extrapolates from the fiducial space to the full phase space by a simple ratio:

$$A = \frac{N_{\text{fiducial}}}{N_{\text{total}}} \quad (7.19)$$

For PDF uncertainties, the standard derivations of 100 PDF replicas of NNPDF3.0 NNLO, as well as comparison to two external PDF sets: MMHT2014 NNLO, CT14

NNLO are considered. For missing QCD higher-order corrections, the effects are studied with truth events by comparing weights corresponding to variations of the renormalization and factorization scale factors, up and down by a factor of two, and the envelop of different variations is used. The parton showering uncertainties are estimated by comparing events with different setting via Pythia8.

Systematic uncertainties are studied for both cut- and MVA- based event categorizations, for cut-based analysis in two different categories: the inclusive ggF-CBA-enriched and VBF-CBA-enriched category, and for MVA-based one in three different categories: inclusive ggF-MVA-high, ggF-MVA-low and VBF-MVA-enriched category. This section shows the MVA-based results as an example.

Table 7.6 and 7.7 show the theoretical uncertainties mentioned above for ggF and VBF signal respectively in MVA-based categorization.

Table 7.6 Summary of acceptance uncertainties of PDF, QCD scale and parton shower variations for ggF production. The MVA-based categorization is used.

Categories	PDF	QCD Scale	Parton Shower
ggF-MVA-high	0.40%	0.06%	2.03%
ggF-MVA-low	0.56%	0.07%	4.86%
VBF-MVA-enriched	0.53%	0.09%	3.43%

Table 7.7 Summary of acceptance uncertainties of PDF, QCD scale and parton shower variations for VBF production. The MVA-based categorization is used.

Categories	PDF	QCD Scale	Parton Shower
ggF-MVA-high	0.18%	1.20%	0.41%
ggF-MVA-low	0.43%	0.26%	0.36%
VBF-MVA-enriched	0.23%	3.19%	0.85%

2. Theoretical uncertainties for SM background processes

The theoretical uncertainties of irreducible ZZ backgrounds are considered in terms of both the variations of shape of $m_{4\ell}$ distributions and the acceptance originating from the event selection.

The PDF and QCD scale uncertainties are considered by using the same method as described for signal. The parton showering uncertainties for those Sherpa samples are evaluated by varying the resummation scale by a factor of 2, changing the CKKW setting and using different showering option, following the PMG recommendation in Ref.^[122], and the quadratic sum between the uncertainties in different kinds of showering option is taken as final result of uncertainties. Moreover, the shape uncertainty associated with electroweak higher-order correction for $q\bar{q} \rightarrow ZZ$ process is also taken into account.

Same as for signals, these theoretical uncertainties for irreducible backgrounds are studied for both cut- and MVA- based event categorizations. The value of shape uncertainties vary from less than 1% at low mass region to 50% at high mass tail due to large statistic fluctuation. As for the acceptance uncertainties, the values vary from about 1% for PDF variations to 40% for parton showering variations. The VBF category has relative larger uncertainties.

Table 7.8 summarizes the acceptance uncertainties of PDF, QCD scale, and parton showering variations for the dominant background: $q\bar{q} \rightarrow ZZ$.

Table 7.8 Summary of acceptance uncertainties of PDF, scale, and parton showering variations for QCD $q\bar{q} \rightarrow ZZ$ background. The MVA-based categorization is used.

Categories	PDF	QCD Scale	Parton showering
ggF-MVA-high	1.15%	10.16 %	3.71%
ggF-MVA-low	1.04%	3.26 %	3.80%
VBF-MVA-enriched	2.91%	27.90 %	23.82%

7.6.2 Experimental systematics

The signal and background predictions used in this analysis are also affected by various sources of experimental systematic uncertainties. Similar as described in section 6.5.2, the dominant experimental uncertainties in this analysis also come from the energy/momentum scales and reconstruction and identification efficiencies of the leptons and jets, as well as the luminosity uncertainty. The systematic uncertainties are calculated using the recommendations from the Combined Performance (CP) groups of ATLAS experiment. In addition, as mentioned in previous sections, the uncertainties of irreducible background modelling, reducible background shape smoothing procedure and signal yield difference between simulation and parameterization are all taken into account. The impact of a few largest systematics and their value from statistical fit are studied in section 7.7.

7.7 Results in $\ell\ell\ell'\ell'$ channel

The statistical treatment in searching for heavy resonances in $ZZ \rightarrow \ell\ell\ell'\ell'$ final state is described in this section. Results are presented in both cut- and MVA- based analysis.

7.7.1 Statistical procedure

The upper limits on heavy resonances are obtained using the unbinned profile likelihood fits. $m_{4\ell}$ is the discriminant. The likelihood function is a product of a Poisson term representing the probability of observing n events and a weighted sum of both signal and background probability distribution functions (pdfs) evaluated for all observed events.

$$L(x_1..x_n|\sigma_{ggF}, \sigma_{VBF}) = \text{Pois}(n|S_{ggF} + S_{VBF} + B) \left[\prod_{i=1}^n \frac{S_{ggF}f_{ggF}(x_i) + S_{VBF}f_{VBF}(x_i) + Bf_B(x_i)}{S_{ggF} + S_{VBF} + B} \right] \quad (7.20)$$

where f_X s are the pdfs of signal and backgrounds modelled in section 7.5 and 7.4, S_X and B are the normalizations of signal and sum of backgrounds.

The parameters of interest (POI) in the search is σ_{ggF} (and σ_{VBF} only for NWA signal), which is the cross section of signal model in ggF (and VBF) production mode. In the case of two POIs, when testing one POI, the other one is profiled along with other nuisance parameters (except left unconstrained) during the minimization. These POIs enter the likelihood inside the expected signal yields S_{ggF} and S_{VBF} as:

$$S_{ggF(VBF)} = \sigma_{ggF(VBF)} \times B(S \rightarrow ZZ) \times A \times C \times \int \mathcal{L} \quad (7.21)$$

where $A \times C$ is the signal acceptance as parameterized in 7.3.4, and $\int \mathcal{L} = 139 \text{ fb}^{-1}$ is the integrated luminosity of the dataset.

The dependence of the expected number of signal and background events (normalizations) and the shape of the PDFs on the systematic uncertainties measured in section 7.6 is described by a set of nuisance parameters (NPs) θ_i , constrained by Gaussian distribution described in section 5.4. The final likelihood function $L(\sigma_{ggF}, \sigma_{VBF}, m_H, \theta_i)$ is therefore a function of σ_{ggF} , σ_{VBF} , m_H , and θ_i .

Furthermore, the normalization of SM background $pp \rightarrow ZZ$, including both $q\bar{q} \rightarrow ZZ$ and $gg \rightarrow ZZ$, is a free parameter (μ_{ZZ}) and profiled during the minimization. Floating ZZ normalization in fit takes the advantage of reducing the dependence on theory predictions and their associated uncertainties, especially given that the increased data luminosity would provide precise determination of the SM ZZ background rate.

At the end, the upper limit on production cross-section $\sigma_{ggF(VBF)}$ at a given heavy resonance model is obtained by setting the mass of signal m_H parameter as constant at the desired value, and maximising the likelihood function with respect to nuisance parameters. The CL_s method described in section 5.3 is used to obtain exclusion limits.

Table 7.9 Expected and observed numbers of events for $m_{4\ell} > 200$ GeV, together with their systematic uncertainties, for three MVA-based categories. The expected number of events, as well as their uncertainties, are obtained from a likelihood fit to the data under the background-only hypothesis. The uncertainties of the ZZ normalisation factors, presented in table 7.10, are also taken into account.

Process	VBF-enriched category	ggF-enriched categories			the “rest” category
		4 μ channel	2e2 μ channel	4e channel	
$q\bar{q} \rightarrow ZZ$	11 ± 4	232 ± 10	389 ± 17	154 ± 7	2008 ± 47
$gg \rightarrow ZZ$	3 ± 2	37 ± 6	64 ± 10	26 ± 4	247 ± 19
ZZ (EW)	4.1 ± 0.4	4.5 ± 0.2	7.5 ± 0.4	3 ± 0.2	14.3 ± 0.7
$Z+jets, t\bar{t}$	0.08 ± 0.02	0.6 ± 0.1	1.7 ± 0.4	0.8 ± 0.1	8.8 ± 2.1
$t\bar{t}V, VVV$	0.97 ± 0.1	9.8 ± 0.2	17.5 ± 0.4	7.8 ± 0.2	21.9 ± 0.5
Total background	19 ± 4.5	284 ± 11.7	480 ± 19.7	192 ± 8.1	2300 ± 50.7
Observed	19	271	493	191	2301

7.7.2 For likelihood function under background-only hypothesis for MVA-based analysis

Both MVA- and cut-based analysis are studied by performing likelihood fit to the (pseudo-) data under the background-only hypothesis and under different signal models. Due to the same background estimation and modelling procedures, as well as the same method of systematic measurements, this section only shows the results of background-only fits for MVA-based analysis under the model of heavy Higgs resonance with narrow-width as an example. The final results of interpretation in both MVA- and cut- based analysis in all signal models described in section 7.5 will be presented in next section.

First of all, table 7.9 summarized the expected and observed number of events for region of $m_{4\ell} > 200$ GeV together with their systematic uncertainties after background-only fit. The post-fit $m_{4\ell}$ spectrum in each category is shown in figure 7.25.

To inspect the likelihood model, pulls and constraints as well as the correlation matrix of NPs are studied by performing a background only fit. Figure 7.26 shows the pulls and constraints when fitting to background only Asimov data (top) and observed data (bottom). Figure 7.27 shows the correlation matrix, only for NPs with correlation between each others greater than 0.1 when fitting to background only Asimov data. The normalization of ZZ background is taken from data for one category each, as shown in table 7.10.

The impact of a systematic uncertainty on the result depends on the production mode and the mass hypothesis. To check the impact of systematic uncertainties on expected

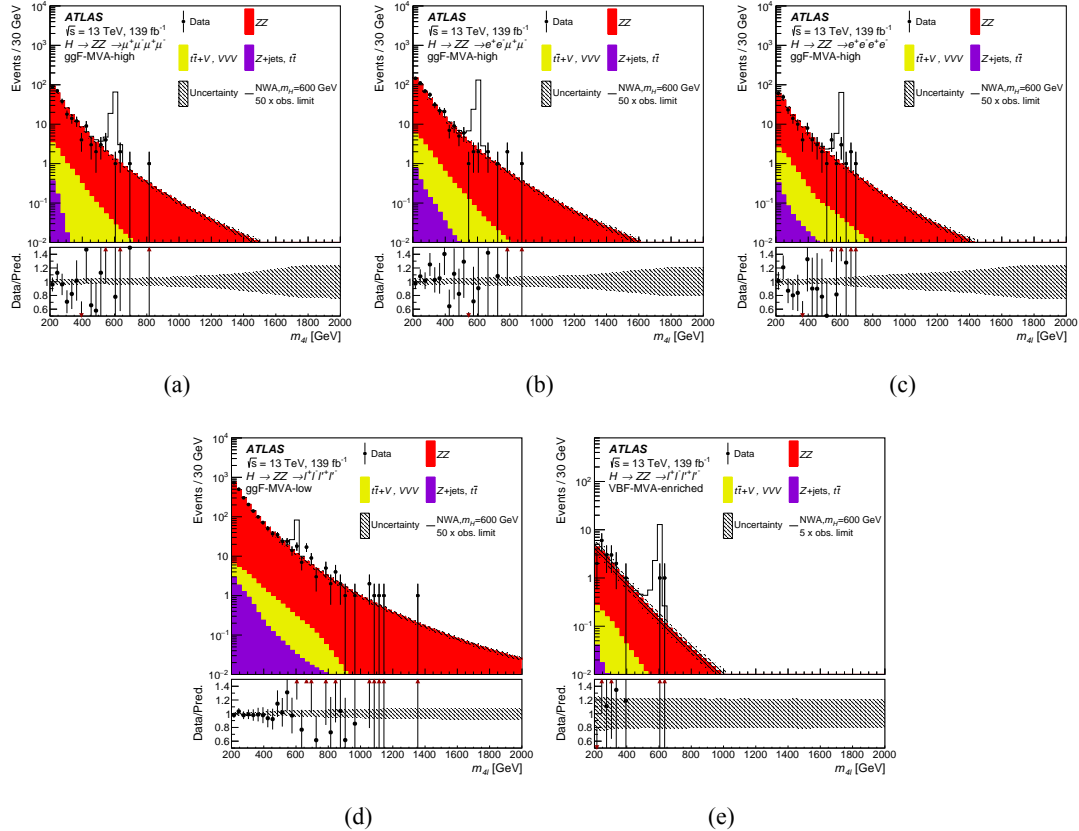


Fig. 7.25 Distribution of the four-lepton invariant mass $m_{4\ell}$ for (a), (b), (c) the ggF-MVA-high categories, (d) the ggF-MVA-low category and (e) the VBF-MVA-enriched category. The backgrounds are determined from a combined likelihood fit to the data under the background-only hypothesis. The simulated signal at 600 GeV is normalized to a cross section corresponding to 50 (5) times the observed upper limit given in section 7.7.3 for the ggF (VBF) production. The error bars on the data points indicate the statistical uncertainty, and the systematic uncertainty in MC prediction is shown by the hatched band. The lower panels show the ratio of data to prediction. The red arrows indicate data points that are outside the displayed range.

signal sensitivity, a NP ranking study is performed using signal injected Asimov data with the injected cross section close to 95% CLs upper limit in figure ?? at the masses of 400 GeV and 1000 GeV. The results are shown in table 7.11. For ggF production, at lower mass, the systematic uncertainties of parton showering variation for signal, the luminosity uncertainty, and the parametrization of signal acceptance dominate, while at higher mass, the shape uncertainties from PDF variation for ZZ ($q\bar{q} \rightarrow ZZ$ and $gg \rightarrow ZZ$) background become important, as also seen in VBF production mode. In addition for VBF, jet related uncertainties become more important comparing to ggF production. Moreover, the dominate uncertainties include the acceptance uncertainty from QCD scale variation for signal and the luminosity uncertainty.

Table 7.10 ZZ normalization factor in each category, obtained from a likelihood fit to the data under the background-only hypothesis.

Normalization factor	Fitted value
$\mu_{ZZ}^{ggF-MVA-high}$	1.07 ± 0.047
$\mu_{ZZ}^{ggF-MVA-low}$	1.12 ± 0.026
$\mu_{ZZ}^{VBF-MVA-enriched}$	0.91 ± 0.314

Table 7.11 Impact of the leading systematic uncertainties, the data statistic uncertainties, as well as the total uncertainties on the predicted signal event yield with the cross section times branching ratio being set to the expected upper limit, expressed as a percentage of the signal yield for the ggF (left) and VBF (right) production modes at $m_H = 400$ and 1000 GeV.

ggF production		VBF production	
Systematic source	Impact [%]	Systematic source	Impact [%]
$m_H = 400$ GeV			
Parton showering of ggF	2.3	QCD scale of VBF	2.7
Luminosity	1.8	Jet flavor composition	2.5
PDF of $q\bar{q} \rightarrow ZZ$	1.6	Luminosity	1.8
Signal yield parameterization	1.4	Jet energy scale (in-su calibration)	1.6
Data stat. uncertainty	48	Data stat. uncertainty	57
Total Uncertainty	49	Total Uncertainty	58
$m_H = 1000$ GeV			
PDF of $q\bar{q} \rightarrow ZZ$	2.5	QCD scale of VBF	2.3
Parton showering of ggF	2.4	PDF of $q\bar{q} \rightarrow ZZ$	2.2
PDF of $gg \rightarrow ZZ$	1.9	Luminosity	1.8
Luminosity	1.8	PDF of $gg \rightarrow ZZ$	1.6
Data stat. uncertainty	84	Data stat. uncertainty	92
Total Uncertainty	86	Total Uncertainty	93

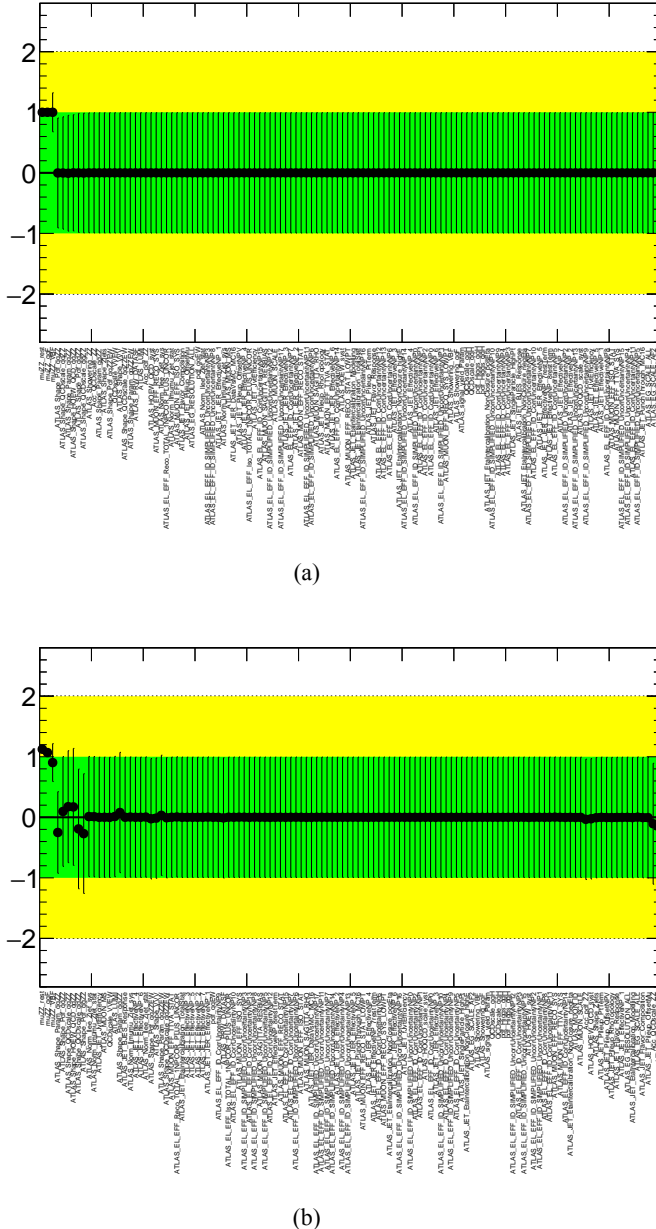
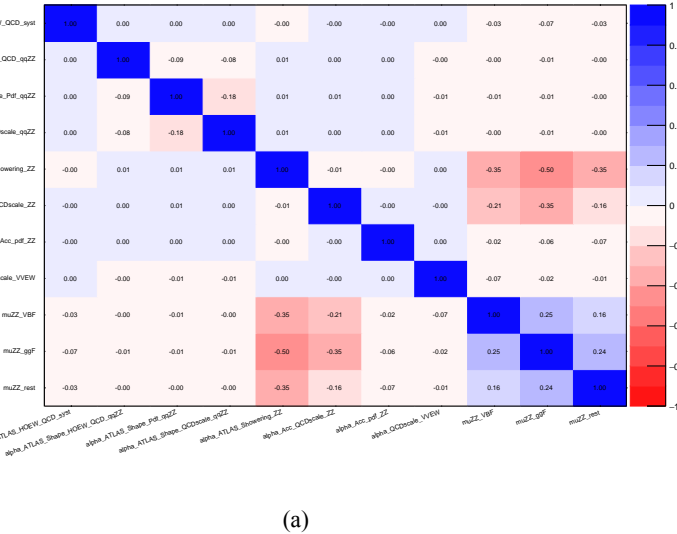


Fig. 7.26 Pulls and constraints of nuisance parameters after a background only fit to (a) Asimov data and (b) observed data in the $\ell\ell\ell'\ell'$ channel. The Asimov data is generated with background data only, and the observed data includes datasets from 2015 to 2018.

7.7.3 Interpretations

1. Spin-0 resonance with NWA

In the absence of a specific model, the ratio of ggF and VBF production mode is unknown for this additional heavy scalar. For this reason, the fits for ggF and VBF processes are done separately, and in each case the cross section of the untested process is allowed to be a free parameter in the statistical fit. The observed and expected upper limit at 95% confidence level (CL) on the $\sigma \times B(H \rightarrow ZZ)$ of a narrow scalar resonance for both



(a)

Fig. 7.27 Correlation of nuisance parameters after a background only fit to Asimov data in the $\ell\ell\ell'\ell'$ channel. The Asimov data is generated with background data only.

ggF and VBF production mode with the integrated luminosity of 139 fb^{-1} is shown in figure 7.28 (7.29) for MVA- (cut-) based analysis.

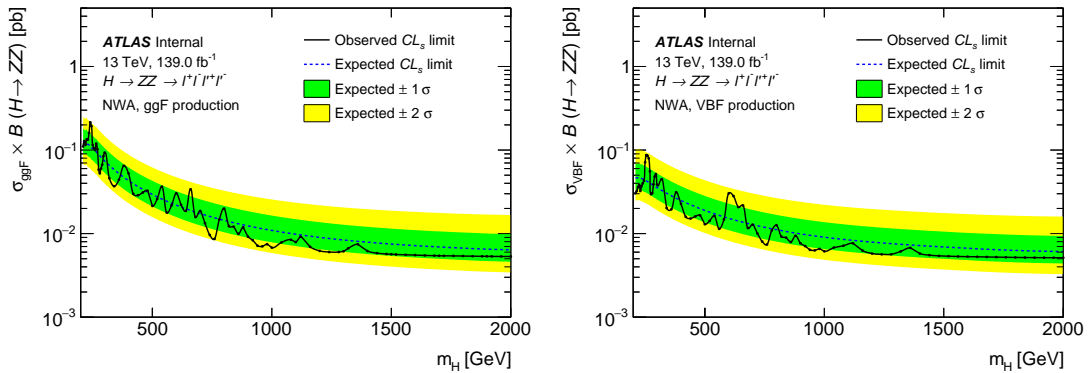


Fig. 7.28 The expected and observed upper limits at 95% CL on $\sigma \times B(H \rightarrow ZZ)$ using the MVA-based analysis for ggF (left) and VBF (right) production. The green and yellow bands represent the $\pm 1\sigma$ and $\pm 2\sigma$ uncertainties in the expected limits.

In order to measure the compatibility of the data with the background-only hypothesis ($\sigma_{\text{ggF}} = \sigma_{\text{VBF}} = 0$), the test statistic q_0 , as described in equation 5.9, is used. Figure 7.30 shows its corresponding p_0 scan for ggF (left) and VBF (right) production as functions of m_H in MVA-based analysis. No excess over 2σ is found for ggF production, while for VBF production, the maximal local significance is found to be 2.46σ at 620 GeV with corresponding global significance of 0.88σ computed from Ref.^[123].

2. Spin-0 resonance with LWA

In the case of LWA model, only ggF production mode is studied. The interference between the heavy scalar and SM Higgs boson (H-h), as well as the heavy scalar and

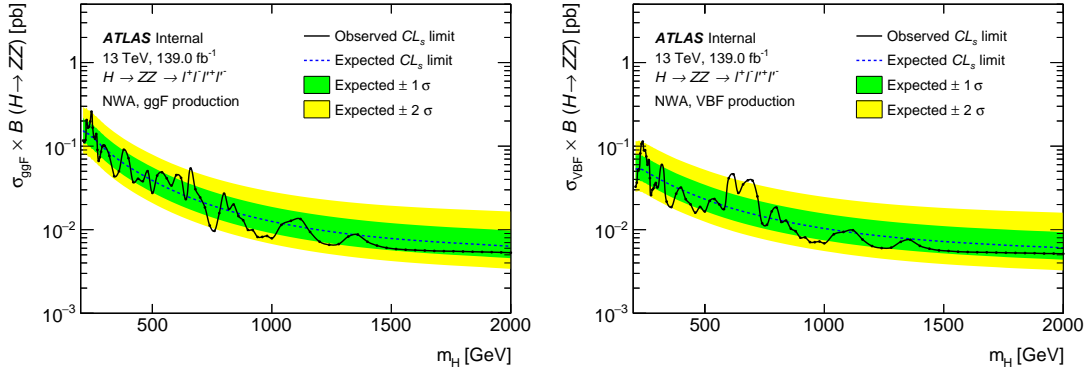


Fig. 7.29 The expected and observed upper limits at 95% CL on $\sigma \times B(H \rightarrow ZZ)$ using the cut-based analysis for ggF (left) and VBF (right) production. The green and yellow bands represent the $\pm 1\sigma$ and $\pm 2\sigma$ uncertainties in the expected limits.

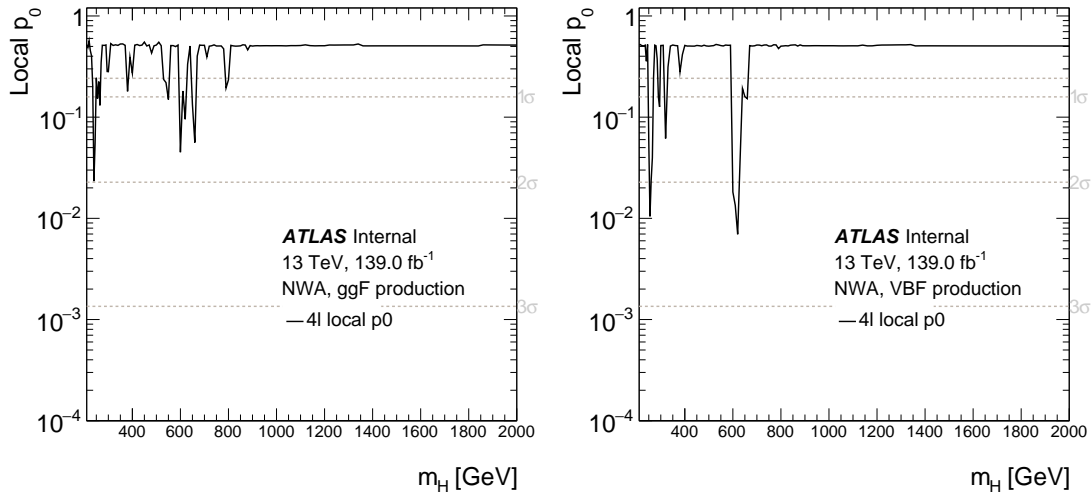


Fig. 7.30 The local p_0 scan as functions of m_H on $\sigma \times B(H \rightarrow ZZ)$ using the MVA-based analysis for ggF (left) and VBF (right) production.

SM $gg \rightarrow ZZ$ continuum background (H-B) as modelled in section 7.5.3 are taken into account. The upper limit at 95% confidence level (CL) on ggF cross section times branch ratio ($\sigma_{ggF} \times B(H \rightarrow ZZ)$) is shown in figure 7.31 for a width of 1, 5, 10 and 15% of m_H .

3. Spin-2 RS Graviton resonance

The observed and expected 95% upper limit on the cross section times branching ratio for RS Graviton (RSG) scenario is shown in figure 7.32. Similar to LWA, only $4e$, 4μ and $2e2\mu$ channel of ggF production mode are used. On top of the expected and observed upper limits in this model, a predicted cross section as function of mass provided by theorist is also shown in the figure. Comparing with the observed result provided by $ZZ \rightarrow \ell\ell\ell'\ell'$ decay, this spin-2 graviton is excluded up to a mass of 1500 GeV.

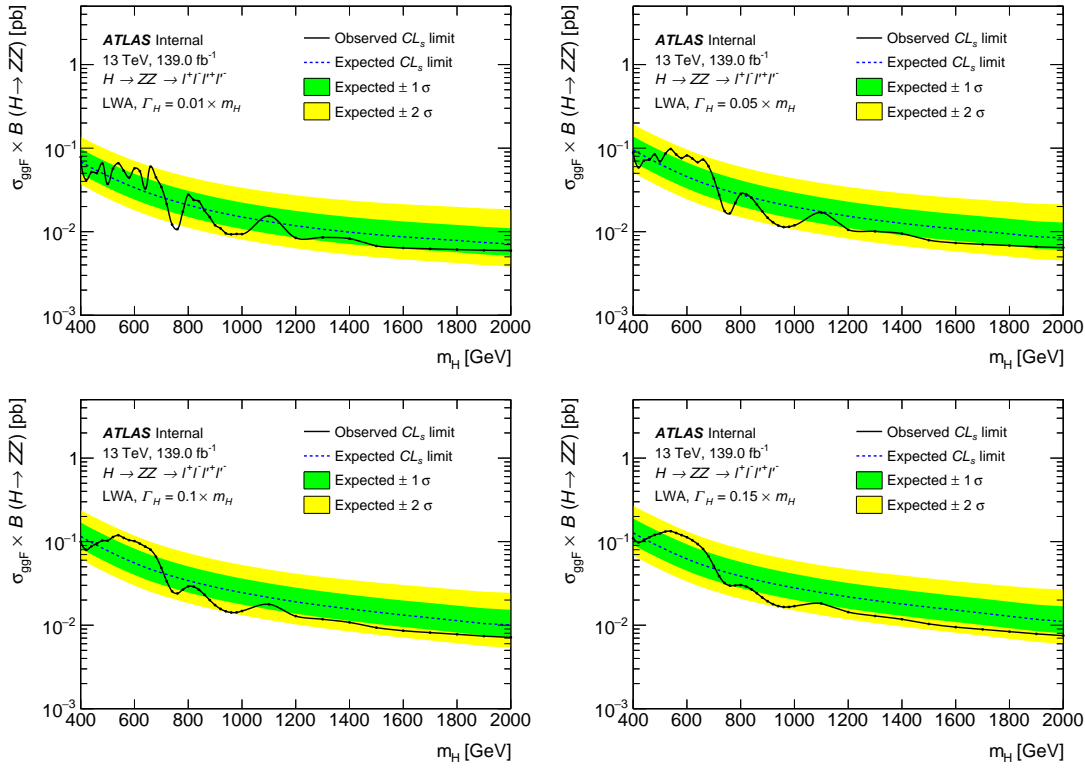


Fig. 7.31 The upper limits at 95% confidence level on $\sigma_{ggF} \times B(H \rightarrow ZZ)$ as a function of the heavy resonance mass m_H for the ggF production mode with an intrinsic width of 1% (top left), 5% (top right), 10% (bottom left) and 15% (bottom right) for both the case where interference with Standard Model processes is considered. The green and yellow bands represent the $\pm 1\sigma$ and $\pm 2\sigma$ uncertainties in the expected limits.

4. Summary of interpretation

As a summary, figure 7.33 shows the comparison of expected and observed 95% CL upper limits between different models described above.

Figure 7.34 compares the expected 95% CL upper limits as a function of the NWA resonance mass in this analysis with full run-2 data and the one in previous publication^[124] with the integrated luminosity of 36.1 fb^{-1} . With a significant increase of integrated luminosity and an improved analysis strategy, comparing to the previous publication, the expected sensitivities of searching for narrow-width heavy resonance reduced by up to 70% in MVA-based analysis, where 50% of reduction is due to luminosity increase while other improvement mainly comes from inviting multivariate method.

Figure 7.35 shows the display of one candidate event passing analysis selection in four-muon final state with four-muon invariant mass of 1.34 TeV.

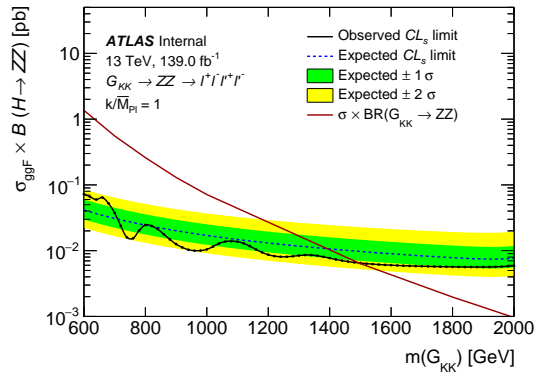


Fig. 7.32 The upper limits at 95% confidence level on $\sigma_{\text{ggF}} \times B(G_{KK} \rightarrow ZZ)$ as a function of the heavy resonance mass $m(G_{KK})$ for the ggF production mode in RS Graviton model. The green and yellow bands represent the $\pm 1\sigma$ and $\pm 2\sigma$ uncertainties in the expected limits.

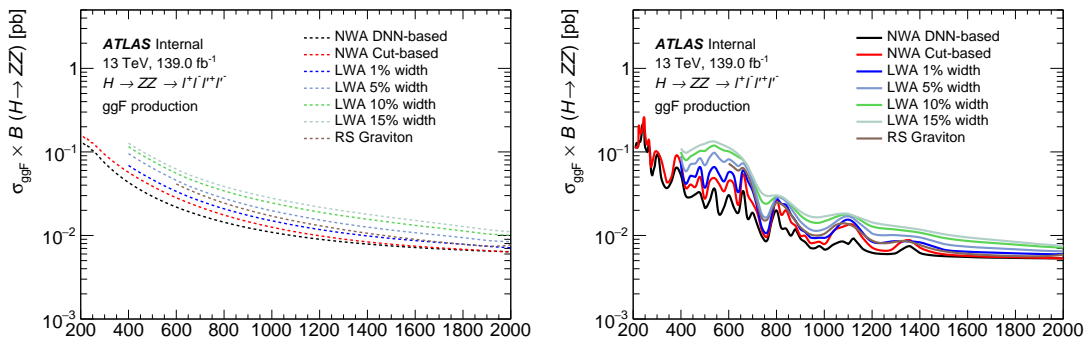


Fig. 7.33 The expected (left) and observed (right) upper limits at 95% CL on $\sigma \times B(S \rightarrow ZZ)$ for ggF production mode at different hypothetical models including the MVA- and cut- based NWA, LWA with width assumptions of 1, 5, 10, 15%, and the RSG.

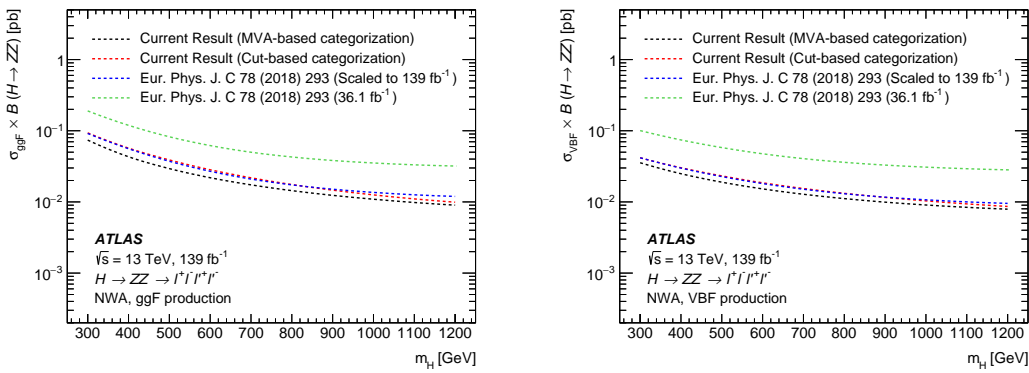


Fig. 7.34 Comparisons of the expected upper limits at 95% CL on the cross section times branching ratio as a function of the heavy resonance mass m_H for the ggF production mode (left) and for the VBF production mode (right) in the case of the NWA. The expected limits from the previous publication are shown in the green dashed line and are projected to the 139 fb^{-1} as shown in the blue dashed line. In addition, the current results based on either cut-based categorisation or the multivariate-based categorisation are shown in red and black lines.

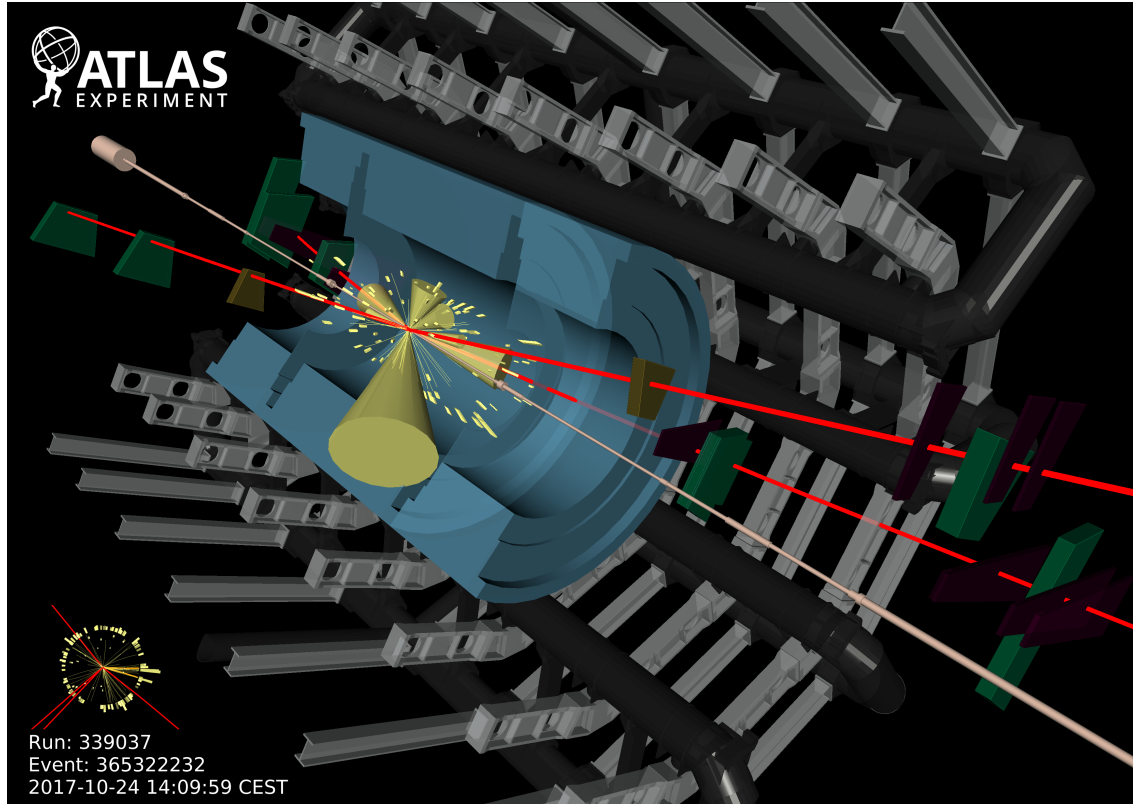


Fig. 7.35 Display of one candidate event in 4μ final state with the mass of 1.35 TeV.

7.8 Conclusion

Searches of heavy resonances decaying into a pair of Z boson to $\ell\ell\ell'\ell'$ final state are performed using 139 fb^{-1} of 13 TeV pp collision data collected by ATLAS experiment at the LHC. The results are interpreted as 95% CL upper limits on the production cross section of a spin-0 and spin-2 resonances under different theoretical models. The search range of the hypothetical resonances is between 200 GeV to 2000 GeV depending on the signal model.

The spin-0 resonance is assumed to be a heavy Higgs like scalar produced predominantly from gluon–gluon fusion (ggF) and vector-boson fusion (VBF) decays, and it is studied under both the narrow-width approximation and with the large-width assumption. For narrow-width approximation, the exclusion limits on cross section of heavy scalar decaying into two Z bosons are set separately for ggF and VBF production modes, under MVA- and cut- based analysis. In MVA-based analysis, the 95% CL upper limit range is from 215 fb at $m_H = 240$ GeV to 5.3 fb at $m_H = 2000$ GeV for ggF production mode, and from 87 fb at $m_H = 255$ GeV to 5.1 fb at $m_H = 1960$ GeV for VBF production mode. In cut-based analysis, the 95% CL upper limit range is from 259 fb at $m_H = 245$ GeV to 5.3 fb at $m_H = 2000$ GeV for ggF production mode, and from 113 fb at $m_H = 240$ GeV to 5.1 fb at $m_H = 2000$ GeV for VBF production mode. MVA-based analysis gains about 20% improvement on upper limits at lower mass region comparing to the cut-based analysis, while for mass above 1500 GeV, both analyses perform closely. For large-width approximation, limits are studied on ggF production rate at four different width assumptions: 1%, 5%, 10% and 15% of resonance’s mass, with the interference between the heavy scalar and the SM Higgs boson as well as the heavy scalar and the SM $gg \rightarrow ZZ$ continuum background taken into account. The maximum and minimum of upper limits are obtained as 78 fb at $m_H = 400$ GeV to 5.9 fb at $m_H = 2000$ GeV for 1% width; 98 fb at $m_H = 540$ GeV to 6.4 fb at $m_H = 2000$ GeV for 5% width; 119 fb at $m_H = 540$ GeV to 7.1 fb at $m_H = 2000$ GeV for 10% width; 133 fb at $m_H = 540$ GeV to 7.5 fb at $m_H = 2000$ GeV for 15% width. Last but not least, the framework of the Randall–Sundrum model with a graviton excitation spin-2 resonance with $m(G_{KK}) < 1500$ GeV is excluded at 95% CL.

Chapter 8 Summary

On December 3rd, 2018, the LHC finished its second run (run-2) after three fantastic years. Thanks to run-2 with large increase in statistics, we now know the masses of the Higgs boson, top quark and W boson to considerably greater precision, and also confirm the Standard Model as a stable theory.

In this dissertation, various physics processes in $ZZ \rightarrow \ell\ell\ell'\ell'$ final state are studied, taking the advantage of full run-2 pp collision data in the LHC. Using this signature, we measured the fiducial cross section of ZZ production to $\ell\ell\ell'\ell' jj$ channel in SM, which is an important physics process and major background in many analysis with ZZ production, eg. Higgs analysis (HZZ). In addition, we searched the electroweak ZZ production via vector boson scattering in associated with 2-jet process in $\ell\ell\ell'\ell'$ final state. In the meantime, the searches of heavy resonances decaying into a pair of Z bosons to $\ell\ell\ell'\ell'$ final state for several different hypothetical resonances are conducted in this dissertation. The results of several analyses are summarized as below:

Measurement of fiducial cross section of ZZ production in $\ell\ell\ell'\ell' jj$ final state

The fiducial cross section of inclusive SM $ZZ \rightarrow \ell\ell\ell'\ell'$ production is measured to be:

$$\sigma_{ZZ \rightarrow \ell\ell\ell'\ell'}^{fid} = 1.27 \pm 0.12(stat) \pm 0.02(theo) \pm 0.07(exp) \pm 0.01(bkg) \pm 0.03(lumi) [fb] \quad (8.1)$$

which is found to be compatible with the SM prediction. The ZZ cross section is calculated with up to one (three) outgoing partons at NLO (LO) using Sherpa 2.2.2 for QCD production, and in LO using MadGraph5_aMC@NLO 2.6.1 for EW production. The total uncertainty is 11%, the analysis is still data statistic dominant (data statistic uncertainty is about 9.5%).

Observation of electroweak ZZ production in $\ell\ell\ell'\ell' jj$ final state

Thanks to the largely increased data statistic collected by ATLAS experiment in the LHC run-2, the electroweak ZZ production (EW- $ZZjj$) to $\ell\ell\ell'\ell'$ channel in association with two jets is observed with a significant deviation from the background-only hypothesis. The signal strength of EW- $ZZjj$ production, the normalization of QCD- $ZZjj$ production, as well as the observed and expected statistical significance measured

in $\ell\ell\ell'\ell' jj$ channel are found to be:

$$\begin{aligned}\mu_{\text{EW}} &= 1.54 \pm 0.42 \\ \mu_{\text{QCD}} &= 0.95 \pm 0.22\end{aligned}\quad (8.2)$$

$$\text{Obs. (Exp.) Significance} = 5.48 \text{ (3.90)} \sigma$$

Then in this dissertation, the differential cross section and expected significance of EW- $ZZjj$ production, using 3000 fb^{-1} simulated pp collision data at a centre-of-mass energy of 14 TeV to be recorded by ATLAS experiment at the HL-LHC, are studied via simulations. The HL-LHC will for sure give us more opportunity to probe rare process like $ZZ \rightarrow \ell\ell\ell'\ell'$ in the future.

Searches of heavy ZZ resonances in $\ell\ell\ell'\ell'$ final state

Searches of heavy ZZ resonances are performed in four-lepton invariant mass $m_{4\ell}$ range from 200 GeV to 2000 GeV. Data are found to agree with the background-only hypothesis, and 95% CL upper limits are set on the production rate under the models of:

- Spin-0 heavy Higgs under narrow-width approximation (NWA).

Search range is from 200 GeV to 2000 GeV.

In DNN-based analysis, the limits range from 215 fb at $m_H = 240$ GeV to 5.3 fb at $m_H = 2000$ GeV for ggF production mode, and from 87 fb at $m_H = 255$ GeV to 5.1 fb at $m_H = 1960$ GeV for VBF production mode.

The DNN-based analysis is found to be at most 20% better than cut-based results.

- Spin-0 heavy Higgs under large-width approximation (LWA) with the width of 1, 5, 10, 15% of its mass.

Search range is from 400 GeV to 2000 GeV, and only ggF production is studied.

The maximum and minimum of upper limits are obtained as 78 fb at $m_H = 400$ GeV to 5.9 fb at $m_H = 2000$ GeV for 1% width; 98 fb at $m_H = 540$ GeV to 6.4 fb at $m_H = 2000$ GeV for 5% width; 119 fb at $m_H = 540$ GeV to 7.1 fb at $m_H = 2000$ GeV for 10% width; 133 fb at $m_H = 540$ GeV to 7.5 fb at $m_H = 2000$ GeV for 15% width.

- Spin-2 graviton excitation under the Randall–Sundrum model.

Search range is from 600 GeV to 2000 GeV, and only ggF production is studied.

The maximum and minimum of limits are 73 fb at $m_H = 600$ GeV and 5.6 fb at $m_H = 1880$ GeV for ggF production mode. And the mass of graviton below 1500 GeV is excluded comparing the observed results with theoretical prediction.

In summary, the $ZZ \rightarrow \ell\ell\ell'\ell'$ production presented in this dissertation are consistent with SM prediction. This result completes the observation of weak boson scattering

that is a new milestone in the study of electroweak symmetry breaking. In the meantime, no indication of new physics is observed. We are looking forward to the HL-LHC, with greatly increased luminosity and higher centre-of-mass energy, which should enhance the sensitivity for new physics search and precise measurement for rare process like $\ell\ell\ell'\ell'$ final state.

Bibliography

- [1] LANGACKER P. Introduction to the Standard Model and Electroweak Physics[C/OL]// Proceedings of Theoretical Advanced Study Institute in Elementary Particle Physics on The dawn of the LHC era (TASI 2008): Boulder, USA, June 2-27, 2008. 2010: 3-48. DOI: [10.1142/9789812838360_0001](https://doi.org/10.1142/9789812838360_0001).
- [2] PICH A. Electroweak Symmetry Breaking and the Higgs Boson[J/OL]. Acta Phys. Polon., 2016, B47:151. DOI: [10.5506/APhysPolB.47.151](https://doi.org/10.5506/APhysPolB.47.151).
- [3] Observation of a new particle in the search for the standard model higgs boson with the atlas detector at the lhc[J/OL]. Physics Letters B, 2012, 716(1):1 - 29. <http://www.sciencedirect.com/science/article/pii/S037026931200857X>. DOI: <https://doi.org/10.1016/j.physletb.2012.08.020>.
- [4] Observation of a new boson at a mass of 125 gev with the cms experiment at the lhc[J/OL]. Physics Letters B, 2012, 716(1):30 - 61. <http://www.sciencedirect.com/science/article/pii/S0370269312008581>. DOI: <https://doi.org/10.1016/j.physletb.2012.08.021>.
- [5] PROFUMO S, RAMSEY-MUSOLF M J, SHAUGHNESSY G. Singlet higgs phenomenology and the electroweak phase transition[J/OL]. Journal of High Energy Physics, 2007, 2007(08): 010-010. <https://doi.org/10.1088%2F1126-6708%2F2007%2F08%2F010>. DOI: [10.1088/1126-6708/2007/08/010](https://doi.org/10.1088/1126-6708/2007/08/010).
- [6] BRANCO G, FERREIRA P, LAVOURA L, et al. Theory and phenomenology of two-higgs-doublet models[J/OL]. Physics Reports, 2012, 516(1):1 - 102. <http://www.sciencedirect.com/science/article/pii/S0370157312000695>. DOI: <https://doi.org/10.1016/j.physrep.2012.02.002>.
- [7] DREMIN I M. Soft and hard processes in QCD[J/OL]. JETP Lett., 2005, 81:307-310. DOI: [10.1134/1.1944068](https://doi.org/10.1134/1.1944068).
- [8] WOMERSLEY J. QCD at the Tevatron: Status and prospects[C/OL]//Proceedings, 5th International Symposium on Radiative Corrections - RADCOR 2000. 2000. <http://www.slac.stanford.edu/econf/C000911/>.
- [9] LIN H W, et al. Parton distributions and lattice QCD calculations: a community white paper [J/OL]. Prog. Part. Nucl. Phys., 2018, 100:107-160. DOI: [10.1016/j.ppnp.2018.01.007](https://doi.org/10.1016/j.ppnp.2018.01.007).
- [10] COLLINS J C, SOPER D E, STERMAN G F. Factorization of Hard Processes in QCD[J/OL]. Adv. Ser. Direct. High Energy Phys., 1989, 5:1-91. DOI: [10.1142/9789814503266_0001](https://doi.org/10.1142/9789814503266_0001).
- [11] STIRLING W J. Perturbative QCD[J/OL]. 2000(CERN-OPEN-2000-296):40 p. <https://cds.cern.ch/record/1194745>. DOI: [10.5170/CERN-2000-007.305](https://doi.org/10.5170/CERN-2000-007.305).
- [12] GROJEAN C. Higgs Physics[J/OL]. 2017(arXiv:1708.00794):143-158. 12 p. <https://cds.cern.ch/record/2243593>. DOI: [10.5170/CERN-2016-005.143](https://doi.org/10.5170/CERN-2016-005.143).

- [13] Cern yellow reports: Monographs: Handbook of LHC Higgs Cross Sections: 4. Deciphering the Nature of the Higgs Sector[M/OL]. 2016. <https://cds.cern.ch/record/2227475>. DOI: [10.23731/CYRM-2017-002](https://doi.org/10.23731/CYRM-2017-002).
- [14] HEINEMEYER S. Cern yellow reports: Monographs: Handbook of LHC Higgs Cross Sections: 3. Higgs Properties: Report of the LHC Higgs Cross Section Working Group[M/OL]. 2013. <https://cds.cern.ch/record/1559921>. DOI: [10.5170/CERN-2013-004](https://doi.org/10.5170/CERN-2013-004).
- [15] CHANG J, CHEUNG K, LU C T, et al. *ww* scattering in the era of post-higgs-boson discovery [J/OL]. Phys. Rev. D, 2013, 87:093005. <https://link.aps.org/doi/10.1103/PhysRevD.87.093005>.
- [16] BRUNING O S, COLLIER P, LEBRUN P, et al. LHC Design Report Vol.1: The LHC Main Ring[J]. 2004.
- [17] BUNING O, COLLIER P, LEBRUN P, et al. LHC Design Report. 2. The LHC infrastructure and general services[J]. 2004.
- [18] BENEDIKT M, COLLIER P, MERTENS V, et al. LHC Design Report. 3. The LHC injector chain[J]. 2004.
- [19] EVANS L, BRYANT P. LHC machine[J/OL]. Journal of Instrumentation, 2008, 3(08):S08001-S08001. <https://doi.org/10.1088%2F1748-0221%2F3%2F08%2Fs08001>. DOI: [10.1088/1748-0221/3/08/s08001](https://doi.org/10.1088/1748-0221/3/08/s08001).
- [20] MOBS E. The CERN accelerator complex. Complexe des accélérateurs du CERN[J/OL]. 2016. <https://cds.cern.ch/record/2197559>.
- [21] COLLABORATION A. The ATLAS experiment at the CERN large hadron collider[J/OL]. Journal of Instrumentation, 2008, 3(08):S08003-S08003. <https://doi.org/10.1088%2F1748-0221%2F3%2F08%2Fs08003>. DOI: [10.1088/1748-0221/3/08/s08003](https://doi.org/10.1088/1748-0221/3/08/s08003).
- [22] PEREZ G. Unitarization models for vector boson scattering at the lhc[D/OL]. 2018. DOI: [10.5445/IR/1000082199](https://doi.org/10.5445/IR/1000082199).
- [23] PEQUENAO J. Computer generated image of the whole ATLAS detector[Z/OL]. 2008. <https://cds.cern.ch/record/1095924>.
- [24] MCFAYDEN J. The lhc and atlas detector. in: Third generation susy and t^-t^+ productin. [D/OL]. 2014. DOI: [10.1007/978-3-319-07191-6_2](https://doi.org/10.1007/978-3-319-07191-6_2).
- [25] COLLABRATION A. Operation and performance of the ATLAS semiconductor tracker. Operation and performance of the ATLAS semiconductor tracker[J/OL]. JINST, 2014, 9(CERN-PH-EP-2014-049. CERN-PH-EP-2014-049):P08009. 80 p. <https://cds.cern.ch/record/1698966>. DOI: [10.1088/1748-0221/9/08/P08009](https://doi.org/10.1088/1748-0221/9/08/P08009).
- [26] ATLAS pixel detector electronics and sensors[J/OL]. Journal of Instrumentation, 2008, 3(07): P07007-P07007. <https://doi.org/10.1088%2F1748-0221%2F3%2F07%2Fp07007>. DOI: [10.1088/1748-0221/3/07/p07007](https://doi.org/10.1088/1748-0221/3/07/p07007).

Bibliography

- [27] MULLIER G. The upgraded pixel detector of the atlas experiment for run-2 at the large hadron collider[J/OL]. *Journal of Instrumentation*, 2016, 11:C02061-C02061. DOI: [10.1088/1748-0221/11/02/C02061](https://doi.org/10.1088/1748-0221/11/02/C02061).
- [28] The silicon microstrip sensors of the atlas semiconductor tracker[J/OL]. *Nuclear Instruments and Methods in Physics Research Section A: Accelerators, Spectrometers, Detectors and Associated Equipment*, 2007, 578(1):98 - 118. <http://www.sciencedirect.com/science/article/pii/S0168900207007644>. DOI: <https://doi.org/10.1016/j.nima.2007.04.157>.
- [29] SULTAN D M S. Development of small-pitch, thin 3d sensors for pixel detector upgrades at hl-lhc[D/OL]. 2017. DOI: [10.13140/RG.2.2.36253.82403/1](https://doi.org/10.13140/RG.2.2.36253.82403/1).
- [30] The ATLAS transition radiation tracker (TRT) proportional drift tube: design and performance [J/OL]. *Journal of Instrumentation*, 2008, 3(02):P02013-P02013. <https://doi.org/10.1088%2F1748-0221%2F3%2F02%2Fp02013>. DOI: [10.1088/1748-0221/3/02/p02013](https://doi.org/10.1088/1748-0221/3/02/p02013).
- [31] BUCHANAN N, CHEN L, GINGRICH D, et al. Design and implementation of the front end board for the readout of the atlas liquid argon calorimeters[J/OL]. *Journal of Instrumentation*, 2008, 3:P03004. DOI: [10.1088/1748-0221/3/03/P03004](https://doi.org/10.1088/1748-0221/3/03/P03004).
- [32] Technical design report atlas: ATLAS liquid-argon calorimeter: Technical Design Report [M/OL]. Geneva: CERN, 1996. <https://cds.cern.ch/record/331061>.
- [33] AAD G, ABBOTT B, ABDALLAH J, et al. Readiness of the atlas tile calorimeter for lhc collisions[J]. *European Physical Journal C*, 2010.
- [34] Technical design report atlas: ATLAS muon spectrometer: Technical Design Report[M/OL]. Geneva: CERN, 1997. <https://cds.cern.ch/record/331068>.
- [35] SLIWA K. "ATLAS Overview and Main Results"[C]//Proceedings, International School on High Energy Physics : Workshop on High Energy Physics in the near Future. (LISHEP 2013): Rio de Janeiro, Brazil, March 17-24, 2013. 2013.
- [36] RUIZ-MARTINEZ A, COLLABORATION A. The Run-2 ATLAS Trigger System: ATL-DAQ-PROC-2016-003[R/OL]. Geneva: CERN, 2016. <https://cds.cern.ch/record/2133909>. DOI: [10.1088/1742-6596/762/1/012003](https://doi.org/10.1088/1742-6596/762/1/012003).
- [37] PÁSZTOR G. The Upgrade of the ATLAS Electron and Photon Triggers towards LHC Run 2 and their Performance: ATL-DAQ-PROC-2015-053. arXiv:1511.00334[R/OL]. Geneva: CERN, 2015. <https://cds.cern.ch/record/2063746>.
- [38] COLLABORATION A. Atlas computing: Technical design report[R/OL]. Geneva: CERN. <http://atlas-computing.web.cern.ch/atlas-computing/packages/athenaCore/athenaCore.php>.
- [39] AAD G, et al. The ATLAS Simulation Infrastructure[J/OL]. *Eur. Phys. J.*, 2010, C70:823-874. DOI: [10.1140/epjc/s10052-010-1429-9](https://doi.org/10.1140/epjc/s10052-010-1429-9).
- [40] HOCHÉ S. Introduction to parton-shower event generators[C/OL]//Proceedings, Theoretical

Bibliography

- Advanced Study Institute in Elementary Particle Physics: Journeys Through the Precision Frontier: Amplitudes for Colliders (TASI 2014): Boulder, Colorado, June 2-27, 2014. 2015: 235-295. DOI: [10.1142/9789814678766_0005](https://doi.org/10.1142/9789814678766_0005).
- [41] GLEISBERG T, HöCHE S, KRAUSS F, et al. Event generation with SHERPA 1.1[J/OL]. Journal of High Energy Physics, 2009, 2009(02):007-007. <https://doi.org/10.1088%2F1126-6708%2F2009%2F02%2F007>. DOI: [10.1088/1126-6708/2009/02/007](https://doi.org/10.1088/1126-6708/2009/02/007).
- [42] BÄHR M, GIESEKE S, GIGG M A, et al. Herwig++ physics and manual[J/OL]. The European Physical Journal C, 2008, 58(4):639-707. <https://doi.org/10.1140/epjc/s10052-008-0798-9>.
- [43] NASON P. A New method for combining NLO QCD with shower Monte Carlo algorithms [J/OL]. JHEP, 2004, 11:040. DOI: [10.1088/1126-6708/2004/11/040](https://doi.org/10.1088/1126-6708/2004/11/040).
- [44] FRIXIONE S, WEBBER B R. Matching NLO QCD computations and parton shower simulations[J/OL]. Journal of High Energy Physics, 2002, 2002(06):029-029. <https://doi.org/10.1088%2F1126-6708%2F2002%2F06%2F029>. DOI: [10.1088/1126-6708/2002/06/029](https://doi.org/10.1088/1126-6708/2002/06/029).
- [45] SJOSTRAND T, MRENNA S, SKANDS P Z. A Brief Introduction to PYTHIA 8.1[J/OL]. Comput. Phys. Commun., 2008, 178:852-867. DOI: [10.1016/j.cpc.2008.01.036](https://doi.org/10.1016/j.cpc.2008.01.036).
- [46] BARBERIO E, et al. The Geant4-Based ATLAS Fast Electromagnetic Shower Simulation [C/OL]//Astroparticle, particle and space physics, detectors and medical physics applications. Proceedings, 10th Conference, ICATPP 2007, Como, Italy, October 8-12, 2007. 2008: 802-806. <http://cdsweb.cern.ch/record/1064665/files/soft-conf-2007-002.pdf>. DOI: [10.1142/9789812819093_0133](https://doi.org/10.1142/9789812819093_0133).
- [47] RICHTER-WAS E, FROIDEVAUX D, POGGIOLI L. ATLFAST 2.0 a fast simulation package for ATLAS: ATL-PHYS-98-131[R/OL]. Geneva: CERN, 1998. <https://cds.cern.ch/record/683751>.
- [48] EDMONDS K, FLEISCHMANN S, LENZ T, et al. The Fast ATLAS Track Simulation (FATRAS): ATL-SOFT-PUB-2008-001. ATL-COM-SOFT-2008-002[R/OL]. Geneva: CERN, 2008. <https://cds.cern.ch/record/1091969>.
- [49] BOYD J T, COSTA M J, TONOYAN A, et al. Commissioning of the ATLAS reconstruction software with first data[J/OL]. Journal of Physics: Conference Series, 2010, 219(3):032059. <https://doi.org/10.1088%2F1742-6596%2F219%2F3%2F032059>. DOI: [10.1088/1742-6596/219/3/032059](https://doi.org/10.1088/1742-6596/219/3/032059).
- [50] CORNELISSEN T, ELSING M, FLEISCHMANN S, et al. Concepts, Design and Implementation of the ATLAS New Tracking (NEWT): ATL-SOFT-PUB-2007-007. ATL-COM-SOFT-2007-002[R/OL]. Geneva: CERN, 2007. <https://cds.cern.ch/record/1020106>.
- [51] AAD G, et al. Muon reconstruction performance of the ATLAS detector in proton-proton collision data at $\sqrt{s} = 13$ TeV[J/OL]. Eur. Phys. J., 2016, C76(5):292. DOI: [10.1140/epjc/s10052-016-3990-0](https://doi.org/10.1140/epjc/s10052-016-3990-0).

- [2-016-4120-y.](#)
- [52] ILLINGWORTH J, KITTLER J. A survey of the hough transform[J/OL]. Computer Vision, Graphics, and Image Processing, 1988, 44(1):87 - 116. <http://www.sciencedirect.com/science/article/pii/S0734189X88800331>. DOI: [https://doi.org/10.1016/S0734-189X\(88\)80033-1](https://doi.org/10.1016/S0734-189X(88)80033-1).
- [53] Vertex Reconstruction Performance of the ATLAS Detector at 13 TeV: ATL-PHYS-PUB-2015-026[R/OL]. Geneva: CERN, 2015. <https://cds.cern.ch/record/2037717>.
- [54] AABOUD M, et al. Reconstruction of primary vertices at the ATLAS experiment in Run 1 proton-proton collisions at the LHC[J/OL]. Eur. Phys. J., 2017, C77(5):332. DOI: <10.1140/epjc/s10052-017-4887-5>.
- [55] Electron efficiency measurements with the ATLAS detector using the 2015 LHC proton-proton collision data: ATLAS-CONF-2016-024[R/OL]. Geneva: CERN, 2016. <https://cds.cern.ch/reCORD/2157687>.
- [56] LAMPL W, LAPLACE S, LELAS D, et al. Calorimeter Clustering Algorithms: Description and Performance: ATL-LARG-PUB-2008-002. ATL-COM-LARG-2008-003[R/OL]. Geneva: CERN, 2008. <https://cds.cern.ch/record/1099735>.
- [57] CORNELISSEN T G, ELSING M, GAVRILENKO I, et al. The global χ^2 track fitter in ATLAS [J/OL]. Journal of Physics: Conference Series, 2008, 119(3):032013. <https://doi.org/10.1088%2F1742-6596%2F119%2F3%2F032013>. DOI: <10.1088/1742-6596/119/3/032013>.
- [58] Electron efficiency measurements with the ATLAS detector using the 2012 LHC proton-proton collision data: ATLAS-CONF-2014-032[R/OL]. Geneva: CERN, 2014. <http://cds.cern.ch/reCORD/1706245>.
- [59] LIMPER M. Track and vertex reconstruction in the ATLAS inner detector[D/OL]. 2009. <http://cds.cern.ch/record/1202457>.
- [60] AAD G, et al. Topological cell clustering in the ATLAS calorimeters and its performance in LHC Run 1[J/OL]. Eur. Phys. J., 2017, C77:490. DOI: <10.1140/epjc/s10052-017-5004-5>.
- [61] ZHENG Z. Identification of very-low transverse momentum muons with the ATLAS experiment: ATL-MUON-PROC-2018-018[R/OL]. Geneva: CERN, 2018. <https://cds.cern.ch/reCORD/2649299>.
- [62] CACCIARI M, SALAM G P. Pileup subtraction using jet areas[J/OL]. Physics Letters B, 2008, 659(1):119 - 126. <http://www.sciencedirect.com/science/article/pii/S0370269307011094>. DOI: <https://doi.org/10.1016/j.physletb.2007.09.077>.
- [63] CACCIARI M, SALAM G P, SOYEZ G. The anti-ktjet clustering algorithm[J/OL]. Journal of High Energy Physics, 2008, 2008(04):063-063. <https://doi.org/10.1088%2F1126-6708%2F2008%2F04%2F063>. DOI: <10.1088/1126-6708/2008/04/063>.
- [64] CACCIARI M, SALAM G P, SOYEZ G. Fastjet user manual[J/OL]. The European Physical

Bibliography

- Journal C, 2012, 72(3):1896. <https://doi.org/10.1140/epjc/s10052-012-1896-2>.
- [65] AAD G, et al. Jet energy measurement and its systematic uncertainty in proton-proton collisions at $\sqrt{s} = 7$ TeV with the ATLAS detector[J/OL]. Eur. Phys. J., 2015, C75:17. DOI: [10.1140/epjc/s10052-014-3190-y](https://doi.org/10.1140/epjc/s10052-014-3190-y).
- [66] AABOUD M, et al. Jet energy scale measurements and their systematic uncertainties in proton-proton collisions at $\sqrt{s} = 13$ TeV with the ATLAS detector[J/OL]. Phys. Rev., 2017, D96(7): 072002. DOI: [10.1103/PhysRevD.96.072002](https://doi.org/10.1103/PhysRevD.96.072002).
- [67] Optimisation of the ATLAS *b*-tagging performance for the 2016 LHC Run: ATL-PHYS-PUB-2016-012[R/OL]. Geneva: CERN, 2016. <https://cds.cern.ch/record/2160731>.
- [68] PIACQUADIO G, WEISER C. A new inclusive secondary vertex algorithm for b-jet tagging in ATLAS[J/OL]. Journal of Physics: Conference Series, 2008, 119(3):032032. [https://doi.org/10.1088/1742-6596/119/3/032032](https://doi.org/10.1088%2F1742-6596%2F119%2F3%2F032032). DOI: [10.1088/1742-6596/119/3/032032](https://doi.org/10.1088/1742-6596/119/3/032032).
- [69] SPECKMAYER P, HÖCKER A, STELZER J, et al. The toolkit for multivariate data analysis, TMVA 4[J/OL]. Journal of Physics: Conference Series, 2010, 219(3):032057. [https://doi.org/10.1088/1742-6596/219/3/032057](https://doi.org/10.1088%2F1742-6596%2F219%2F3%2F032057). DOI: [10.1088/1742-6596/219/3/032057](https://doi.org/10.1088/1742-6596/219/3/032057).
- [70] Performance of missing transverse momentum reconstruction with the atlas detector using proton–proton collisions at $\sqrt{s}=13$ TeV[J/OL]. The European Physical Journal C, 2018, 78(11):903. <https://doi.org/10.1140/epjc/s10052-018-6288-9>.
- [71] COWAN G, CRANMER K, GROSS E, et al. Asymptotic formulae for likelihood-based tests of new physics[J/OL]. Eur. Phys. J. C, 2011, 71:1554. DOI: [10.1140/epjc/s10052-011-1554-0](https://doi.org/10.1140/epjc/s10052-011-1554-0).
- [72] READ A L. Presentation of search results: theCLstechnique[J/OL]. Journal of Physics G: Nuclear and Particle Physics, 2002, 28(10):2693-2704. [https://doi.org/10.1088/0954-3899/28/10/313](https://doi.org/10.1088%2F0954-3899/28/10/313). DOI: [10.1088/0954-3899/28/10/313](https://doi.org/10.1088/0954-3899/28/10/313).
- [73] BELLOS P. Background estimation, search for heavy resonances and off-shell Higgs boson signal strength measurement in the 4 lepton final state with the ATLAS detector[EB/OL]. 2020. <http://cds.cern.ch/record/2725027>.
- [74] LEE B W, QUIGG C, THACKER H B. The Strength of Weak Interactions at Very High-Energies and the Higgs Boson Mass[J/OL]. Phys. Rev. Lett., 1977, 38:883-885. DOI: [10.1103/PhysRevLett.38.883](https://doi.org/10.1103/PhysRevLett.38.883).
- [75] CHANOWITZ M S, GAILLARD M K. The TeV Physics of Strongly Interacting W's and Z's [J/OL]. Nucl. Phys., 1985, B261:379-431. DOI: [10.1016/0550-3213\(85\)90580-2](https://doi.org/10.1016/0550-3213(85)90580-2).
- [76] SZLEPER M. The Higgs boson and the physics of WW scattering before and after Higgs discovery[J]. 2014.
- [77] Evidence for electroweak production of $W^\pm W^\pm jj$ in pp collisions at $\sqrt{s} = 8$ TeV with the atlas detector[J/OL]. Phys. Rev. Lett., 2014, 113:141803. <https://link.aps.org/doi/10.1103/PhysRevLett.113.141803>.

- sRevLett.113.141803.
- [78] Observation of electroweak production of a same-sign w boson pair in association with two jets in pp collisions at $\sqrt{s} = 13$ TeV with the atlas detector[J/OL]. Phys. Rev. Lett., 2019, 123: 161801. <https://link.aps.org/doi/10.1103/PhysRevLett.123.161801>.
- [79] SIRUNYAN A M, et al. Observation of electroweak production of same-sign W boson pairs in the two jet and two same-sign lepton final state in proton-proton collisions at $\sqrt{s} = 13$ TeV [J/OL]. Phys. Rev. Lett., 2018, 120(8):081801. DOI: [10.1103/PhysRevLett.120.081801](https://doi.org/10.1103/PhysRevLett.120.081801).
- [80] Observation of electroweak $w \pm z$ boson pair production in association with two jets in pp collisions at $s=13$ tev with the atlas detector[J/OL]. Physics Letters B, 2019, 793:469 - 492. <http://www.sciencedirect.com/science/article/pii/S0370269319303211>. DOI: <https://doi.org/10.1016/j.physletb.2019.05.012>.
- [81] Measurement of vector boson scattering and constraints on anomalous quartic couplings from events with four leptons and two jets in proton–proton collisions at $s=13$ tev[J/OL]. Physics Letters B, 2017, 774:682 - 705. <http://www.sciencedirect.com/science/article/pii/S0370269317308328>. DOI: <https://doi.org/10.1016/j.physletb.2017.10.020>.
- [82] AAD G, et al. Observation of electroweak production of two jets and a Z -boson pair with the ATLAS detector at the LHC[J]. 2020.
- [83] ZHU H. Measurement of inclusive cross section and observation of electroweak production of two jets in association with a Z -boson pair in pp collisions at $\sqrt{s} = 13$ TeV with the ATLAS detector: ATL-PHYS-PROC-2020-032[R/OL]. Geneva: CERN, 2020. <https://cds.cern.ch/record/2714092>.
- [84] ALWALL J, FREDERIX R, FRIXIONE S, et al. The automated computation of tree-level and next-to-leading order differential cross sections, and their matching to parton shower simulations[J/OL]. JHEP, 2014, 07:079. DOI: [10.1007/JHEP07\(2014\)079](https://doi.org/10.1007/JHEP07(2014)079).
- [85] BALL R D, et al. Parton distributions with LHC data[J/OL]. Nucl. Phys. B, 2013, 867:244-289. DOI: [10.1016/j.nuclphysb.2012.10.003](https://doi.org/10.1016/j.nuclphysb.2012.10.003).
- [86] GLEISBERG T, HÖCHE S, KRAUSS F, et al. Event generation with SHERPA 1.1[J/OL]. JHEP, 2009, 02:007. DOI: [10.1088/1126-6708/2009/02/007](https://doi.org/10.1088/1126-6708/2009/02/007).
- [87] BALL R D, et al. Parton distributions for the LHC run II[J/OL]. JHEP, 2015, 04:040. DOI: [10.1007/JHEP04\(2015\)040](https://doi.org/10.1007/JHEP04(2015)040).
- [88] CAOLA F, MELNIKOV K, RÖNTSCH R, et al. Qcd corrections to zz production in gluon fusion at the lhc[J/OL]. Phys. Rev. D, 2015, 92:094028. <https://link.aps.org/doi/10.1103/PhysRevD.92.094028>.
- [89] FRIXIONE S, RIDOLFI G, NASON P. A positive-weight next-to-leading-order Monte Carlo for heavy flavour hadroproduction[J/OL]. JHEP, 2007, 09:126. DOI: [10.1088/1126-6708/2007/09/126](https://doi.org/10.1088/1126-6708/2007/09/126)

- [07/09/126.](#)
- [90] LAI H L, et al. New parton distributions for collider physics[J/OL]. Phys. Rev. D, 2010, 82: 074024. DOI: [10.1103/PhysRevD.82.074024](https://doi.org/10.1103/PhysRevD.82.074024).
- [91] ALIOLI S, NASON P, OLEARI C, et al. NLO single-top production matched with shower in POWHEG: s- and t-channel contributions[J/OL]. JHEP, 2009, 09:111. DOI: [10.1088/1126-6708/2009/09/111](https://doi.org/10.1088/1126-6708/2009/09/111).
- [92] FREDERIX R, RE E, TORRIELLI P. Single-top t-channel hadroproduction in the four-flavour scheme with POWHEG and aMC@NLO[J/OL]. JHEP, 2012, 09:130. DOI: [10.1007/JHEP09\(2012\)130](https://doi.org/10.1007/JHEP09(2012)130).
- [93] RE E. Single-top Wt-channel production matched with parton showers using the POWHEG method[J/OL]. Eur. Phys. J. C, 2011, 71:1547. DOI: [10.1140/epjc/s10052-011-1547-z](https://doi.org/10.1140/epjc/s10052-011-1547-z).
- [94] COLLABORATION A. ATLAS Pythia 8 tunes to 7 TeV data[M/OL]. 2014. <https://cds.cern.ch/record/1966419>.
- [95] ATLAS Collaboration. Performance of pile-up mitigation techniques for jets in pp collisions at $\sqrt{s} = 8$ TeV using the ATLAS detector[J/OL]. Eur. Phys. J. C, 2016, 76:581. DOI: [10.1140/epjc/s10052-016-4395-z](https://doi.org/10.1140/epjc/s10052-016-4395-z).
- [96] BELLM J, et al. Herwig 7.0/Herwig++ 3.0 release note[J/OL]. Eur. Phys. J. C, 2016, 76(4): 196. DOI: [10.1140/epjc/s10052-016-4018-8](https://doi.org/10.1140/epjc/s10052-016-4018-8).
- [97] BAHR M, et al. Herwig++ Physics and Manual[J/OL]. Eur. Phys. J. C, 2008, 58:639-707. DOI: [10.1140/epjc/s10052-008-0798-9](https://doi.org/10.1140/epjc/s10052-008-0798-9).
- [98] Luminosity determination in pp collisions at $\sqrt{s} = 13$ TeV using the ATLAS detector at the LHC: ATLAS-CONF-2019-021[R/OL]. Geneva: CERN, 2019. <http://cds.cern.ch/record/2677054>.
- [99] The new LUCID-2 detector for luminosity measurement and monitoring in ATLAS[J/OL]. Journal of Instrumentation, 2018, 13(07):P07017-P07017. [https://doi.org/10.1088/1748-0221/13/07/p07017](https://doi.org/10.1088/1748-0221/2F13%2F07%2Fp07017). DOI: [10.1088/1748-0221/13/07/p07017](https://doi.org/10.1088/1748-0221/13/07/p07017).
- [100] COADOU Y. Boosted decision trees and applications[J/OL]. EPJ Web of Conferences, 2013, 55:02004-. DOI: [10.1051/epjconf/20135502004](https://doi.org/10.1051/epjconf/20135502004).
- [101] COLLABORATION A. Technical Design Report for the ATLAS Inner Tracker Pixel Detector: CERN-LHCC-2017-021. ATLAS-TDR-030[R/OL]. Geneva: CERN, 2017. <https://cds.cern.ch/record/2285585>.
- [102] COLLABORATION A. Technical Design Report for the Phase-II Upgrade of the ATLAS Muon Spectrometer: CERN-LHCC-2017-017. ATLAS-TDR-026[R/OL]. Geneva: CERN, 2017. <https://cds.cern.ch/record/2285580>.
- [103] COLLABORATION A. Technical Proposal: A High-Granularity Timing Detector for the AT-

Bibliography

- LAS Phase-II Upgrade: CERN-LHCC-2018-023. LHCC-P-012[R/OL]. Geneva: CERN, 2018. <https://cds.cern.ch/record/2623663>.
- [104] Expected performance for an upgraded ATLAS detector at High-Luminosity LHC: ATL-PHYS-PUB-2016-026[R/OL]. Geneva: CERN, 2016. <https://cds.cern.ch/record/2223839>.
- [105] HILL A, VAN DER BIJ J J. Strongly interacting singlet-doublet higgs model[J/OL]. Phys. Rev. D, 1987, 36:3463-3473. <https://link.aps.org/doi/10.1103/PhysRevD.36.3463>.
- [106] DAVOUDIASL H, HEWETT J, RIZZO T. Bulk gauge fields in the randall–sundrum model1work supported by the department of energy, contract de-ac03-76sf00515.1[J/OL]. Physics Letters B, 2000, 473(1):43 - 49. <http://www.sciencedirect.com/science/article/pii/S03700269399014306>. DOI: [https://doi.org/10.1016/S0370-2693\(99\)01430-6](https://doi.org/10.1016/S0370-2693(99)01430-6).
- [107] AAD G, et al. Search for heavy resonances decaying into a pair of Z bosons in the $\ell^+\ell^-\ell'^+\ell'^-$ and $\ell^+\ell^-\nu\bar{\nu}$ final states using 139 fb^{-1} of proton-proton collisions at $\sqrt{s} = 13 \text{ TeV}$ with the ATLAS detector[J]. 2020.
- [108] FREDERIX R, FRIXIONE S. Merging meets matching in MC@NLO[J/OL]. JHEP, 2012, 12: 061. DOI: [10.1007/JHEP12\(2012\)061](https://doi.org/10.1007/JHEP12(2012)061).
- [109] AGASHE K, DAVOUDIASL H, PEREZ G, et al. Warped Gravitons at the LHC and Beyond [J/OL]. Phys.Rev., 2007, D76:036006. DOI: [10.1103/PhysRevD.76.036006](https://doi.org/10.1103/PhysRevD.76.036006).
- [110] ATLAS Collaboration. Jet reconstruction and performance using particle flow with the ATLAS Detector[J/OL]. Eur. Phys. J. C, 2017, 77:466. DOI: [10.1140/epjc/s10052-017-5031-2](https://doi.org/10.1140/epjc/s10052-017-5031-2).
- [111] BRADLEY A P. The use of the area under the roc curve in the evaluation of machine learning algorithms[J/OL]. Pattern Recognition, 1997, 30(7):1145 - 1159. <http://www.sciencedirect.com/science/article/pii/S0031320396001422>. DOI: [https://doi.org/10.1016/S0031-3203\(96\)00142-2](https://doi.org/10.1016/S0031-3203(96)00142-2).
- [112] BALDI P, CRANMER K, FAUCETT T, et al. Parameterized neural networks for high-energy physics[J/OL]. Eur. Phys. J. C, 2016, 76(5):235. DOI: [10.1140/epjc/s10052-016-4099-4](https://doi.org/10.1140/epjc/s10052-016-4099-4).
- [113] Cousins R D, Linnemann J T, Tucker J. Evaluation of three methods for calculating statistical significance when incorporating a systematic uncertainty into a test of the background-only hypothesis for a Poisson process[J/OL]. Nuclear Instruments and Methods in Physics Research A, 2008, 595(2):480-501. DOI: [10.1016/j.nima.2008.07.086](https://doi.org/10.1016/j.nima.2008.07.086).
- [114] Measurements of higgs boson production and couplings in the four-lepton channel in pp collisions at center-of-mass energies of 7 and 8 tev with the atlas detector[J/OL]. Phys. Rev. D, 2015, 91:012006. <https://link.aps.org/doi/10.1103/PhysRevD.91.012006>.
- [115] CRANMER K S. Kernel estimation in high-energy physics[J/OL]. Comput. Phys. Commun., 2001, 136:198-207. DOI: [10.1016/S0010-4655\(00\)00243-5](https://doi.org/10.1016/S0010-4655(00)00243-5).
- [116] OREGLIA M. A Study of the Reactions $\psi' \rightarrow \gamma\gamma\psi$ [M/OL]. SLAC, 1980. <https://www.slac.stanford.edu/cgi-bin/getdoc?10232/1/oreglia.pdf>

Bibliography

- [tanford.edu/cgi-wrap/getdoc/slac-r-236.pdf](https://www.slac.stanford.edu/cgi-wrap/getdoc/slac-r-236.pdf).
- [117] GAISER J. Charmonium Spectroscopy From Radiative Decays of the J/ψ and ψ' [M/OL]. SLAC, 1982. <https://www.slac.stanford.edu/cgi-wrap/getdoc/slac-r-255.pdf>.
- [118] GORIA S, PASSARINO G, ROSCO D. The Higgs Boson Lineshape[J/OL]. Nucl.Phys., 2012, B864:530-579. DOI: [10.1016/j.nuclphysb.2012.07.006](https://doi.org/10.1016/j.nuclphysb.2012.07.006).
- [119] SPIRA M, DJOUADI A, GRAUDENZ D, et al. Higgs boson production at the LHC[J]. Nucl. Phys., 1995, B 453:17-82.
- [120] BALL R D, et al. Parton Distribution Benchmarking with LHC Data[J/OL]. JHEP, 2013, 04: 125. DOI: [10.1007/JHEP04\(2013\)125](https://doi.org/10.1007/JHEP04(2013)125).
- [121] BIJNENS J, EEROLA P, MAUL M, et al. Qcd signatures of narrow graviton resonances in hadron colliders[J/OL]. Physics Letters B, 2001, 503(3-4):341-348. DOI: [10.1016/s0370-2693\(01\)00238-6](https://doi.org/10.1016/s0370-2693(01)00238-6).
- [122] ATLAS Collaboration. PMG Systematic Uncertainty Recipes[EB/OL]. <https://twiki.cern.ch/twiki/bin/view/AtlasProtected/PmgSystematicUncertaintyRecipes>.
- [123] GROSS E, VITELLS O. Trial factors for the look elsewhere effect in high energy physics [J/OL]. Eur. Phys. J. C, 2010, 70:525-530. DOI: [10.1140/epjc/s10052-010-1470-8](https://doi.org/10.1140/epjc/s10052-010-1470-8).
- [124] AABOUD M, et al. Search for heavy ZZ resonances in the $\ell^+\ell^-\ell^+\ell^-$ and $\ell^+\ell^-v\bar{v}$ final states using proton–proton collisions at $\sqrt{s} = 13$ TeV with the ATLAS detector[J/OL]. Eur. Phys. J. C, 2018, 78(4):293. DOI: [10.1140/epjc/s10052-018-5686-3](https://doi.org/10.1140/epjc/s10052-018-5686-3).